Title
Understanding Type II-Plateau Supernovae and the Red Supergiants that Cause Them

Permalink
https://escholarship.org/uc/item/65m867f0

Author
Goldberg, Jared Austin

Publication Date
2022

Peer reviewed|Thesis/dissertation

UNIVERSITY of CALIFORNIA
Santa Barbara

Understanding Type II-Plateau Supernovae and the Red Supergiants that Cause Them

A dissertation submitted in partial satisfaction of the
requirements for the degree of

Doctor of Philosophy

in

Physics

by

Jared A. Goldberg

Committee in charge:

Professor Lars Bildsten, Chair

Professor D. Andrew Howell

Professor Omer Blaes

September 2022

The dissertation of Jared A. Goldberg is approved:

Professor Omer Blaes

Professor D. Andrew Howell

Professor Lars Bildsten, Chair

August 2022

This work is dedicated to those who have recycled their supernova-enriched material back into the universe before they got a chance to see its culmination. It is dedicated to the stable spirit of Dr. Ernestina Konig. It is dedicated to the watchful eye of Anita Schonbrun. It is dedicated to Arnold Schonbrun and Ruth-Ann Kalisher, whose conversion back to stardust punctuated the first and final years of my PhD studies. It is dedicated to Fern and Paco, to Bracha, to Joan, to Boris, to Eddie. To Rosie. To ancestors throughout the cosmos.

Their memories are so much more than a blessing.

Acknowledgements

I would like to start by acknowledging the tremendous privilege it is to be able to do this work, and to be welcomed into the astronomical community.

My PhD advisor, Lars Bildsten, once quoted that the key to a good life is working on difficult problems with good people. This dissertation exists because I have been very fortunate to have had such a good life. So first and foremost, I thank Lars for the years of thought-provoking conversations, guidance, patience, encouragement, feedback, and support. Your insight into all things stellar is expansive, your love for astrophysics genuine and inspiring, and your leadership unparalleled. My development as a researcher, writer, scientist, and human is astronomically better for having you as a mentor and colleague, and I look forward to our continued collaboration.

I must next thank Bill Paxton, without whom none of this work would be possible, as well as Josiah Schwab, and the whole MESA Development team. You have revolutionized the field towards open-source, reproducible work, sending ripples through all of astronomy. I also thank Yan-Fei Jiang for scientific guidance, technical expertise, and for implementing and utilizing these tools to solve incredibly challenging problems. I would also like to recognize the tremendous value of my conversations and connections within the Zwicky Transient Facility Theory Network, MESA Development network, academic conferences, and all of our extended collaborations. I especially thank Eliot Quataert and Dan Kasen, Frank Timmes, Rich Townsend, Anne Thoul.

I would also like to thank the other members of my committee, Andy Howell and Omer Blaes, for their moral and intellectual support and guidance throughout my PhD. I also must acknowledge the many phenomenal professors I have had the pleasure of learning from during my studies at UCSB. I recall particularly enlightening and enjoyable courses with Omer Blaes, Tim Brandt, Gary Horowitz, Crystal Martin, and Peng Oh, as well as exciting discussions in less formal settings with professors Max Miller-Blanchaer, Teja Nerella, Jean Carlson, and many others. I would also like to acknowledge my colleagues in the Santa Barbara City College Earth and Planetary Sciences Department, especially Sean Kelly and Erin O'Connor in the Astronomy group, and also Bill Dinklage, Kristen Sneddon, Geordie Armstrong, and Stephanie Mendes, for conversations about teaching, equity, justice, society, and more. I also thank the SBCC Museum of Natural History staff, especially the planetarium support from Javier Rivera and Krissie Cook, and Jacques the security guard for putting up with my presence right up until closing time. I also thank my students for adding your own insights and perspectives and questions and inquiry, for inspiring clarity, and for laughing at my jokes. I thank the KITP staff for making me and many other scholars feel at home, especially but in no meaningful order Lisa Stewart, Bibiana Rojas, Mark Bowick, Susie Groves, Alina Gutierrez, Kristi Newton, Maggie Sherriffs, and Craig Kunimoto. Perhaps most importantly, I thank the custodians, groundskeepers, support staff, and all those who maintain our spaces and enable us to do this work. Without you, science and discovery and society do not and cannot progress.

I am deeply grateful for the passion for teaching embodied and instilled during my

Undergraduate at Claremont McKenna College and in particular the W. M. Keck Science Department joint with Pitzer College and Scripps College. I thank the entire Keck Science Department for my development as a learner and lover of physics, and for empowering me to come to graduate school in the first place. I want to give special thanks to Kevin Moore, my undergraduate thesis advisor, who introduced me to this whole world of stellar evolution. I am also grateful to Adam Landsberg for the spark that ignited my passion for physics and support along the way, to Scot Gould for advising me throughout my undergraduate years, and to Steve Naftilan z"l and Jim Higdon for encouraging my astronomical and computational interests, respectively. I am grateful for the technical support of the late Boyle Ke when I was just learning what it meant to ssh into a supercomputer. I am grateful also for the intellectual development afforded to me by the CMC Philosophy department, and particularly inspiring conversations and courses with Amy Kind, James Kreines, Dustin Locke, Suzanne Obdrzalek, and Alex Rajczi. I thank Eric Helland for introducing me to academic research.

My friends and colleagues in and out of academia also made this work possible. I especially thank the other members of the Bildsten group for vibrant conversations and insight, computational prowess, aesthetic feedback, and so much more. Thank you to my academic "siblings" Bill Wolf, Jared Brooks, Evan Bauer, Will Schultz, and Sunny Wong, grad fellows Matthieu Renzo, Joel Zinn, and Marcus DuPont, former and current postdocs Jennifer Barnes, Matteo Cantiello, Jim Fuller, Yan-fei Jiang, Adam Jermyn, Rocio Kiman, May Gade Pedersen, Benny Tsang, and Chris White. It has also been a pleasure to converse with and learn from my other officemates, Suoqing Ji, Stephanie Ho, and Zixuan Peng.

I also must acknowledge the astro group grad students, especially the LCOGT clan including Daichi Hiramatsu, Jamie Burke, Estefania Padilla-Gonzalez, Megan Newsome, Craig Pellegrino, and Griffin Hosseinzadeh, for invigorating conversations about transient observations, as well as Mirek Brandt, Sarah Steiger, Noah Swimmer, and Molly Wolfson. I thank those friends who have allowed me to flourish at home: Mark Arildsen, Jakkarin Lingwongyut, Adolfo Holguin, Mike Lipatov, and Qile Wu. I thank my fellow Santa Barbarians (again in no particular order) Katharine Dickson, Harrison Tasoff, Amber Cai, Dan Kutner, Farzan Vafa, Peter Dotti, Isabel Lipartito, Neelay Fruitwala, Eric Jones, Dillon Cislo, Joe Swearngin, Alex Dorsett, Jenni Smith, Zach Porter, Nic Zobrist, Dylan Nesbit, Byron Mayes, Gabi Abraham and Bryant Baker, and Kieutran Phan. I have also been lucky enough to have many old friends who have been a crucial source of moral support throughout these years: Kate Jesse, Genevieve Donahey, Jessica Valenzuela, Nicole Orozco, Ted Hall, Amanda McQuade, Marcel Hite, Angelo Liao, Lawrence Beall, Andrew Clary and Angel Key, Nina Kamath, Caroline Lu, Rachel Choi, Andrew Atwong, Chris Rojas, Vicky Bouche; Carl Fields, Ignacio Magana, Samantha Usman, Eve Chase, Megan Kelly; Heather and Josh Epstein, Aaron Nelson; Geordan Waldman and Brigand Blake, Sumedh and Megan Shah, Josh Andersen, Cavan Donohoe, Jason and Savannah Avina, Maegan Richards. There are many more Finally, I would not have made it through these recent years without Zarina Dhillon. You empower me to constantly grow as a learner, teacher, ally, and human; you inspire excitement and awe about the universe in the face of a challenging world; you bring the stars to life.

These acknowledgements cannot be complete without expressing my limitless gratitude for the boundless support of my family, who empower me to ask questions, think deeply, and investigate the world. You have been supportive of my education from the time I was learning to count and checking out How the Coyote Stole The Sun from the library every single week, to now, when my permanent Sun-related library loan items are textbooks on shock waves and radiation-hydrodynamics and stellar structure. I do not have the words to even come close to capturing my gratitude for my parents, Gil and Cindy, for everything you've done and for your support on every journey I've ever embarked on. Nor my grandparents, Maya, Richard (and Becky), Myron (and Doreen), and Anita, for shaping our family into lovers-of-learning. Nor my many aunts, uncles, cousins, extended family, who have shared in all manner of roles in my development as a scholar and human. And it would be literally impossible to overstate my gratitude for my siblings, Shai and Eden — my life-long closest friends. You taught me how to ask and how to answer, how to play (and how to learn, think, work, speak, grow), and perhaps most essentially to science, how to collaborate.

I am certain that there are individuals and entire groups of people who deserve acknowledgement whose names may not appear above. If you the reader are one of such names, it is no less true that you mean the universe to me.

Curriculum Vitæ

Jared A. Goldberg

Education

2022	*Ph.D., Physics*, University of California, Santa Barbara, CA, USA
2019	*M.A., Physics*, University of California, Santa Barbara, CA, USA
2016	*B.A., Physics & B.A., Philosophy*, Claremont McKenna College, Claremont, CA, USA

Publications

"Shock Breakout in Three-Dimensional Red Supergiant Envelopes," **Jared A. Goldberg**, Yan-fei Jiang, and Lars Bildsten, *The Astrophysical Journal, 933, 164* (2022b)

"Numerical Simulations of Convective Three-Dimensional Red Supergiant Envelopes," **Jared A. Goldberg**, Yan-fei Jiang, and Lars Bildsten, *The Astrophysical Journal*, 929, 156 (2022a)

"The Electron-Capture Origin of Supernova 2018zd," Daichi Hiramatsu, D. Andrew Howell, Schuyler D. Van Dyk, **Jared A. Goldberg,** et al., Nature Astronomy (2021b)

"Luminous Type II Short-Plateau Supernovae 2006Y, 2006ai, and 2016egz: A Transitional Class from Stripped Massive Red Supergiants," Daichi Hiramatsu, D. Andrew Howell, Takashi J. Moriya, **Jared A. Goldberg,** et al., The Astrophysical Journal, 913, 55 (2021a)

"Comparing Moment-based and Monte Carlo Methods of Radiation Transport Modeling for Type II-Plateau Supernova Light Curves," Benny Tsang, **Jared A. Goldberg**, Lars Bildsten, and Daniel Kasen, The Astrophysical Journal, 898, 29 (2020)

"The Value of Progenitor Radius Measurements for Explosion Modeling of Type II-Plateau Supernovae," **Jared A. Goldberg** and Lars Bildsten, *The Astrophysical Journal Letters*, 895L, 45 (2020)

"A Massive Star's Dying Breaths: Pulsating Red Supergiants and Their Resulting Type IIP Supernovae," **Jared A. Goldberg**, Lars Bildsten, and Bill Paxton, *The Astrophysical Journal*, 891, 15 (2020)

“Modules for Experiments in Stellar Astrophysics (MESA): Pulsating Variable Stars, Rotation, Convective Boundaries, and Energy Conservation,” Bill Paxton, et al. including **Jared A. Goldberg**, The Astrophysical Journal Supplement Series, 243, 10 (2019)

“Inferring Explosion Properties from Type II-Plateau Supernova Light Curves,” **Jared A. Goldberg**, Lars Bildsten, and Bill Paxton, *The Astrophysical Journal*, 879, 3 (2019)

“Modules for Experiments in Stellar Astrophysics (MESA): Convective Boundaries, Element Diffusion, and Massive Star Explosions,” Bill Paxton, et al. including **Jared A. Goldberg**, *The Astrophysical Journal Supplement Series*, 234, 34 (2018)

Abstract

Understanding Type II-Plateau Supernovae and the Red Supergiants that Cause Them

by

Jared A. Goldberg

Observations of the transient, explosive deaths of massive stars are well-poised to provide insight into stellar physics when combined with theoretical understanding. From spherically symmetric stellar evolution models, we confirm and sharpen early analytic calculations for the Supernova (SN) plateau luminosity and duration as a function of the red supergiant (RSG) progenitor properties. When the RSG radius at the time of the explosion is known, we show how the explosion energy and ejecta mass can be directly inferred; otherwise, we show that a family of explosions could produce the same plateau luminosity, duration, and photospheric velocity. We also explore the impact of large-scale radial stellar pulsations on these predictions. Then, motivated in part as an effort to understand the turbulent outer envelope responsible for early-time SN emission, we complete global 3D radiation-hydrodynamics (RHD) simulations of RSG envelopes with Athena++. These simulations reveal an extended density structure with large-scale convective plumes spanning large fractions of the stellar surface. These computations also provide insights to guide evolutionary modeling efforts, such as a physically-motivated calibration of the convective mixing length which helps determine the envelope density structure. Driving a strong shock through these 3D simulations, we then show novel results on how the inhomogeneous 3D convective structure leads to a longer-duration, fainter shock breakout (SBO) signal compared to predictions from semi-analytic and spherically-symmetric models.

Contents

Chapter 1

Introduction

1.1 Background

As massive ($9M_\odot \lesssim M \lesssim 25M_\odot$) stars approach the end of their lives, they expand to become Red Supergiants (RSGs), which are characterized by their cool effective temperatures ($T_{\rm eff} \lesssim 4000$K), large stellar radii ($R \approx 300 - 1200R_\odot$), and relatively high luminosities ($L \approx 10^4 - 10^{5.5}L_\odot$) (see, e.g. Levesque et al., 2006; Drout et al., 2012; Massey et al., 2021). Although their luminosity is generated in the core via nuclear fusion of He, C, O, and heavier and heavier elements, their observable properties are primarily moderated by the physics of their hydrogen-rich, fully-convective stellar envelope and the outer surface layers. These dynamic outer layers are also intrinsically variable, in many cases exhibiting large-amplitude fluctuations in brightness caused both by coherent oscillation modes (e.g. Kiss et al. 2006; Soraisam et al. 2018; Dorn-Wallenstein et al. 2020) and stochastic convective processes (e.g. Ren & Jiang, 2020). Moreover, due to the low densities and large pressure scale heights ($H/R \approx 0.1 - 0.5$), individual convective plumes can span a significant fraction of the stellar envelope (see, e.g. Schwarzschild, 1975; Freytag et al., 2002). Thus, spectro-interferometric observations of nearby RSGs (e.g. Arroyo-Torres et al. 2015; Kravchenko et al. 2019, 2021; Montargès et al. 2021; Norris et al. 2021) can probe their large-scale 3D surfaces and reveal their (often asymmetric) surface properties via tomographic measurements.

As the RSG runs out of nuclear fuel, an Fe-rich core accumulates and eventually collapses under its own gravity, forming a proto-neutron star or black hole. During the collapse, neutrinos are released which drive turbulence in the core material surrounding the proto-neutron star (e.g. Janka, 2012). In many cases, this imparts sufficient energy ($\sim 10^{51}$ erg) into the star to overcome its binding energy ($\sim 10^{49} - 10^{50}$ erg), causing a strong shockwave to propagate through the star. In this explosion, the stellar envelope and outer core material mix via the Rayleigh-Taylor Instability (RTI; see e.g. Chevalier & Klein 1978; Weaver & Woosley 1980; Wongwathanarat et al. 2015; Duffell 2016; Utrobin et al. 2017). After the shock reaches the stellar surface in a bright flash called "shock breakout" (SBO; see Colgate 1968; Lasher & Chan 1979 for early work, as well as the review by Waxman & Katz 2017), the Hydrogen-rich ejecta expands and cools, emitting radiation which is observed as a Hydrogen-rich ("Type II") Supernova (SN). Once the temperature in the outer ejecta reaches the H-recombination temperature of $\approx$ 6000K, the photospheric emission reaches a "plateau" for $\approx$ 100 days, with heat trapped in the optically thick ejecta released only where the expanding envelope has cooled enough for ionized H to recombine into neutral H. Finally, once the ejecta has become optically thin, late-time emission (after ≈100 days) is powered by the radioactive decay of ^{56}Ni. In this way Type II-Plateau Supernovae (SNe-IIP) provide a unique time-lapse glimpse into the structure of the star. Emission from the outer ejecta occurring early in the SN reveals the outer stellar layers, and we see deeper and deeper "into the star" as the photosphere migrates inwards in mass coordinate in the expanding ejecta.

While this qualitative picture of the endpoint of massive stellar evolution is well-established, there are still important uncertainties left to be explained both from theoretical modeling and from observations. In fact, it is still a subject of debate which stars will collapse directly into black holes and which will explode as core-collapse SNe in the first place. At the heart of the controversy is the so-called "Missing Red Supergiant Problem," which claims that, for SNe-IIP which have both observations of the SN explosion and observations of the RSG progenitor from archival data, the stellar luminosities of confirmed SN progenitors are typically lower compared to the distribution of RSG luminosities observed in resolved stellar populations (see, e.g. Smartt, 2009, 2015; Van Dyk, 2017; Kochanek, 2020). In fact, there is an apparent lack of any observed SN-IIP progenitor with a luminosity of $\log(L/L_\odot) \gtrsim 5.2$, while particularly massive RSGs have been seen with luminosities above $10^{5.5} L_\odot$ (with some debate the statistical significance of the "problem" is subject to debate, see discussions by Davies & Beasor (2018, 2020b,a)). This is corroborated by some modeling efforts which suggest that more massive RSGs are less likely to explode (e.g. Sukhbold et al., 2016; Ertl et al., 2016; Patton & Sukhbold,

2020) with some sensitivity to input physics including nuclear reaction rates (such as C burning Sukhbold et al., 2018), core-boundary mixing (e.g. Davis et al., 2019), stellar winds (e.g. Renzo et al., 2017), and binarity (e.g. Zapartas et al., 2021).

Luckily, recent years have seen an explosion of time-domain astronomical data which can shed light on some of these uncertain physical processes, thanks to an expanding network of ground- and space-based telescopes including the Zwicky Transient Facility (ZTF; Masci et al. 2019), the Dark Energy Survey (DES; Flaugher et al. 2015), the All-Sky Automated Survey for Supernovae (ASAS-SN; Shappee et al. 2014; Kochanek et al. 2017b), Las Cumbres Observatory (LCOGT; Brown et al. 2013a) and its Global Supernova Project, and many others. And this wealth of data will expand with upcoming surveys — starting in 2023, the Vera Rubin Observatory will revolutionize time-domain astronomy with repeated nightly imaging of the entire sky with outstanding spatial resolution in its Legacy Survey of Space and Time (LSST; Ivezić et al. 2019). Additionally, from around Fall 2024, the ULTRASAT mission (Sagiv et al., 2014; Asif et al., 2021) will capture hundreds of elusive ultraviolet SN SBOs from space, which have only been seen in a few serendipitous detections by NASA's GALEX mission (2003-2013). Because SNe encode information about the stellar physics, such observations have the potential to yield insights into the structure, composition, explosion mechanism, and environments surrounding stars as they end their lives. This carries implications beyond constraining stellar physics; for example, SNe inject thermal and kinetic energy into the circumstellar and interstellar medium, leading to feedback which drives galactic winds and strews heavy elements into the universe (e.g. Hopkins et al., 2014). Ongoing theoretical work is therefore valuable in order to uncover the underlying physical properties of observed events and realize the data's scientific potential.

To this end, there has been considerable work describing the relationship between SN lightcurves and the bulk properties of their progenitor stars (e.g. Arnett, 1980; Litvinova & Nadyozhin, 1983; Popov, 1993; Kasen & Woosley, 2009; Nagy et al., 2014; Nagy & Vinkó, 2016; Nakar et al., 2016; Sukhbold et al., 2016; Shussman et al., 2016b). These works yield a variety of analytically-motivated scaling relations for observables such as the plateau brightness at day 50 L_{50} and the plateau duration t_{p}, with the mass of the H-rich ejecta M_{ej}, explosion energy E_{exp}, and progenitor radius R, built on a variety of assumptions for the composition, density, opacity, and velocity structure of the ejecta. This work has been complemented by detailed numerical studies calculated for suites of stellar evolution models evolved assuming spherical symmetry (1D models), such as the work of, e.g., Kasen & Woosley (2009); Dessart & Hillier (2010); Dessart et al. (2013, 2017); Bersten et al. (2011); Morozova et al. (2016); Sukhbold et al. (2016); Martinez & Bersten (2019); Eldridge et al. (2019). When combined with data, these theoretical efforts can shed light on physical prescriptions which can be fed back into 1D stellar models. For example, Dessart et al. 2013 found that spectroscopic models of observed SNe-IIP favor smaller-radius progenitors for a given ejecta mass than most stellar evolution codes at the time were producing, which can be rectified by using a larger convective efficiency parameter α in the H-rich envelope (which we discuss further in Chapter 5).

Predictions for the SN emission across a range of explosions also enable parameter-space studies comparing grids of models to samples of observed SNe. In some cases, direct recovery of $M_{\rm ej}$, $E_{\rm exp}$, R is claimed by matching models to individual observed SNe, such as Pejcha & Prieto (2015b) using the scaling relations from Litvinova & Nadyozhin (1983); Popov (1993) to recover explosion energies, radii, and ejecta masses from the bolometric lightcurves from their (Pejcha & Prieto, 2015a) sample. We discuss the value and limitations of such approaches in in Chapters 2 and 4.

At early times ($t \lesssim 20-30$ days) SN-IIP emission comes from the shock breakout (Lasher & Chan, 1979; Matzner & McKee, 1999; Katz et al., 2010; Waxman & Katz, 2017) and radiative shock-cooling (such as Nakar & Sari, 2010; Rabinak & Waxman, 2011; Sapir et al., 2011; Katz et al., 2012; Sapir et al., 2013; Morozova et al., 2016; Shussman et al., 2016a; Sapir & Waxman, 2017; Faran et al., 2019) of the outermost $\lesssim 0.01-0.1 M_\odot$ of material. The density structure of that material is uncertain, and potentially three-dimensional in nature, yielding differences between models of early lightcurves for different assumed progenitor model surface profiles. Moreover, even beyond the theoretical uncertainties, observations of these epochs often show an excess in luminosity compared to 1D explosion models with "barren" photospheres (e.g. Khazov et al., 2016; Förster et al., 2018; Hosseinzadeh et al., 2018). These early lightcurves are then fit by invoking additional circumstellar material (CSM) around the progenitor model (e.g. Dessart et al., 2017; Moriya et al., 2017, 2018; Morozova et al., 2017, 2018), often assumed to be in the form of a dense wind with $\rho(r) \propto 1/r^2$, though recent efforts have calculated self-consistent CSM profiles due to mass-loss due to pre-supernova outburts in 1D (Morozova et al., 2019) and 3D (Tsang et al., 2022). Moreover, the outer structure may be influenced by the presence of large-scale 3D asymmetries seen in both simulations and observations of RSG stellar envelopes, which are by design absent in spherically symmetric models.

1.2 Summary

This dissertation complements and builds upon this body of theoretical work, exploring the relationship between various properties of Red Supergiant stellar structure and the impact on the SN emission in their ensuing explosions. Chapter 2 (Goldberg et al., 2019) begins by characterizing the relationship between bulk properties of the explosion, namely $M_{\rm ej}$, $E_{\rm exp}$, and R, with properties of the lightcurve, such as L_{50}, $t_{\rm p}$, and the observable ET (Nakar et al., 2016). We confirm and sharpen early analytical scaling relations for these SN observables with stellar properties, but show that measurements of the photospheric velocity during the plateau phase cannot be simply leveraged to lift degeneracies inherent in lightcurve modeling. Rather, for a given SN, we find that a family of explosions will produce the same light curve and velocities on the plateau.

Chapter 3 (Goldberg et al., 2020) goes beyond bulk properties of static RSG models by exploring the implications of large-amplitude radial pulsations for the resulting SN emission. We find that the effects of fundamental-mode pulsations are well-described by the scalings introduced in Chapter 2 between lightcurve observables and the stellar radius for a hydrostatic star. However, if a star is pulsating in an overtone, with some regions of the star undergoing expansion and other regions undergoing contraction at the moment of explosion, then the resulting SN reveals the progenitor's over-dense or under-dense interior structure depending on the location of the SN photosphere within the ejecta as a function of time.

Keeping in mind the uncertainties in R due to stellar pulsations, but armed with the confidence that the effects of R at the moment of the explosion are generally well-described by the scaling relations in Chapter 2, Chapter 4 (Goldberg & Bildsten, 2020) then leverages those relations to estimate the families of possible explosion properties for a selection of observed SNe with independent constraints on the progenitor radius. We show that a huge grid of progenitor models which takes into account reasonable uncertainties in 1D stellar evolution modeling prescriptions and input physics (such as rotation, the efficiency of convection, convective boundary mixing, and wind mass-loss rates) spans nearly the entire $M_{\rm ej} - R$ parameter space expected for RSGs. This allows us to produce multiple valid models for each SN with $> 50\%$ variations in $M_{\rm ej}$, $E_{\rm exp}$, and R; constraints on the progenitor radius then allow $E_{\rm exp}$ and $M_{\rm ej}$ to be further recovered to within $\approx 20\%$.

Motivated in part by the desire to understand the outermost layers of the RSG envelope, which might then enable the ability to extract additional information from early-time observations, we turn to global 3D radiation-hydrodynamics (RHD) simulations of RSG envelopes with `Athena++`, which are described in Chapter 5 (Goldberg et al., 2022).

This work reveals a number of interesting properties of convection in the RSG envelope regime, including a radius, $R_{\rm corr}$, around which the nature of the convection changes, and the presence of an outer "halo" of material much more extended than 1D stellar evolution predicts. We also use these 3D models to calibrate Mixing Length Theory (MLT; Böhm-Vitense 1958; Henyey et al. 1965) parameters used in 1D models.

The bulbous extended RSG surface, which also exhibits large-scale fluctuations in density, velocity, and temperature in agreement with the work of (Chiavassa et al., 2011a), is exactly the region responsible for early SN emission. Therefore, in Chapter 6 (Goldberg et al., 2022), we develop and validate a method to deposit a strong SN shock into the simulation domain of our 3D envelope models, and calculate the resulting shock breakout emission. The extended halo entails a SBO at lower densities than in 1D models, and the large-scale density fluctuations cause the shock to break out at different radii at different times, prolonging the SBO duration (which is in better agreement with existing observations). While these intrinsically 3D properties eliminate the possibility of using observed rise times to directly measure R, they also suggest that observations of the UV SBO encode and therefore could probe the 3D surface inhomogeneity in the outer RSG layers.

Finally, we discuss some implications of this work, open questions, and possible future directions in Chapter 7.

1.3 Software

This work makes extensive use of the open-source software instrument `MESA` (Modules for Experiments in Stellar Astrophysics). The `MESA` instrument papers are often referred to using roman numerals: Paxton et al. (2011, MESA I), Paxton et al. (2013, MESA II), Paxton et al. (2015, MESA III), Paxton et al. (2018, MESA IV), Paxton et al. (2019, MESA V), and Jermyn et al. (2022, MESA VI). Additionally, Chapter 3 utilizes the `GYRE` stellar pulsation software (Townsend & Teitler, 2013; Townsend et al., 2018). Chapters 2, 3, and 4 make extensive use of the open-source version of the multi-group radiation-hydrodynamics software `STELLA` (Blinnikov & Sorokina, 2004; Baklanov et al., 2005; Blinnikov et al., 2006). Chapters 5 and 6 utilize the 3D fluid simulation software instrument `Athena++` (Stone et al., 2020), and in particular, the radiation-hydrodynamics modules described by Jiang et al. (2014); Jiang (2021).

Analysis made significant use of the following packages: `py_mesa_reader` (Wolf & Schwab, 2017), `NumPy` (Harris et al., 2020), `SciPy` (Virtanen et al., 2020), and `matplotlib` (Hunter, 2007). Figure colors made use of the additional `python` packages `cmocean` (Thyng et al., 2016) and `cmasher` (van der Velden, 2020).

1.4 Permissions and Attributions

1. The content of Chapter 2 and Appendices A and B are adapted and reproduced from Goldberg et al. (2019) with permission from *The Astrophysical Journal*.

2. The content of Chapter 3 is adapted and reproduced from Goldberg et al. (2020) with permission from *The Astrophysical Journal*.
3. The content of Chapter 4 is adapted and reproduced from Goldberg & Bildsten (2020) with permission from *The Astrophysical Journal Letters*.
4. The content of Chapter 5 and Appendices C and D are adapted and reproduced from Goldberg et al. (2022) with permission from *The Astrophysical Journal*.
5. The content of Chapter 6 is adapted and reproduced from Goldberg et al. (2022) with permission from *The Astrophysical Journal*.

My graduate work has also afforded me opportunities to participate in exciting research efforts led by others (Tsang et al., 2020; Hiramatsu et al., 2021a,b) as well as two MESA instrument papers (Paxton et al., 2018, 2019), but that work does not appear in this dissertation.

Chapter 2

Inferring Explosion Properties from Type II-Plateau Supernova Light Curves

Through an expanding network of ground- and space-based telescopes, the astrophysical community has an unprecedented ability to probe transient events. Along with a host of facilities, such as the All Sky Automated Survey for Supernovae (ASAS-SN; Kochanek et al. 2017b), the Las Cumbres Observatory (Brown et al., 2013b) is building the largest set of data ever collected on all nearby supernova (SN) events. Some SNe discovered have known progenitors in distant galaxies (Smartt, 2009). And the data are improving — The Zwicky Transient Facility (ZTF; Bellm et al. 2019) has begun discovering multiple SNe on a nightly basis, and the Large Synoptic Survey Telescope (LSST; LSST Science

Collaboration et al. 2009) will revolutionize time-domain astronomy with repeated nightly imaging of the entire sky with outstanding spatial resolution.

In this Chapter (and in fact, in this dissertation) we focus on Type IIP SNe, core-collapse events of dying massive stars ($M > 10M_{\odot}$) which yield distinctive light curves that plateau over a period of ≈100 days. The duration and brightness of these light curves reflect the progenitor's radius (R), ejected mass ($M_{\rm ej}$), energy of the explosion ($E_{\rm exp}$), and ^{56}Ni mass ($M_{\rm Ni}$). Inferring these properties from the observations has broad applications. Extracting progenitor information from SN observations could lend insight into which stars explode as SNe and which collapse directly into black holes. It would also have implications for the missing red supergiant (RSG) problem identified by Smartt (2009) and updated by Smartt (2015), whereby Type II SNe with known progenitors seem to come from explosions of RSGs with initial masses of $M_{\rm ZAMS} \lesssim < 18M_{\odot}$, whereas evolutionary models have a cutoff mass of around $30M_{\odot}$.

Our understanding has benefitted from 3-dimensional modeling of light curves and spectroscopic data for specific Type IIP events, such as the work of Wongwathanarat et al. (2015) and Utrobin et al. (2017), as well as 3D simulations which probe specific regions of parameter space of these SNe (e.g. Burrows et al. 2019). Although 3D models are incredibly useful for describing specific systems and probing specific regions of the possible parameter space of progenitors and their explosions, substantial effort is required to estimate the parameters of a single observed explosion. The computational demand for individual 3D calculations presents a challenge for probing the parameter space of possible progenitor models for a large ensemble of explosions.

Here, we utilize the open-source 1-dimensional stellar evolution software instrument, Modules for Experiments in Stellar Astrophysics (`MESA`; Paxton et al. 2011, 2013, 2015, 2018, 2019), to model an ensemble of Type IIP SN progenitors, interfacing with the radiative transfer code `STELLA` (Blinnikov et al., 1998; Blinnikov & Sorokina, 2004; Baklanov et al., 2005; Blinnikov et al., 2006) to simulate their light curves and photospheric evolution. We include the effects of the Duffell (2016) prescription for mixing via the Rayleigh-Taylor Instability, which allows for significant mixing of important chemical species such as ^{56}Ni, and yields a more realistic density and temperature profile in the ejecta at shock breakout (Paxton et al. 2018, MESA IV).

The increasing abundance of data has led to a new approach to understanding Type IIP progenitors and explosions in an ensemble fashion. Pejcha & Prieto (2015b,a), and Müller et al. (2017) took such an approach, characterizing a total of 38 Type IIP SNe by their luminosity and duration of the plateau, as well as the velocity at day 50 as inferred via the Fe II 5169 Å line. By fitting these three measurements to the analytics of Popov (1993)[1] and early numerics of Litvinova & Nadyozhin (1983), these authors inferred $M_{\rm ej}$, $E_{\rm exp}$ and R from these observables.

To this end, we show that `MESA`+`STELLA` reproduces a scaling for plateau luminosity at day 50, L_{50}, similar to that of Popov (1993), and we introduce new best-fit scaling laws for L_{50} and for the duration of the plateau $t_{\rm p}$ in the limit of ^{56}Ni-rich events. We

---

[1] See also Sukhbold et al. 2016's update to the `Kepler` results of Kasen & Woosley 2009, which find similar scalings.

also discuss the relationship between our model properties and the observable ET, the time-weighted integrated luminosity that would have been generated if there was no ^{56}Ni in the ejecta (Shussman et al., 2016a; Nakar et al., 2016), and show how ET can also be used to provide similar constraints on explosion properties. As an observable, ET is defined by Equations (2.14) and (2.15). Additionally, we show that the measured velocity at day 50 from the Fe II 5169Å line does not scale with ejecta mass and explosion energy in the way assumed by Popov (1993). Rather, as found observationally by Hamuy & Pinto (2002); Hamuy (2003) and explained by Kasen & Woosley (2009), agreement in L_{50} entails agreement in velocities measured near the photosphere at day 50 (as we show in Figures 2.21 and 2.22).

As our work was being completed, Dessart & Hillier (2019) submitted a paper that also highlights the non-uniqueness of light curve modeling for varied progenitor masses due to core size and mass loss due to winds. Here we additionally highlight the non-uniqueness of light curve modeling even for varied ejecta mass. As such, our calculated scaling relationships yield families of explosions with varied R, $M_{\rm ej}$, and $E_{\rm exp}$ which could produce comparable light curves and similar observed Fe II 5169Å line velocities (e.g. see Figures 2.25 and 2.26). Given an independent measurement of the progenitor R, along with a bolometric light curve and an observed nickel mass ($M_{\rm Ni}$) extracted from the tail, one can directly constrain $M_{\rm ej}$ and $E_{\rm exp}$. Otherwise, these families of explosions can be used as a starting point to guide further detailed, possibly 3D, modeling for observed events.

2.1 Our Models

Our modeling takes place in three steps. First, we construct a suite of core-collapse supernova progenitor models through the Si burning phase using `MESA` following the `example_make_pre_ccsn` test case, described in detail in Paxton et al. 2018 (MESA IV). Second, we load a given progenitor model at core infall, excise the core (as described in section 6.1 of MESA IV), inject energy and Ni, and evolve the model until it approaches shock breakout. This closely follows the `example_ccsn_IIp` test case. Third, to calculate photospheric evolution and light curves after shock breakout, we use the shock breakout profile produced in the second step as input into the public distribution of `STELLA` included within `MESA`, and run until day 175. At the end of the `STELLA` run, a post-processing script produces data for comparison to observational results (specifically bolometric light curves and Fe II 5169Å line velocities as described in MESA IV).

In order to create a diversity of progenitor characteristics, we chose models with variations in initial mass $M_{\rm ZAMS}$, core overshooting $f_{\rm ov}$ and $f_{0,\rm ov}$, convective efficiency $\alpha_{\rm MLT}$ in the hydrogen envelope, wind efficiency $\eta_{\rm wind}$, modest surface rotation $\omega/\omega_{\rm crit}$, and initial metallicity Z. This study concerns itself especially with achieving diversity in the ejecta mass $M_{\rm ej}$ by means of the final mass at the time of explosion $M_{\rm final}$, and the radius R at the time of the explosion. Table 2.1 lists physical characteristics of all progenitor models utilized in this Chapter with $L_{\rm prog}$ = the stellar luminosity just prior to explosion. Our naming convention is determined by the ejecta mass and radius at shock breakout, M<$M_{\rm ej}$>_R<R>. For our sample of Type IIP SNe models, we use three progenitor models from MESA IV, the 99em_19, 99em_16, and 05cs models, renamed M16.3_R608, M12.9_R766, and M11.3_R541, respectively. Additionally, we create three new models using `MESA` revision 10398 to capture different regions of parameter space. We created a model with the same input parameters as 99em_19, here named M15.7_R800. In order to explore a diversity of radii for similar parameters, we also created M15.0_R1140, a model with nearly identical input to M15.7_R800, except for reduced efficiency of convective mixing $\alpha_{\rm MLT} = 2.0$ (the default value is $\alpha_{\rm MLT} = 3.0$) to create a more radially extended star with otherwise similar properties. Finally, in order to include smaller progenitor radii and mass in our suite, we created M9.3_R433, which has the same progenitor parameters as the 12A-like progenitor model from MESA IV, except greater overshooting $f_{\rm ov} = 0.01$. These "standard suite" models are denoted by a * in Table 2.1. All models are solar metallicity, except the 05cs-like progenitor from MESA IV, M11.3_R541, which has metallicity $Z = 0.006$.

Beyond this standard suite, we construct M20.8_R969, a $M_{\rm ZAMS} = 25 M_\odot$ non-rotating model with no overshooting and wind efficiency $\eta_{\rm wind} = 0.4$, which has a very tightly bound core and leads to significant fallback at energies $E_{\rm exp} < 2 \times 10^{51}$ ergs (see also Appendix A). Additionally, to highlight the families of explosions which produce comparable light curves (see Section 2.6), we construct three progenitor models which, when exploded with the proper explosion energy, all produce light curves similar to that of our M12.9_R766 model exploded with 0.6×10^{51} ergs and $M_{\rm Ni} = 0.045 M_\odot$. M9.8_R909 was $M_{\rm ZAMS} = 13.7 M_\odot$ with a final mass of $11.4 M_\odot$, created with overshooting

$f_{\rm ov} = 0.016$, $f_{0,\rm ov} = 0.006$, initial rotation $(v/v_c)_{\rm ZAMS} = 0.2$, wind efficiency $\eta_{\rm wind} = 1.0$, and $\alpha_{\rm MLT} = 2.0$. M10.2_R848 was $M_{\rm ZAMS} = 13.5 M_\odot$ with a final mass of $12.0 M_\odot$, which was created with overshooting $f_{\rm ov} = 0.01$, $f_{0,\rm ov} = 0.004$, initial rotation $(v/v_c)_{\rm ZAMS} = 0.2$, wind efficiency $\eta_{\rm wind} = 0.8$, and $\alpha_{\rm MLT} = 2.0$. M17.8_R587 was $M_{\rm ZAMS}$ $=20.0 M_\odot$ with a final mass of $19.41 M_\odot$, which was created with no overshooting, no rotation, wind efficiency $\eta_{\rm wind} = 0.2$, and $\alpha_{\rm MLT} = 3.5$.

During the explosion phase, which we carry out using `MESA` revision 10925 to include an updated treatment of fallback (see Appendix A), we vary the total energy of the stellar model at the time of explosion ($E_{\rm tot}$) from 2×10^{50} ergs to 2×10^{51} ergs, with 0.2, 0.3, 0.4, 0.5, 0.6, 0.7, 0.8, 1.0, 1.2, 1.4, 1.6, and 2.0 $\times 10^{51}$ ergs. These models are significantly impacted by the Duffell (2016) prescription for mixing via the Rayleigh-Taylor instability, which smooths out the density profile and leads to the mixing of H deep into the interior of the ejecta and ^{56}Ni out towards the outer ejecta (see MESA IV). We use the RTI coefficient $D_{\mathcal{R}} = 3.0$. For a further exploration of the impact of changing the strength of RTI-driven mixing on ejecta and light curve evolution, see the work of P. Duffell et al. (2019, in preparation).

Table 2.1: Properties of our RSG progenitor models at the time of the explosion. Models indicated by a * are part of our standard suite, upon which the majority of our analysis is based. $M_{\rm c,i}$ is the mass of the excised core, and $M_{\rm He\ core}$ is the He core mass in the pre-explosion model. Names are determined by the ejecta mass and radius of each progenitor model at shock breakout, M<$M_{\rm ej}$>_R<R>.

model	$M_{\rm ZAMS}$ $[M_\odot]$	$M_{\rm final}$ $[M_\odot]$	$M_{\rm c,i}$ $[M_\odot]$	$M_{\rm He\ core}$ $[M_\odot]$	$M_{\rm ej}$ $[M_\odot]$	$M_{\rm env}$ $[M_\odot]$	$\omega/\omega_{\rm crit}$	$\lvert E_{\rm bind}\rvert$ $[10^{50}$ erg$]$	$T_{\rm eff}$ [K]	$\log(L_{\rm prog}/L_\odot)$	R $[R_\odot]$
M9.3_R433*	11.8	10.71	1.44	3.58	9.28	7.13	0.2	1.39	4370	4.79	433
M11.3_R541*	13.0	12.86	1.57	4.22	11.29	8.65	0.0	2.65	4280	4.95	541
M12.9_R766*	16.0	14.46	1.58	5.44	12.88	9.02	0.2	4.45	3960	5.11	766
M16.3_R608*	19.0	17.79	1.51	5.72	16.29	12.07	0.2	1.29	4490	5.13	608
M15.7_R800*	19.0	17.33	1.66	6.83	15.67	10.50	0.2	2.39	4040	5.18	800
M15.0_R1140*	19.0	16.77	1.78	7.55	14.99	9.22	0.2	3.31	3660	5.32	1140
M20.8_R969	25.0	22.28	1.77	8.85	20.76	13.43	0.0	8.45	4870	5.68	969
M9.8_R909	13.7	11.36	1.60	7.75	9.8	3.61	0.2	1.81	2380	4.99	909
M10.2_R848	13.5	11.99	1.77	4.24	10.22	7.75	0.2	1.92	3510	5.13	848
M17.8_R587	20.0	19.41	1.62	7.23	17.79	12.18	0.0	2.41	5480	5.44	587

At the handoff between `MESA` and `STELLA`, we initialize `STELLA` with 400 zones and 40 frequency bins, and an error tolerance 0.001 for the Gear-Brayton method (Gear, 1971; Brayton et al., 1972), which leads to converged models. We also rescale the abundance profile of ^{56}Ni and ^{56}Co to match a specified total Nickel mass $M_{\rm Ni}$. This resets the Nickel decay clock to the time of shock breakout. We consider ^{56}Ni masses of $M_{\rm Ni}/M_\odot$ =0.0, 0.015, 0.03, 0.045, 0.06, and 0.075; the impact of ^{56}Ni in our models is discussed in detail in Section 2.4. As most of the mixing is accounted for by Duffell RTI, we only employ modest boxcar smoothing of abundance profiles at handoff as recommended in MESA IV, using 3 boxcar passes with a width of 0.8 $M_\odot$. Additionally, as described in Paxton et al. 2019 and Appendix A here, we use a minimum innermost velocity cut of material moving slower than 500 km s^{-1} to prevent numerical artifacts in `STELLA` caused during interactions between reverse shocks and slow-moving material near `STELLA`'s inner boundary. This study concerns itself with intrinsic properties of the SNe and their progenitors, determined primarily by quantities on the plateau, and therefore we do not include circumstellar material (CSM) in `STELLA`.

2.1.1 Estimating Fallback

Even when the total energy of a stellar model is greater than zero (i.e. the star is unbound), it is possible for some of the mass which does not collapse into the initial remnant object to become bound and fall back onto the central object, which we define as $M_{\rm fallback}$. This typically occurs as a result of inward-propagating shock waves generated at

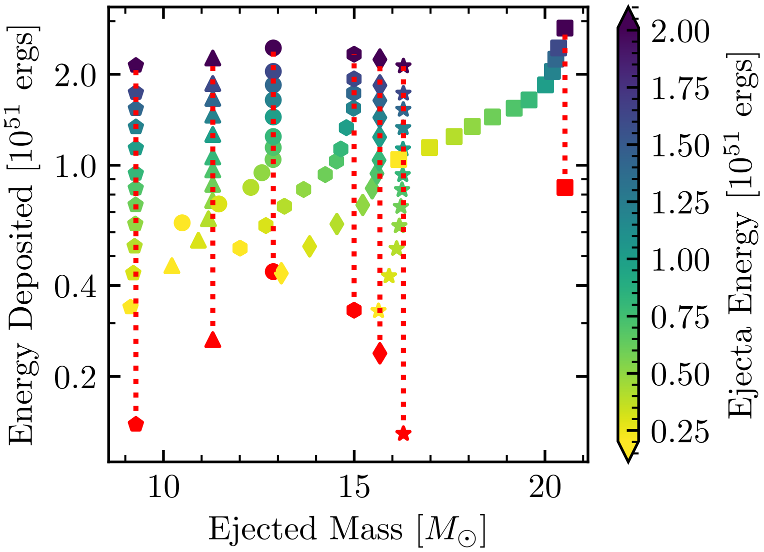

Figure 2.1: Energy deposited in the explosion versus ejected mass for our standard suite, as well as for the M20.8_R969 model, all exploded at 12 different explosion energies. Marker shapes correspond to different initial progenitor models as follows — pentagon: M9.3_ R433; triangle: M11.3_R541; circle: M12.9_R766; hexagon: M15.0_R1140; diamond: M15.7_R800; star: M16.3_R608; square: M20.8_R969. Explosions which would have $E_{\rm tot} = 0$ (corresponding to $E_{\rm dep} = |E_{\rm bind}|$) are shown as red points whose x-coordinate is determined by the same model assuming no fallback. The red dotted line serves as a visual guide, indicating explosions with no fallback for each progenitor model. Color corresponds to the total energy of the ejecta just after the explosion $E_{\rm tot}$.

compositional boundaries within the ejecta. The relationship between progenitor binding energy, explosion energy, and fallback can be seen in Figure 2.1, which shows the final mass of our models versus the total energy deposited $E_{\rm dep}$, which is equal to the total energy of the model after the explosion $E_{\rm tot}$ plus the magnitude of the total energy of the bound progenitor model at the time of explosion $E_{\rm bind}$. Fallback is particularly common in explosions where the explosion energy is not significantly larger than the binding energy of the model at the time of explosion. In general, more tightly bound models require larger total final energies to unbind the entirety of the potential ejecta.

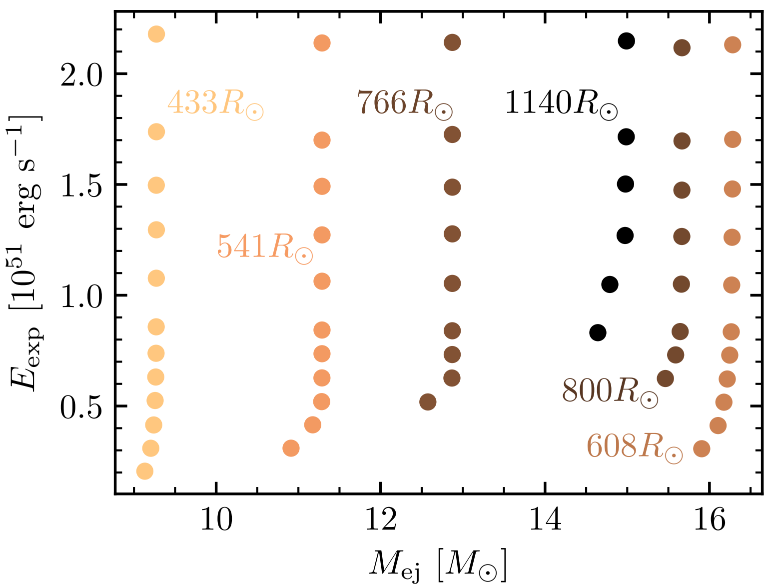

Figure 2.2: Ejecta masses and explosion energies as determined by the kinetic energy at day 50 in `STELLA` considered as a part of our standard suite, with fallback masses $M_{\rm fallback} < 0.4 M_\odot$. Lighter colors correspond to smaller progenitor radii, which are labeled.

The proper treatment of fallback in 1D simulations remains an open question because of complexities such as the interaction between accretion-powered luminosity and the inner boundary of the explosion models. In `MESA`, the current implementation of fallback is effective as a computationally robust approximation that allows experimentation, but it should not be viewed as an accurate model of the physical processes at work. Consequently we restrict our study to models with little fallback material: $M_{\rm fallback} < 0.4 M_\odot$. The models which survive this cut are shown in figure 2.2. For a full description of our treatment of fallback, see Appendix A.

2.2 Analytic Expectations

The luminosity of a Type IIP SN is, approximately, powered by shock cooling due to expansion out to around 20 days (the "shock cooling phase"), then Hydrogen recombination until around 100 days (the "plateau phase"), and the radioactive decay chain of ^{56}Ni → ^{56}Co → ^{56}Fe beyond that (the "Nickel tail").

The expansion time of the SN ejecta is expressed as $t_{\rm e} \approx R/v_{\rm SN}$, where R is the radius of the star at the time of the explosion, and the velocity $v_{\rm SN}$ is defined by the mass of the ejecta $M_{\rm ej}$ and kinetic energy of the ejecta at infinity $E_{\rm exp} = M_{\rm ej}\, v_{\rm SN}^2/2$.[2] Similarly, the time it takes to reach shock breakout after core collapse ($t_{\rm SB}$) scales with $t_{\rm e}$, such that

$$t_{\rm SB} \approx 0.91{\rm d}\ R_{500} E_{51}^{-1/2} M_{10}^{1/2}, \tag{2.1}$$

where $R_{500} = R/500R_\odot$, $E_{51} = E_{\rm exp}/10^{51}\,{\rm ergs}$, and $M_{10} = M_{\rm ej}/10M_\odot$, and the dimensionful prefactor comes from a linear fit to our numerical models. This timescale is primarily a property of the models, but would observationally correspond to the difference in time between the first neutrino signal from core collapse and the first detection in the electromagnetic spectrum from shock breakout.

Following Kasen & Woosley (2009), in the limit of no accumulated heating of the ejecta due to ^{56}Ni decay, the luminosity on the plateau (taken here to be at day 50, denoted L_{50}) is set by the total internal energy (E) to be radiated out divided by the duration of the plateau:

---

[2] During the the homologous phase, the kinetic energy of the ejecta is approximately equivalent to the total energy of the explosion, since radiation accounts only for a small fraction of the total energy at late times.

$$L_{50} = \frac{E(t_{\rm p})}{t_{\rm p}} = \frac{E_0 t_{\rm e}}{t_{\rm p}^2}, \tag{2.2}$$

where $t_{\rm p}$ is the duration of the plateau, $E_0 \approx E_{\rm exp}/2$ is the initial internal energy of the ejecta at shock breakout, and the second equality comes from assuming the internal energy evolution for homologous expansion (where $r(t) \approx vt$, for a Lagrangian fluid element with constant velocity v) in a radiation-dominated plasma, $E_0 t_{\rm e} = E(t_{\rm p}) t_{\rm p}$.

Here we compare to the analytics of Popov (1993), which consider the effects of both H recombination and radiative diffusion. Historically, analytic scalings which ignore recombination (Arnett, 1980) or radiative diffusion (Woosley & Weaver, 1988; Chugai, 1991) have also been considered. These scalings are also detailed in Kasen & Woosley (2009) and Sukhbold et al. (2016). From a 2-zone model including an optically thick region of expanding ejecta behind the photosphere and an optically thin region outside the photosphere, Popov finds that the luminosity on the plateau (here taken at day 50) and duration of the plateau should scale as

$$\begin{aligned} L_{50} &\propto M^{-1/2} E_{\rm exp}^{5/6} R^{2/3} \kappa^{-1/3} T_{\rm I}^{4/3}, \\ t_0 &\propto M^{1/2} E_{\rm exp}^{-1/6} R^{1/6} \kappa^{1/6} T_{\rm I}^{-2/3}, \end{aligned} \tag{2.3}$$

where κ is the opacity in the optically thick component of the ejecta, and $T_{\rm I}$ is the ionization temperature of Hydrogen, and M is the relevant mass (which could depend on the extent to which H is mixed throughout the ejecta). Kasen & Woosley (2009) recovers a similar set of scalings from their models:

$$\begin{aligned} L_{50} &\propto M_{\rm ej}^{-1/2} E_{\rm exp}^{5/6} R^{2/3} X_{\rm He}^{1}, \\ t_0 &\propto M_{\rm ej}^{1/2} E_{\rm exp}^{-1/4} R^{1/6} X_{\rm He}^{1/2}, \end{aligned} \tag{2.4}$$

where $X_{\rm He}$ is the mass fraction of He. There is some disagreement in the literature as to whether the mass M used in the Popov scalings should be the mass of the hydrogen-rich envelope ($M_{\rm env}$) or the mass of the ejecta ($M_{\rm ej}$). Sukhbold et al. (2016), for example, use $M_{\rm env}$ in recreating these scalings, since recombination in the Hydrogen-rich envelope drives the evolution of the supernova, with little contribution from the hydrogen-poor innermost ejecta coming from the core. However, in our models, the relevant mass is the *total* ejecta mass $M_{\rm ej}$, as we see mixing of hydrogen deep into the interior of the star and core elements into the envelope due to RTI. Since hydrogen recombination thus plays a significant role in setting the temperature throughout the entirety of the ejecta, it is the entire ejecta mass that is used in the scalings we derive later. Additionally, we make the assumption that by day 50, $E_{\rm exp}$ is equal to the kinetic energy of the ejecta.

Popov also recommended assuming that the observed photospheric velocity of the supenova ejecta should scale like $v_{\rm SN}$, such that $v_{\rm Ph} \propto (E_{\rm exp}/M_{\rm ej})^{1/2}$. However, this scaling, which does describe the *typical* velocity of the SN ejecta, should not be used when describing photospheric velocities at a fixed time, for reasons we discuss in Section 2.5.

The above scalings do not take into account additional heating by the radioactive decay chain of ^{56}Ni, which does not significantly affect the luminosity on the plateau, but does extend the duration of the plateau by heating the ejecta at late times. We discuss more detailed expectations for the effects of ^{56}Ni in Appendix B, and its impact on our models in Section 2.4. This correction is typically written as

$$t_{\mathrm{p}} = t_0 \times f_{\mathrm{rad}}^{1/6}, \tag{2.5}$$

where f_{rad} can be expressed as

$$f_{\mathrm{rad}} = 1 + C_f M_{\mathrm{Ni}}\, M_{\mathrm{ej}}^{-1/2} E_{\mathrm{exp}}^{-1/2} R^{-1}, \tag{2.6}$$

and C_f is a numerical prefactor which encodes the energy and decay time of the ^{56}Ni decay chain (Kasen & Woosley 2009; Sukhbold et al. 2016; and Appendix B).

These scaling relationships serve as a useful guide when modeling Type IIP supernova light curves. However, complexities arising from changes in temperature profiles, density profiles, realistic distributions of important elements such as H and ^{56}Ni, and stellar structure can lead to differences between these simplified analytic expectations and numerical models. For example, the Popov analytics are derived for emission from a two-zone model with an optically thick inner region with a single opacity κ and an optically thin outer region and a flat density profile. More realistic evolution of the temperature and density profiles of one of our SN ejecta models is shown in Figure 2.3, akin to Figure 11 of Utrobin (2007). Thus, in the following sections we aim to provide expressions which relate observables to the physical properties of the explosions, namely the progenitor R, M_{ej}, and E_{exp}, while also capturing the ejecta structure underlying these events.

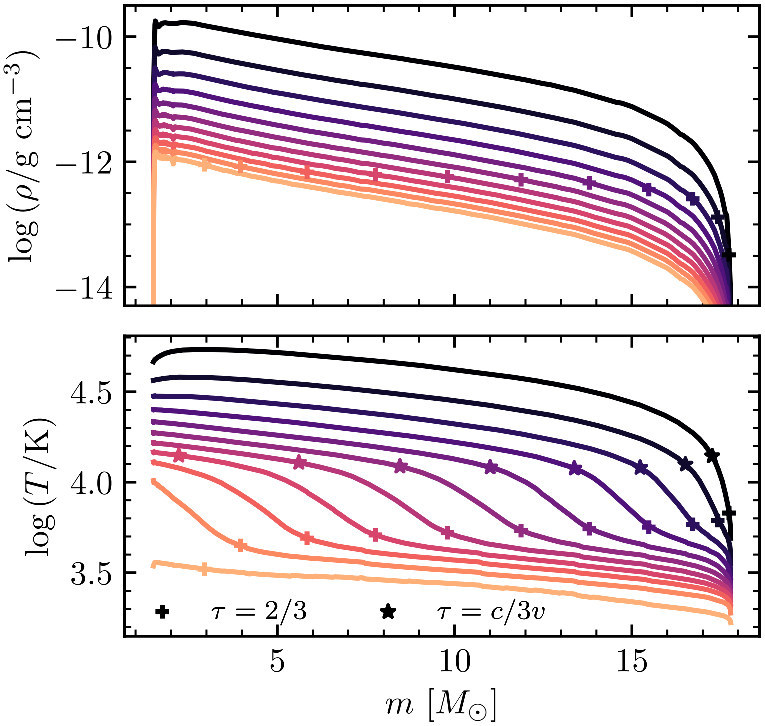

Figure 2.3: Density (upper panel) and temperature (lower panel) of the ejecta at every 10 days in the evolution starting at day 20 for our M16.3_R608 model exploded with 10^{51} ergs and $M_{\rm Ni} = 0.03 M_\odot$. Darker colors indicate earlier times. Also plotted are the photosphere ($\tau = 2/3$; plus markers), and the location where $\tau = c/3v$ (star markers), which is shown only on the temperature plot to reduce clutter, to demonstrate the extent of the region where the photon diffusion time is shorter than the expansion time.

2.3 Luminosity at day 50

We use the bolometric luminosity 50 days after shock breakout, L_{50}, as our diagnostic for the plateau luminosity, as in most cases, this is beyond the time where shock heating of CSM would affect the luminosity (Morozova et al., 2017). Moreover, for all but one progenitor model, increasing the amount of ^{56}Ni has a negligible impact on L_{50}, as the internal energy at day 50 of the outer region of the ejecta is still dominated by the initial shock. However, in explosions where the plateau is naturally short, there can be marginal, but noticeable, additional luminosity at day 50 from ^{56}Ni decay. This can be seen in Figure 2.4, which shows the differences between a selection of light curves and the corresponding light curves with no ^{56}Ni. We show light curves for M16.3_R608, a typical model with a typical $M_{\mathrm{Ni}} = 0.03 M_{\odot}$ (left), and for high $M_{\mathrm{Ni}} = 0.075 M_{\odot}$ explosions of the only progenitor model in which we see significant deviation in L_{50} as a result of ^{56}Ni heating, M9.3_R433 (right), where L_{50} varies by up to 15% between an explosion with no ^{56}Ni and one with $M_{\mathrm{Ni}} = 0.075 M_{\odot}$. Noting this, we choose a moderate, constant value of $M_{\mathrm{Ni}} = 0.03 M_{\odot}$ typical of observed events (Müller et al., 2017), and calculate how L_{50} scales with M_{ej}, E_{exp}, and R.

We fit two formulae to our sample suite of 57 explosions. First, we assume the power law coefficients of Popov (1993), and let the normalization float, finding

$$\log(L_{50}/[\mathrm{erg\,s^{-1}}]) = 42.18 - \frac{1}{2}\log M_{10} + \frac{5}{6}\log E_{51} + \frac{2}{3}\log R_{500}, \tag{2.7}$$

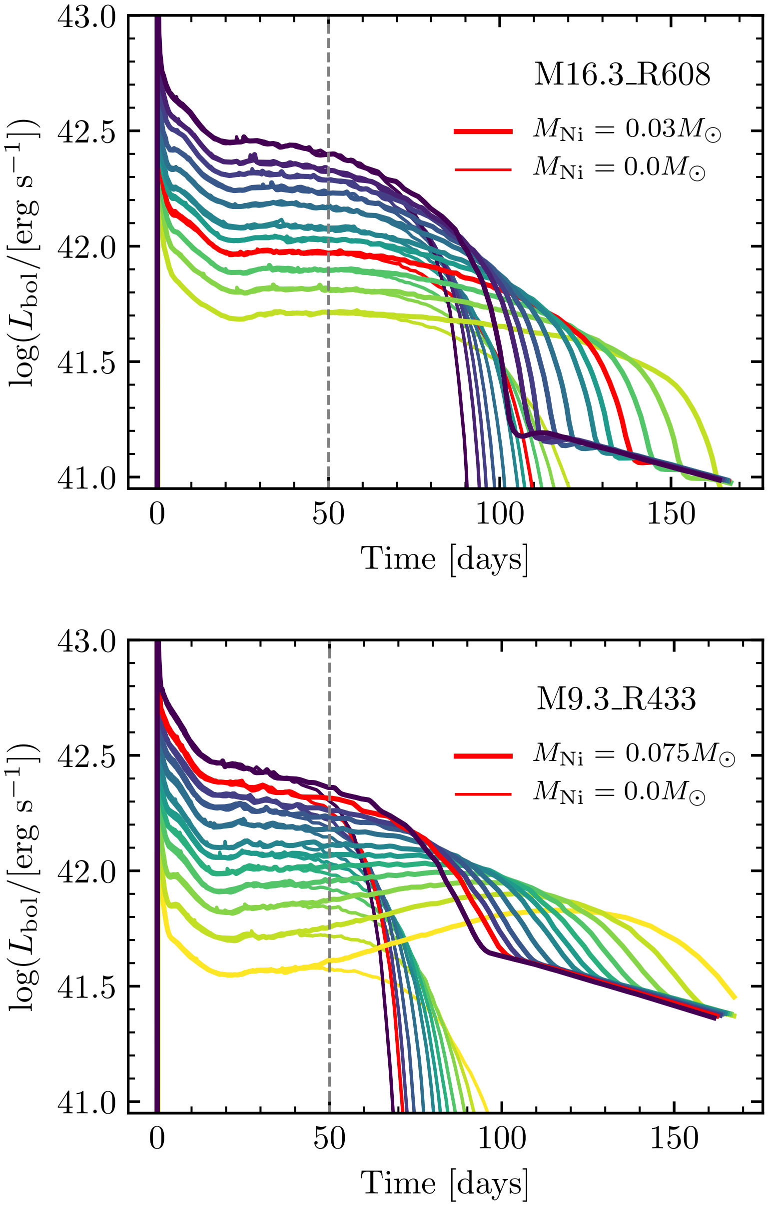

Figure 2.4: Light curves for increasing explosion energies of our M16.3_R608 model with $M_{\rm Ni} = 0.03 M_\odot$ (left) and our smallest model, M9.3_R433, with $M_{\rm Ni} = 0.075 M_\odot$ (right). Thin lines correspond to the same explosions, but with no ^{56}Ni. The red lines correspond to the models with the typical $M_{\rm Ni}$ given L_{50}, from the relationship in Pejcha & Prieto (2015b), and their no-nickel counterparts.

where 42.18 is a linear fit from our models and logarithms are base 10, with $M_{10} = M_{\rm ej}/10M_\odot$, $R_{500} = R/500R_\odot$, and $E_{51} = E_{\rm exp}/10^{51}\,$ergs. For these models, root mean square (RMS) deviations of L_{50} from values derived by applying Equation (2.7), corresponding to the blue points in Figure 2.5, are 7.9%, with a maximum deviation in L_{50} of 32%. The normalization for an explosion with $M_{10} = R_{500} = E_{51} = 1$ is comparable to but somewhat lower than the value of 42.27 given in Sukhbold et al. (2016) (who use $M_{\rm env}$ rather than $M_{\rm ej}$), as well as the value of 42.21 calculated in Popov (1993) for default H recombination temperatures and opacities. Kasen & Woosley (2009) give a value of $42.10 + \log(X_{\rm He}/0.33)$, letting $X_{\rm He}$ range from 0.33 to 0.54.

We perform a second fit for the normalization *and* the power laws in M_{10}, E_{51}, and R_{500}, and recover scalings that are similar to those in Equation (2.7). We find a slightly shallower scaling with $M_{\rm ej}$ and $E_{\rm exp}$, and a slightly steeper dependence on R_{500}:

$$\log(L_{50}/[{\rm erg\,s^{-1}}]) = 42.16 - 0.40\log M_{10} + 0.74\log E_{51} + 0.76\log R_{500}, \tag{2.8}$$

where the normalization and power law coefficients are fit from our models. The RMS deviation of the models from Equation (2.8), shown as red triangles in Figure 2.5, is 4.7%, with deviations not exceeding 14.3% for any model with $M_{\rm Ni} = 0.03M_\odot$. This is a better fit than the one that assumes the exact Popov scaling.

The luminosities of our models, as they compare to the fitted formulae, are shown in Figure 2.5. Most models agree with the Popov scaling, while the Popov scaling overpredicts L_{50} in low-ejecta mass high-explosion energy cases. The x-axis of Figure 2.5 is

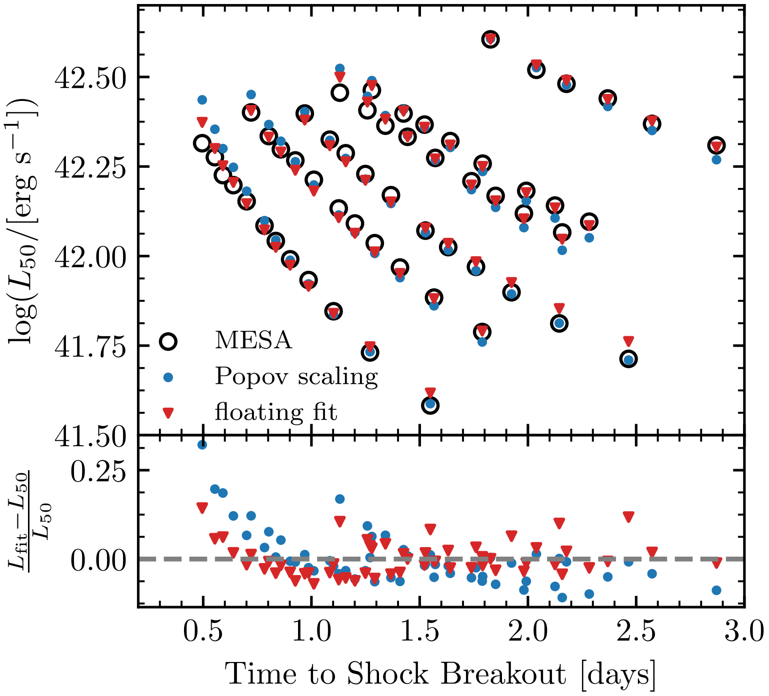

Figure 2.5: Fitting formulae predictions for L_{50} (colored markers) compared with the model L_{50} (black circles; upper panel), and their residuals (lower panel) for our suite of 57 explosions at constant $M_{\rm Ni} = 0.03 M_\odot$. Each diagonal family of points reflects one progenitor model exploded with different energies.

$t_{\rm SB}$, chosen because it scales with explosion energy for a fixed ejecta mass and radius (Equation (2.1)), and increases with increasing $M_{\rm ej}$ and R, visually distinguishing the six different progenitor models and different explosion energies.

Although the presence of ^{56}Ni does not affect light curve properties at day 50 in a majority of models, in a few explosions there is slight variation in L_{50} introduced by the extra heating from ^{56}Ni (seen in Figure 2.4). Because this effect is only distinctly noticeable in our model with the smallest values of $M_{\rm ej}$ and R, this can lead to variations in our recovered power laws when fitting to different fixed ^{56}Ni masses. However, this correction is typically small, falling within the scatter in which our models agree with the fitted formulae. We find that the power law scalings of Equation (2.8) describe all models with $M_{\rm Ni}$ ranging from $0.0 - 0.075 M_\odot$ within 18.2%, with RMS deviations of 4.8%, where the largest deviations occur in events where $M_{\rm Ni} = 0.0 M_\odot$, which are not consistent with any observed Type IIP SNe.

We now use Equation (2.8) to compare our `MESA+STELLA` results to models from other software instruments. In Table 2.2, we show our predictions for L_{50} compared against luminosities from the `MESA+CMFGEN` models (without Duffell RTI) of Dessart et al. (2013), the `Kepler+Sedona` models of Kasen & Woosley (2009), and the `MESA+CMFGEN` models in Lisakov et al. (2017). In general, the disagreement between our formula and these other models is similar to the scatter within our own models, with the exception of the two lowest-energy explosions in Kasen & Woosley (2009) and the low luminosity suite in Lisakov et al. (2017). Equation (2.8) agrees with the Dessart et al. (2013) models with an RMS error of 9%, but slightly underpredicts luminosity in a majority of cases. Compared to the models of Kasen & Woosley (2009), Equation (2.8) gives RMS errors of 17% with no clear under- or overprediction. The low-luminosity models from Lisakov et al. (2017) have greater disagreement, with RMS errors 23% from Equation (2.8). This is not surprising, as on the low-luminosity end, our treatment of fallback discussed in Section 2.1 and Appendix A excludes most models in this region of parameter space from our fitting formulae, as significant fallback after the initial core collapse is often seen for low explosion energies.

Table 2.2: Comparison of Equation (2.8) to `CMFGEN` models from Dessart et al. (2013), `Kepler+Sedona` models from Kasen & Woosley (2009), and low-luminosity `CMFGEN` models from Lisakov et al. (2017). Bolometric luminosities at day 50 for Dessart et al. (2013) are recovered from light curves provided by L. Dessart (private communication). These luminosities are compared to Equation (2.8) applied to $M_{\rm ej}$, $E_{\rm exp}$, and R from the various models.

Source	Model	$M_{\rm ej}$	$E_{\rm exp}$	R	L_{50}	Equation (2.8)	% diff
		[$M_\odot$]	[10^{51} erg]	[$R_\odot$]	[10^{42} erg s^{-1}]	[10^{42} erg s^{-1}]	
Dessart+13	m15Mdot	10.01	1.28	776	2.55	2.40	-5%
	m15	12.48	1.27	768	2.56	2.17	-15%
	m15e0p6	12.46	0.63	768	1.19	1.29	8%
	m15mlt1	12.57	1.24	1107	3.13	2.81	-10%
	m15mlt3	12.52	1.34	501	1.61	1.63	1%
	m15os	10.28	1.40	984	3.49	3.05	-12%
	m15r1	11.73	1.35	815	2.62	2.44	-7%
	m15r2	10.39	1.34	953	3.30	2.87	-13%
	m15z2m3	13.29	1.35	524	1.70	1.65	-3%
	m15z4m2	11.12	1.24	804	2.48	2.31	-6%
	s15N	10.93	1.20	810	2.51	2.29	-9%
	s150	13.93	1.20	610	2.47	2.29	-8%
K&W 2009	M12_E1.2_Z1	9.53	1.21	625	1.91	1.99	4%
	M12_E2.4_Z1	9.53	2.42	625	3.67	3.33	-9%
	M15_E1.2_Z1	11.29	1.21	812	2.16	2.27	5%
	M15_E2.4_Z1	11.29	2.42	812	4.35	3.80	-12%
	M15_E0.6_Z1	11.25	0.66	812	1.26	1.45	15%
	M15_E4.8_Z1	10.78	4.95	812	7.80	6.59	-15%
	M15_E0.3_Z1	11.27	0.33	812	0.59	0.87	46%
	M20_E1.2_Z1	14.36	1.22	1044	2.61	2.52	-4%
	M20_E2.4_Z1	14.37	2.42	1044	4.85	4.18	-13%
	M20_E0.6_Z1	14.36	0.68	1044	1.40	1.63	17%
	M20_E4.8_Z1	14.37	4.99	1044	8.57	7.16	-17%
	M25_E1.2_Z0.1	13.27	1.26	632	1.67	1.82	8%
	M25_E2.4_Z0.1	13.24	2.48	632	3.08	3.00	-2%
	M25_E0.6_Z0.1	13.28	0.65	632	0.86	1.11	29%
	M25_E4.8_Z0.1	13.18	4.90	632	5.31	4.98	-6%
Lisakov+17	X	8.29	0.25	502	0.446	0.550	24%
	XR1	8.08	0.26	581	0.513	0.643	23%
	XR2	7.90	0.27	661	0.592	0.737	24%
	XM	9.26	0.27	510	0.423	0.567	34%
	YN1	9.45	0.25	405	0.381	0.446	17%
	YN2	9.45	0.25	405	0.381	0.446	17%
	YN3	9.45	0.25	405	0.375	0.446	19%

2.4 Plateau Duration and ET

Although the plateau duration $t_{\rm p}$ is theoretically motivated by Popov (1993); Kasen & Woosley (2009), and others, it is important to reliably extract it from our models as well as observations. We discuss two ways of extracting $t_{\rm p}$, one defined by observables, and the other extracted from properties of the theoretical models, which we use to evaluate the impact of ^{56}Ni.

For a definition which can be applied to observed or calculated light curves, we follow Valenti et al. (2016), fitting the following functional form to the logarithm, $y(t)$, of the bolometric luminosity around the fall from the plateau:

$$y(t) = \log_{10}(L_{\rm bol}) = \frac{-A_0}{1 + e^{(t-t_{\rm p})/W_0}} + (P_0 \times t) + M_0. \tag{2.9}$$

An example is shown in Figure 2.6. We use the python routine `scipy.optimize.curve_fit` to fit the light curve starting at the time when the luminosity evolution is 75% of the way to its steepest descent, defined when $\mathrm{d}\log L_{\rm bol}/\mathrm{d}t$ is at its most negative after the initial drop at shock breakout, which occurs shortly before transitioning to the nickel tail. We fix the value of P_0 to be the slope on the ^{56}Ni tail. We interpret the fitting parameter $t_{\rm p}$ to be the plateau duration.

As the recombination-powered photosphere moves into the innermost ejecta, the optical depth at the inner boundary declines orders of magnitude and the photospheric temperature plummets. This transition, shown in Figure 2.7, is the physical end of the plateau. Thus, for our modeling definition of the plateau duration, we use the time, post-shock breakout, when the optical depth $\tau_{\rm IB}$ through the ejecta becomes < 10. This

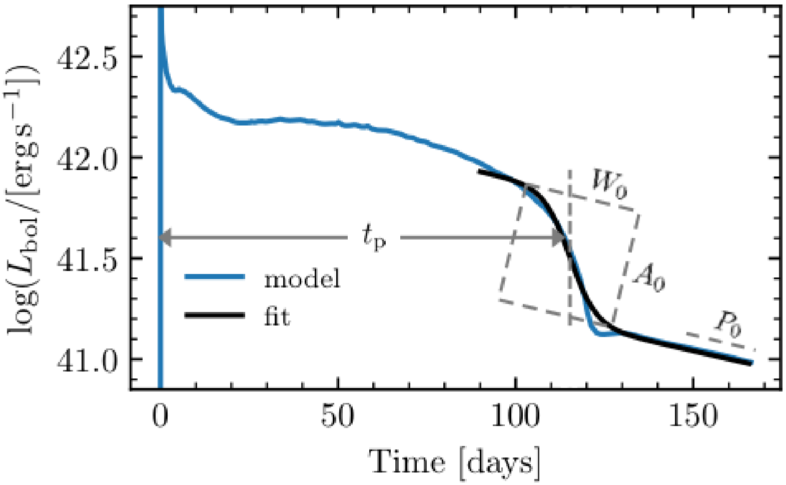

Figure 2.6: Diagram of fitting Equation (2.9) to find the 115 day duration of the plateau for our model M16.3_R608 exploded with $E_{\rm exp} = 10^{51}$ ergs and $M_{\rm Ni} = 0.03M_{\odot}$. Fitting parameters are labelled, but we only ascribe physical significance to $t_{\rm p}$.

time will be denoted hereafter as $t_{\tau=10}$, and can be used as a metric for plateau duration when comparing to models where there is no ^{56}Ni, where Equation (2.9) does not accurately capture the fall from the plateau. As shown by the black markers in Figure 2.7, the observable $t_{\rm p}$ roughly corresponds to the physical end of the plateau phase around $t_{\tau=10}$. Across all progenitor models, explosion energies, and nonzero nickel masses which we consider, RMS differences between $t_{\tau=10}$ and $t_{\rm p}$ are 4.1% and all differences are within ±7%.

2.4.1 Impact of ^{56}Ni on plateau duration in our models

The presence of radioactive ^{56}Ni prolongs the photospheric evolution and extends the plateau by providing extra heat to the ejecta. This is shown in Figure 2.8, where we show ejecta temperature profiles of the same SN explosion with different $M_{\rm Ni}$. At day 50,

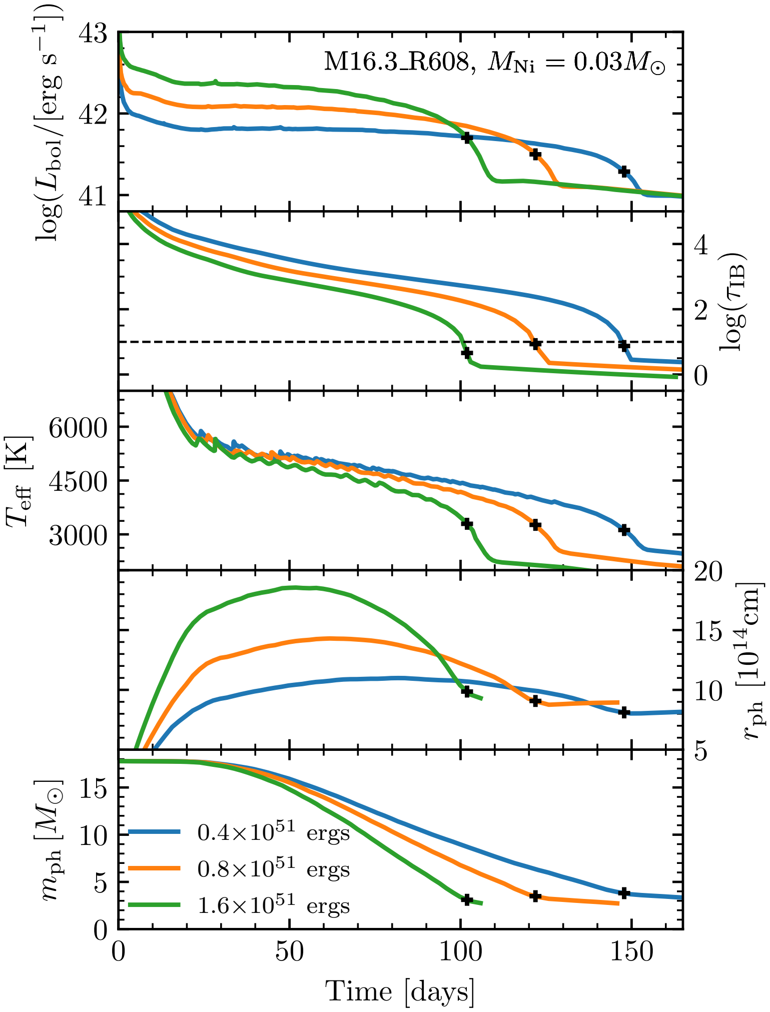

Figure 2.7: Evolution of luminosity, optical depth at the inner boundary ($\tau_{\rm IB}$), effective Temperature ($T_{\rm eff}$), photospheric radius ($r_{\rm ph}$), and mass coordinate of the photosphere ($m_{\rm ph}$) for our M16.3_R608 model, exploded with $M_{\rm Ni} = 0.03 M_\odot$ at three different explosion energies, showing the transition to the end of the plateau. Black plus markers indicate the end of the plateau determined from fitting Equation (2.9). The thin dashed line in the second panel indicates $\tau_{\rm IB} = 10$.

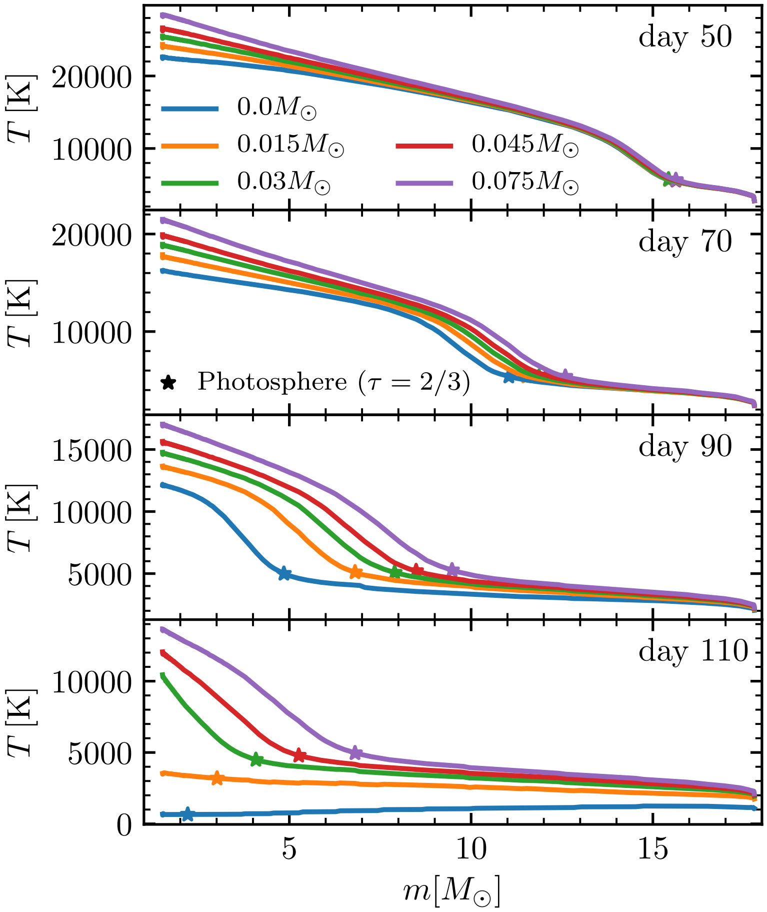

Figure 2.8: Ejecta temperature profiles at different times with increasing amounts of ^{56}Ni for our M16.3_R608 model exploded with 10^{51} ergs. The location of the photosphere is shown for each model by the colored stars.

the photosphere for all models remains in the outer ejecta, where there is very little ^{56}Ni. At later times, the photosphere has moved in farther for models with lower M_{Ni}, whereas additional heat from the ^{56}Ni decay chain causes the recombination-powered photosphere to move in more slowly in models with higher M_{Ni}.

The analytics in Appendix B and Section 2.2 treat the ejecta as a single zone, with heating from ^{56}Ni decay throughout. However, ^{56}Ni is more highly concentrated in the

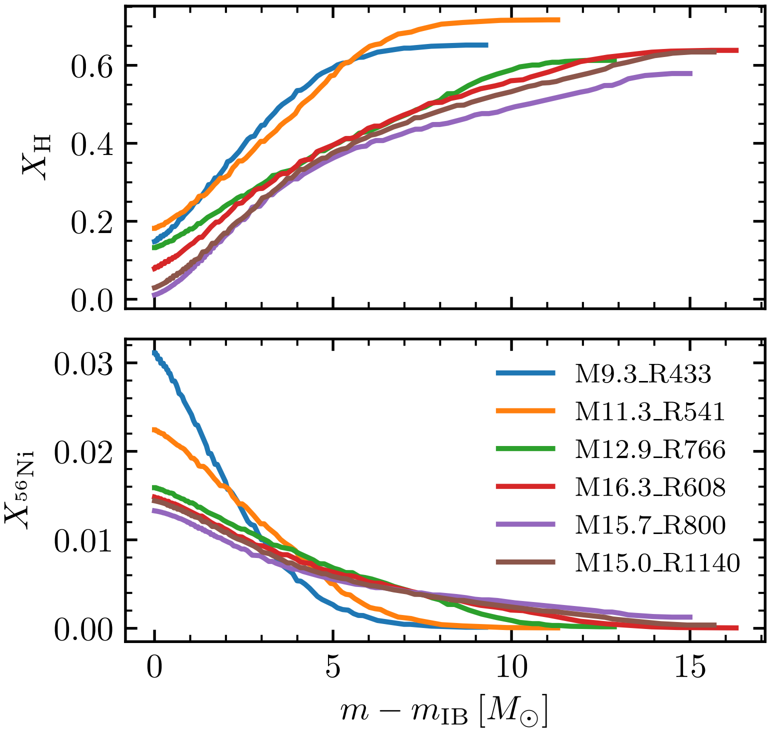

Figure 2.9: The diversity of H (upper panel) and ^{56}Ni (lower panel) profiles for our standard suite of models, exploded with our highest $E_{\rm exp}$ and $M_{\rm Ni}$. The x-axis is the mass coordinate within the ejecta.

center of the ejecta. Thus, heat from ^{56}Ni decay remains trapped in the optically thick inner region, extending the plateau more at late times. This more concentrated ^{56}Ni heating should have a more significant impact on the plateau duration than it would for an analytic one-zone model, as the internal energy of the inner ejecta is more relevant than that of the ejecta as a whole at the end of the plateau. Figure 2.9 shows the diversity of asymptotic ^{56}Ni and Hydrogen distributions within our standard suite of models at handoff to `STELLA` for the highest-energy ($E_{\rm tot} = 2 \times 10^{51}$ ergs) highest-Nickel ($M_{\rm Ni} = 0.075 M_\odot$) cases.

Moreover, the distribution of ^{56}Ni, which can vary amongst different progenitors de-

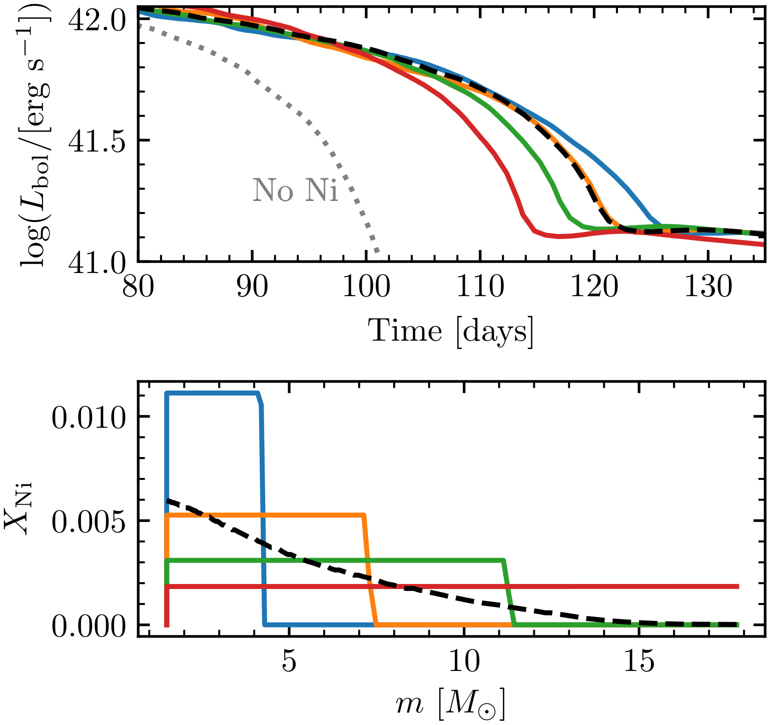

Figure 2.10: Light curves at the end of the plateau (upper panel) and ^{56}Ni distributions (lower panel) for the M16.3_R608 model exploded with $E_{\rm exp} = 10^{51}$ ergs and $M_{\rm Ni} = 0.03 M_\odot$, for the fiducial explosion (black dashed line), compared to models where ^{56}Ni is re-distributed by hand out to some fraction of the ejecta at the time of shock breakout (solid colored lines). The light curve for the same explosion with no Ni is given by the grey dashed line in the upper panel.

pending on core structure and mixing, can also introduce inherent scatter to the plateau duration (Kozyreva et al., 2018). Figure 2.10 shows light curves and ^{56}Ni profiles for the M16.3_R608 model exploded with $E_{\rm exp} = 10^{51}$ ergs and $M_{\rm Ni} = 0.03 M_\odot$, where the same ^{56}Ni mass is re-distributed by hand at the time of shock breakout out to some fraction of the ejecta. Although this exercise spans a greater diversity in ^{56}Ni concentration than any of our models, we see for this otherwise unexceptional light curve that the plateau duration $t_{\rm p}$ can vary by almost 10 days.

A full examination of the effects of changing the distributions in the framework of the Duffell RTI prescription (Paxton et al., 2018) is beyond the scope of this Chapter, and will be the subject of future study (P. Duffell et al. in Prep.). Here we examine the impact of ^{56}Ni on the value of $f_{\rm rad}$ in $t_{\rm p} = t_0 \times f_{\rm rad}^{1/6}$ (Equation (2.5)), where t_0 is the plateau duration for the same explosion with no ^{56}Ni.

Following Kasen & Woosley (2009), Sukhbold et al. (2016), and others, ^{56}Ni extends the plateau as

$$t_{\rm p}/t_0 = (1 + C_f M_{\rm Ni} E_{51}^{-1/2} M_{10}^{-1/2} R_{500}^{-1})^{1/6}, \tag{2.10}$$

we can extract C_f by fitting to our models using the $t_{\tau=10}$ definition of plateau duration. We consider all six progenitor models with explosion energies sufficient to cause minimal fallback, with $M_{\rm Ni}/M_\odot$=0.0, 0.015, 0.03, 0.045, 0.06, and 0.075. We exclude models where the plateau is so long that the Nickel tail does not appear at any point in our simulations, and models which have a less than half a decade drop in $L_{\rm bol}$ from day 50 to the top of the nickel tail, as no such events have been observed.[3]

This gives a total of 332 light curves including the 57 with no ^{56}Ni, which we compare to the light curves of identical explosions with no ^{56}Ni. Figure 2.11 shows the ratio of the plateau duration, $t_{\tau=10}$, of each of these light curves compared to $t_{\tau=10}$ for an identical explosion with no ^{56}Ni, t_0, following Kasen & Woosley (2009) but with our suite of 332 model light curves. We recover $C_f \approx 87$, which is an order of magnitude larger than

---

[3] This primarily excludes models at high nickel masses and low explosion energies, specifically: M9.3_R433: $E_{51} = 0.2$ with $M_{\rm Ni} = 0.075 M_\odot$; M11.3_R541: $E_{51} = 0.3$ with $M_{\rm Ni} = 0.06 M_\odot$ and $M_{\rm Ni} = 0.075 M_\odot$; and M16.3_R608: $E_{51} = 0.3$ with $M_{\rm Ni} = 0.045 M_\odot$, $M_{\rm Ni} = 0.06 M_\odot$, and $M_{\rm Ni} = 0.075 M_\odot$; $E_{51} = 0.4$ with $M_{\rm Ni} = 0.06 M_\odot$ and $M_{\rm Ni} = 0.075 M_\odot$; and $E_{51} = 0.4$ with $M_{\rm Ni} = 0.075 M_\odot$.

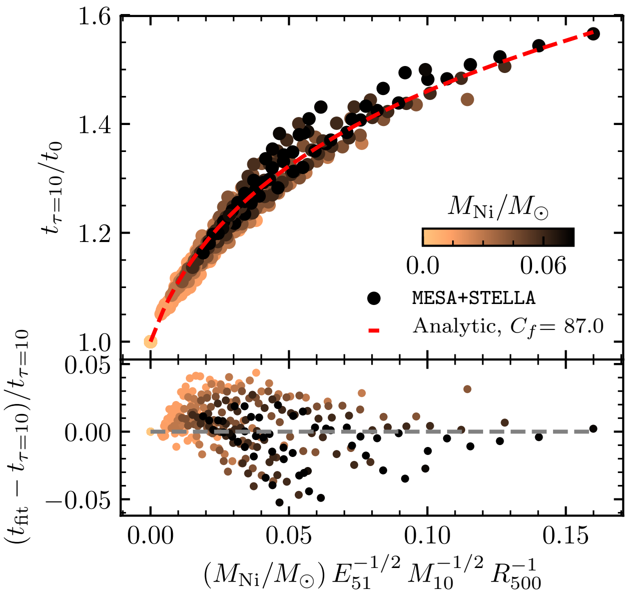

Figure 2.11: Plateau duration when the optical depth at the inner boundary $\tau_{\rm IB} = 10$, divided by plateau duration for the same explosion with no ^{56}Ni, as compared to the analytic scaling Equation (2.10) (red dashed line) with C_f determined from our fits. Color corresponds to $M_{\rm Ni}$ in units of solar masses. Deviations of each of the models from this relationship are shown on the lower panel.

the approximate lower bound $C_f \approx 7.0$ derived in Appendix B, and roughly a factor of 4 larger than $C_f = 24$ (derived in Kasen & Woosley 2009, typographical error corrected in Sukhbold et al. 2016). This likely results from the different ^{56}Ni mass distributions in our models from those in Kasen & Woosley (2009). As demonstrated in Figure 2.10, this can yield significant differences in the plateau duration. Our fit shows similar scatter for all ^{56}Ni masses considered, with more scatter introduced by intrinsic differences among the individual models than by the changing $M_{\rm Ni}$. For $M_{\rm Ni} \gtrsim 0.03 M_\odot$, this typically leads to a 20 - 60% increase in the plateau duration.

2.4.2 Plateau Durations for Nickel Rich Events

For Nickel-rich events, the ^{56}Ni and ^{56}Co decay dominates the internal energy of the inner ejecta, such that $C_f M_{\rm Ni} M_{10}^{-1/2} E_{51}^{-1/2} R^{-1} > 1$. Assuming that t_0 scales as in Popov (1993), we can approximate

$$\begin{aligned} & t_{\rm p} \propto M_{\rm ej}^{1/2} E_{\rm exp}^{-1/6} R^{1/6} \times (1 + C_f M_{\rm Ni} M_{\rm ej}^{-1/2} E_{\rm exp}^{-1/2} R^{-1})^{1/6} \\ & \rightarrow t_{\rm p} \overset{\propto}{\sim} M_{\rm Ni}^{1/6} M_{\rm ej}^{5/12} E_{\rm exp}^{-1/4}. \end{aligned} \tag{2.11}$$

The two features of interest are the power law behavior and the disappearing scaling with the progenitor radius. We thus expect that the plateau duration for ^{56}Ni-rich events does not depend on the progenitor radius. To check, we perform a power law fit for $t_{\rm p}$ as a function of $M_{\rm Ni}$, $M_{\rm ej}$, $E_{\rm exp}$, and R for 218 model light curves where $M_{\rm Ni} \gtrsim 0.03 M_\odot$. We find that $\log(t_{\rm p}/{\rm days}) = 2.184 + 0.134 \log(M_{\rm Ni}) + 0.429 \log(M_{10}) - 0.280 \log(E_{51}) - 0.018 \log(R_{500})$ with RMS deviations of 2.10% and a maximum deviation of 8.1%. Since the dynamic range in R is a factor of two and the scaling is negligible, we perform a fit for these same models to only $M_{\rm Ni}$, $M_{\rm ej}$, and $E_{\rm exp}$, recovering

$$\log(t_{\rm p}/{\rm days}) = 2.184 + 0.134 \log(M_{\rm Ni}) + 0.411 \log(M_{10}) - 0.282 \log(E_{51}). \tag{2.12}$$

These coefficients are excellent matches to the power laws in Equation (2.11). Our models, and their agreement with this fit, are shown in Figure 2.12. RMS deviations between this fit and our models are 2.13%, with maximum deviation of 7.5%. Typical

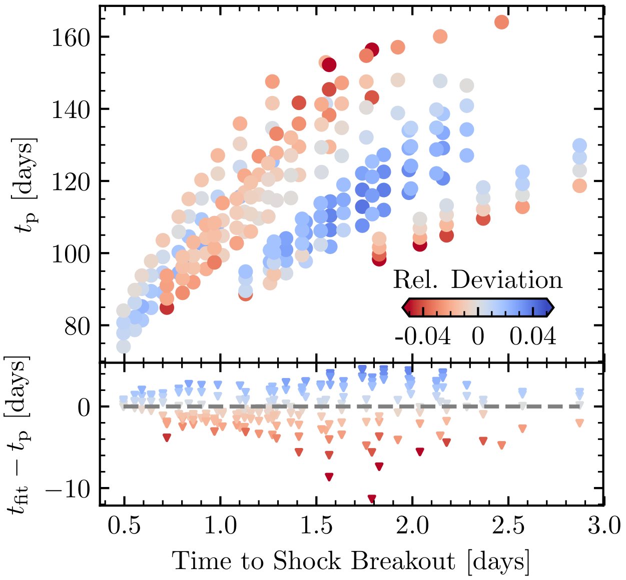

Figure 2.12: Plateau durations for our 218 SN light curves with $M_{\mathrm{Ni}} \gtrsim 0.03 M_{\odot}$ (upper panel) and the difference in plateau duration between the model t_{p} and the plateau duration t_{fit} extracted by applying Equation (2.12) to the M_{ej}, E_{exp}, and M_{Ni} of each model (lower panel), colored by $(t_{\mathrm{fit}} - t_{\mathrm{p}})/t_{\mathrm{p}}$, the fractional deviation between t_{p} from the models and t_{fit}. The x-axis is the time the model takes to reach shock breakout.

differences between the plateau durations recovered from the fit and those extracted from our models are $2 - 5$ days, with the largest discrepancy being 11 days, which is for a relatively low-luminosity SN with a plateau duration of 156 days. For all of the scaling equations of this section, the scatter in our models does not require that we report the fits to three decimal places; this is done for the sake of completeness.

We also checked the agreement of Equation (2.12) with the publicly available light curves from Dessart et al. (2013). For all of those models where the light curve has a clear end of plateau and nickel tail, we found that our fitting formula recovers a plateau which is 7 - 20% shorter when using the values for M_{Ni}, M_{ej}, and E_{exp} reported in Dessart et al. (2013). This amounts to a difference of 8 - 27 days, with the worst agreement in the case of the low-metallicity (1/10 solar) model m15z2m3, and the best agreement in the case of their "new" s15N model. The RMS difference in $|t_\mathrm{p} - t_\mathrm{fit}|$ is 18 days, about 14% relative to the average plateau in their models.

2.4.3 Constraining Explosion Parameters with ET

Following the work of Shussman et al. (2016a), Nakar et al. (2016), Kozyreva et al. (2018), and others, we can also express the impact of ^{56}Ni on t_p in terms of the ratio of the time-weighted energy contribution of the ^{56}Ni decay chain to the observable quantity ET. This ratio is defined in Nakar et al. (2016) as

$$\eta_\mathrm{Ni} = \frac{\int_0^{t_\mathrm{p}} t Q_\mathrm{Ni}(t)\mathrm{d}t}{ET}, \tag{2.13}$$

where

$$ET = \int_0^\infty t(L_\mathrm{bol}(t) - Q_\mathrm{Ni}(t))\,\mathrm{d}t, \tag{2.14}$$

is the time-weighted energy radiated away which was generated by the initial shock and not by ^{56}Ni decay, and

$$Q_\mathrm{Ni} = \frac{M_\mathrm{Ni}}{M_\odot}\left(6.45e^{-t/8.8\mathrm{d}} + 1.45e^{-t/113\mathrm{d}}\right) \times 10^{43}\ \mathrm{erg\ s^{-1}}, \tag{2.15}$$

is the instantaneous heating rate of the ejecta due to the decay chain of radioactive ^{56}Ni assuming complete trapping given in Nadyozhin (1994), and t is the time in days since the explosion. It is generally assumed that $L_\mathrm{bol}(t) = Q_\mathrm{Ni}(t)$ after the photospheric phase, on the Nickel tail, and so the integral for ET is often expressed to be bounded at $t_\mathrm{Ni} \approx t_\mathrm{p}$. We find this to be valid; see the lower panel of Figure 2.13.

Figure 2.13 shows the impact of ^{56}Ni on light curves and the integrated ET for the M16.3_R608 model exploded with $E_{\rm exp} = 10^{51}$ ergs at different $M_{\rm Ni}$. The lower panel gives the cumulative ET, integrated from shock breakout to the time on the x-axis. Most of the contribution to ET comes from luminosity on the plateau, with little contribution at early times ($t < 20\,$d) and no contribution from the Nickel tail. In the very ^{56}Ni-rich case, the cumulative integral may dip slightly negative around day 20, as radiative cooling is briefly less efficient than heating from the ^{56}Ni decay chain ($L_{\rm bol} < Q_{\rm Ni}$ in this region). This is more pronounced in models exploded at lower energies. As expected, although heating from the radioactive decay chain of ^{56}Ni extends the plateau and elevates the Nickel tail, it has very little impact on the final integrated value of ET calculated from our model light curves. Indeed, the variations of ET for the same explosion but different ^{56}Ni are at a few per-cent level.

Dimensionally, using the Popov scalings for L_{50} and plateau duration with no ^{56}Ni (t_0), ET is expected to scale as

$$ET \propto L_{50} t_0^2 \propto M_{\rm ej}^{1/2} E_{\rm exp}^{1/2} R, \tag{2.16}$$

and thus $\eta_{\rm Ni}$ should scale as $M_{\rm Ni}/ET$. A more detailed derivation of this same scaling is given in Shussman et al. (2016a). This recovers the extension to the plateau duration given by Equation (2.10), recast as

$$t_{\tau=10}/t_0 = (1 + a\eta_{\rm Ni})^{1/6}, \tag{2.17}$$

where the scaling factor a can be fit from models and encodes information about the internal structure of the ejecta, and in particular the concentration of ^{56}Ni. Kozyreva

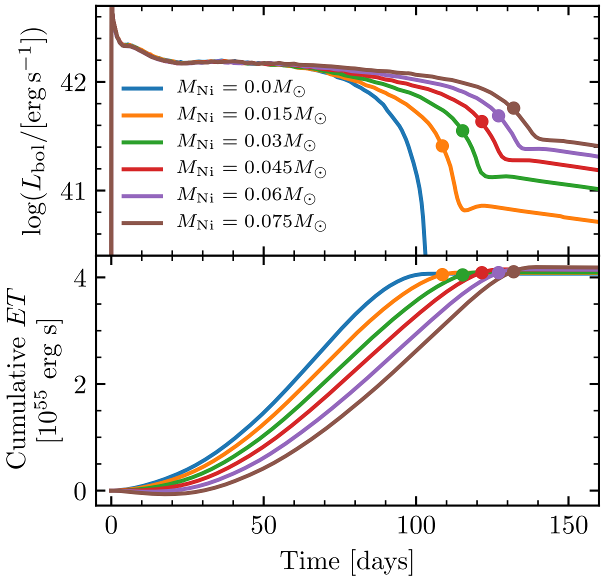

Figure 2.13: Impact of ^{56}Ni on $L_{\rm bol}$ (upper panel) and cumulative ET integrated from shock breakout to the time on the x-axis (lower panel) for M16.3_R608 model exploded with $E_{\rm exp} = 10^{51}$ ergs and $M_{\rm Ni}/M_\odot = 0.0,\ 0.015,\ 0.03,\ 0.045,\ 0.06,$ and 0.075. Points indicate $t_{\rm p}$ for the events where $M_{\rm Ni} > 0.0M_\odot$.

et al. (2018) find that for typical models, $a \approx 4$ (their Figure 5). Figure 2.14 shows the extension of the plateau as a function of $\eta_{\rm Ni}$ in our models. We find slightly higher values for a, with more models falling along $a \approx 5.5$, indicating a larger impact of ^{56}Ni on the plateau duration, in part because $\eta_{\rm Ni}$ encodes information about ^{56}Ni mixing, and our models make use of the Duffell RTI prescription whereas mixing is parameterized in Kozyreva et al. (2018). We show good agreement with the functional form in Equation (2.17).

For SNe with a reasonably well-sampled bolometric light curve where $M_{\rm Ni}$ is measured from the Nickel tail, ET can be calculated and used to constrain $M_{\rm ej}$, $E_{\rm exp}$, and progenitor R for a given explosion. In addition, ET can provide a critical constraint for

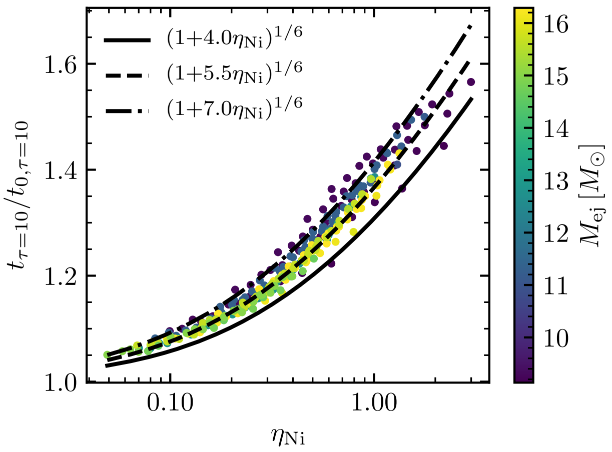

Figure 2.14: Plateau duration for models with ^{56}Ni relative to the same explosion with no ^{56}Ni, versus the parameter $\eta_{\rm Ni}$. Color corresponds to ejecta mass, and can be used to distinguish between the individual progenitor models. Black lines correspond to the plateau extension factor $(1 + a\eta_{\rm Ni})^{1/6}$ for different values of a.

explosions with lower $M_{\rm Ni}$, where the ^{56}Ni decay chain does not dominate the internal energy of ejecta and thus the power law of Equation (2.12) should not apply. Although observationally $M_{\rm Ni}$ must be extracted from the Nickel tail in order to calculate ET, ET does not follow any scaling with $M_{\rm Ni}$, as it subtracts the contribution of ^{56}Ni heating in the light curve evolution.

To determine how ET scales with $M_{\rm ej}$, $E_{\rm exp}$, and R in our models, we use the same 218 model light curves as with $t_{\rm p}$ in Equation (2.12), to recover

$$\log(ET/\mathrm{erg\,s}) = 55.460 + 0.299\log(M_{10}) + 0.435\log(E_{51}) + 0.911\log(R_{500}) \tag{2.18}$$

for our suite of models, which does not include interactions with CSM. This scaling has a slightly shallower dependence on $M_{\rm ej}$, $E_{\rm exp}$, and progenitor R than Equation (2.16).

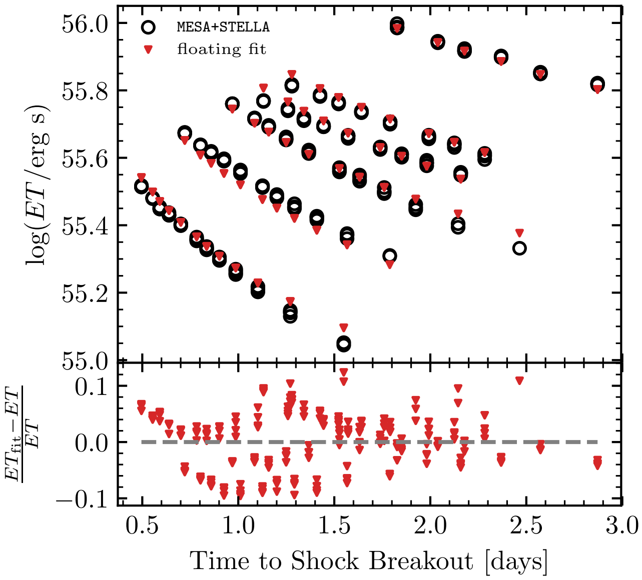

Figure 2.15: Calculated values of ET for 218 SN light curves and the values recovered with the fitted Equation (2.18) (upper panel), and fractional deviations between ET in the models and recovered using Equation (2.18) (lower panel).

The agreement between our models and Equation (2.18) is shown in Figure 2.15. RMS deviations between our models are 5.0%, with a maximum deviation of 12.4%. Although the fit was performed on models with $M_{\rm Ni} \gtrsim 0.03 M_\odot$ to be consistent with our set of models for $t_{\rm p}$, the recovered scaling applies similarly well for our models with $M_{\rm Ni} < 0.03 M_\odot$, with RMS deviations of 5.3% and all deviations under 20%. The overlapping black rings in Figure 2.15 show the typical scatter in values of ET for the same explosion when varying $M_{\rm Ni}$. Each set of overlapping rings corresponds to ET for a single progenitor model exploded with a single $E_{\rm exp}$, but with different values of $M_{\rm Ni}$. This scatter in ET when only varying $M_{\rm Ni}$ is well within the scatter between the models and the fitted Equation (2.18).

2.5 Observed Velocity Evolution

We now discuss the diagnostic value of the material velocity inferred from the absorption minimum of the Fe II 5169Å line, often measured and reported at day 50, $v_{\rm Fe,50}$. Ideally, the measured Fe line velocities would provide an additional quantitative measurement that would allow for estimation of progenitor and explosion properties (Pejcha & Prieto, 2015a; Müller et al., 2017). However, as we show here, these measurements are highly correlated with bolometric luminosity measurements at a fixed time on the plateau, and are largely redundant at day 50. If there is no substantial CSM around the star, than earlier time ($\lesssim$ 20 day) measurements may prove more useful (see Section 2.6.2).

The Fe II 5169Å velocity is typically used to approximate the velocity at the photosphere ($v_{\rm Ph}$), although there is substantial evidence that measured line velocities are typically higher than that predicted for the model photosphere ($\tau = 2/3$) (e.g. Utrobin et al. 2017; MESA IV). In a homologously expanding medium, the strength of a given line is quantified using the Sobolev optical depth (Sobolev, 1960; Castor, 1970; Mihalas, 1978; Kasen et al., 2006), which accounts for the shift in the line profile due to the steep velocity gradient in the ejecta. This is captured in `MESA+STELLA` following MESA IV, where the $\tau_{\rm Sob} = 1$ condition is used to measure iron line velocities ($v_{\rm Fe}$). Although in the following we discuss both this velocity and the velocity at the model photosphere, we recommend using $v_{\rm Fe}$ defined when $\tau_{\rm Sob} = 1$ when comparing to observations.

2.5.1 Velocities in Explosion Models

When the velocity profile of the ejecta becomes fixed in time, this material is said to be in homologous expansion. Analytically, homology is often approximated $r = vt$ for a fluid element at radial coordinate r with velocity v at time t. While not quite true for material in the center of the ejecta, which is expanding more slowly and therefore the initial radial coordinate is still relevant, this approximation generally holds for faster-moving material which has experienced more significant expansion at a given time, as well as for the slower-moving material at late times when it is becoming visible. This is reflected in Figure 32 of MESA IV.

Many software instruments devoted to modeling radiative transfer, such as `Sedona`, assume homologous expansion in the true sense of a fixed velocity profile. Figure 2.16 shows the extent to which this is satisfied in our M16.3_R608 model exploded with 10^{51} ergs. The upper panel shows the relative error in predicting the radial coordinate of a fluid element at day 160 by assuming $r_{\rm h}(\text{day } 160) = r(t_0) + v(t_0)(160\text{d} - t_0)$ for homology starting at $t_0 =$ days 10, 20, and 50. We define $\Delta r_{160} = r_{160} - r_{\rm h}(\text{day}160)$, where $r_{160} =$ the true radius of that fluid element at day 160 in `STELLA`. The lower panel shows the deviation between the velocity profiles at days 10, 20, and 50, and that at day 160. Before homology, the innermost material is moving slightly faster than its day 160 value, and the outer material is moving slightly slower. Even in the envelope, there is deviation between the day 10 velocity profile and day 160 at the level of a few per-cent. By day 20 this falls below 2%, and by day 50 typical deviations of the velocity profile in the bulk of

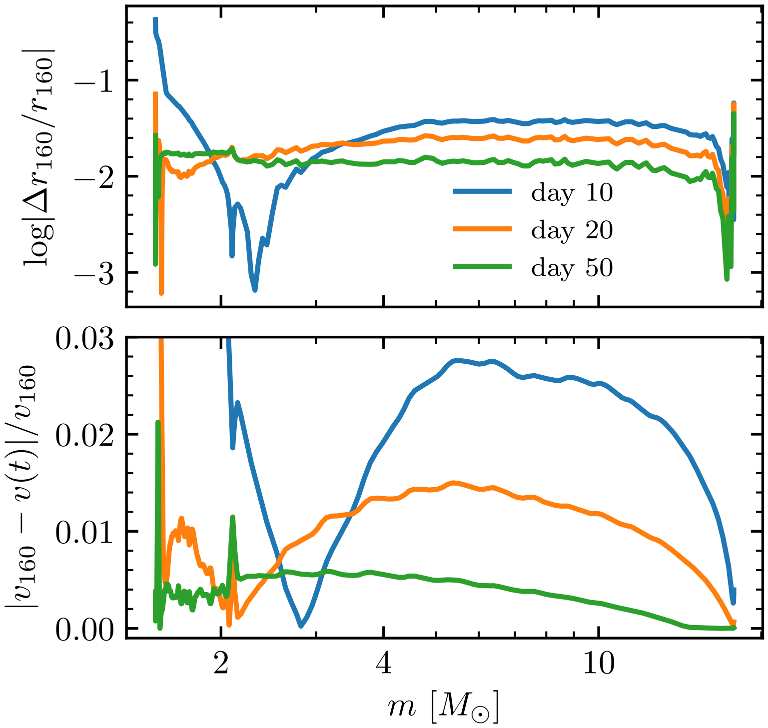

Figure 2.16: Agreement between hydrodynamical models and homologous expansion. The upper panel shows the relative error in predicting the radial profile day 160 by assuming homology starting at days 10, 20, and 50, compared to the true radial coordinate at day 160 in `STELLA`. The lower panel shows the absolute relative deviation between the velocity profiles at days 10, 20, and 50, and the profile at day 160.

the ejecta from the velocity profile at day 160 are at the level of 0.5%. Generally, by day 20, the difference in predicted radial coordinate of the half-mass fluid element at day 160 is below 3% of its true value in the hydrodynamical simulation. At this time the radial coordinate predicted for day 50 is also within 2% of its true value at day 50.

Figure 2.17 shows approximately homologous velocity profiles (taken here at day 50) scaled by the square root of $E_{\rm exp}$ for all 6 progenitor models at all energies that cause sufficiently little fallback. Each family of colored lines reflects explosions of an individual model, and each of the 6 families of lines contains the profiles for multiple explosion

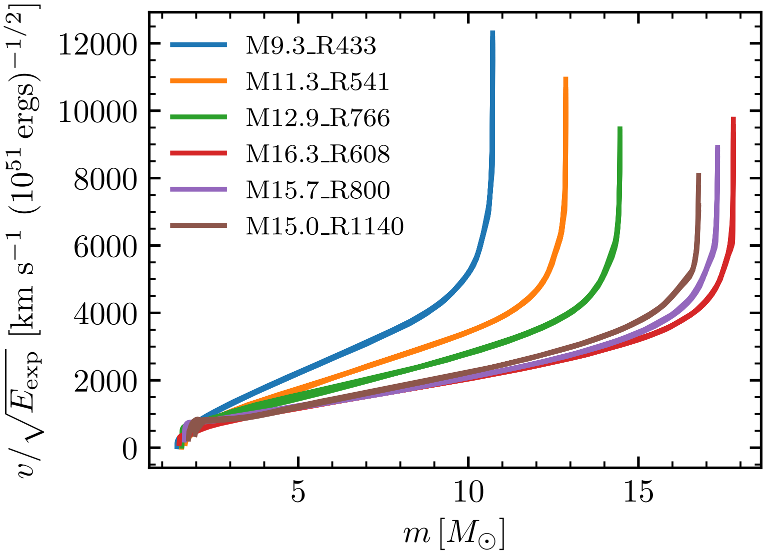

Figure 2.17: Day 50 velocity profiles in `STELLA`, divided by the square root of $E_{\rm exp}$, versus mass coordinate for 6 unique progenitor models with a variety of explosion energies. Each colored line represents a different model, and lies on top of a collection of $6 - 12$ nearly identical lines which correspond to different explosion energies for the same progenitor model.

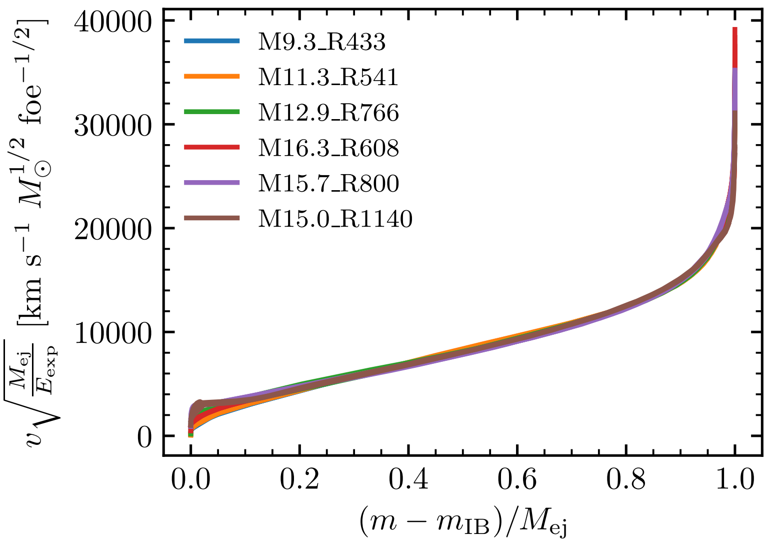

Figure 2.18: Day 50 velocity profiles in `STELLA`, multiplied by $\sqrt{M_{\rm ej}/E_{\rm exp}}$, versus dimensionless ejecta mass coordinate for all 57 explosions with energies sufficient to yield little fallback. For a fixed fractional position within the ejecta, velocities obey the scaling in Equation (2.19).

energies for that model. When looking at any fixed mass coordinate within a single progenitor model, the fluid velocity divided by $\sqrt{E_{\rm exp}}$ is constant. Moreover, as shown in Figure 2.18, looking at the same dimensionless mass coordinate inside the ejecta and scaling also by the square root of $M_{\rm ej}$, this relationship holds for any dimensionless ejecta mass coordinate throughout the entire velocity profile, with small variations only near the inner boundary, where the reverse shock becomes relevant and where fallback has a greater effect.

Popov (1993), Pejcha & Prieto (2015a), and others, have often assumed that

$$E_{\rm exp} \approx \frac{1}{2} M_{\rm ej} v_{\rm Ph,50}^2, \tag{2.19}$$

where $v_{\rm Ph,50}$ is the photospheric velocity at day 50, in order to close the system of equations for L_{50} and $t_{\rm p}$ as a function of $M_{\rm ej}$, $E_{\rm exp}$ and progenitor radius R. While the scaling law suggested in Equation (2.19) holds for the fluid velocity at a fixed dimensionless ejecta mass coordinate, as shown in Figure 2.18, as the photosphere moves deeper into the ejecta, it does not probe velocities at the same mass coordinate at a given time post shock-breakout. Rather, at a fixed time in the evolution, faster-expanding ejecta in higher energy explosions allows the observer to see deeper mass coordinates, compared to a lower energy explosion of the same star. This is evident in Figure 2.19, which shows velocity profiles for the M16.3_R608 model at 5 different explosion energies, marking the location of the photosphere and Fe II 5169Å line at fixed times. As a result of the expanding ejecta, we expect a shallower scaling for velocity as a function of energy at fixed mass than the naive $v_{\rm Ph,50} \propto E_{\rm exp}^{1/2}$. Indeed a linear fit for a single model with

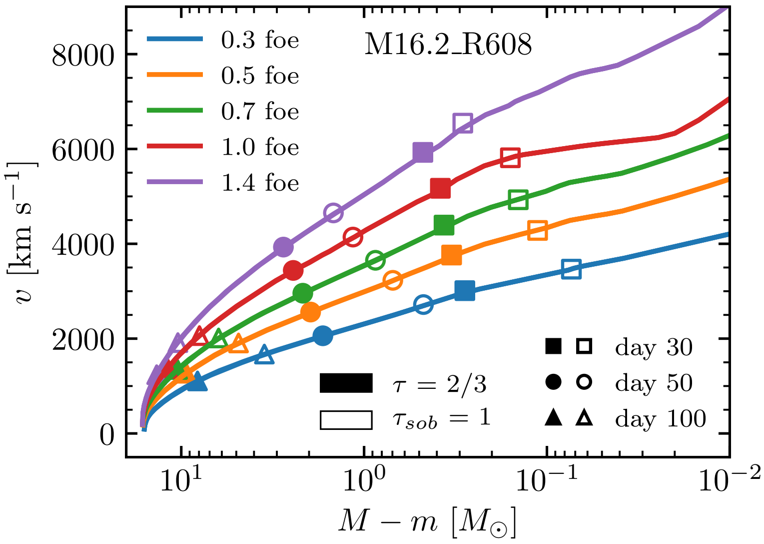

Figure 2.19: Day 50 velocity profiles versus overhead mass coordinate in `STELLA` for our M16.3_R608 model at 5 different explosion energies. We have included photospheric (filled markers) and Fe II 5169Å line velocities (open markers) for day 30, 50, and 100 as denoted by shape of the marker.

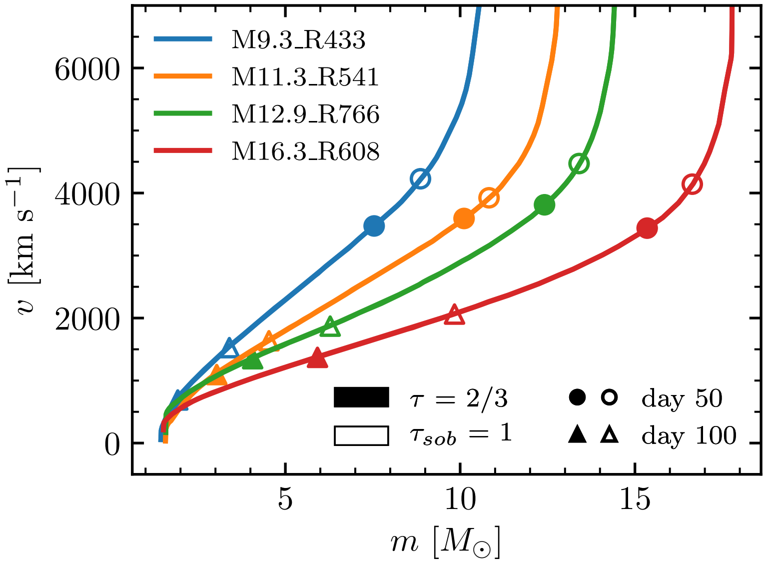

Figure 2.20: Day 50 velocity profiles for 4 different models all exploded with an energy of 1.0×10^{51} ergs. Filled markers indicate the location of the photosphere and open markers indicate where the Fe II 5169Å line is formed. Velocities at days 50 and 100 are denoted by the shape of the marker.

fixed ejecta mass and radius finds shallower scalings: $v_{\mathrm{Ph},50} \propto E_{\mathrm{exp}}^{0.36}$, and $v_{\mathrm{Fe},50} \propto E_{\mathrm{exp}}^{0.30}$. These scalings approximately hold for the other individual models.

Additionally, a velocity scaling with M_{ej} and E_{exp} becomes murkier when comparing across models of different masses at fixed explosion energy, since there is no reason for the same explosion energy to yield the "same" mass coordinate at the same time in two different progenitors. In fact, as seen in Figure 2.20, v_{Fe} and v_{Ph} at day 50 are not even monotonic in M_{ej} for different stars at fixed E_{exp}. Thus, we cannot derive any power law for $v_{\mathrm{Ph},50}$ or $v_{\mathrm{Fe},50}$ solely as a function of M_{ej} and E_{exp}. As we show in the following section, additional dependences are relevant (Equation 2.20).

2.5.2 L_{50} - $v_{\mathrm{Ph},50}$ Relation

This result highlights a true degeneracy, discovered observationally by Hamuy (2003) and explained by Kasen & Woosley (2009). We start with the Stefan-Boltzmann formula for luminosity, $L = 4\pi R_{\mathrm{phot}}^2 \sigma T_{\mathrm{eff}}^4$, where R_{phot} is the photospheric radius, and note that T_{eff} is roughly constant at the photosphere and set by H recombination to $T_{\mathrm{eff}} \approx 6000\,\mathrm{K}$. At fixed time on the plateau, (e.g. day 50) while the ejecta is expanding homologously with radial position $r \approx vt$ for any given mass coordinate, for the photosphere at day 50 $L_{50} \propto v_{\mathrm{Ph},50}^2$ and so $v_{\mathrm{Ph},50} \propto \sqrt{L_{50}}$. In this way, the luminosity, together with homologous expansion, sets the location of the photosphere within the expanding ejecta, which in turn sets the velocity measured at or near the photosphere.

Figure 2.21 shows $v_{\mathrm{Ph},50}$ and $v_{\mathrm{Fe},50}$ versus L_{50} for all 57 explosions which experience

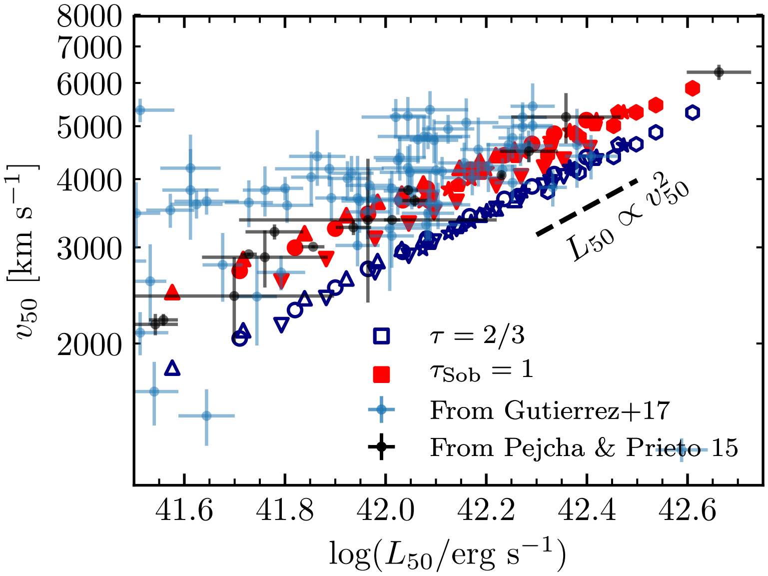

Figure 2.21: Velocity versus Luminosity at day 50 for a variety of progenitor models and explosion energies. Open navy blue markers denote photospheric velocities ($\tau = 2/3$) and closed red markers denote Fe II 5169 Å velocities ($\tau_{\rm Sob} = 1$). Points with error bars are data from 2 samples: Gutiérrez et al. (2017a) (blue) and Pejcha & Prieto (2015b) (black).

sufficiently little fallback (6 models with 6-12 explosion energies each). Also plotted are data from Pejcha & Prieto (2015b) and Gutiérrez et al. (2017a).[4] In both observational data sets, velocities are inferred from the Fe II 5169Å line, suggesting that these velocities are better captured in our models at $\tau_{\rm Sob} \approx 1$, rather than assuming the line is formed at the photosphere ($\tau = 2/3$). We also see good agreement between our models and the scaling $v_{\rm Ph,50} \propto \sqrt{L_{50}}$.

It is therefore unsurprising that the Fe velocities during the plateau phase match the

---

[4] Luminosities from Pejcha & Prieto (2015b) are bolometric luminosities provided by O. Pejcha (private communication). Luminosities from Gutiérrez et al. (2017a) were estimated from M_V measurements at day 50 provided by C. Gutierrez (private communication), assuming negligible bolometric correction BC$\approx$ 0 for M_V following the correction for SN1999em on the plateau, shown in Bersten & Hamuy (2009). Typical V band bolometric corrections on the plateau of Type IIP SNe are BC≈ -0.15 to 0.1, and the variation in $\log L_{50}$ from assuming a BC of 0 versus other values within that range is smaller than the error bars on the data.

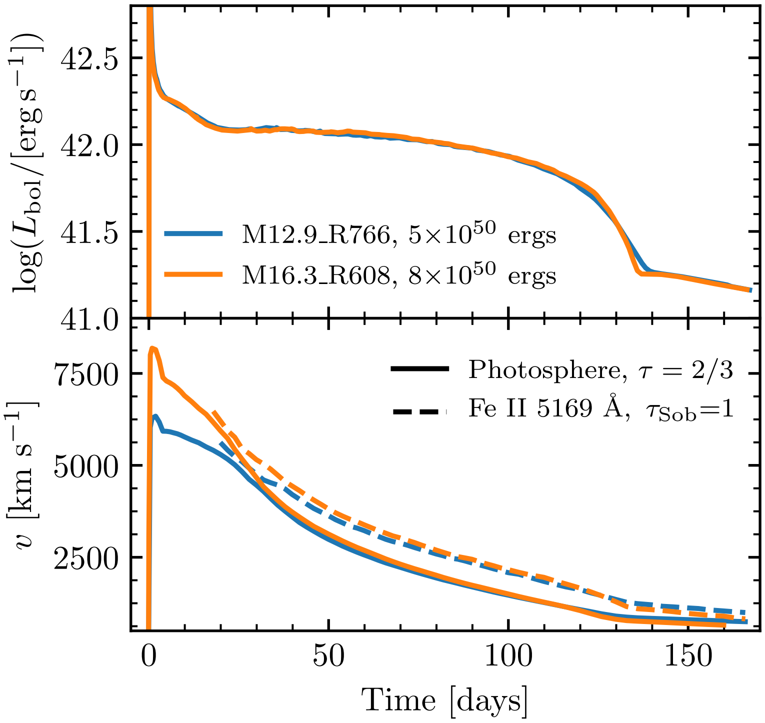

Figure 2.22: Luminosity and velocity for the 99em_16 (renamed M12.9_R766) and 99em_19 (renamed M16.3_R608) models from Paxton et al. (2018) with different explosion energies in order to attain light curve agreement.

data for a model with a luminosity match at day 50. This was seen in Section 6 of MESA IV, Figure 42, where two models with light curve agreement with SN199em show identical velocity evolution. Figure 2.22 shows the luminosity and velocity of those two progenitor models, renamed M12.9_R766 and M16.3_R608 in our suite, blown up with slightly adjusted explosion energies to produce even better light curve agreement. In the case where models match closely in both L and t_p, the agreement in velocity is excellent throughout the evolution of the SN.

As with L_{50} in Section 2.3, we fit a power law for v_{50} as a function of $M_{\rm ej}$, $E_{\rm exp}$, and R to our models with constant nickel mass $M_{\rm Ni} = 0.03M_\odot$. We do this with both $v_{\rm Fe,50}$

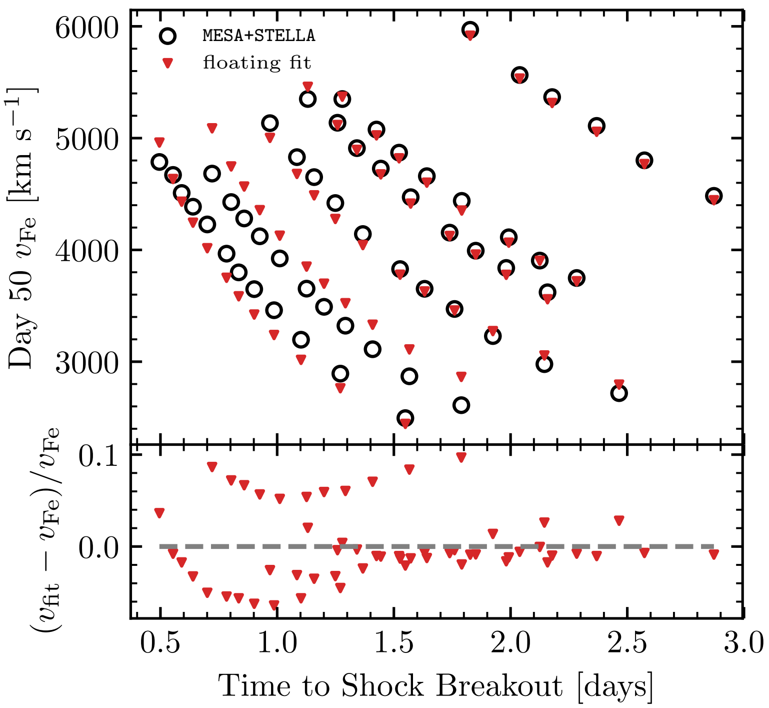

Figure 2.23: Model v_{Fe} ($\tau_{\mathrm{Sob}} = 1$) at day 50, and velocities recovered with the fitting formulas (upper panel), and their residuals (lower panel) for our suite of 57 explosions with $M_{\mathrm{Ni}} = 0.03 M_{\odot}$. So as to clarify the model space, we use time to shock breakout as the x-axis.

and $v_{\mathrm{Ph},50}$ at day 50, noting that observationally, $v_{\mathrm{Fe},50}$ is the relevant scaling. For the photospheric velocity at day 50, we found power laws that are very similar to the scaling found if $v_{\mathrm{Ph},50} \propto L_{50}^{1/2}$:

$$\log(v_{\mathrm{Ph}}/\mathrm{km\ s^{-1}}) = 3.54 - 0.19 \log M_{10} + 0.36 \log E_{51} + 0.32 \log R_{500}, \tag{2.20}$$

where the prefactor and power law coefficients are all fit from our models.

This is valuable insofar as it reinforces the degeneracy highlighted in Figures 2.21 and 2.22, but, as discussed, this velocity is unmeasurable, and observed Fe II 5169Å line velocities are better estimated by ($\tau_{\mathrm{Sob}} = 1$). A similar fit to v_{Fe} at day 50,

$$\log(v_{\mathrm{Fe},50}/\mathrm{km\ s^{-1}}) = 3.61 - 0.12 \log M_{10} + 0.30 \log E_{51} + 0.25 \log R_{500}, \tag{2.21}$$

yields higher predicted velocities everywhere, and shows somewhat shallower dependence on each of the explosion properties. The model Fe line velocities and their residuals as compared with Equation (2.21) are shown in Figure 2.23.

Although the degeneracy is less pronounced for $\tau_{\mathrm{Sob}} = 1$ than for the photosphere, with some scatter in Figure 2.21 and differences in the recovered power laws, this scatter is small compared to intrinsic variations in luminosity and plateau duration, and is therefore insufficient to break the degeneracy between v and L in order to provide accurate estimates for M_{ej}, E_{exp}, and R. It is for this reason that we do not advocate using measured velocities at day 50 to infer explosion properties.

2.6 Families of Explosions

2.6.1 Inverting Our Scalings

Due to the degeneracies highlighted in Section 2.5, we cannot simply extract M_{ej}, E_{exp}, and R from light curve measurements and $v_{\mathrm{Fe},50}$. Attempting to invert all three scalings (Equations (2.8), (2.18), and (2.12)) is ill-conditioned and within the scatter within our models. However, we can use the scalings to solve for two of the three relevant explosion properties as a function of the third, revealing a family of possible explosions that yield nearly identical bolometric light curves.

SNe with direct progenitor observations are improving with time, so we solve Equations (2.8) and (2.12) for $M_{\rm ej}$ and $E_{\rm exp}$ as a function of $M_{\rm Ni}$, L_{50}, $t_{\rm p}$, and R, to find

$$\begin{aligned} \log(E_{51}) &= -0.728 + 2.148\log(L_{42}) - 0.280\log(M_{\rm Ni}) + 2.091\log(t_{\rm p,2}) - 1.632\log(R_{500}),\\ \log(M_{10}) &= -0.947 + 1.474\log(L_{42}) - 0.518\log(M_{\rm Ni}) + 3.867\log(t_{\rm p,2}) - 1.120\log(R_{500}), \end{aligned} \tag{2.22}$$

where $M_{\rm Ni}$ is in units of $M_\odot$, $L_{42} = L_{50}/10^{42}$ erg s^{-1} and $t_{\rm p,2} = t_{\rm p}/100\,{\rm d}$. Alternatively, we can use a measured ET rather than $t_{\rm p}$ to find

$$\begin{aligned} \log(E_{51}) &= -0.587 - 1.497\log(R_{500}) + 1.012\log(ET_{55}) + 0.756\log(L_{42}),\\ \log(M_{10}) &= -0.685 - 0.869\log(R_{500}) + 1.872\log(ET_{55}) - 1.101\log(L_{42}), \end{aligned} \tag{2.23}$$

where $ET_{55} = ET/10^{55}{\rm erg\,s}$.

Before demonstrating how to apply these fitting formula to observed SNe, we show how well modeled events can be matched. The upper panel of Figure 2.24 shows the fraction of models with light curve properties matching their fitted values (applying Equations (2.8), (2.12), and (2.18)) within a given deviation tolerance shown on the x-axis. The lower panel shows the fraction of models in which we can recover the values of $M_{\rm ej}$ and $E_{\rm exp}$ within a given deviation tolerance by applying Equation (2.22) (solid lines) or Equation (2.23) (dashed lines) to the model light curve observables and R. Given that there is no statistical meaning to the sample of models beyond probing different regions of parameter space, this merely provides a heuristic guide to how well our sample of models match with the fitted formulae.

Applying Equation (2.22) using $t_{\rm p}$ to our suite of Nickel-rich SNe, we recover $M_{\rm ej}$ and

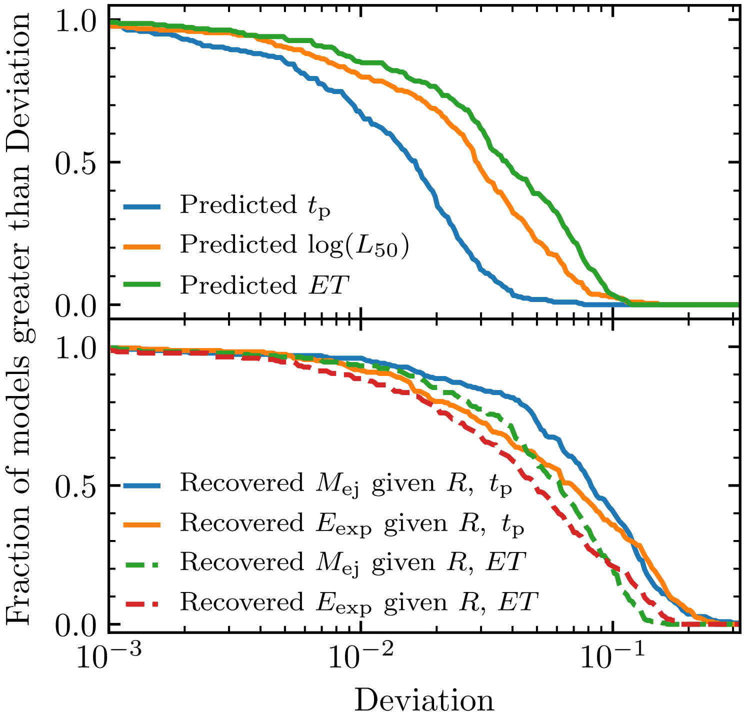

Figure 2.24: Distribution of deviations between our models and Equations (2.8) and (2.12) (upper panel), and the distribution of deviations between recovered values of M_ej and E_exp by applying the inverted scalings (Equation (2.22)) to the model light curve properties and radii, and the models themselves (lower panel). This gives a heuristic for the agreement between the fitted formulae and our suite of models.

E_exp with RMS deviations between the models and the fits of 10.7% and 10.4%, respectively, with maximum deviations of 35% and 27%. Using ET and Equation (2.23), we recover M_ej and E_exp with RMS deviations between the models and the fits of 7.3% and 7.6%, respectively, with maximum deviations of 16% and 18%. Although the modeling uncertainties for the inverted ET scalings are smaller than those which use t_p, the observable uncertainty is greater and may be accompanied by an offset, as excess emission within the first 10-40 days due to interaction with CSM may cause an excess in ET as compared to our models.

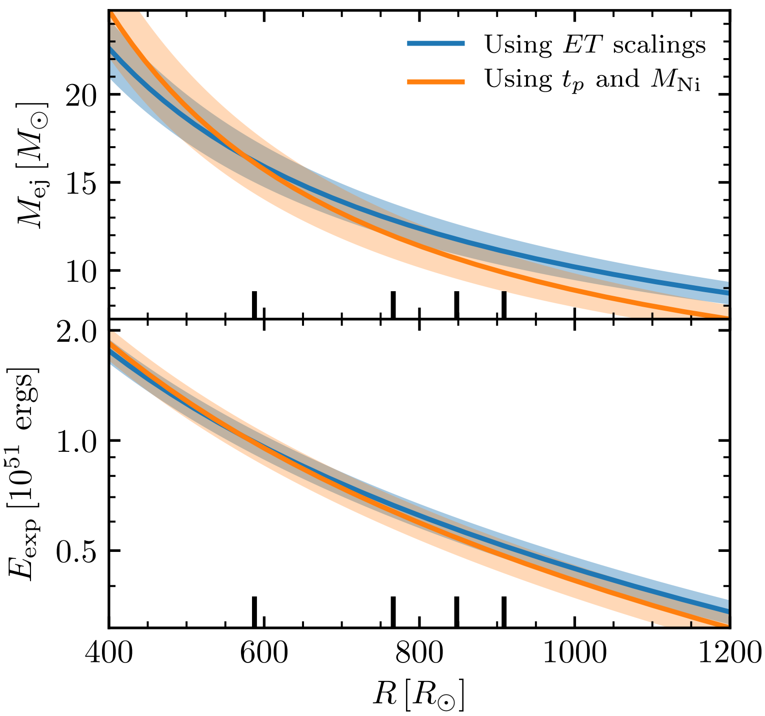

Figure 2.25: Degeneracy curves applying Equation (2.22) (orange) and Equation (2.23) (blue) as a function of progenitor radius R for an "observed" SN with $\log(L_{50}/\mathrm{erg\,s^{-1}})$=42.13, $\log(ET/\mathrm{erg\,s})$=55.58, $t_{\rm p}$=123, and $M_{\rm Ni} = 0.045 M_\odot$. The shaded region corresponds to the RMS deviations between our models and the values recovered by applying Equations (2.22) and (2.23). Short black lines correspond to the radii of the M17.8_R587, M12.9_R766, M10.2_R848, and M9.8_R909 models, which produce the light curves, velocities, and ET evolution shown in Figure 2.26.

Using these relations, we now show how very comparable light curves (and thus comparable Fe II 5169Å line velocities on the plateau) can be produced with different progenitors exploded at different energies. Figure 2.25 shows an example of the family of models in $M_{\rm ej} - E_{\rm exp}$ parameter space as a function of R that could produce an "observed" SN light curve with $\log(L_{50}/\mathrm{erg\,s^{-1}})$=42.13, $\log(ET/\mathrm{erg\,s})$=55.58, $t_{\rm p}$=123, and $M_{\rm Ni} = 0.045 M_\odot$, which are the values matching a randomly selected model out of our suite: the M12.9_R766 model exploded with $E_{\rm exp} = 6 \times 10^{50}$ ergs and that $M_{\rm Ni}$.

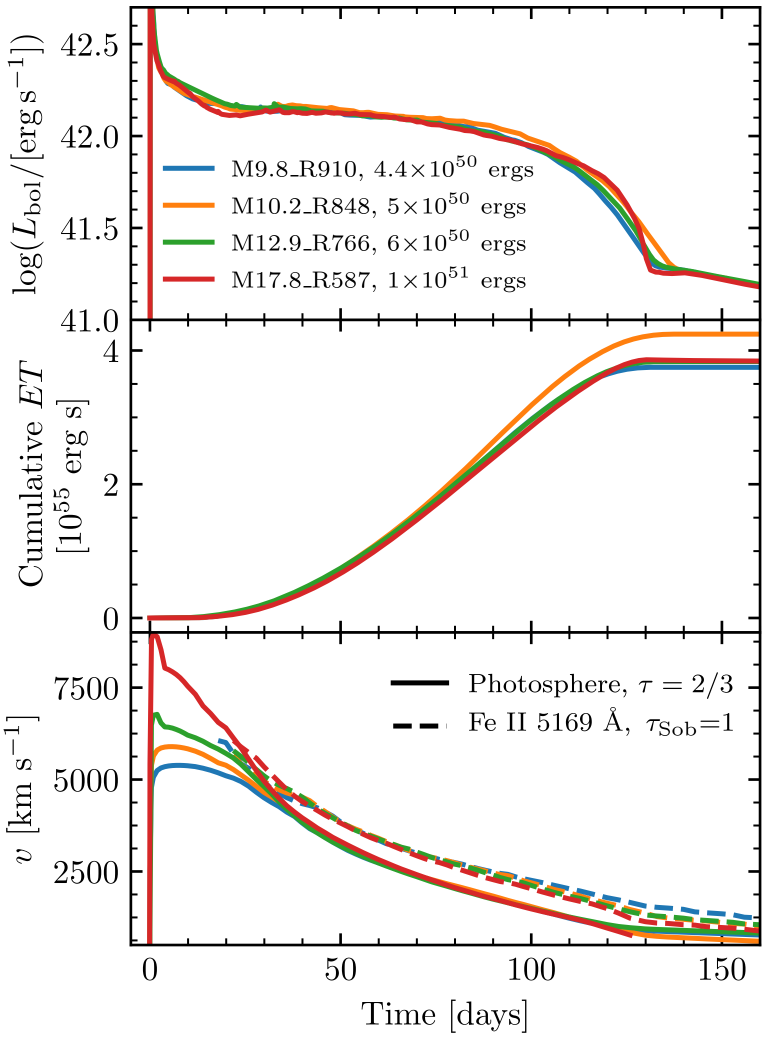

Figure 2.26: Light curves, cumulative ET, and velocities for four different explosions which yield nearly the same L_{50}, $t_{\rm p}$, and velocities at day 50.

To exhibit how this exercise would proceed, we construct three additional models consistent with the bands in Figure 2.25, based off Equation (2.22) using t_{p}. We then exploded these progenitor models with E_{exp} as dictated by the degeneracy curve: one with $M_{\mathrm{ej}} = 17.8M_{\odot}$ and $R = 587R_{\odot}$, which we explode with 1×10^{51} ergs, one with $M_{\mathrm{ej}} = 10.2M_{\odot}$ and $R = 848R_{\odot}$, which we explode with 5×10^{50} ergs, and one with $M_{\mathrm{ej}} = 9.8M_{\odot}$ and $R = 909R_{\odot}$, which we explode with 4.5×10^{50} ergs. The values of R for these three models, and for M12.9_R766 exploded with 6×10^{50} ergs, are shown as black tick marks in Figure 2.25. Figure 2.26 shows the resulting light curves, velocities, and accumulated ETs. We see very good agreement in L_{50} and along the plateau, and recover t_{p} values from 120 to 125 days for all four light curves.

The values of ET for three of the four light curves agree within $\approx 2\%$, ranging from 3.75 to 3.84×10^{55} erg s; however, the 5×10^{50} erg explosion of the M10.2_R848 model has a value of ET which is noticeably higher, at 4.26×10^{55} erg s. Additionally, velocities agree on the plateau, and thus cannot be used to break the light curve degeneracy, which at least spans a factor of 2 in explosion energy, nearly a factor of 2 in M_{ej}, and a factor of 1.5 in progenitor R. This captures much of the parameter space in which IIP SNe from RSG progenitors could be produced to begin with!

2.6.2 The Importance of Velocities at Early Times

Although velocity measurements at day 50 are largely degenerate with measurements of L_{50}, as discussed in detail in Section 2.5, early time velocities up to day $\approx$20 could be used to distinguish between low-energy explosions of large-radius lower-mass RSGs and high-energy explosions of compact-radius high-mass RSGs in cases where there is minimal CSM present. As seen in the lower panel of Figure 2.26, higher energy explosions of compact stars yield faster velocities at early times. Before around day 20, the radial coordinate of the photosphere is moving outward, and the declining photospheric temperature is set by shock cooling rather than by recombination. Thus in this phase the velocity measured near the photosphere is not dictated by the plateau luminosity as it is at day 50. Early light curves and photospheric velocities are discussed in detail by Morozova et al. (2016) and Shussman et al. (2016b). Shussman et al. (2016b) find an expression for the photospheric velocity at early times as a function of $M_{\rm ej}$, $E_{\rm exp}$, and R (their Equation 48), assuming that the density profile of the progenitor model behaves like a power law in radial coordinates. After the photosphere leaves the so-called breakout shell ($5{\rm d} \lesssim t \lesssim 20{\rm d}$), Shussman et al. (2016b) find that $v_{\rm Ph}(t)/{\rm km\,s^{-1}} \approx 1.2 \times 10^4 M_{15}^{-0.3} E_{51}^{0.38} R_{500}^{-0.14} t_{\rm d}^{-0.2}$ where $M_{15} = M_{\rm ej}/15M_\odot$ and $t_{\rm d} = t/{\rm d}$. At day 15 this equation describes our full suite of models with RMS deviations of 5.5% and with all deviations under 15%.

As is also seen in Figure 2 of Morozova et al. (2016), no single power law fully describes progenitor density profiles around the photospheric mass coordinate in our models for any fixed time in the light curve evolution. Nonetheless our entire suite of models, which does not include the presence of circumstellar material, can approximately be described by the fitted power law

$$\log(v_{\mathrm{Ph},15}) = 3.90 - 0.22\log(M_{10}) + 0.43\log(E_{51}) - 0.13\log(R_{500}), \tag{2.24}$$

where $v_{\mathrm{Ph},15}$ is the photospheric velocity at day 15 in km s^{-1}, with RMS deviations of 3.7% and a maximum deviation of 10% between the models and Equation (2.24). The dynamic range in $v_{\mathrm{Ph},15}$ in our models is a factor of ≈ 3, ranging from $\approx 4,000 - 12,000$ km s^{-1}.

Although Equation (2.24) and Shussman's Equation 48 describe our models well, we warn the reader that velocities at this time are sensitive to the density structure of the outermost ejecta including any asphericity, as well as any interactions with any circumstellar material present. Thus more work is needed in order to faithfully capture the early-time velocities and their dependence on the relevant properties of the explosion, especially in cases where CSM is present. Nonetheless, early time velocity measurements could in principle provide a third constraint and break the light curve degeneracies, thus allowing an inference of M_{ej}, progenitor R, and E_{exp} for a given observed Type IIP SN.

2.7 Concluding Remarks

We have shown the utility of using `MESA`+`STELLA` to model an ensemble of Type IIP SN progenitors, a capability introduced by Paxton et al. (2018). We introduced new best-fit scaling laws for the plateau luminosity at day 50, L_{50} (Equation 2.8), and for the duration of the plateau $t_{\rm p}$ in the limit of Nickel-rich ($M_{\rm Ni} \geq 0.03 M_{\odot}$) events (Equation 2.12) as a function of ejecta mass, explosion energy, and progenitor radius. We also recovered a similar fit for the observable ET (Equation 2.18). Velocity measurements on the plateau cannot be described by $v_{\rm Ph,50} \approx (2E_{\rm exp}/M_{\rm ej})^{1/2}$ assumed by Popov (1993) or the scaling given in Litvinova & Nadyozhin (1983), but rather scale with L_{50} as noted by Hamuy (2003); Kasen & Woosley (2009) and others, shown in our Figure 2.21. While early-time velocities observed during the photospheric phase ($\approx$ day 15) could provide a promising third independent constraint on $M_{\rm ej}$, $E_{\rm exp}$, and R, these velocities can be affected by interaction with CSM, deviations from spherical symmetry, and the specifics of the density profile of the progenitor star. Thus early velocities require more work in order to simply interpret in observed systems. Presently, given a bolometric light curve, one can at best recover a family of explosions which produce comparable light curves and thereby velocities on the plateau, as demonstrated in Figures 2.22 and 2.26. This can then be used to guide modeling efforts, especially when coupled with other constraints, such as a measurement of the core mass and thereby progenitor mass at the time of explosion (as in Jerkstrand et al. 2012). With a clear independent constraint on one explosion parameter, such as an observed progenitor radius, the other explosion properties can be recovered to around 15%.

Chapter 3

A Massive Star's Dying Breaths: Pulsating Red Supergiants and Their Resulting Type IIP Supernovae

Periodic variability is prevalent in Red Supergiant (RSG) stars, and is interpreted as being a result of radial pulsations (Stothers, 1969; Stothers & Leung, 1971; Guo & Li, 2002). The mechanism driving these pulsations is not fully understood, but they are thought to be driven by a κ mechanism in the hydrogen ionization zone with some uncertain feedback within the convective envelope (Heger et al., 1997; Yoon & Cantiello, 2010). Kiss et al. (2006) and Percy & Khatu (2014) identified periods of a few hundred to a few thousand days with varying stellar lightcurve morphology for RSGs in the AAVSO International Database. Such pulsations have also been observed occurring in RSGs within the Small and Large Magellanic Clouds (Feast et al., 1980; Ita et al., 2004; Szczygieł et al., 2010; Yang & Jiang, 2011; Yang & Jiang, 2012; Yang et al., 2018), M31 and M33 (Soraisam et al., 2018; Ren et al., 2019), M51 (Conroy et al., 2018), M101 (Jurcevic et al., 2000), within HST archival data of NGC 1326A, NGC 1425, and NGC 4548 (Spetsieri et al., 2019), and within the GAIA DR2 RSG sample (Chatys et al., 2019). These works identify these RSG pulsations as consistent with radial fundamental modes and some first radial overtones.

More luminous RSGs generally exhibit longer periods and higher pulsation amplitudes, with all RSGs in M31 brighter than $M_k \approx -10$ mag ($\log[L/L_{\odot}] > 4.8$) varying with $\Delta m_R > 0.05$ mag, with R-band variability around $\Delta m_R \approx 0.4$ in some of the more luminous objects (Soraisam et al., 2018). Although it is expected that the metallicity of the host environment might have some small impact on the period-luminosity relationship (Guo & Li, 2002), this effect is weak compared to the scatter within the data (see, e.g. Conroy et al. 2018; Ren et al. 2019; Chatys et al. 2019). It is not known whether there is a strong relationship between the host metallicity and pulsation amplitude, but the amplitudes reported for metal-rich M31 are similar to the pulsation amplitudes of RSGs in M33 despite the ≈0.25 dex difference in metallicity (Ren et al., 2019). There is, however, a noticeable increase in the number ratio of RSGs pulsating in their fundamental mode versus the first overtone mode with increasing metallicity (Ren et al., 2019).

Multi-epoch studies of Red Supergiants as potential progenitors for direct collapse into black holes are underway (Kochanek et al., 2008), which are ideal for probing the variability of these objects as candidates for core-collapse supernovae (CCSNe) as in Kochanek et al. (2017a) and Johnson et al. (2018). So far, the majority of supernovae (SNe) whose progenitors have been monitored are consistent with no variability, with the exception of the progenitor of the Type IIb SN 2011dh (Kochanek et al., 2017a), which was variable in R-band by 0.039 ± 0.006 mags per year (Szczygieł et al., 2012). This is not inconsistent with the near ubiquity of RSG pulsations at high luminosities, as most progenitors observed before undergoing Type II SNe have been on the lower end of the RSG luminosity spectrum (Smartt, 2009, 2015), where pulsation amplitudes are likewise generally lower. However, still relatively few such events have been monitored, and there is an open theoretical question about how CCSN lightcurves are influenced by the presence of progenitor pulsations.

Recent work highlights that modeling of lightcurves and photospheric velocities alone is insufficient to extract progenitor characteristics from observed SNe (Dessart & Hillier, 2019; Goldberg et al., 2019; Martinez & Bersten, 2019). A progenitor radius can provide a crucial constraint, allowing to distinguish between, say, a more compact higher ejecta-mass event with a higher explosion energy, and an event with a larger progenitor radius, lower ejecta mass, and lower explosion energy. This has been done recently by creating matching lightcurve models for SNe with observed progenitor radii (e.g. Martinez &

Bersten 2019), fixing a mass-radius relationship by fixing stellar evolution parameters (such as metallicity, mixing length in the H-rich envelope, overshooting, winds) and fitting to a large set of population synthesis lightcurve models (e.g. Eldridge et al. 2019), and in an ensemble fashion by using a prior on the radius of RSGs to extract explosion energies statistically for an existing sample of IIP lightcurves (Murphy et al., 2019). Because, in reality, the progenitor radius could be affected by RSG pulsations, this could lend itself to additional uncertainty in any explosion parameters recovered from SN observations, especially in the case of directly using an observed progenitor radius at an unknown phase relative to the time of explosion.

Observed Type IIP SNe are also often reported to show excess emission before day $\approx$30, often attributed to interaction with the extended environment surrounding the progenitor (e.g. Khazov et al. 2016; Morozova et al. 2017, 2018; Förster et al. 2018; Hosseinzadeh et al. 2018). Because models of early emission depend sensitively on the progenitor density profile (e.g. Nakar & Sari 2010; Sapir et al. 2011; Katz et al. 2012; Sapir & Waxman 2017; Faran et al. 2019), any modification of the outer stellar structure and surrounding environment could translate to distinct changes in the early SN emission (see, e.g., Morozova et al. 2016). For example, the effects of pulsation-driven superwinds (Yoon & Cantiello, 2010) on early SN-IIP lightcurves have been directly considered by Moriya et al. (2011, 2017). However, 1D modeling of the extended atmospheres of massive stars is inherently limited, as 1D codes cannot reproduce the detailed 3D structure of the outermost envelope (see e.g. Chiavassa et al. 2011a; Arroyo-Torres et al. 2015;

Kravchenko et al. 2019). Therefore, in this work we primarily restrict our discussion to plateau properties after day ≈30, at which point the SN emission comes from the modified interior of the star and not the outermost $\approx 0.2 M_{\odot}$.

In this work, we consider effects of pulsations on the bulk density structure of the stellar envelope and the impact these structural differences have on the resulting Type IIP SNe. In Section 3.1 we discuss our approach to capturing the effects of radial pulsations on the internal structure of the star using the open-knowledge 1D stellar evolution software instrument Modules for Experiments in Stellar Astrophysics (`MESA`; Paxton et al. 2011, 2013, 2015, 2018, 2019), and compare our pulsating models to expectations from linear theory. In Section 3.2 we demonstrate the effects these structural changes have on the resulting SN lightcurves. We show the luminosity at day 50 (L_{50}), time-integrated shock energy (ET), and plateau duration (t_{p}) for SNe of progenitors pulsating in their fundamental mode scale with the progenitor radius at the moment of explosion as given by Popov (1993); Kasen & Woosley (2009); Nakar et al. (2016); Goldberg et al. (2019) and others. Furthermore, we show that for pulsations where the displacement is not monotonic, such as the first overtone, SN emission from different regions within the ejecta is influenced by the differing structure.

3.1 Modeling Radial Pulsations

We construct our fiducial model of a CCSN progenitor with `MESA` revision 11701. We choose a nonrotating, solar-metallicity ($Z = 0.02$) model of $18 M_{\odot}$ at ZAMS, with a convective efficiency of $\alpha_{\rm MLT} = 3.0$ in the Hydrogen-rich envelope. We use modest convective overshooting parameters $f_{\rm ov} = 0.01$ and $f_{0,\rm ov} = 0.004$, and winds following `MESA`'s 'Dutch' prescription with efficiency $\eta_{\rm wind} = 0.4$ (Glebbeek et al., 2009; Vink et al., 2001; Nugis & Lamers, 2000). After the end of core carbon burning, identified when the central fraction of ^{12}C falls below 10^{-6}, we introduce a maximum timestep of 10^{-3} years. This is to ensure that the model remains numerically converged, as well as to ensure that we resolve changes its structure when causing it to pulsate on a timescale of hundreds of days. Other inputs are determined following the `25M_pre_ms_to_core_collapse` case of the `MESA` test suite. At the time of core-collapse, 1715 days after the end of core Carbon burning, the unperturbed model has a total mass of $M = 16.3 M_\odot$, a radius of $R = 880 R_\odot$, and a luminosity of $L = 1.56 \times 10^5 L_\odot$.

After evolving the model through the end of core carbon burning, we use the pulsation instrument `GYRE` (Townsend & Teitler, 2013; Townsend et al., 2018) to identify the periods and radial displacement eigenfunctions for the first 3 radial ($l = 0$) modes. We recover a fundamental pulsation period of 534 days, a first overtone period of 240 days, and a second overtone period of 154 days. The radial displacement eigenfunction $\xi(r)$ for the fundamental mode, and the first and second overtones, normalized to $\max(\xi(r)) = 1$, are shown in Figure 3.1.

To model the effects of pulsation on the density structure of the envelope, we inject the fundamental eigenmode as a velocity proportional to the radial displacement given by `GYRE`. For a zone with radial coordinate r, we set $v(r) = 1.2\, c_{\rm s,surf}\, \xi(r)$, where $c_{\rm s,surf}$ is

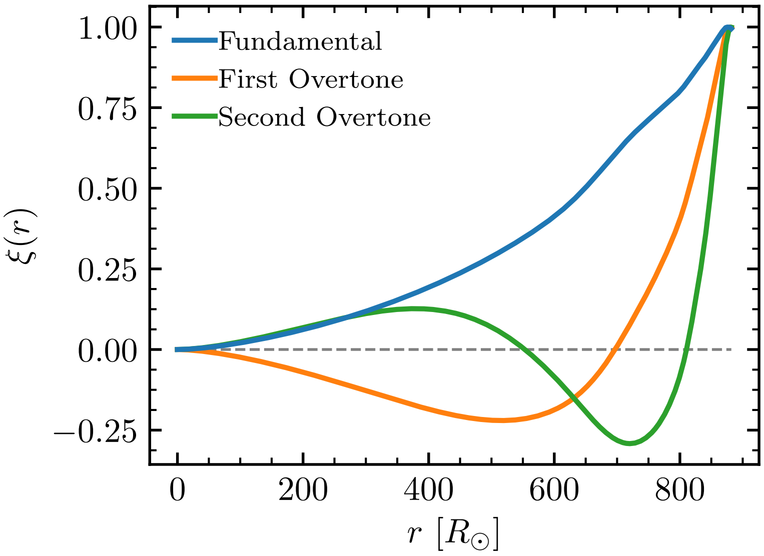

Figure 3.1: Normalized radial displacement eigenfunctions for our fiducial stellar model at core Carbon depletion.

the sound speed at the surface of the unperturbed model and $\xi(r)$ is normalized to be 1 at its maximum value. The resulting pulsation causes significant variation in the radius, from 760 - 1100 $R_\odot$ over the course of a few pulsations. This amplitude was chosen to resemble the 0.3-0.4 mag amplitudes seen by Soraisam et al. (2018). We do not claim that the growth in the pulsations is being modeled correctly; rather, we are only interested in the effects of realistically large pulsations on the SN properties. In order to achieve core collapse at different phases of the pulsation, we inject this velocity eigenfunction starting at increments of 36.5 days up to 474.5 days after core carbon depletion and allow the model to ring as it evolves to core collapse, as shown in Figure 3.2. For the fundamental mode, the recovered average peak-to-peak period is 535 days, and trough-to-trough period is 550 days, as the pulsation becomes increasingly nonlinear, especially near the minimum radius. However, both are close to the 534 day period expected of a small amplitude pulsation.

The process of causing our models to pulsate with the first radial harmonic is nearly identical to that described above. However, since the overtone pulsation period of 240 days is approximately half that of the fundamental mode, and there is a node in the radial displacement eigenfunction such that the surface displacement is only caused by oscillation in the outer envelope, the radial pulsation amplitude is comparatively small for a given injected velocity amplitude. Figure 3.3 shows the overtone pulsation injected with different amplitudes. A fundamental mode is also shown for comparison. The recovered average peak-to-peak and trough-to-trough periods are 236 days and 241 days, respectively, taken over the first 4 pulsation cycles. Particularly for larger amplitude pulsations, the fundamental mode grows in the overtone-injected models, causing modulation on longer timescales than the overtone period. This effect gets stronger with increasing initial pulsation amplitude, making it very difficult to create a model which rings with a "pure" overtone and has a sizeable pulsation amplitude.

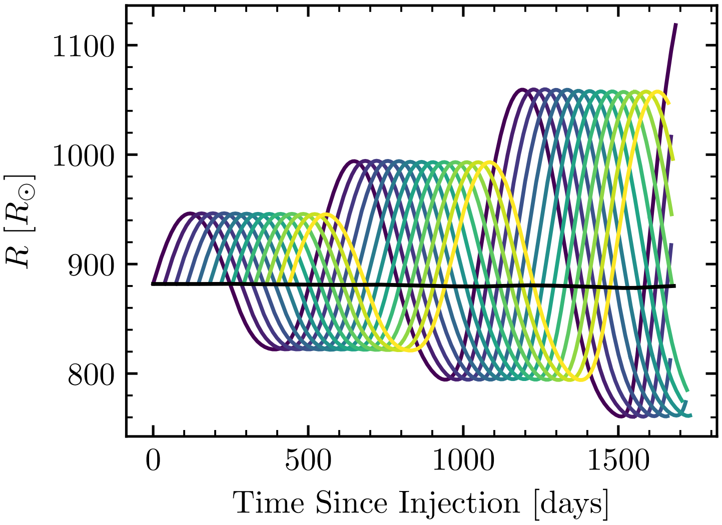

Figure 3.2: Stellar radius as a function of time, after injecting the velocity eigenfunction of the fundamental radial mode. The left-most point on each curve corresponds to the time of injection relative to the earliest injection, and the right-most point corresponds to the model at the time of core collapse. The black line shows the negligible variation in the stellar radius of the unperturbed model.

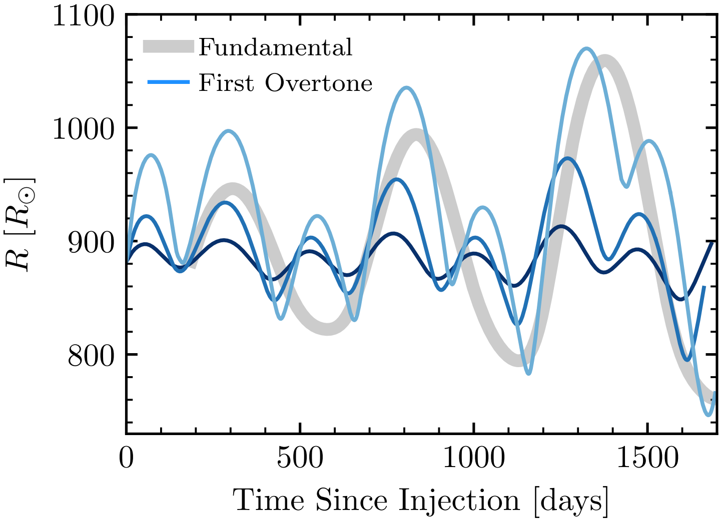

Figure 3.3: Stellar radius as a function of time in our models injected with first overtone velocity eigenfunctions. The injected initial velocity amplitudes shown here are $A = 0.69$ (dark blue), 1.71 (average blue), and 3.42 (light blue), for velocities injected of the form $v(r) = A\, c_{\rm s,surf}\, \xi(r)$ where ξ is the displacement eigenfunction for the first overtone. A fundamental mode pulsation is also shown, with its starting point chosen to visually resemble the modulation seen in the overtone models.

3.1.1 Analytic Expectations in the Linear Regime

For a small perturbation, we can express the radius of that element as $\vec{r} = \vec{r}_0 + \vec{\xi}$, where $\vec{r}_0$ is the unperturbed radius and $\vec{\xi}$ is the Lagrangian displacement. For a radial oscillation with $\vec{\xi} = \xi e^{i\omega t}\,\hat{r}$, where ω is the frequency of oscillation, the velocity of that fluid element is $\vec{v} = i\omega\vec{\xi}$. By continuity, the density of the fluid element changes as

$$\frac{d\rho}{dt} + \rho\vec{\nabla}\cdot\vec{v} = 0, \tag{3.1}$$

where d/dt represents the Lagrangian time derivative $d/dt = \partial/\partial t + \vec{v}\cdot\vec{\nabla}$. Equation (3.1) yields the Lagrangian density perturbation $\Delta\rho$,

$$\Delta\rho = -\rho_0\vec{\nabla}\cdot\vec{\xi} = -\rho_0\frac{1}{r^2}\frac{d}{dr}r^2\xi. \tag{3.2}$$

In order to check the agreement between our pulsating model and the expectations from linear theory, we save the density profile at the maximum and minimum radius for fundamental mode and overtone pulsations. Figure 3.4 shows the agreement between our models and Equation (3.2). Here we normalize ξ to match the displacement in the pulsating model at the mass coordinate corresponding to $300R_\odot$ in the unperturbed model, at an overhead mass of $5.7M_\odot$. This location was chosen because it corresponds to roughly half of the envelope mass and half of the stellar radius in log-space. The surface is most severely affected by nonlinearities, and this work primarily explores effects on the bulk of the material. We also choose to display the overtone profiles at the first maximum (1/4 period after injecting the velocity eigenfunction) and the second minimum (7/4 period after injection) of the model with an injected velocity of $v(r) = 1.71\,c_{\mathrm{s,surf}}\,\xi(r)$,

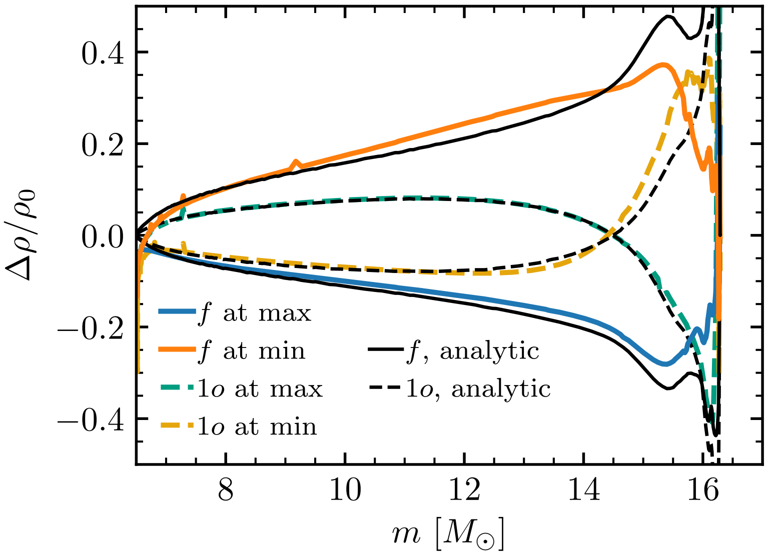

Figure 3.4: Comparison of linear theory for the Lagrangian density perturbation (black lines) with differences in the model density profiles from the density profile of the unperturbed starting model (colored lines) for fundamental mode pulsations (solid) and first overtone pulsations (dashed).

as these times are most consistent with being "pure" overtones. The agreement is very good in the interior of the star. Deviations from linear theory occur primarily near the surface, where nonlinearities due to nearly sonic motion cause a larger impact.

3.2 Exploding Pulsating Models

At the time of explosion, the density profiles in the envelope vary significantly for different pulsation phases. This can be seen in Figure 3.5, which shows density profiles in the envelope at core-collapse for the fundamental-mode models as a function of radius (left panel). Additionally, Figure 3.5 shows a comparison between Lagrangian density profiles of the unperturbed model, a fundamental mode pulsation near maximum, and a large-amplitude overtone near maximum (right panel). In order to achieve a large-amplitude overtone pulsations, we inject a velocity profile with $v(r) = 5.48\, c_{\rm s,surf}\, \xi(r)$, where ξ is the displacement for the first overtone, approximately quarter-period before core-collapse, 1533 days after core C depletion, so that it is approaching its first maximum at the time of explosion. To produce a fundamental mode pulsator with the same stellar radius and similar phase, we inject a velocity profile $v(r) = 2.86\, c_{\rm s,surf}\, \xi(r)$ approximately a quarter-period before core-collapse, 1460 days after core C depletion. Our models show significant diversity in their density profiles, particularly near the surface. Moreover, the overtone pulsation at maximum phase is denser in the interior of the star compared to the unperturbed model, but less dense near the surface, whereas the fundamental mode near maximum is less dense everywhere.

We explode our models at different radii. At a central temperature of $\log(T_c/{\rm K}) = 9.9$, we instantaneously zero out the velocity profile to "freeze in" the density structure of the envelope, since the time to shock breakout ($\approx$ 2 days) is much shorter than the pulsation period, and since the kinetic energy associated with the pulsation is orders of magnitude below the total binding energy of the star. This also helps quell artificial velocity fluctuations which begin to arise in the core around the time of core Si burning. We then continue to evolve the model until core infall. At that point, we excise the core, as described in section 6.1 of Paxton et al. (2018) (hereafter MESA IV). Because each model is evolved independently after core C burning, there is some small variation in the excised mass, ranging from 1.6 to $1.74 M_\odot$, leading to ejecta masses of $M_{\rm ej}$ =14.54

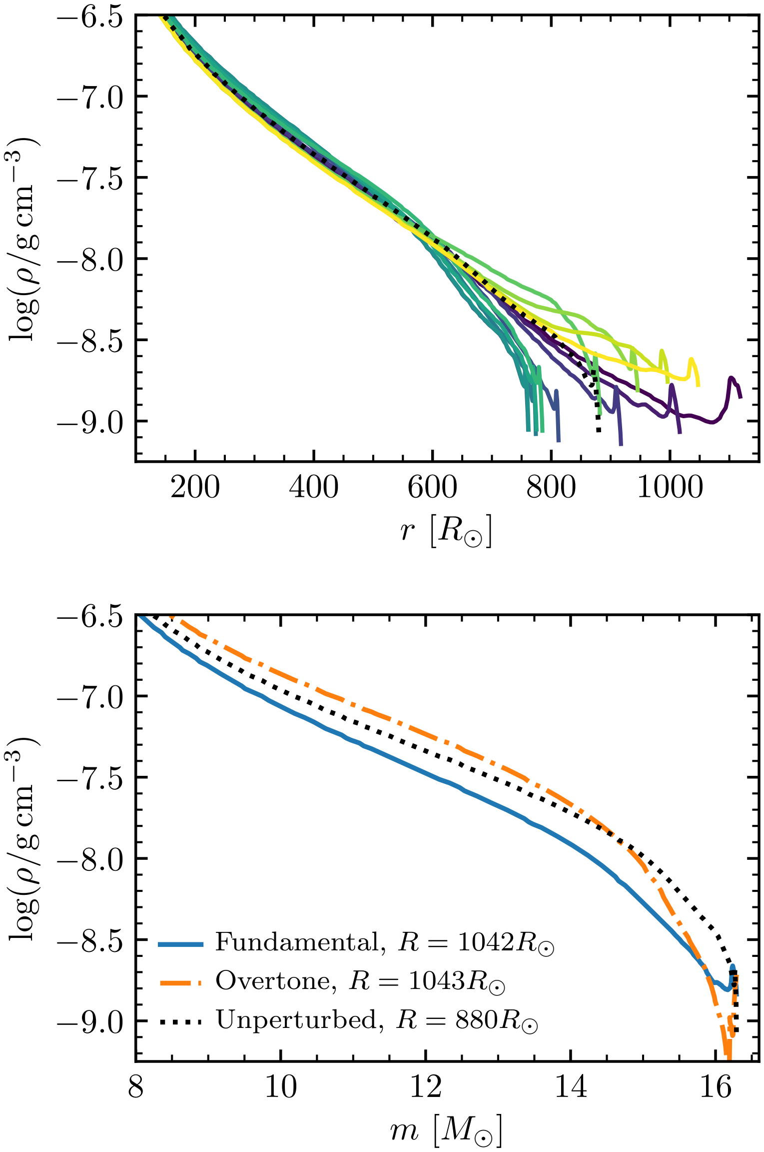

Figure 3.5: Left: Density profiles in the envelope of our pulsating models just before core collapse, where color corresponds to time the pulsation was injected as in Figure 3.2. Right: Lagrangian density profiles at core-collapse for large-amplitude pulsations approaching maximum displacement, where the velocity eigenfunctions were injected just 1/4 phase before core-collapse to preserve the purity of the modes. In both panels, the dotted black line shows the unperturbed model.

to $14.68 M_\odot$. The unperturbed model has an excised mass of $1.73 M_\odot$. We allow the new inner boundary to infall until it reaches an inner radius of 500 km. We then halt the infall, and inject energy in the innermost 0.1 $M_\odot$ of the star for 10^{-4} seconds, until each model reaches a total energy of 10^{51} ergs.

We proceed by modeling the evolution of the shock including Duffell RTI (Duffell, 2016), and hand off the ejecta model at shock breakout to the 1D radiation-hydrodynamics software `STELLA` (Blinnikov et al., 1998, 2000, 2006; Baklanov et al., 2005) as described in MESA IV. The time to shock breakout is 2 days for the unperturbed model, and varies from 1.7 days for our smallest-radius model to 2.5 days for our largest-radius model. At this explosion energy, there is negligible additional fallback, which we evaluate using the fallback scheme described in Appendix A of Goldberg et al. (2019) with an additional velocity cut of 500 km s^{-1} at handoff to `STELLA`. We then rescale the distribution of ^{56}Ni to match a total mass of 0.06 $M_\odot$, which is typical of observed events and roughly matches the Ni masses observed in SNe with L_{50} equal to that of the unperturbed model via the $L_{50} - M_{\mathrm{Ni}}$ relations from Pejcha & Prieto (2015a) and Müller et al. (2017). We use 1600 spatial zones and 40 frequency bins in `STELLA`, which yields convergence in the bolometric lightcurves for the given ejecta models (see also Figure 30 of MESA IV and the surrounding discussion). While a significant fraction of SNe II-P have excess emission for the first ~ 20 days (e.g. Morozova et al. 2017), and pulsation-driven outbursts have been proposed as one means of mass loss at the end of the lives of RSGs (e.g. Yoon & Cantiello 2010), we do not include any extra material beyond the progenitor photosphere to generate our model lightcurves. In addition, we are focused on the emission from the bulk of the ejecta, that occurs after day 30.

3.2.1 Pulsations and Plateau Properties

As discussed in detail by Arnett (1980), Popov (1993), Kasen & Woosley (2009), Sukhbold et al. (2016), Goldberg et al. (2019), and others, the plateau luminosity of a Type IIP SN at day 50, L_{50}, depends on the radius of the progenitor. Popov (1993) gives $L_{50} \propto R^{5/6}$ at fixed ejecta mass M_{ej} and explosion energy E_{exp}. From a suite of `MESA+STELLA` models, Goldberg et al. (2019) recovered a similar scaling, $L_{50} \propto R^{0.76}$. Figure 3.6 shows lightcurves for the 13 phases of pulsation shown in Figure 3.2, as well as for the unperturbed model denoted by the black line in Figure 3.2. As expected from the scalings, the luminosity at day 50 varies by 0.13 dex, or 0.33 mag, with the brighter explosions corresponding to larger radii, with radii ranging from 760-1120$R_{\odot}$. The slope on the plateau is somewhat steeper in the brighter SNe, such that the variation at early time is greater than closer to the end of the plateau. Additionally, following Goldberg et al. (2019), in the ^{56}Ni-rich limit $M_{\mathrm{Ni}} \gtrsim 0.03 M_{\odot}$, the plateau duration should be approximately independent of the progenitor radius, with some variation for varied distributions of ^{56}Ni and Hydrogen. This can also be seen in our lightcurves in Figure 3.6, where the recovered plateau durations (using the method of Valenti et al. 2016 as in Goldberg et al. 2019) ranges from 116.8 to 119.5 days with no correlation with progenitor radius. These trends are shown in greater detail in the upper and lower panel of Figure 3.7, which show

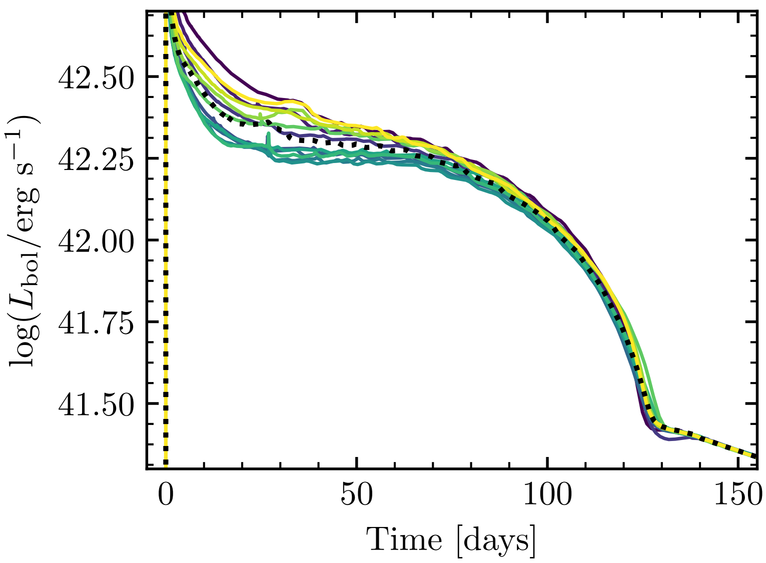

Figure 3.6: Lightcurves for our fundamental mode pulsator at different phases of pulsation. Color corresponds to time the pulsation was injected, as in Figure 3.2, and tracks pulsation phase. The dotted black line shows the lightcurve of the unperturbed model.

good agreement between our models and the scalings.

Figure 3.5 also shows changes in the outer density profiles and their slopes as a result of these pulsations. These changes do modify the calculated early lightcurves shown in Figure 3.6, causing greater luminoisty excesses at early times in the more extended models. In observations, such apparent excesses are often interpreted as evidence for material beyond the normal stellar photosphere. However, because this part of the outer envelope is intrinsically uncertain in 1D models, we are not in a position to make strong claims about whether the variety seen in early lightcurve observations can be explained by pulsations alone.

Additionally, the total energy deposited by the shock is reflected in the observable ET (Nakar et al., 2016; Shussman et al., 2016a), defined as the total time-weighted energy

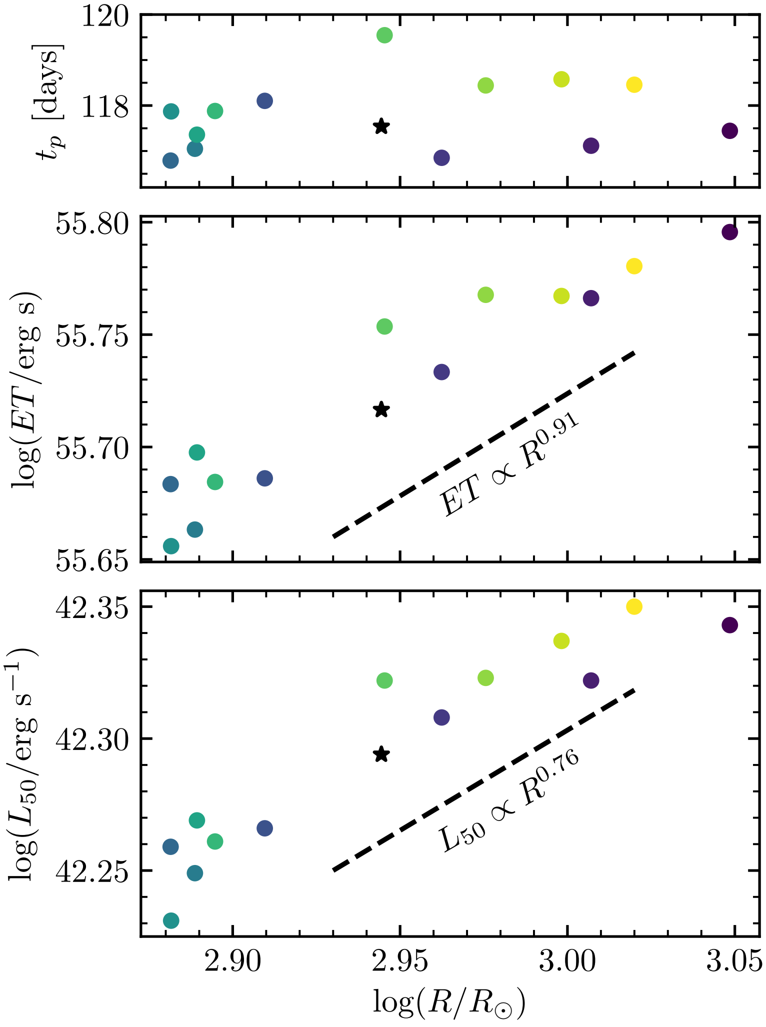

Figure 3.7: Lightcurve observables versus progenitor radius at the time of explosion for our unperturbed model (black star) and pulsating models (colored points). The plateau duration (upper panel), ET (middle panel), and L_{50} (lower panel) are shown along with scalings from Goldberg et al. (2019). Colors match the colors in Figures 3.2 and 3.6.

radiated away in the SN which was generated by the initial shock and not by ^{56}Ni decay:

$$ET = \int_0^\infty t \left[L_{\rm bol}(t) - Q_{\rm Ni}(t)\right] \, {\rm d}t, \tag{3.3}$$

where t is the time in days since the explosion and

$$Q_{\rm Ni} = \frac{M_{\rm Ni}}{M_\odot} \left(6.45 e^{-t/8.8{\rm d}} + 1.45 e^{-t/113{\rm d}}\right) \times 10^{43} \ {\rm erg\ s^{-1}}, \tag{3.4}$$

is the ^{56}Ni decay luminosity given in Nadyozhin (1994), which is taken to be equivalent to the instantaneous heating rate of the ejecta assuming complete trapping. ET also scales with the progenitor radius for constant $M_{\rm ej}$ and $E_{\rm exp}$, given as $ET \propto R$ by the analytics and modeling of Nakar et al. (2016); Shussman et al. (2016a); Kozyreva et al. (2018), and as $ET \propto R^{0.91}$ recovered from `MESA`+`STELLA` models by Goldberg et al. (2019). The middle panel of Figure 3.7 shows the agreement between ET in our model lightcurves and the scalings. Like with L_{50}, ET as a function of progenitor radius exhibits some scatter, which is not surprising given the significant differences in the density profiles especially in the models near pulsation minima at core-collapse, but overall agrees well with the predicted scalings.

3.2.2 Comparing Fundamental and Overtone Pulsations

Although a majority of observed pulsating RSGs are dominated by the fundamental mode, there is evidence for some pulsating with the first overtone (e.g. Kiss et al. 2006; Soraisam et al. 2018; Ren et al. 2019). Because of the radial crossing in the overtone, the progenitor radius used in scaling laws may not be sufficient to predict L_{50}. Typically, the expansion time characterized by the time to shock breakout and the mean density of the SN ejecta are considered in analytics. However, the local radius and density profile of the progenitor at the mass coordinate of the SN photosphere, which is located near the H-recombination front and is defined by the location where the mean optical depth $\tau = 2/3$, must be taken into account. As seen in the left panel of Figure 3.5, inside the mass coordinate of $\approx 14.5 - 15 M_{\odot}$, which is near the zero-crossing in the radial displacement (see Figure 3.4), the overtone progenitor model is denser than the unperturbed model, and outside that coordinate it is less dense. On the other hand, the fundamental mode pulsation is less dense everywhere when it is at a positive radial displacement, suggesting that at fixed photospheric mass coordinate in the SN, the star should appear "larger" and therefore the SN would be brighter.

As shown in the upper panel of Figure 3.8, the evolution of the mass coordinate of the SN photosphere does not change significantly for the pulsating models compared to the unperturbed model. At day 50, the SN photosphere has moved $1.5 M_{\odot}$ into the ejecta for the unperturbed and overtone models, corresponding to a stellar mass coordinate of $14.8 M_{\odot}$, which is near the zero-crossing in the overtone displacement and density perturbation in the progenitor model. This is reflected by the lightcurves shown in the lower panel of Figure 3.8. The evolution of the photospheric radius (middle panel of Figure 3.8) and mass coordinate do not differ tremendously on the plateau between the three models, but the lightcurves show a distinct difference. Whereas the progenitor radii for the fundamental and overtone are nearly identical, the overtone explosion at day 50 is fainter by 0.046 dex or 0.115 mags, and in fact much closer in L_{50} to the unperturbed

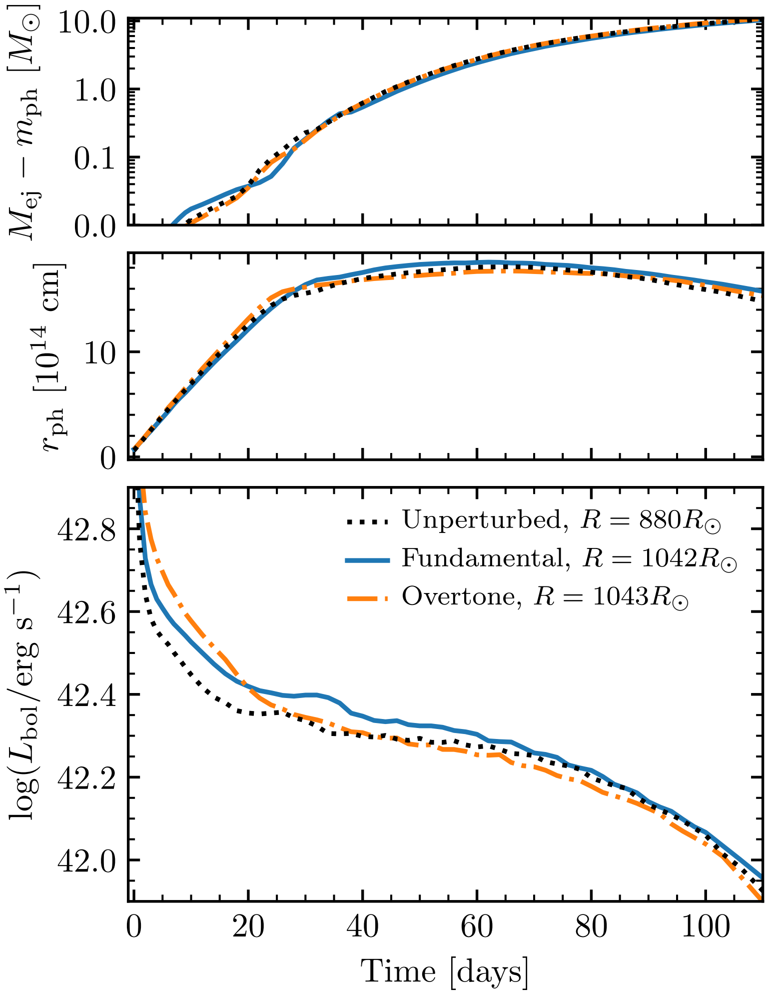

Figure 3.8: Overhead mass coordinate of the SN photosphere (upper panel), photospheric radius (middle panel), and lightcurves (lower panel) for explosions of large-amplitude fundamental mode and overtone pulsations near maximum, compared to the unperturbed model.

progenitor model than to the fundamental mode. Additionally, the SN from the overtone pulsator is brighter at early times, when the SN emission is coming from what appears to be a more radially extended star with a steeper density profile, and fainter at later times, when the emission appears to be coming from a more compact star.

3.3 Discussion & Conclusions

There is strong observational evidence for variability in large samples of RSGs caused by radial pulsations in their envelopes, typically with periods between a few hundred and a few thousand days (Kiss et al., 2006; Soraisam et al., 2018; Chatys et al., 2019). Since the final stages of burning take place over week-long timescales, much shorter than the pulsation period, the density structure of the envelope can reflect any pulsation phase at the time of explosion. This is significant, as the radius and density structure of a given Type IIP SN progenitor are important in determining the luminosity evolution of its resulting SN.

We consider the effects of pulsations on the stellar envelope and SN emission after core-collapse. We show that SNe of fundamental mode pulsators, which account for the majority of observed pulsating RSGs, behave like "normal" Type IIP SNe from progenitors at different radii. We find that L_{50} and ET scale with the progenitor radius at the time of explosion consistent with the work of Popov (1993); Kasen & Woosley (2009); Nakar et al. (2016); Goldberg et al. (2019) and others, and that the plateau duration remains independent of progenitor radius as expected in the ^{56}Ni$-$rich regime.

The luminosity plateau declines more steeply for brighter events between days 30 and 80, which in this study correspond to models with positive radial displacement at the time of core collapse. This is consistent with the observed correlation seen in Type II SNe more broadly between the brightness and steeper plateau decline (e.g. Anderson et al. 2014; Valenti et al. 2016).

Additionally, we show that large-amplitude pulsations in the first overtone yield different lightcurves compared to fundamental-mode pulsations at the same radius. This results from the nonmonotonic overtone density perturbation, which, for an explosion near pulsation maximum, causes the SN to "see" a puffier star at early times, but a more compact star at later times. This yields a supernova which is initially brighter than either the fundamental-mode pulsator at equivalent radius or the unperturbed model at a smaller radius, but fainter once emission is coming from the denser interior. In all cases, the differing stellar radii and density profiles also yield signatures in the calculated early SN emission, but future work aided by a more accurate treatment of the progenitor's extended atmosphere is necessary to make definitive statements and quantitative predictions.

Motivated by the observed oscilllations, we only considered the impact of radial pulsations on the resulting SNe light curves. Non-radial pulsations, if present, would lead to additional phenomena, for example apparent asymetries during the plateau phase. Existing spectropolarimetric observations (Wang et al. 2001; Leonard & Filippenko 2001; Leonard et al. 2001, 2006; Wang & Wheeler 2008; Kumar et al. 2016; Nagao et al. 2019) sometimes show very low (or undetectable) levels of assymetries during the plateau, with increasing polarization evident in the late time tail attributed to asymmetries deep in the helium core.

Because a fundamental uncertainty in recovered explosion properties from Type IIP SNe stems from the unknown radius at the time of core-collapse, the presence of a pulsation would translate to an additional uncertainty in recovering progenitor properties from SN lightcurves even in conjunction with progenitor detections. Therefore, continued studies of RSG variability will be important in determining the uncertainties within a single progenitor radius detection. Future work is also needed to accurately model the winds and surface layers of massive stars, as well as the density profile of any extended material, all of which are required to effectively model early SN emission and could be affected by these pulsations. Nonetheless, this work highlights the influence of the complete density profile of the progenitor star on the SN emission on the plateau, beyond the initial shock cooling and early spherical phase.

Chapter 4

The Value of Progenitor Radius Measurements for Explosion Modeling of Type II-Plateau Supernovae

Massive stars ($M \gtrsim 10M_{\odot}$) at the end of their evolution become red supergiants (RSGs) with radii of $\approx 400 - 1000R_{\odot}$, before ending their lives as core-collapse Type IIP supernovae (SNe) with lightcurves that plateau over $\approx$ 100 days. The progenitor radius (R), ejected mass ($M_{\rm ej}$), explosion energy ($E_{\rm exp}$), and ^{56}Ni mass ($M_{\rm Ni}$) determine these lightcurves (e.g. Popov, 1993; Sukhbold et al., 2016), and inferring these properties from observations could lend insight into which stars explode as SNe. Although early work provided scaling relations attempting to uniquely relate plateau properties and expansion velocities to explosion characteristics (e.g. Litvinova & Nadyozhin, 1983; Popov, 1993), recent work highlights the nonuniqueness of lightcurve and velocity modeling for a given SN after ≈20 days (Dessart & Hillier, 2019; Goldberg et al., 2019; Martinez & Bersten, 2019).

Building on Goldberg et al. (2019, hereafter GBP19) (reproduced in Chapter 2), we verify these degeneracies by comparing explosions of very different progenitor models to Nickel-rich ($M_{\rm Ni} > 0.03 M_\odot$) events with bolometric lightcurves, a well-sampled decline from the plateau, and constraints on the progenitor radius. We utilize the open-source 1D stellar evolution code Modules for Experiments in Stellar Astrophysics (`MESA`, Paxton et al., 2011, 2013, 2015, 2018, 2019) for our evolutionary and explosion models and the multi-group radiation-hydrodynamics instrument `STELLA` (Blinnikov et al., 1998, 2000, 2006) to produce lightcurves and model expansion velocities. Emission in the first 20 days depends on the radial density structure of the outer $< 0.1 M_\odot$ of matter around a vigorously convecting RSG progenitor (e.g. Morozova et al., 2016). SN emission during this time can be modified by the uncertain circumstellar environment (e.g.Morozova et al. 2017), and may reflect the intrinsically 3D structure of these outer layers (see e.g. Chiavassa et al. 2011a). Therefore we restrict our analysis to observations after day ≈20, when emission comes from the bulk of the stellar envelope. However, we still show our results for earlier times, where the qualitative trends may hold.

4.1 Observed SNe & Their Degeneracy Curves

GBP19 showed that Type IIP supernovae with ^{56}Ni mass ($M_{\rm Ni} \geq 0.03 M_\odot$), luminosity at day 50 (L_{50}), and plateau duration ($t_{\rm p}$) can approximately yield the ejected mass ($M_{10} \equiv M_{\rm ej}/10 M_\odot$) and asymptotic explosion energy ($E_{51} \equiv E_{\rm exp}/10^{51}$ergs) as a function of progenitor radius ($R_{500} \equiv R/500 R_\odot$), via the following relations:

$$\begin{aligned} \log(E_{51}) &= -0.728 + 2.148 \log(L_{42}) - 0.280 \log(M_{\rm Ni}) \\ &\quad + 2.091 \log(t_{\rm p,2}) - 1.632 \log(R_{500}), \\ \log(M_{10}) &= -0.947 + 1.474 \log(L_{42}) - 0.518 \log(M_{\rm Ni}) \\ &\quad + 3.867 \log(t_{\rm p,2}) - 1.120 \log(R_{500}), \end{aligned} \tag{4.1}$$

where $M_{\rm Ni}$ is in units of $M_\odot$, $L_{42} = L_{50}/10^{42}$ erg s^{-1} and $t_{\rm p,2} = t_{\rm p}/100\,{\rm d}$, and log is base 10. Moreover, because expansion velocities inferred from the Fe II 5169Å line are determined by line-forming regions near the photosphere, velocity data during the plateau period do not break this degeneracy ($L_{50} \underset{\sim}{\propto} v_{50}^2$, Hamuy & Pinto 2002; Kasen & Woosley 2009). Rather, SNe with the same L_{50}, $t_{\rm p}$, and $M_{\rm Ni}$ and similar expansion velocities during the plateau can be realized by a family of explosions with a range of R, $E_{\rm exp}$, and $M_{\rm ej}$ obeying the Equation (4.1) relations.

4.1.1 Measuring Nickel Mass and Plateau Duration of SNe-IIP

We estimate the plateau duration $t_{\rm p}$ following Valenti et al. (2016), fitting the functional form $y(t)$ to the bolometric luminosity ($L_{\rm bol}$) around the fall from the plateau:

$$y(t) \equiv \log(L_{\rm bol}) = \frac{-A_0}{1 + e^{(t-t_{\rm p})/W_0}} + (P_0 \times t) + M_0. \tag{4.2}$$

We use the python routine `scipy.optimize.curve_fit` to fit the lightcurve starting when the luminosity evolution is 75% of the way to its steepest descent, fixing P_0 to be the slope on the ^{56}Ni tail (GBP19). The fitting parameter $t_{\rm p}$ is the plateau duration. We also extract the ^{56}Ni mass from $L_{\rm bol}$ by calculating the cumulative observable ET (Nakar et al., 2016), which corresponds to the total time-weighted energy radiated away in the SN generated by the initial shock and not by ^{56}Ni decay:

$$ET_{\rm c}(t) = \int_0^t t' \left[L_{\rm bol}(t') - Q_{\rm Ni}(t')\right] {\rm d}t', \tag{4.3}$$

where t is the time in days since the explosion and

$$Q_{\rm Ni} = \frac{M_{\rm Ni}}{M_\odot}\left(6.45 e^{-t'/t_{\rm Ni}} + 1.45 e^{-t'/\tau_{\rm Co}}\right) \times 10^{43}\ {\rm erg\ s^{-1}}, \tag{4.4}$$

is the $^{56}{\rm Ni} \rightarrow {}^{56}{\rm Co} \rightarrow {}^{56}{\rm Fe}$ decay luminosity given by Nadyozhin (1994), equivalent to the heating rate of the ejecta assuming complete trapping with $t_{\rm Ni} = 8.8$ days and $\tau_{\rm Co} = 111.3$ days. As $t \rightarrow \infty$ and all shock energy has radiated away, the slope of the $ET_{\rm c}$ curve on the ^{56}Co decay tail should be zero when the estimate of $M_{\rm Ni}$ is correct. This method yields excellent agreement between the resulting model lightcurve tails and observed lightcurves, and with the ^{56}Co decay luminosity (Nadyozhin, 1994):

$$L(t \rightarrow \infty) = 1.45 \times 10^{43} \exp\left(-\frac{t}{\tau_{\rm Co}}\right) \frac{M_{\rm Ni}}{M_\odot}\ {\rm erg\ s^{-1}}. \tag{4.5}$$

4.1.2 Supernova Selection

In order to further explore this degeneracy, we apply these scalings to five observed supernovae: **SN2004A**, **SN2004et**, **SN2009ib**, **SN2017eaw**, and **SN2017gmr**.

SN2004A was discovered by K. Itagaki on 9 January 2004 in NGC6207 (Hendry et al., 2006). Following Pejcha & Prieto (2015a) we adopt an explosion date of MJD 53001.53. Progenitor observations indicate $\log(L_{\rm p}/L_{\odot}) = 4.9 \pm 0.3$ and $T_{\rm eff} = 3890 \pm 375\,{\rm K}$, implying a radius of $\approx 625 R_{\odot}$ (Smartt, 2015). From the Pejcha & Prieto (2015a) bolometric lightcurve, we get $\log(L_{42}) = -0.07$. Estimates for the ^{56}Ni mass include $M_{\rm Ni}/M_{\odot} = 0.050^{+0.040}_{-0.020}$ from points on the bolometric-corrected V-band tail and $M_{\rm Ni}/M_{\odot} = 0.042^{+0.017}_{-0.013}$ comparing to the tail of 1987A, which the original authors average to yield $M_{\rm Ni}/M_{\odot} = 0.046^{+0.0031}_{-0.017}$ (Hendry et al., 2006). We measure a plateau duration of $t_{\rm p}$ =124 days and use $M_{\rm Ni} = 0.042 M_{\odot}$.

SN2004et was discovered in NGC6946 by S. Moretti on 2004 September 27, with a well-constrained explosion date of 22.0 September 2004 (MJD 53270.0) (Li et al., 2005). There is some disagreement in the literature about the progenitor (see Smartt 2009 and Davies & Beasor 2018) since follow-up imaging show R- and I-band flux excesses in the location of the inferred progenitor in HST pre-imaging (Crockett et al., 2011). As a result, Martinez & Bersten (2019) report a progenitor radius of $350 R_{\odot} - 980 R_{\odot}$. We adopt the bolometric lightcurve given by Martinez & Bersten (2019), which indicates $\log(L_{42}) = 0.27$. Estimates for the ^{56}Ni mass include $M_{\rm Ni}/M_{\odot} = 0.048 \pm 0.01$ from the scaled ^{56}Co decay tail of 1987A to $M_{\rm Ni} = 0.06 \pm 0.02$ estimated using V-magnitudes from 250-315 days (Sahu et al., 2006). We measure $t_{\rm p} = 123.1$ days and use $M_{\rm Ni} = 0.063 M_{\odot}$.

SN2009ib was discovered by the Chilean Automatic Supernova Search on 6.30 August 2009 in NGC1559, with an estimated explosion date of MJD 55041.3 (Takáts et al., 2015). HST pre-images indicate either a yellow source with $\log(L_{\rm p}/L_{\odot}) = 5.04 \pm 0.2$, or possibly a fainter RSG with $\log(L_{\rm p}/L_{\odot}) = 5.12 \pm 0.14$ and $R \approx 1000 R_{\odot}$ assuming $T_{\rm eff} \approx 3400$K (Takáts et al., 2015). This event is peculiar in that there is a shallow drop from the plateau luminosity to the ^{56}Co decay tail, falling noticeably off of the Müller et al. (2017) relation between L_{50} and $M_{\rm Ni}$. From the Takáts et al. (2015) lightcurve, we measure $\log(L_{42}) = -0.33$ and $M_{\rm Ni}/M_{\odot} = 0.043$, and $t_{\rm p} = 139.8,$days. Nakar et al. (2016) also highlighted that this event had a ratio of the integrated ^{56}Ni decay chain energy to integrated shock energy of $\eta_{\rm Ni} = 2.6$, much larger than typical values of $\eta_{\rm Ni} \approx 0.2 - 0.6$ (e.g. $\eta_{\rm Ni}$ for SN1999em ≈ 0.54).

SN2017eaw was discovered by P. Wiggins on 14.238 May 2017 in NGC6946, with an estimated explosion date of MJD 57886.0 (Szalai et al., 2019). Pre-explosion imaging suggestslog$(L_{\rm p}/L_{\odot}) = 4.9 \pm 0.2$ and $T_{\rm eff} = 3350^{+450}_{-250}$ K, corresponding to $R \approx 845 R_{\odot}$, obscured by a $> 2 \times 10^{-5} M_{\odot}$ dust shell extending out to $4000 R_{\odot}$ (Kilpatrick & Foley, 2018), assuming the distance to NGC6946 to be $D = 6.72 \pm 0.15\,$Mpc (from the tip of the red giant branch (TRGB) by Tikhonov 2014).[1] We adopt the bolometric lightcurve of Szalai et al. (2019) using $D = 6.85$ Mpc, although more recent TRGB measurements suggest $D = 7.72 \pm 0.78$ Mpc (Van Dyk et al., 2019). Estimates for the ^{56}Ni mass assuming $D = 6.85$ Mpc range from $M_{\rm Ni}/M_{\odot} = 0.036 - 0.045$ (Szalai et al., 2019) to $M_{\rm Ni} = 0.05 M_{\odot}$ (Tsvetkov et al., 2018). From the Szalai et al. (2019) lightcurve, we measure $t_{\rm p} = 117.2$ days, $M_{\rm Ni} = 0.048 M_{\odot}$, and $\log(L_{42}) = 0.21$.

SN2017gmr occurred in NGC988, discovered on MJD 58000.266 during the DLT40

---

[1] See also Rui et al. (2019), who infer a radius of $636 \pm 155 R_{\odot}$ from early SN temperature observations (consistent with the progenitor SED), in an expanding dusty environment.

SN search with the explosion epoch assumed to be MJD 57999.09 at $D = 19.6 \pm 1.4$ Mpc (Andrews et al., 2019). No progenitor detection was made, but shock-cooling modeling of the early SN recovers $R \approx 500 R_\odot$. Andrews et al. (2019) find $M_{\rm Ni} = 0.13 \pm 0.026 M_\odot$ assuming all late-time luminosty comes from Ni decay, although multipeaked emission lines emerging after day 150 suggest asymmetries present either in the core's explosion or in late-time interaction with the surrounding environment. We adopt the Andrews et al. (2019) bolometric lightcurve, and measure $\log(L_{42}) = 0.57$, $M_{\rm Ni}/M_\odot = 0.13$, and $t_{\rm p}$ =94.5 days.

4.1.3 The Degeneracy Curves

The families of explosion parameters recovered by inserting each SN's $M_{\rm Ni}$, L_{50}, and $t_{\rm p}$ into Equations (4.1) are shown in Figure 4.1 as a function of R. Also shown is a large suite of RSG progenitor models to demonstrate the potential variety of $M_{\rm ej}$ and R within reasonable stellar evolution assumptions. For each event, $M_{\rm ej}$ and $E_{\rm exp}$ can be inferred from the plot for a given R.

The progenitor models were constructed using `MESA` revision 10398, and evolved to Fe core infall, following the `example_make_pre_ccsn` test case described in detail by Paxton et al. (2018, hereafter MESA IV). We varied the initial mass ($M_{\rm ZAMS}/M_\odot$ =10.0-15.0 in increments of $0.5 M_\odot$, and 15.0-25.0 in increments of $1.0 M_\odot$), surface rotation ($\omega/\omega_{\rm crit}$ = 0.0; 0.2), mixing length α in the H-rich envelope ($\alpha_{\rm env}$=2.0; 3.0; 4.0), core overshooting ($f_{\rm ov}$ = 0.0; 0.01; 0.018), and wind efficiency ($\eta_{\rm wind} = 0.1 - 1.0$, increments

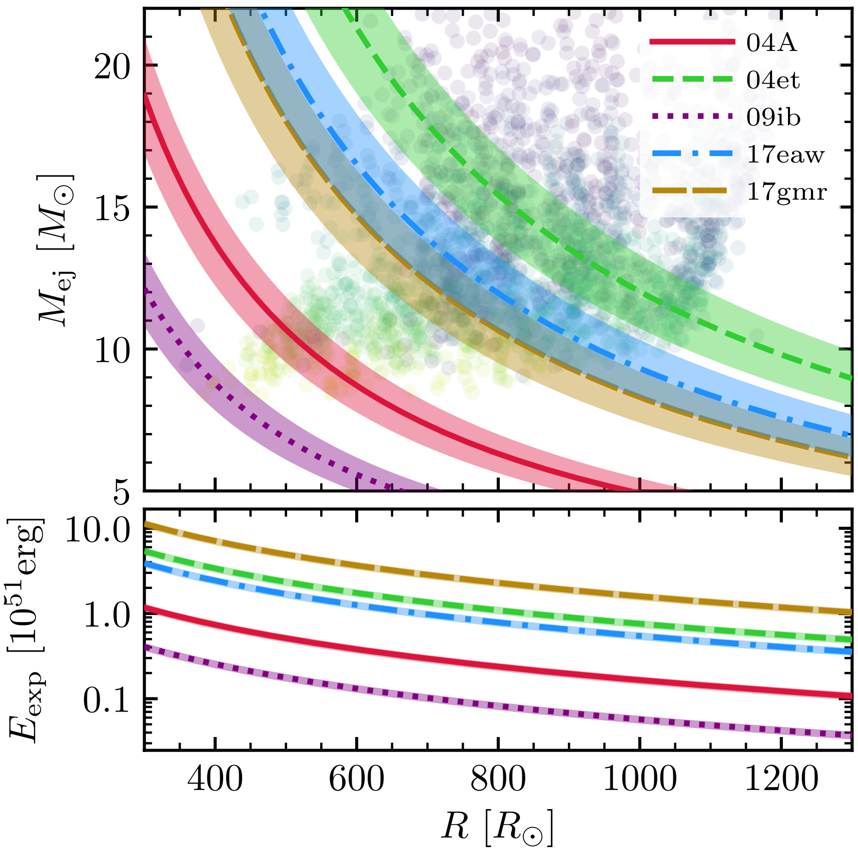

Figure 4.1: Degeneracy curves for $M_{\rm ej}$ (top) and $E_{\rm exp}$ (bottom) recovered from Equations (4.1) as a function of R for the observed SNe considered here. Shaded solid-color regions correspond to the $\approx 11\%$ RMS deviations between the models of GBP19 and their recovered parameters. Additional observational uncertainties are not included. The $M_{\rm ej}$ and R of 2179 progenitor models are also shown in the background, with color ranging from yellow to purple tracking $M_{\rm ZAMS} = 10 - 25 M_\odot$.

of 0.1) using `MESA`'s 'Dutch' wind scheme. All models had $Z = 0.02$. Only models which reached Fe core infall are shown. Rather than one relationship between $M_{\rm ej}$ and R, this set of models suggests a wide range in which RSGs can exist. This diversity reflects the importance of winds in determining the final masses and radii of stellar models (Renzo et al., 2017), and supports recent work showing diversity in progenitor masses for comparable positions on the HR diagram (Farrell et al. 2020).

4.2 Explosion Models & Comparison to Observations

We then select progenitor models to explode in order to match observations guided by Equations (4.1) applied to a SN's respective L_{42}, $M_{\rm Ni}$, and $t_{\rm p}$. For SNe 2004A, 2004et, SN2017eaw, and 2017gmr, we chose three progenitor models each, consistent with the respective degeneracy curves in Figure 4.1, with ejecta masses near the larger-$M_{\rm ej}$, middle-$M_{\rm ej}$, and smaller-$M_{\rm ej}$ intersections of the theoretical curves and the progenitor model suite. For SN2017eaw, we chose three additional models consistent with a distance 10% farther away (i.e. increasing L_{50} and $M_{\rm Ni}$ by 21%, not shown in Figure 4.1). Very low $M_{\rm ej}$ and radii are recovered for SN2009ib, with little overlap with our progenitor grid, so we exploded only two progenitors, one off the grid ($\alpha = 6$). Properties of these models at the moment of explosion, input physics, and values for $M_{\rm Ni}$ are shown in Table 4.1. Also shown are the time to shock breakout ($t_{\rm sb}$) and the mass above the photosphere at day 20 ($\delta m_{\rm ph,20}$).

We then excised the Fe cores with an entropy cut of 4 erg g^{-1} K^{-1}, and exploded these models using `MESA` with Duffell RTI (Duffell, 2016) and the fallback estimation technique described in Appendix A of GBP19, with an additional velocity cut of 500 km s^{-1} at handoff to `STELLA` at shock breakout.[2] All explosions resulted in negligible fallback. At shock breakout, we rescaled the ^{56}Ni distribution to match the desired $M_{\rm Ni}$, and imported the ejecta profile into `STELLA` to model the evolution post-shock-breakout. We used 400 spatial zones and 40 frequency bins in `STELLA`, which yields convergence in bolometric lightcurves on the plateau (see Figure 30 of MESA IV and the surrounding discussion). For SN2017eaw at 6.85 Mpc, we used 800 spatial zones in order to more faithfully capture the outermost layers of the ejecta. Because we are focused on matching plateau emission from the bulk of the ejecta, occurring after day ≈ 20, we do not include any extra material beyond the progenitor photosphere for most of our model lightcurves.

---

[2] For all models except 2017eaw at 6.85 Mpc, `MESA` revision 10925 was used, as in GBP19. Because we consider excess emission in the early lightcurve of 2017eaw at 6.85 Mpc, revision 11701 was used with a dense mesh near the surface set by '`split_merge_amr_logtau_zoning=.true.`' in `inlist_controls` to ensure that the outer region is adequately resolved.

Table 4.1: Model Properties

SN Name	Model name	$M_{\rm ZAMS}$	$f_{\rm ov}$, $\alpha_{\rm env}$, $\omega/\omega_{\rm crit}$, $\eta_{\rm w}$	$M_{\rm final}$	$M_{\rm c,f}$	$M_{\rm c,He}$	$\log(\frac{L_p}{L_\odot})$	$T_{\rm eff}$	$t_{\rm sb}$	$\delta m_{\rm ph,20}$
($M_{\rm Ni}/M_\odot$)	$[M_{\rm ej,\odot}][R_\odot][E_{51}]$	$[M_\odot]$		$[M_\odot]$	$[M_\odot]$	$[M_\odot]$		[K]	[days]	$[M_\odot]$
2004A	M9.3_R596_E0.4	11.5	0.018, 3.0, 0.0, 0.5	10.87	1.62	3.79	4.86	3900	1.6	0.032
(0.042)	M10.6_R482_E0.5	12.5	0.01, 4.0, 0.0, 0.2	12.28	1.64	3.89	5.20	5250	1.2	0.061
	M15.2_R438_E0.8	17.0	0.0, 4.0, 0.0, 0.2	16.66	1.48	5.33	5.23	5610	1.0	0.096
2004et	M11.8_R945_E0.76	14.0	0.018, 2.0, 0.2, 0.2	13.42	1.59	4.89	5.22	3790	2.2	0.031
(0.063)	M14.9_R816_E1.0	18.0	0.0, 2.0, 0.0, 0.5	16.53	1.62	5.85	5.44	4640	1.8	0.036
	M18.3_R791_E1.2	22.0	0.0, 3.0, 0.0, 0.5	19.89	1.55	7.70	5.25	4160	1.7	0.040
2009ib	M7.86_R375_E0.23	10.0	0.018, 4.0, 0.2, 0.7	9.41	1.55	3.15	5.05	5450	1.1	0.074
(0.043)	M10.2_R356_E0.3	12.0	0.01, 6.0, 0.2, 0.4	11.65	1.48	3.69	3.99	3040	1.1	0.082
2017eaw	M10.2_R850_E0.65	13.5	0.01, 2.0, 0.2, 0.8	11.99	1.77	4.24	4.92	3370	2.0	0.032
at 6.85Mpc	M12.7_R719_E0.84	15.0	0.01, 3.0, 0.0, 0.2	14.53	1.80	5.09	5.04	3910	1.7	0.036
(0.048)	M17.2_R584_E1.3	20.0	0.0, 4.0, 0.0, 0.4	18.92	1.70	6.79	5.10	4490	1.2	0.072
2017eaw, mod.	M11.9_R849_E0.9	14.0	0.016, 2.0, 0.0, 0.2	13.64	1.70	4.55	5.08	3690	1.8	0.032
at 7.54Mpc	M15.7_R800_E1.1	19.0	0.0, 3.0, 0.2, 0.4	17.33	1.66	6.83	5.18	4040	1.7	0.041
(0.0581)	M19.0_R636_E1.5	22.0	0.0, 4.0, 0.0, 0.2	20.51	1.55	7.74	5.54	5550	1.2	0.056
2017gmr	M9.5_R907_E1.9	12.0	0.018, 2.0, 0.2, 0.6	11.01	1.48	3.86	5.70	5110	1.1	0.076
(0.13)	M12.5_R683_E3.0	14.5	0.01, 3.0, 0.0, 0.2	14.09	1.55	4.80	5.46	5120	0.81	0.11
	M16.5_R533_E4.6	19.0	0.0, 4.0, 0.0, 0.4	18.09	1.57	6.28	5.29	5250	0.55	0.22

4.2.1 Comparison to Observed SNe

Despite intrinsic scatter amounting to ≈11% RMS deviations between model parameters and $M_{\rm ej}$ and $E_{\rm exp}$ recovered from Equations (4.1) applied to model radii and lightcurves (GBP19), computations approximately obeying Equations (4.1) produce bolometric lightcurves which match the observations. Figure 4.2 shows the results for SN2004A (top two panels) and SN2004et (bottom two panels). Both SN2004A and SN2004et exhibit good agreement between models, lightcurves, and velocity evolution on the plateau, with no model being the "best-fit" for either event. Photospheric velocities at very early times ($\lesssim$ 20 days) do differ between different models, with more compact, higher-$E_{\rm exp}$ models yielding faster early-time velocities. However, velocity measurements before day 20 are rare, and at these times velocities might be modified by the circumstellar environment (e.g. Moriya et al. 2018). The early observed lightcurve ($\lesssim$ 30 days) of SN2004et also exhibits a clear luminosity excess compared to the lightcurve models. Such excess is often attributed to interaction with an extended envelope or wind, or with pre-SN outbursts(e.g. Morozova et al., 2017, 2019).

All three models for SN2004et are consistent with the reported $R = 350 - 980R_{\odot}$. For SN2004A, only the low-mass/low-energy model M9.3_R596_E0.4 is consistent with the progenitor observations, and we conclude for that SN that $M_{\rm ej} \lesssim 10M_{\odot}$ and $E_{\rm exp} \lesssim 0.4 \times 10^{51}$ erg.

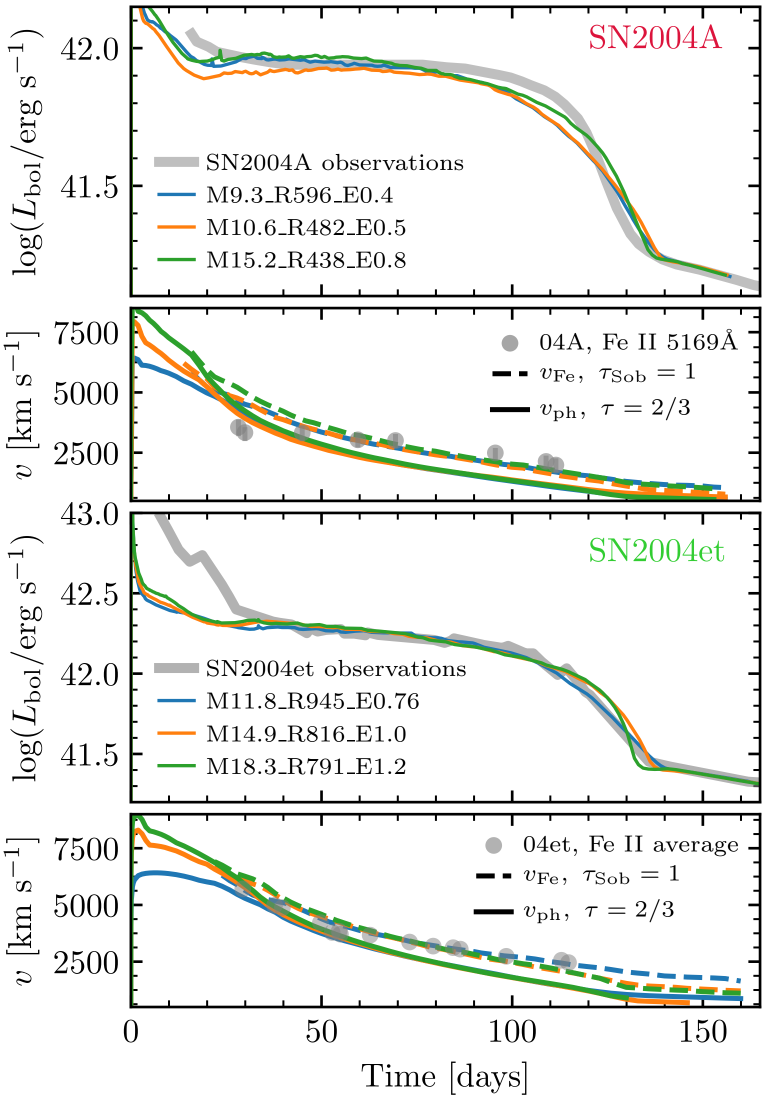

Figure 4.2: Lightcurves and Fe line velocities for SN2004A (top two panels) and SN2004et (bottom two panels). Grey markers correspond to the observations, and colored lines correspond to explosion models, ordered in ascending $M_{\rm ej}$ and $E_{\rm exp}$, and descending R.

4.2.2 SN2017eaw at Two Distances

To show the impact of changing the assumed distance on our modeling, we model SN2017eaw at two different distances: 6.85 Mpc, using the fiducial Szalai et al. (2019) lightcurve, and at 7.54 Mpc, with the same t_p but with 21% brighter L_bol and $M_\mathrm{Ni} = 0.0581 M_\odot$. Models were selected to match Equations (4.1) with the appropriate L_{42}, t_p, and M_Ni for each distance. Figure 4.3 compares models to observations. The top two panels correspond to $D = 6.85$ Mpc, and the bottom two panels to $D = 7.54$ Mpc.[3] Like SN2004A and SN2004et, models agree well with the data, and agreement in L_{50} also yields agreement in the velocity of the models after day ≈ 20. Agreement between models and *both* velocity and luminosity data is better for $D = 7.54$ Mpc. For $D = 6.85$ Mpc, two of our models, M10.2_R850_E0.65 and M12.7_R719_E0.84, match the progenitor properties within the uncertainties. At a 10% farther distance, assuming 21% brighter L_p and the same T_eff, only our M11.9_R849_E0.9 model is consistent with the updated progenitor properties. Assuming the measured progenitor radius of $845 R_\odot$, we chose models with $R \approx 850 R_\odot$ for both distances. The 10% greater distance leads to $\approx 17\%$ increase in M_ej, from $10.2 M_\odot$ to $11.9 M_\odot$ and $\approx 40\%$ increase in E_exp, from 0.65×10^{51} ergs to 0.9×10^{51} ergs.

For $D = 6.85$ Mpc, we also show lightcurves with and without a dense wind to reproduce the early excess emission (top two panels of Figure 4.3). We affix a wind

---

[3] The farther distance was motivated by the fact that velocities of models matching L_{50} and t_p of the fiducial distance are $\approx 10\%$ discrepant with observed velocities. Since $L_{50} \propto D^2 \overset{\propto}{\sim} v^2_{\mathrm{Fe},50}$ (Hamuy & Pinto 2002; Kasen & Woosley 2009; GBP19), an intrinsically brighter SN at a distance $\approx 10\%$ farther produces models which better match the velocity data. This distance is also consistent with a recent TRGB estimate of 7.72 ± 0.78 Mpc (Van Dyk et al., 2019).

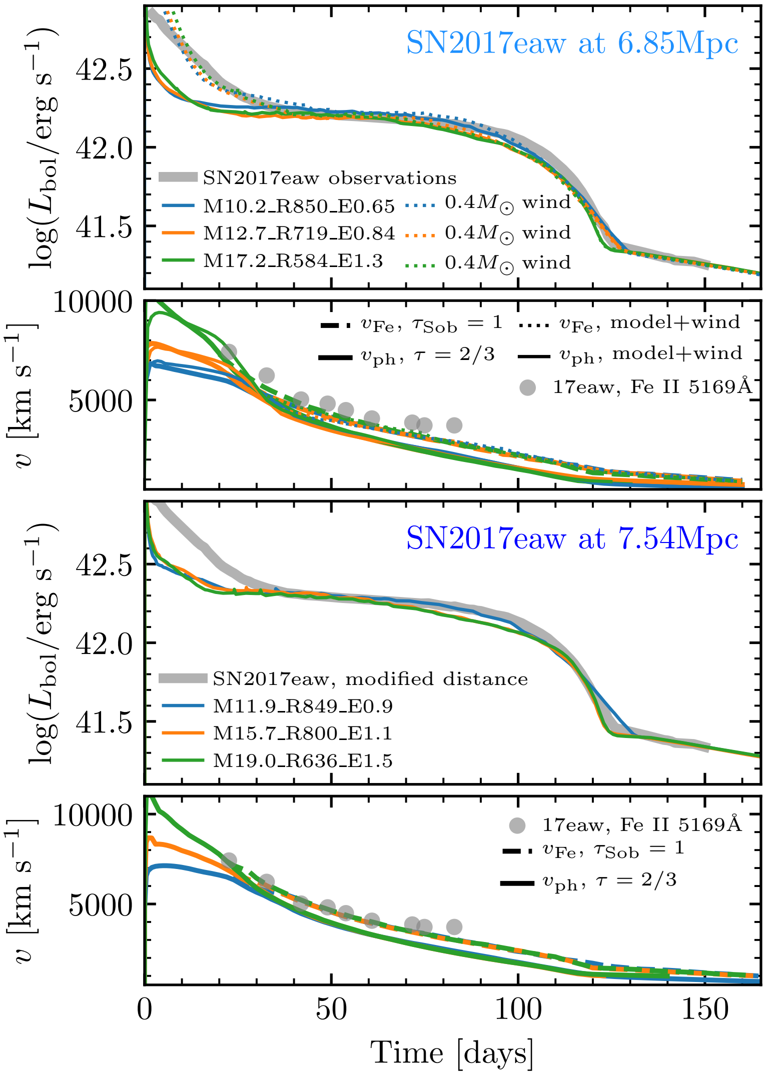

Figure 4.3: Lightcurves and Fe-line velocities for observations and models of SN2017eaw at D =6.85 Mpc (top two panels) and D =7.54 Mpc (bottom two panels). Grey markers correspond to observations, and colored lines correspond to explosion models. Colored dotted lines in the upper panels correspond to models with an additional $0.4M_\odot$ wind ($v_{\rm wind}=8\,{\rm km\,s^{-1}}$, $\dot{M}_{\rm wind}=0.2\,M_\odot/{\rm year}$).

density profile with total mass $M_{\rm wind}$ and $\rho_{\rm wind}(r) = \dot{M}_{\rm wind}/4\pi r^2 v_{\rm wind}$, where $\dot{M}_{\rm wind}$ is a constant, and $v_{\rm wind}$ is the wind velocity. We varied $\dot{M}_{\rm wind} = (0.1, 0.2, 0.3, 0.4)\, M_\odot/{\rm yr}$ and $v_{\rm wind} = (3, 5, 8, 12)\,{\rm km/s}$ with $M_{\rm wind}$ from $0.2 - 0.8\, M_\odot$. In the top of Figure 4.3 we show values of $v_{\rm wind} = 8\,{\rm km\,s^{-1}}$, $\dot{M}_{\rm wind} = 0.2\, M_\odot/{\rm year}$, and $M_{\rm wind} = 0.4 M_\odot$. We find that the same wind parameters produce comparable early excesses when added to the three degenerate lightcurves, suggesting that the excess is set by properties of the wind itself and the underlying lightcurve, rather than, e.g. $E_{\rm exp}$. This wind also modifies the early velocity evolution. We do not claim that this is the only way to reproduce the early excess, as a variety of other outer density profiles can give rise to similar early excesses without affecting plateau properties (e.g. Morozova et al., 2019).

4.2.3 Modeling Challenges

For two events, SN2009IB and SN2017gmr, we see general agreement between models and bulk properties of the lightcurves (L_{50} and $t_{\rm p}$), with distinct differences shown in Figure 4.4. Specifically, these models differ beyond an early luminosity excess which might be explained by pulsations, a wind, varied structure of the extended stellar atmosphere, or other early interaction.

In SN2009ib (top two panels of Figure 4.4), the relatively low luminosity and high ^{56}Ni heating yield lightcurve models which rise significantly between days $20 - 80$. The narrow overlap between Equations (4.1) and our model grid suggests low $M_{\rm ej}$ and small R. For a reasonable range of R, explosion energies recovered are also low ($E_{51} \approx 0.2 - 0.3$).

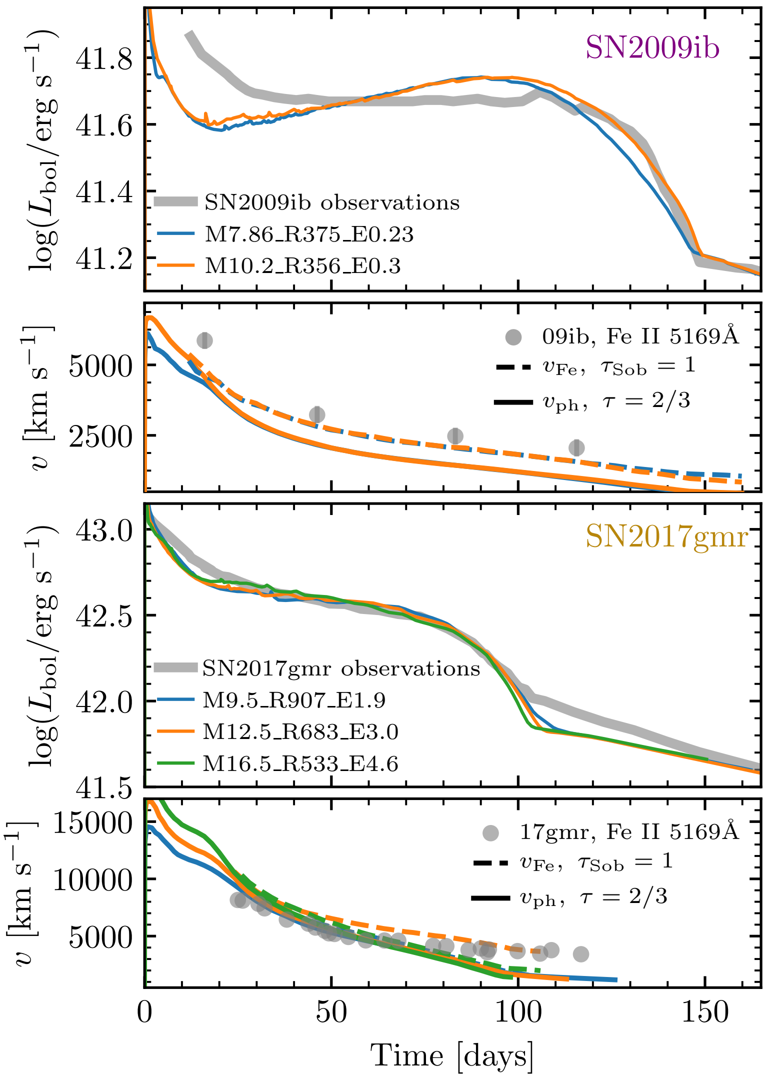

Figure 4.4: Lightcurves and Fe line velocities for SN2009ib (top two panels) and SN2017gmr (bottom two panels). Grey markers correspond to observations, and colored lines correspond to explosion models.

The disagreement between the models and the velocity data may indicate that $L_{\rm bol}$ is underestimated in some way (see the discussion in section 4.2.2). However, we found that additional models consistent with the velocity data and a brighter lightcurve of the same $t_{\rm p}$ still exhibit a similar, slightly shallower positive plateau slope. It is also possible that the estimated explosion epoch is too early. Moreover, neither explosion is consistent with a RSG of $R \approx 1000 R_\odot$ (derived assuming $T_{\rm eff} = 3400$K), as $R = 1000 R_\odot$ implies exceedingly low $M_{\rm ej} \approx 3 M_\odot$ and $E_{\rm exp} \approx 6 \times 10^{49}$erg. However, model M7.86_R375_E.023 is able to reproduce the observed $\log(L_{\rm p}/L_\odot) = 5.04 \pm 0.2$ with $T_{\rm eff} \approx 5450$K, thus favoring the yellower source scenario.

For SN2017gmr (bottom two panels of Figure 4.4), all models agree equally well with the lightcurve, but indicate an excess in observed luminosity after the plateau as the lightcurve transitions to the ^{56}Co-decay tail. Observed velocities are taken from the reported Fe-line radius evolution, and are only shown before day 120, after which point the evolution is not photospheric. The slight disagreement between modeled and observed velocities suggests that perhaps the distance is overestimated, but modeling to match a fainter bolometric lightcurve provides no change in the apparent late-time excess.

Although this event has no progenitor pre-image, if R at the time of explosion is consistent with $\approx 500 R_\odot$ recovered from fitting shock-cooling models to the photometric bands (Andrews et al., 2019), Equations (4.1) imply an enormous $E_{\rm exp} \approx 5 \times 10^{51}$ ergs! Our $533 R_\odot$ progenitor model indeed matches L_{50} and $t_{\rm p}$ when exploded with 4.6×10^{51} ergs, shown in green in the lower two panels of Figure 4.4.

Our modeling procedure only considers matching L_{50} and t_p. To compare directly to the day 1 results in Andrews et al. (2019) Figure 9, we re-ran the SN2017gmr models with a surface resolution adequate to resolve emission at day 1 ($\delta m_\mathrm{ph} \sim 10^{-3} - 10^{-4} M_\odot$). All three of our models yield luminosities at 1 day post-shock-breakout (L_1) a factor of ≈ 2 lower than L_1 of SN2017gmr recovered by their Sapir & Waxman (2017) shock-cooling model fits. Of our models, the day 1 photospheric temperature (T_1) of M16.5_R533_E4.6 does come closest to the reported shock-cooling $T_1 = 25,900$K, with $T_1 \approx 27,000$K, as compared to 29,000K for M12.5_R683_E3.0 and 30,000K for M9.5_R907_E1.9. At this time in the lightcurve evolution, the emitting region is coincident with the location of a density inversion in the stellar models, which is the focus of current ongoing studies.

For the lightcurve morphological differences, we have no easily available remedy without additional free parameters. Because we use the Duffell (2016) mixing prescription with coefficients calibrated to the 3D simulations as recommended in MESA IV, the resulting smoothing of the density profile and compositional mixing are held 'fixed.' Nonetheless, the Equations (4.1)-motivated models agree well with the L_{50} and t_p observations.

4.3 Discussion

The capability of `MESA+STELLA` to model observed SNe was introduced in MESA IV and demonstrated there and by Ricks & Dwarkadas (2019) to model a few Type IIP SNe. GBP19 introduced scaling relations (Equations 4.1) fit from a suite of `MESA+STELLA` models in order to guide explosion modeling efforts for an observed SN lightcurve with a given L_{50}, $t_{\rm p}$, and $M_{\rm Ni}$. In the absence of understanding in models of the first 20 days, our application of these relations to the observed SNe 2004A, 2004et, 2009ib, 2017eaw, and 2017gmr shows families of explosion models that match the data for a wide range of $M_{\rm ej}$, R, and $E_{\rm exp}$. These degeneracies will not be easily lifted without an observed progenitor radius (and understanding the progenitor's variability; see Goldberg & Bildsten 2020) or other constraints. However, when combined with a radius given by progenitor pre-imaging or fitting the shock-cooling phase, we show that explosion models can be constrained following $E_{\rm exp} \propto R^{-1.63}$ and $M_{\rm ej} \propto R^{-1.12}$.

If there was confidence in stellar evolutionary input constraining a $R - M_{\rm ej}$ relation at the time of explosion, then these degeneracies could be broken, as assumed in the population synthesis/lightcurve modeling of Eldridge et al. (2019). However, when varying rotation, winds, core overshooting, and mixing length within a reasonable range of values, we find no single ejecta-mass−radius relation.

It remains possible that detailed spectral modeling will lend insights which might aid in uniquely determining explosion properties from plateau observations. Additionally, velocity observations before day ≈ 20 or photospheric radii derived from shock-cooling models with a secure density structure in the outer $< 0.1\,M_\odot$ remain other promising paths forward to breaking the remaining degeneracies exhibited here.

Chapter 5

Numerical Simulations of Convective Three-Dimensional Red Supergiant Envelopes

As massive ($M \gtrsim 10M_\odot$) stars leave the main sequence, they expand to become Red Supergiants (RSGs), reaching radii of $\approx 300-1200R_\odot$ and luminosities of $\approx 10^4-10^{5.5}L_\odot$ (e.g. Levesque et al., 2006; Drout et al., 2012; Massey et al., 2021), approaching the Eddington limit and receiving increasing hydrostatic support from radiation pressure. These stars are characterized by low-density convective hydrogen-rich envelopes with large scale heights ($H/r \approx 0.3$) and sonic convection near their surfaces. They are intrinsically variable and pulsate in large-amplitude coherent modes (e.g. Kiss et al. 2006; Soraisam et al. 2018; Chatys et al. 2019; Ren et al. 2019; Dorn-Wallenstein et al.

2020) and their 3D nature is revealed to us in spectro-interferometric observations of nearby stars (e.g. Arroyo-Torres et al. 2015; Kravchenko et al. 2019, 2021; Montargès et al. 2021; Norris et al. 2021).

It is a theoretical challenge to realistically model stars, or even parts of stars, in 3D. This is especially true when radiative transfer must also be simultaneously solved through a highly turbulent medium with large density variations over optical depths ranging from far above unity down to the radiating photosphere. This radiation hydrodynamic (RHD) challenge has been very well-addressed in cases where this region is close to plane-parallel, starting with the fundamental work for the Sun (Stein & Nordlund, 1989, 1998), and now ranging across the HR diagram (e.g. Trampedach et al., 2013, 2014a,b; Magic et al., 2013a,b, 2015; Chiavassa et al., 2018a; Sonoi et al., 2019), building on earlier 2D RHD work (see Ludwig et al. 1999 for an excellent summary). These 3D computations have yielded a physical understanding of the nature of RHD convection in this limit, and provide a quantitative ability to set the outer boundary condition in 1D stellar models (e.g. Trampedach et al., 2014a; Salaris & Cassisi, 2015; Magic, 2016; Mosumgaard et al., 2018; Spada et al., 2021) for $\log g \gtrsim 1.5$, including for asteroseismic applications (Mosumgaard et al., 2020). While we have detailed understanding of the outer layers and quantitative surface relations for more compact, less luminous stars as guided by these works, such clarity has not been reached where the region requiring RHD calculations necessitates spherical geometry to capture large-scale plumes, and where the luminosity is locally super-Eddington.

In fainter giants, some of these aspects have been further addressed with global 3D simulations. In Red Giant Branch (RGB) stars, simulations of the convective interior reveal relatively flat velocity profiles set by large-scale convective plumes, and large temperature and density fluctuations (Brun & Palacios, 2009). These large-scale plumes extend up through the photosphere and produce granulation effects which can be interpreted by comparison of 3D models to interferometric data (e.g. Chiavassa et al., 2010a, 2017). In Asymptotic Giant Branch (AGB) stars, 3D simulations have revealed additional insights about the pulsational and circumstellar structure, with nearly-spherical shock fronts from large-scale convective cells which also levitate material to radii at which they can form dust (e.g. Freytag & Höfner, 2008; Freytag et al., 2017). These simulations can then be used to, e.g., generate inner boundary conditions for 1D wind models (Liljegren et al., 2018), and interpret both interferometric and photometric observations (e.g. Chiavassa et al., 2018b, 2020).

In the luminous RSG regime, early simulations focused on surface turbulence and magnetic properties (e.g. Freytag et al. 2002; Dorch 2004). Further simulations have been used to provide limb darkening coefficients and confirm the presence of large convective cells from interferometric observations of Betelgeuse (Chiavassa et al., 2009, 2010b). Chiavassa et al. (2011b) provide photocentric noise models towards quantifying Gaia astrometric parallax uncertainties and explain the "cosmic noise" impacting Hipparcos photometric measurements of Betelgeuse and Antares, while Chiavassa et al. (2011a) characterize microturbulence and macroturbulence parameters in grey- and frequency-dependent RSG atmosphere simulations. Further predictions from these models have been made with radiation transfer post-processing with the software `OPTIM3D` (Plez & Chiavassa, 2013) and reveal the inability to define a single "surface" responsible for setting the effective temperature, $T_{\rm eff}$.

A unifying feature of theory and observations of RSGs is the turbulent, extended outer envelope which manifests these inherently 3D convective properties. In 1D stellar evolution models, convection is conventionally handled by the Mixing Length Theory (MLT). The MLT approach derives from considering the fate of fluid elements as they move vertically a distance referred to as the mixing length $\ell \equiv \alpha H$, where α is a free parameter which can be calibrated to observations or by 3D simulations (Böhm-Vitense, 1958; Henyey et al., 1965; Cox & Giuli, 1968). Especially in Red Giants and Supergiants, mixing length assumptions, especially the value of α (and assumptions relevant to the structure and location of convective boundaries, which we will not explore in this work) strongly influence the stellar radii and $T_{\rm eff}$ (e.g. Stothers & Chin, 1995; Meynet & Maeder, 1997; Massey & Olsen, 2003; Meynet et al., 2015). While empirical constraints are useful, even crucial, for producing RSG models which match observed stars in luminosity, L, and $T_{\rm eff}$ (e.g. Chun et al., 2018), a first-principles calibration of MLT to 3D simulations of RSG envelopes remains an open channel for theoretical progress in characterizing the nature of convection in these very luminous objects.

The turbulent RSG envelope also plays a crucial role at the end of the star's life, as a strong shock emerges from the collapsed core and propagates rapidly through the envelope. Such explosions result in Type II-P SNe with $\simeq$100-day plateaus in their lightcurves whose properties depend on the envelope structure, and especially the progenitor radius, ejected mass, explosion energy and ^{56}Ni mass (e.g. Popov 1993; Kasen & Woosley 2009; Sukhbold et al. 2016). The exact initial mass range of stars exploding as Type II-Ps is still a matter of significant debate (the so-called "RSG problem", e.g. Smartt, 2009, 2015; Davies & Beasor, 2018; Kochanek, 2020; Davies & Beasor, 2020b,a). If the RSG radius is known at the moment of explosion, then light curve modeling can be used to constrain the ejected mass (Goldberg et al., 2019; Martinez & Bersten, 2019; Goldberg & Bildsten, 2020), with some sensitivity to the pulsation mode and phase at the time of explosion (see discussion in Goldberg et al. 2020). However, if the progenitor radius is unknown, very different stellar properties can yield identical lightcurves and photospheric velocities after the first ≈ 30 days (Dessart & Hillier, 2019; Goldberg et al., 2019), limiting our ability to infer masses and explosion energies solely from these observations.

Early Supernova observations can assist with breaking these degeneracies, but doing so is hampered by our lack of understanding of the density structure of the outermost RSG layers responsible for the early time emission (see, e.g. Morozova et al., 2016). In addition, Type II-P SNe frequently exhibit luminosities in excess of explosion models that assume a simple stellar photosphere (e.g. Morozova et al. 2017, 2018). This early excess is often attributed to interaction between the SN ejecta and the progenitor's outgoing wind (e.g. Moriya et al., 2018) or ejecta from pre-SN outbursts (Fuller, 2017; Morozova et al., 2019), and poses challenge in cleanly interpreting these early phases of SN evolution (see, e.g. Hosseinzadeh et al., 2018). It is also possible that these discrepancies are because the density structure in the vicinity of the photosphere is simply not well-described by conventional 1D stellar models. One important long-term goal of our effort is to better constrain the role of the 3D gas distribution in early SN emission.

This Chapter is organized as follows: In §5.1, we describe motivating expectations for the 3D regime we aim to explore, making use of Modules for Experiments in Stellar Astrophysics (`MESA` Paxton et al., 2011, 2013, 2015, 2018, 2019) to illustrate the importance of a proper 3D treatment of RSG envelopes. In §5.2 we describe our 3D `Athena++` (Stone et al., 2020) RHD setup for RSG envelopes, and in §5.3 we discuss the convective properties of these envelopes, comparing where possible to findings of earlier 3D RSG models. We then compare our 3D envelope models to predictions from MLT where appropriate (§5.4). Finally, we discuss our results and comment on future directions in §5.5.

5.1 Properties of 1D Red Supergiant Models and Open Challenges

For our initial exploration, we constructed a suite of solar-metallicity ($Z = 0.02$) models in `MESA`, following the test suite case `make_pre_ccsn_IIp` in revision 15140, shown in Fig. 5.1 from the onset of core H burning through the end of core Si burning. Our fiducial non-rotating models have modest exponential overshoot with overshooting parameter $f_{\rm ov} = 0.016$, a wind efficiency of $\eta_{\rm wind} = 0.2$ using the `'Dutch'` scheme in `MESA` (Glebbeek

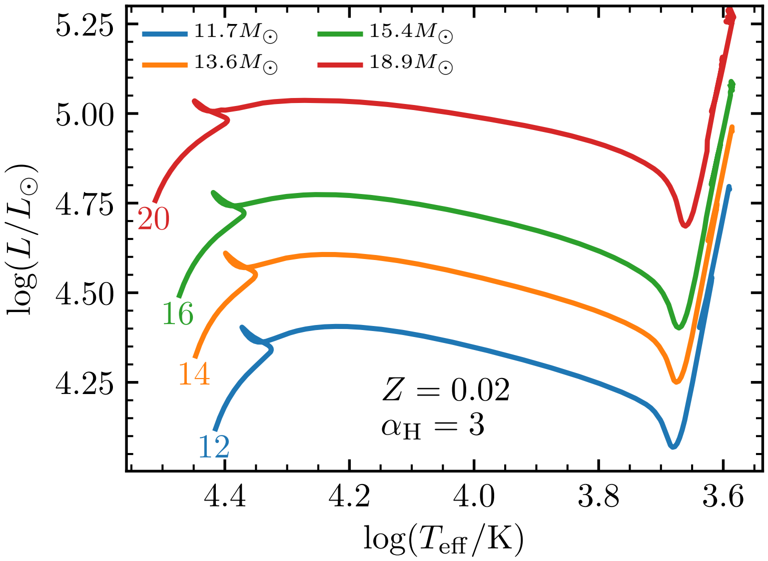

Figure 5.1: H-R diagrams of non-rotating `MESA` models with initial masses of $M_i/M_\odot$=12 (blue), 14 (orange), 16 (green), and 20 (red), from the main sequence through core Si burning. Final masses are given in the legend.

et al., 2009; Vink et al., 2001; Nugis & Lamers, 2000), core mixing length $\alpha_c = 1.5$ in regions where the H fraction $X_H \leq 0.5$, and mixing length $\alpha_H = 3$ in the H-rich envelope ($X_H > 0.5$). These parameters were chosen to be similar to those of the Type IIP Supernova progenitor models in Paxton et al. (2018), motivated also by the findings of Farmer et al. (2016).

The left panels of Figure 5.2 show the structure of four model RSG envelopes at the end of core C burning (central $X_C < 10^{-6}$) with initial masses ranging from 12 to 20 $M_\odot$. The x-axis excludes the He core, which is always inside of $r = 10R_\odot$ for all models. Through the envelope, the density falls by 3-4 orders of magnitude, nearly matching $\rho \propto 1/r^2$ through most of the inner envelope. The pressure scale height, $H = P/\rho g$, is large due to the weak gravity in the envelope, with $H/r \approx 0.3$ even at the half-radius coordinate. The envelope is fully convective, and both radiation pressure and gas pressure contribute significantly to the total pressure, with gas pressure dominating near the surface. Additionally, the opacity is very large throughout the envelope, dominated by opacity peaks from H and He ionization transitions inside the convective region.

Where convection is "efficient", ∇ is nearly $\nabla_{\mathrm{e}} \approx \nabla_{\mathrm{ad}}$ and the fluid structure follows the adiabat. There are two senses in which convection is said to be inefficient. When the convection is inefficient in the superadiabatic sense (i.e. $\nabla \gg \nabla_{\mathrm{e}}$, where $\nabla = d\ln T/d\ln P$ and ∇_{e} is the internal ∇ of a convective parcel; see Table D.1 in Appendix D), a rising fluid element will be hotter than the surrounding medium, and it will accelerate as it moves outwards in order to carry the flux. The stellar entropy profile thus declines. The convection can also be inefficient in the radiative sense, or "lossy", when a convective fluid parcel has sufficient time to radiate its internal energy to the cooler surrounding as it rises. In a medium with $P_{\mathrm{gas}} \gg P_{\mathrm{rad}}$, the optical depth at which radiation is able to contribute significantly to the energy transport and lossy convection is expected is $\tau < \tau_{\mathrm{crit}}$, where

$$\tau_{\mathrm{crit}} \approx \frac{P_{\mathrm{rad}}}{P_{\mathrm{gas}}}\frac{c}{v_c}, \tag{5.1}$$

where c is the speed of light, and v_c is the radial component of the convective velocity. The factor of $P_{\mathrm{rad}}/P_{\mathrm{gas}}$ comes from the fact that in the gas-pressure-dominated region near the cool stellar surface the parcel must evacuate the radiation field $P_{\mathrm{rad}}/P_{\mathrm{gas}}$ times in order to carry the same flux by radiation as convection (Kippenhahn et al., 2013). For $\tau > \tau_{\mathrm{crit}}$ where a parcel is unable to lose heat to radiation, $\nabla_{\mathrm{e}} \approx \nabla_{\mathrm{ad}}$. We will note

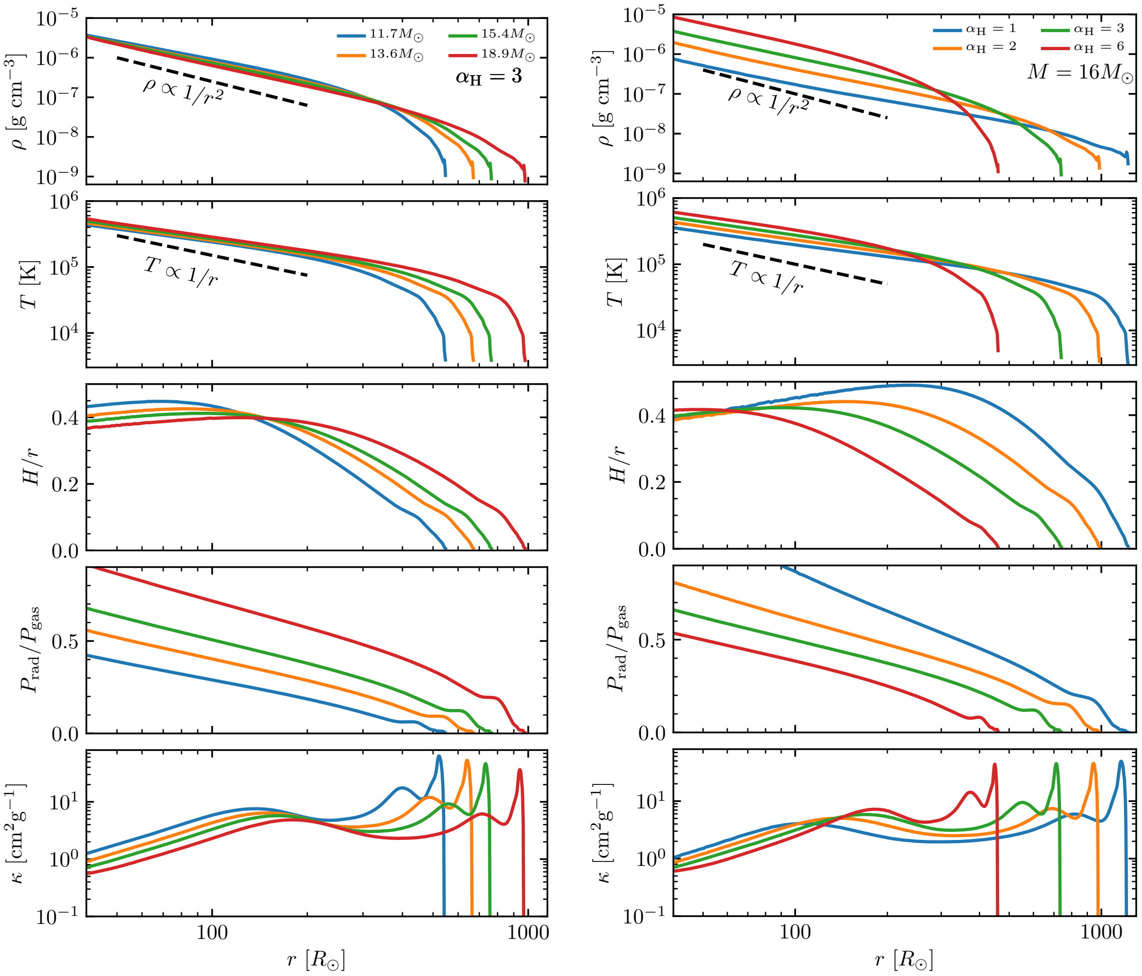

Figure 5.2: Top to bottom: Density, temperature, pressure scale height divided by radius, radiation to gas pressure ratio, and opacity as a function of radial coordinate r in $Z = 0.02$ RSG models. Left: Initial masses of $M_i/M_\odot$=12 (blue), 14 (orange), 16 (green), and 20 (red), all with $\alpha_{\rm H} = 3$. Right: Masses of $M = 16M_\odot$, varying the mixing length in the Hydrogen-rich envelope, $\alpha_{\rm H}$, for $\alpha_{\rm H} = 1$ (blue), $\alpha_{\rm H} = 2$ (orange), $\alpha_{\rm H} = 3$ (green), and $\alpha_{\rm H} = 6$ (red); here winds were neglected to isolate the effects of varying $\alpha_{\rm H}$, leading to the slight differences between the green lines in the left and right panels.

later, in §5.3.4, the close relationship between $\tau/\tau_{\rm crit}$ and the more commonly-discussed convective efficiency parameter, γ.

In MLT, $\nabla - \nabla_{\rm e}$ is directly related to the mixing length $\ell = \alpha H$ by (Kippenhahn et al., 2013)

$$F_{\rm conv} = \rho c_P T \sqrt{gQ} \frac{\ell^2}{\sqrt{\nu}} H^{-3/2} (\nabla - \nabla_{\rm e})^{3/2}, \tag{5.2}$$

where $F_{\rm conv}$ is the flux carried by convection, $Q = -{\rm D} \ln T / {\rm D} \ln \rho = (4 - 3\beta_P)/\beta_P$ where $\beta_P = P_{\rm gas}/(P_{\rm rad} + P_{\rm gas})$ for an equation of state (EOS) made up of radiation and gas, $\nu = 8$ following Henyey et al. (1965) and others, and c_P is the specific heat at constant pressure.

So as to explore the dependence of the RSG envelope structure on the mixing length $\alpha_{\rm H}$, we constructed additional $16 M_\odot$ RSG models varying α_H from 1 to 6. In these, we neglect mass loss due to winds ($\eta_{\rm wind} = 0.0$) and vary $\alpha_{\rm H}$ away from the fiducial value of $\alpha_{\rm H} = 3$ only at the end of core He burning in order to ensure that the resulting models have comparable core masses, $M_{\rm c,He} = 5.2 M_\odot$, and luminosities, $\log(L/L_\odot) = 5.06$. The structure of these models is shown in the right panels of Figure 5.2. Lower values of $\alpha_{\rm H}$ produce models with larger radii, lower densities, and lower temperatures throughout the envelope.

The upper panels of Fig. 5.3 show the specific entropy, s, profiles for models varying the initial mass (left) and $\alpha_{\rm H}$ (right) at the end of core C burning. The lower panels compare $\tau_{\rm crit}$ (dashed lines) to the optical depth τ (solid lines). The transition to lossy convection with radiation-dominated transport typically occurs around $T \approx 10^4$K and

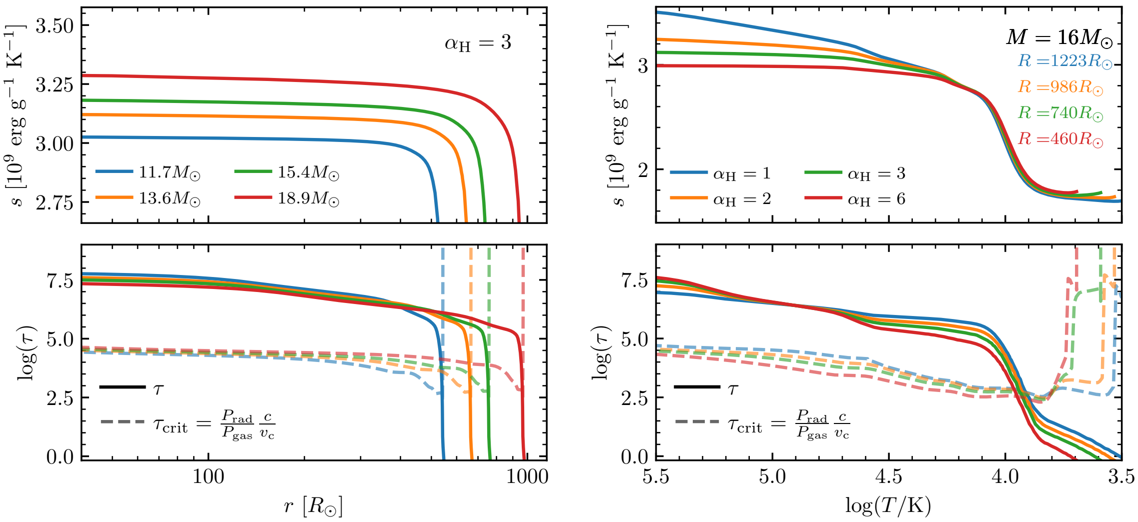

Figure 5.3: Specific entropy (upper panels) and optical depths (lower panels) for RSG models of different initial mass and $\alpha_H = 3$ (left panels), and varying α_H with $M = 16M_\odot$ (right panels). The optical depth remains much higher than τ_{crit} (dashed lines) until $\tau \approx 300$ near $T \approx 10^4$ K.

$\tau = \tau_{crit} \approx 300$, which is near the H opacity peak seen in Fig. 5.2. At that location, the peak in opacity and large luminosity implies $L \gg L_{Edd}$ there, a critical distinction for RSG models compared to main-sequence, RGB, or AGB stars. As T approaches T_{eff}, v_c declines to zero in a very thin radiative region above the convection zone. The green models are comparable between the left and right panels, with the only substantive difference being the inclusion of mass loss in the left panel leading to a slightly lower core mass, $M_{c,He} = 4.9M_\odot$, and luminosity, $\log(L/L_\odot) = 5.02$.

Varying initial mass increases the luminosity and thereby s, with relatively flat entropy profiles that begin to decline near the surface. Decreasing α_H decreases the efficiency of the convection, causing a steeper temperature gradient and an entropy decline. Larger mixing lengths correspond to more efficient convection and produce higher T_{eff}.

For a given luminosity, this leads to different radii with varying $\alpha_{\rm H}$, from $R = 460R_\odot$ when $\alpha_{\rm H} = 6$ to $R = 1223R_\odot$ when $\alpha_{\rm H} = 1$, despite comparable envelope masses and luminosities.

The assumed mixing length thus plays a dual role in determining the stellar structure. Foremost, the entropy profile declines even where $\tau \gg \tau_{\rm crit}$, especially for lower $\alpha_{\rm H}$, suggesting true superadiabatic convection with nonnegligible $\nabla - \nabla_{\rm e}$. The choice of $\alpha_{\rm H}$ influences $\nabla - \nabla_{\rm e}$ via Eq. (5.2) for a given $F_{\rm conv}$, and therefore determines the deviation of the temperature profile from the adiabat. Secondly, $\alpha_{\rm H}$ determines the adiabat on which the envelope sits. This effect can also be seen in models of cool stars more generally (e.g. Stothers & Chin, 1995; Meynet & Maeder, 1997; Massey & Olsen, 2003; Meynet et al., 2015) and is pronounced where convection occurs over orders of magnitude in radius, such as in cool giants. Running a further suite of models where we varied the location where the mixing length coefficient changes from a fixed $\alpha_{\rm c}$=1.5 to variable $\alpha_{\rm H}$ at different temperature coordinates, rather than setting the transition to be at the H-He interface as in our fiducial models, we find that changing $\alpha_{\rm H}$ in the lossy outer envelope below a few times 10^4K (where $\tau \lesssim \tau_{\rm crit}$) is what primarily determines the outer radius of the star, as the entropy decline in that region is fixed (as seen in the upper right panel of Fig. 5.3). Since $\rho \overset{\propto}{\sim} 1/r^2$, the stellar radius determines the density at the base of the envelope, the radiation to gas pressure ratio, the entropy, and thereby the adiabat. So even though less efficient convection at lower $\alpha_{\rm H}$ would predict a steeper radial temperature profile for fixed inner boundary, this is more than offset by the fact that the entropy deep within the envelope is larger for lower $\alpha_{\rm H}$. Although $\alpha_{\rm H}$ has been constrained for stellar models where $P_{\rm rad} \ll P_{\rm gas}$ and $H/r \ll 1$ throughout their convective regions (see, e.g. Trampedach et al., 2014b; Magic et al., 2015; Sonoi et al., 2019), the 'true' value of $\alpha_{\rm H}$ in the RSG envelope regime has never been calibrated to 3D simulations. Comparisons of 1D stellar models to observed RSG populations suggests $\alpha_{\rm H} \approx 2 - 3$ in different environments based on their location on the HR diagram, and in particular their effective temperatures (e.g. Ekström et al. 2012; Georgy et al. 2013; Chun et al. 2018).[1]

In MLT, the convective velocity v_c is related to the superadiabaticity and the mixing length by

$$v_c^2 = gQ\left(\nabla - \nabla_{\rm e}\right)\frac{\ell^2}{\nu H}. \tag{5.3}$$

Where $\tau > \tau_{\rm crit}$, a fluid parcel retains most of its heat and $\nabla_{\rm e} \approx \nabla_{\rm ad}$. Note that superadiabatic convection with $\nabla > \nabla_{\rm e} \approx \nabla_{\rm ad}$ leads to an increase in the convective velocity, while lossy convection yields a decrease in the convective velocity required to carry the flux as $\nabla_{\rm e}$ deviates from $\nabla_{\rm ad}$ and approaches ∇.

Fig. 5.4 shows the superadiabaticity $(\nabla - \nabla_{\rm ad})/\nabla_{\rm ad}$ (upper panel) and convective Mach number (middle panel) as a function of temperature coordinate for four $16 M_\odot$ models with varying $\alpha_{\rm H}$. As the superadiabaticity becomes large, particularly for larger $\alpha_{\rm H}$, convective velocities become nearly supersonic.

In the plane parallel limit, the turbulent pressure term needed to incorporate the

---

[1] See also the discussion by Joyce et al. (2020) of how MLT uncertainties bear on stellar evolutionary and hydrodynamical models of α Ori compared to asteroseismic observations.

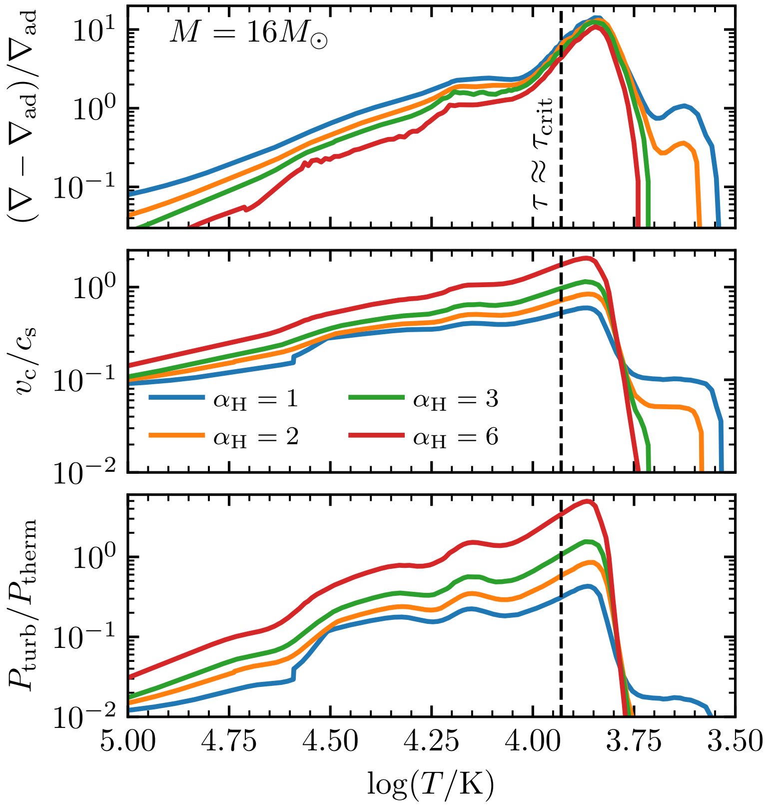

Figure 5.4: The superadiabaticity (upper panel), convective Mach number (middle panel), and estimated turbulent pressure (lower panel) versus $\log(T/{\rm K})$ for $M = 16M_\odot$, $Z = 0.02$ RSG models as $\alpha_{\rm H}$ varies. The vertical dashed lines indicate where $\tau \approx \tau_{\rm crit}$ in these models.

effects of the 3D Reynolds stress in a radial 1D model is $P_{\rm turb} = \rho v_r v_r \approx \beta \rho v_c^2$ up to a prefactor β typically assumed to be unity (Henyey et al., 1965).[2] This quantity is shown in the lower panel of Fig. 5.4 for v_c given by `MESA` assuming $\beta = 1$. Moving towards the stellar surface, the expected turbulent pressure rises, even exceeding the thermal pressure ($P_{\rm therm} = P_{\rm gas} + P_{\rm rad}$) in the cooler ($T \lesssim 10^4$ K) regions of the $\alpha_{\rm H} \geq 3$ models. Due to the intrinsically 3D nature of large-scale convection and the resulting turbulent pressure, the handling of this large expected pressure contribution is another way in which 3D results can guide 1D models.

Moreover, the envelopes of these models are only very loosely gravitationally bound. The lower panel of Fig. 5.5 shows the local total energy (dashed lines) and cumulative total energy integrated from the surface inwards (solid lines). The upper panel shows the ratio of the cumulative total energy to the gravitational energy. The kinetic energy assuming $v = v_c$ is neglected, as it only contributes only a few times 10^{45} erg in total for these models. As seen in the upper panel, the gravitational energy and the internal energy nearly cancel, and for our $\alpha_{\rm H} = 1$ model the internal energy exceeds the gravitational binding energy inside the envelope. This demonstrates the precariousness of these RSG envelopes, and why they can become unbound even from small energy deposited there from direct collapse of the He core to a black hole (e.g. Nadezhin 1980; Coughlin et al. 2018). This also highlights the importance of incorporating the envelope's self-gravity in

---

[2] In a plane parallel atmosphere where the z-direction is identified with radial gravity, the radial component of the gradient of $\rho \boldsymbol{v}\boldsymbol{v}$ is equal to the gradient of $\rho v_r v_r$ when deriving $P_{\rm turb}$ from the Euler equations. However, in spherical polar geometry the gradient of $\rho \boldsymbol{v}\boldsymbol{v}$ yields geometric terms $(\rho v_\theta v_\theta + \rho v_\phi v_\phi)/r$ which contribute to the momentum equation Landau & Lifshitz (1987). These terms are a small correction when $H \ll r$, which is not strictly the case in the RSG regime, or could vanish if $2 v_r v_r - (v_\theta v_\theta + v_\phi v_\phi) \approx 0$.

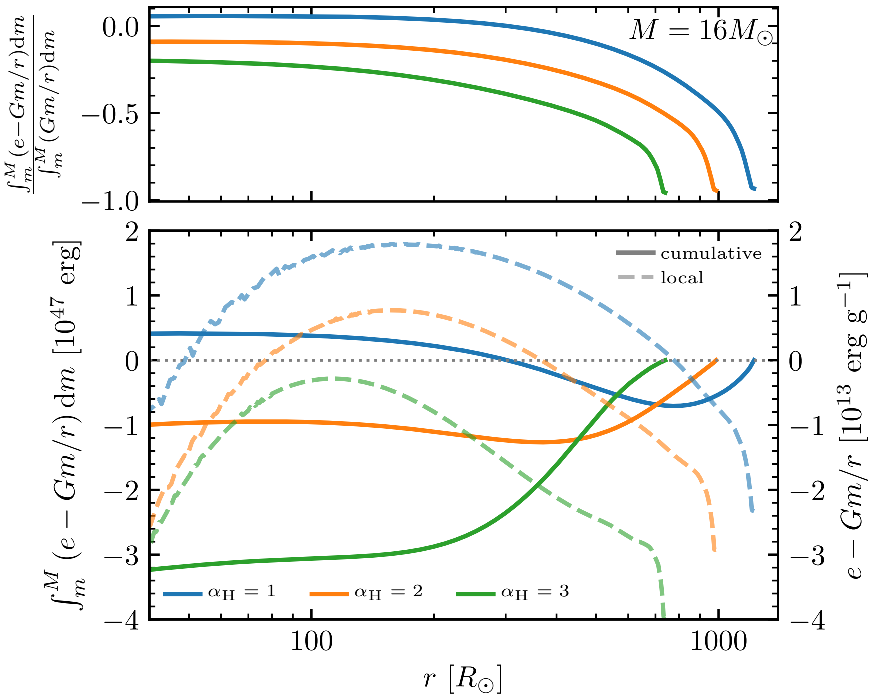

Figure 5.5: Upper panel: The ratio of the cumulative internal energy to the magnitude of the cumulative potential energy, integrated from the surface. Lower panel: Specific (solid) and cumulative (dashed) total energy (IE + PE) calculated from the surface inward in the envelope of 16 $M_\odot$ RSG models with α_H=1, 2, 3.

Name	$R_{\rm IB}/R_\odot$	$R_{\rm out}/R_\odot$	heat source	resolution ($r \times \theta \times \phi$)	duration	$m_{\rm c}/M_\odot$	$M_{\rm final}/M_\odot$
RSG1L4.5	400	22400	"hot plate"	$384 \times 128 \times 256$	5865 d	12.8	16.4
RSG2L4.9	300	6700	fixed L	$256 \times 128 \times 256$	5766 d	10.79	12.9

Table 5.1: Simulation properties, including inner boundary ($R_{\rm IB}$), outer boundary ($R_{\rm IB}$), heat source (as described in the text), resolution, run duration, core mass $m_{\rm c}$, and total mass at the simulation end ($M_{\rm final}$). All models have $\theta = \pi/4 - 3\pi/4$ and $\phi = 0 - \pi$, with $\delta r/r \approx 0.01$, and we restrict our analysis to material outside $450R_\odot$. The naming scheme indicates $\log(L/L_\odot)$.

our 3D calculations.

5.2 3D Model Setup and Equilibration

5.2.1 Model Setup in `Athena++`

To explore the 3D convective properties of RSGs, we constructed two large-scale simulations using `Athena++`. For these simulations, we use spherical polar coordinates with 128 uniform bins in polar angle θ from $\pi/4 - 3\pi/4$ and 256 bins in azimuth ϕ from $0 - \pi$ with periodic boundary conditions in θ and ϕ, covering 70.6% of the face-on hemisphere (i.e. solid angle $\Omega = 1.41\pi$). Outside of the simulation domain, `Athena++` uses ghost zones to enforce its boundary conditions (see Stone et al. 2020 for more details). For the "periodic" boundary in θ, the ghost zones from $\pi/4$ ($3\pi/4$) are copied from last active zones around the $3\pi/4$ ($\pi/4$) boundary, so that the mass and energy flux across the theta boundary is conserved. Although the spherical polar grid in `Athena++` can in principle include the whole sphere, such a setup will cause a timestep that is too small to perform these simulations. That is why we only cover the polar region between $\pi/4$

and $3\pi/4$, which is designed to represent a large typical wedge of the star. There are 2 options for a boundary condition in order to conserve mass and energy in the θ/ϕ direction. The method described here is preferred over a reflective boundary condition, which will lead to "splashback" (as is seen at the inner boundary). `Athena++` solves the ideal hydrodynamic equations coupled with the time-dependent, frequency-integrated radiation transport equation for specific intensities over discrete angles (Jiang et al., 2014; Jiang, 2021). We adopt the spherical polar angular system as defined in Section 3.2.4 of Jiang (2021) with 120 total angles per grid for the specific intensities. In this initial work, we consider a non-rotating stellar model and neglect magnetic fields. This is likely a safe assumption, as the envelope rotation reduces dramatically as the stars ascend the Hayashi track after core H depletion, though some RSG envelopes may have non-negligible rotation due to interaction or a merger with a companion (see, e.g., Joyce et al. 2020).

The RHD equations are (Jiang, 2021):

$$\begin{aligned}
\frac{\partial \rho}{\partial t} + \boldsymbol{\nabla} \cdot (\rho \boldsymbol{v}) &= 0, \\
\frac{\partial (\rho \boldsymbol{v})}{\partial t} + \boldsymbol{\nabla} \cdot (\rho \boldsymbol{v}\boldsymbol{v} + \mathsf{P}_{\rm gas}) &= -\mathbf{G}_r - \rho \boldsymbol{\nabla} \Phi, \\
\frac{\partial E}{\partial t} + \boldsymbol{\nabla} \cdot [(E + P_{\rm gas})\boldsymbol{v}] &= -cG_r^0 - \rho \boldsymbol{v} \cdot \boldsymbol{\nabla} \Phi, \\
\frac{\partial I}{\partial t} + c\boldsymbol{n} \cdot \boldsymbol{\nabla} I &= S(I, \boldsymbol{n}),
\end{aligned} \tag{5.4}$$

where ρ is the gas density and $\boldsymbol{v}$ is the flow velocity. The gas pressure tensor and scalar are given by $\mathsf{P}_{\rm gas}$ and $P_{\rm gas}$, respectively. The total gas energy density is $E = E_g + \rho v^2/2$, where $E_g = 3P_{\rm gas}/2$ is the gas internal energy density. Source terms G_r^0 and $\mathbf{G}_r$ are the time-like and space-like components of the radiation four-force Mihalas & Mihalas (1984). The frequency-integrated intensity I is a function of time, spatial coordinate, and photon propagation direction $\boldsymbol{n}$.

The mass in the simulation domain is not negligible, and because the envelope is expected to be only loosely bound, it is important to include an accurate gravitational acceleration, which we take to be spherically symmetric, with $-\nabla\Phi = -Gm(r)/r^2$. Here G is the gravitational constant, r is the radial coordinate, and $m(r)$ is the total mass inside r. We calculate $m(r)$ as the sum of the "core" mass interior to the inner boundary (IB) and the total mass between the IB and r at each time step.[3] The gas temperature is $T = (P_{\rm gas}\mu m_{\rm p})/(k_{\rm B}\rho)$, where k_B is the Boltzmann constant, and m_p is the proton mass, with mean molecular weight $\mu = 0.643$ to match our `MESA` models. A radiation temperature T_r can be calculated from the radiation energy density E_r included in the G_r^0 source term as $T_r = (E_r/a_r)^{1/4}$ where $a_r = 4\sigma_{\rm SB}/c$ is the radiation constant and $\sigma_{\rm SB}$ is the Stefan-Boltzmann constant; this is typically, but not necessarily, identical to T.

To calculate the radiation energy and momentum source terms, the lab frame intensity $I(\boldsymbol{n})$ with angle $\boldsymbol{n}$ is first transformed to the co-moving frame intensity $I_0(\boldsymbol{n}_0)$ with angle $\boldsymbol{n}_0$ via Lorentz transformation (Mihalas & Mihalas, 1984; Jiang, 2021). The source terms describing the interactions between gas and radiation in the comoving frame are

$$S_0(I_0, \boldsymbol{n}_0) = c\rho\kappa_{aP}\left(\frac{ca_rT^4}{4\pi} - J_0\right) + c\rho(\kappa_s + \kappa_{aR})\left(J_0 - I_0\right), \tag{5.5}$$

---

[3] An exploratory simulation did not include the self-gravity of the material within our simulation domain, instead using only a fixed mass from inside the inner boundary. In that simulation, the envelope rapidly expanded to $R_{\rm phot}{>}3000R_\odot$ with a sharp increase in mass in the simulation domain coming from the IB, and never reached a quasi-hydrostatic convective steady state.

where κ_{aR} and κ_{aP} are the Rosseland and Planck mean absorption opacities determined by interpolation of the OPAL opacity tables (Iglesias & Rogers, 1996), and κ_s is the electron scattering opacity, all evaluated in the comoving frame. The angular quadrature of the intensity in the co-moving frame is $J_0 = \int I_0(\boldsymbol{n}_0) d\Omega_0/(4\pi)$. After the specific intensities $I_0(\boldsymbol{n}_0)$ are updated in the co-moving frame, they are Lorentz transformed back to the lab frame. The radiation momentum and energy source terms G_r^0 and $\mathbf{G}_r$ are calculated by the differences between the angular quadratures of $I(\boldsymbol{n})$ in the lab frame before and after adding the source terms. See Jiang (2021) for more details of the implementation. The hydrodynamic equations are solved using the standard Godunov method in `Athena++` (Stone et al., 2020). Similar numerical methods and setup have been successfully used to model stellar envelopes in different locations of the HR diagram (Jiang et al., 2015, 2018).

5.2.2 RSG Setup and Model Evolution

We used the NASA supercomputer Pleiades to run two 3D RHD simulations. Each run takes about two months to finish with 80 skylake nodes in Pleiades. For this study, we motivate our initial and boundary conditions with the fiducial $15.4 M_\odot$, $Z = 0.02$, $\alpha_{\rm H} = 3$ model at the end of core C burning discussed in §5.1 (shown in green in the left panels of Fig. 5.2). Our first model, referred to hereafter RSG1L4.5, is initialized in 3D by assuming a purely radiative envelope with luminosity equal to the radiative luminosity at $r = 400 R_\odot$ in the `MESA` model (which is a few % of the total luminosity). The mass and radius of the IB are $400R_{\odot}$ and $12.8M_{\odot}$. To generate the initial conditions, the temperature ($T = 7.19 \times 10^4$ K) at the IB is first set to equal the $400R_{\odot}$ coordinate in the `MESA` model, and density ($\rho = 5.45 \times 10^{-8}$ g/ cm^{-3}) selected to approximately recover the $15.4M_{\odot}$ total mass. To perturb from the radiatively stable initial conditions and supply the convective luminosity, we increase the temperature at the IB by 10% compared with the initial condition (a "hot plate"), while density is fixed and velocity is reflective at the inner boundary, akin to the setup of Jiang et al. (2018). This boundary condition produces a radiative layer near the bottom with the desired luminosity, which causes the envelope away from the bottom boundary to be convective. In this setup, we do not know in advance what the luminosity will be. RSG1L4.5 was one of 3 initial runs with this inner boundary condition; the other two at 20% and 40% Temperature increases gained mass too rapidly and never reached a convective steady state.

All our analysis will be done in the convective region starting from $\approx 450R_{\odot}$. As convection sets in, the luminosity reaches $\log(L/L_{\odot}) = 4.5$, with some periodic and stochastic variability which we will discuss in more detail in §5.3.4. Because mass flux through the inner boundary cannot be exactly 0 on a spherical polar mesh even with our reflective velocity boundary condition, a small amount of additional mass enters the simulation domain as time goes on. At the end of the simulation, the total mass of this model is $16.4M_{\odot}$. This 6.5% increase in the total mass of the star (≈20% in the mass inside our simulation domain) is not of concern, as the aim of this work is to create realistic 3D envelope models to study the convective structure, not to diagnose a mass-luminosity relation in 3D models (which would also be sensitive to core properties). The simulation domain for this model is 384 radial zones, with $\delta r/r \approx 0.01$, with a free outer boundary at $r = 22400 R_\odot$. The choice of a large simulation domain was motivated, in part, to capture any wind structure or extended atmosphere, make sure we capture the stellar photosphere so that the outer boundary is always in the optically thin limit for the radiation field, as well as to provide ample space for expansion in explosions of this envelope model in forthcoming work. With a logarithmic radial grid spacing, the large outer boundary is achieved with small additional cost for our simulation, and 87 zones lie within $r < 1000 R_\odot$.

Our second model, referred to hereafter RSG2L4.9, is initialized with the same method as RSG1L4.5 for the region that will become convective. This model has the IB at $300 R_\odot$ with $10.79 M_\odot$ enclosed, and the total initial mass at $14 M_\odot$. The simulation domain has 256 radial zones (98 at $r < 1000 R_\odot$) with $\delta r/r \approx 0.01$, with a free outer boundary at $r = 6700 R_\odot$, still far away from the stellar surface. Between $300 R_\odot$ and $400 R_\odot$, the initial profile is constructed with the radiative luminosity to be $10^5 L_\odot$ and this is kept fixed in the inner boundary ("fixed L"). This serves the same purpose as the boundary condition used in the previous model to drive convection for the region above. We therefore similarly only perform our analysis for the region above $\approx 450 R_\odot$. We first run for 740 days with fixed total F_r at the inner boundary (including advection and diffusion). After an initial relaxation period, this scheme begins to add mass somewhat rapidly, so we switch to fixing only the diffusive $F_{\mathrm{rad},0}$ at the inner boundary. This leads to a small,

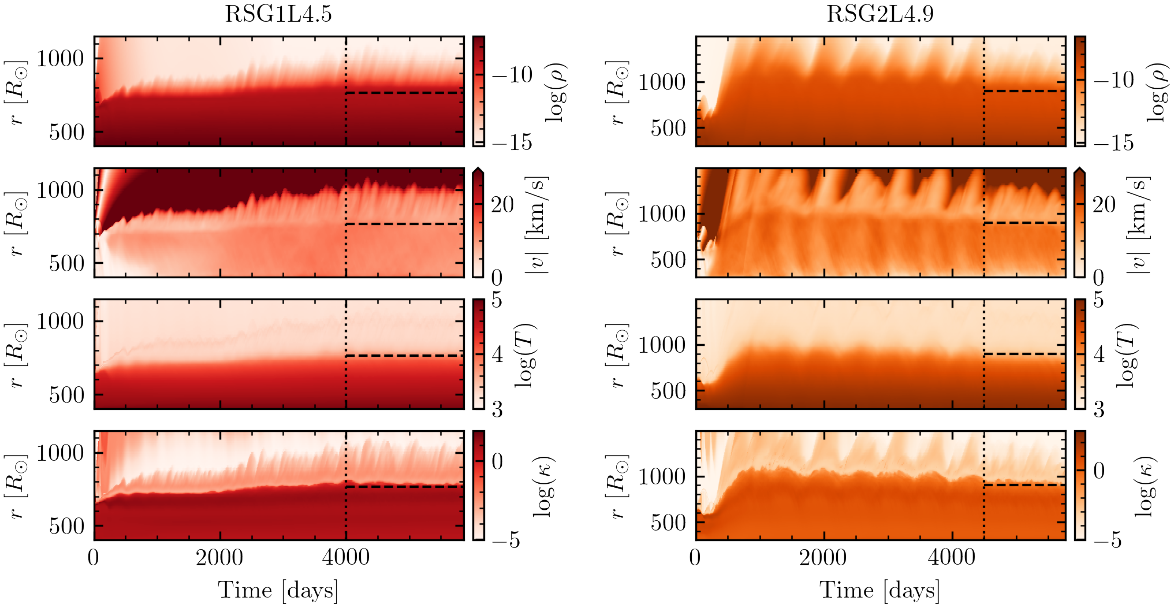

Figure 5.6: History of the averaged radial profiles for our RSG1L4.5 (red, left) and RSG2L4.9 (orange, right) models. Top to bottom show log(density), convective velocity, log(temperature), and log(opacity). All logarithms are base 10 and units inside the logarithms are cgs, and velocites are reported in km/s. Vertical dotted lines indicate when the envelope appears to have reached a convective steady state. Horizontal dashed lines approximate the region where some fraction of the stellar area has $\tau > \tau_{\rm crit}$.

steady decrease in the total envelope mass from the inner boundary. At the end of the simulation, the total mass of this model is $12.9 M_\odot$. In both cases, most of the mass change happens during the initial transient relaxation from the initial conditions to a convective structure. From day 4500 to the end of the simulation, the mass inside the simulation domain changes by less than 1% ($0.03 M_\odot$) for RSG1L4.5, and 10% ($0.2 M_\odot$) for RSG2L4.9. The properties of these models are summarized in Table 5.2.

Radial profiles of both simulations as a function of time are shown as space-time diagrams in Fig. 5.6. Radial density, opacity, and temperature are calculated by finding the volume-weighted average over spherical shells at each time (which we hereafter denote with $\langle \cdots \rangle$), and the magnitude of the velocity, is calculated from the mass-weighted average over spherical shells (which we hereafter denote with $\langle \cdots \rangle_m$), $|v| = \sqrt{\langle v_r^2 + v_\theta^2 + v_\phi^2 \rangle_m}$. Horizontal dashed lines approximate the location where radiation begins to dominate the energy transport at late times. Inside the dashed line, convection is expected to resemble MLT, with denser material sinking as less dense material rises. We will explore this expectation in more detail in §5.3.4 and 5.4. For computational reasons, both models have density floors imposed with $\rho_{\rm floor} = 5.35 \times 10^{-16}$ g/cm^3. The fast-moving low-density material at very large radii is caused by negligible amounts of density-floor material falling onto the star due to gravity.

The two simulations begin with an initial transient phase, as convection sets in from the unstable spherically symmetric initial conditions. In RSG1L4.5, the intial transient phase is accompanied by some material being launched outwards, falling back onto the stellar surface around day 2500. Additionally, convection begins to appear at the density inversion near the stellar surface, and makes its way to the IB by ≈ 1000 days. By day 2000, the amplitudes of the convective velocities steady and by day 4000 the RSG1L4.5 simulation appears to have fully settled into equilibrium, with regular fluctuations in the stellar properties particularly in the region above $\tau = \tau_{\rm crit}$.

In RSG2L4.9, the fixed luminosity at the IB triggers convection at small radii in addition to the surface, so convection sets in quickly. The initial transient causes a sharp increase in the mass contained in the stellar envelope coming from the inner boundary, accompanied by a rapid expansion of the envelope around day 500. With the change in

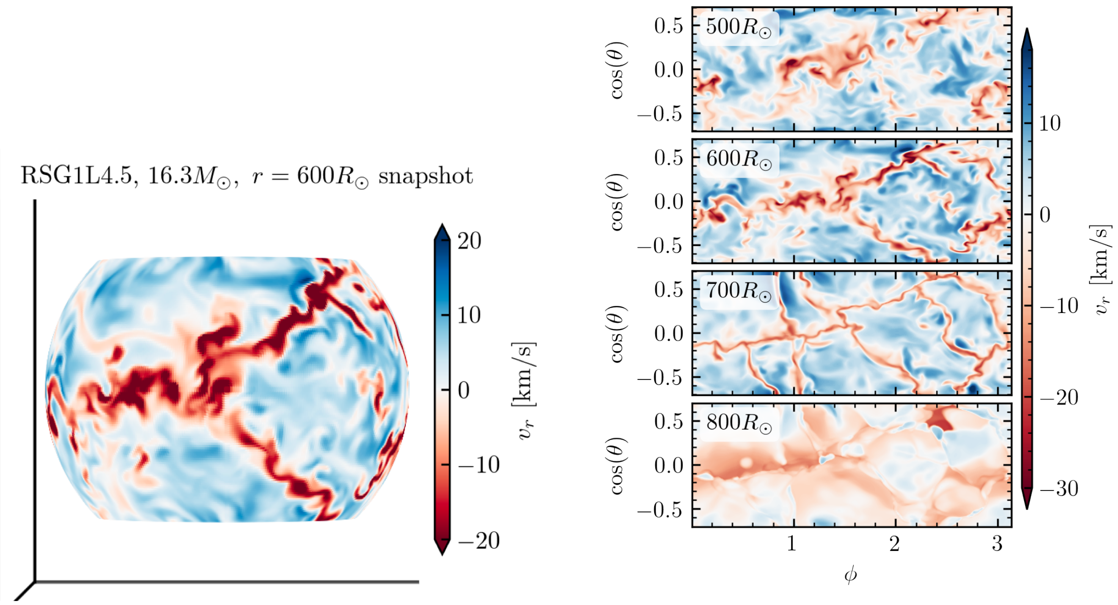

Figure 5.7: Left: Surface rendering of the radial velocity fluctuations at $r = 600R_\odot$ in RSG1L4.5 at day 4707. Right: Snapshot of radial velocity slices for the same model. Panels show radial slices at $r = 500R_\odot$ (top) to $800R_\odot$ (bottom) in $100R_\odot$ intervals, and axes show the extent in azimuth ϕ and co-polar angle $\cos(\theta)$. The volume-weighted mean sound speed is 33 km/s at $r = 500R_\odot$, 26 km/s at $600R_\odot$, 19 km/s at $700R_\odot$, and 8 km/s at $800R_\odot$.

inner boundary condition at day 740, the rapid growth ceases, and by day 2000 the model begins to settle into a pattern of semi-regular oscillations. By day 4500, the amplitude of radial fluctuations dies down and the envelope exhibits similar steady-state behavior to the RSG1L4.5 simulation with larger radial extent and higher velocities. We now check this apparent steady-state behavior for both simulations.

5.2.3 Defining a 'Steady State'

By the end of the simulations, both models have thermal and kinetic energy content $E_{\rm fluid} = \int(E + E_r)\mathrm{d}V$ comparable to the binding energy $E_{\rm bind} = \int(\rho\Phi)\mathrm{d}V$, with a ratio of $E_{\rm fluid}/|E_{\rm bind}|$ of 0.23 for RSG1L4.5 (with $E_{\rm tot} = E_{\rm fluid} + E_{\rm bind} = -3.0 \times 10^{47}$erg extending the volume to $\Omega = 4\pi$) and 0.32 for RSG2L4.9 ($E_{\rm tot} = -1.4 \times 10^{47}$erg). The comparable gas and binding energies reinforce our choice of including the envelope mass in our gravitational.

The convective plumes show large ($\gtrsim 200 R_\odot$) vertical and lateral extents, leading to a nearly-radius-independent velocity profile with an-order-of-magnitude scatter, shown in Fig. 5.7. When fluid flow is this coherent, the velocity field will be time-correlated for around an eddy-turnover time at any given spatial location. Beyond this timescale, we expect no memory of past convective plumes at a fixed coordinate. To start our exploration of the timescale required for the model to reach equilibrium, we calculate the autocorrelation of the radial velocity at fixed coordinates. The autocorrelation function for an arbitrary time-dependent parameter $Y(t)$ is defined for time lag Δt by

$$\mathrm{acf}(Y, \Delta t) = \frac{\int (Y(t) - \bar{Y})(Y(t+\Delta t) - \bar{Y})\mathrm{d}t}{\int (Y(t) - \bar{Y})^2 \mathrm{d}t}, \tag{5.6}$$

where $\bar{Y}$ is the time-averaged value. Fig. 5.8 shows the autocorrelation function for the radial velocity, $\mathrm{acf}(v_r, \Delta t)$, for a few different radii in each model. Dark lines give the mean of the autocorrelation functions at 169 angles distributed across the stellar model, and the shaded areas give the standard deviation of the acf at each radius. Only radial velocities after day 1000 are considered for each model. The less luminous RSG1L4.5 model stays correlated for ≈550 days, whereas the more luminous RSG2L4.9 model decorrelates faster, over a timescale of ≈300 days. This is because the more luminous model exhibits larger convective velocities as required to carry the flux, even though the

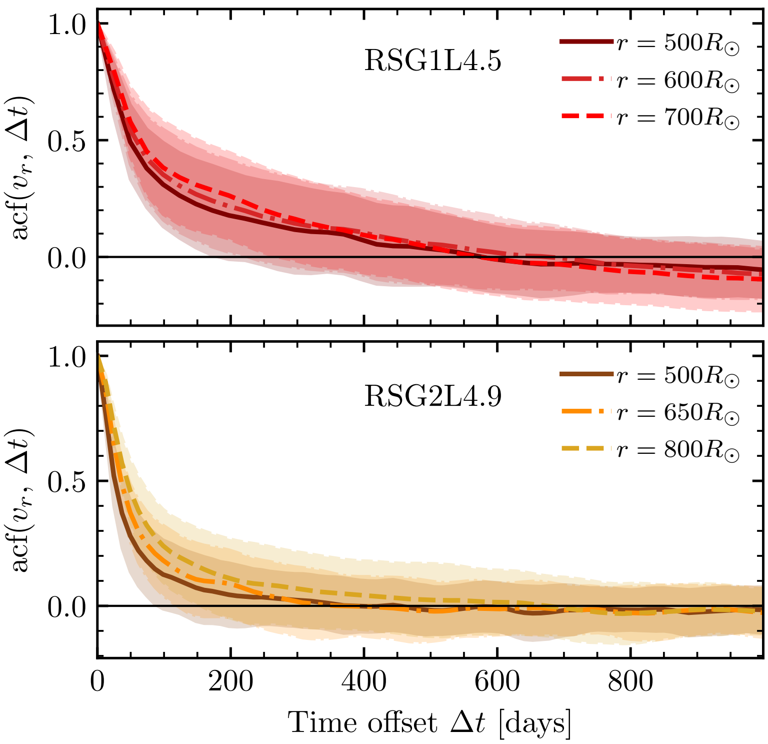

Figure 5.8: Average autocorrelation of radial velocities across different angles at different radii for the RSG1L4.5 model (upper panel) and the RSG2L4.9 model (lower panel) as a function of the time lag. All data in this plot are after the simulations have run for 1000 days. The shaded region gives the standard deviation of the acf across the different angles.

mass and radii are comparable. These timescales are short compared to the simulation duration, so we can proceed in our analysis with additional confidence that both models have reached their convective steady state after ≈4000 days.

A direct check as to whether the models have reached a convective steady state is to explore the RHD equations for the time-averaged profiles. The momentum equation quickly equilibrates such that $\partial \rho \boldsymbol{v}/\partial t \to 0$ when taking the time-average on a dynamical timescale (i.e. the sound-crossing time across a pressure scale height, 10s to 100s of days in the outer envelope), but the energy equation will only reach equilibrium in our region of interest as convection is able to distribute the luminosity over a few eddy turnover times, which is significantly longer. Combining and rearranging RHD Eqs. (5.4) including the source term

$$G_r^0 = \frac{\partial E_\mathrm{r}}{\partial t} + \nabla \cdot \boldsymbol{F}_\mathrm{r}, \tag{5.7}$$

where $\boldsymbol{v}F_r$ is the total radiation flux (including $F_{\mathrm{rad},0} = -1/3(c/\kappa\rho)(\mathrm{d}a_r T_r^4/\mathrm{d}r)$ for radiative diffusion and $F_{\mathrm{adv}} = E_r v_r$ for advection), with $g = -\nabla\Phi \cdot \hat{r}$, for spherically symmetric $\Phi(r)$, we recover

$$\frac{\partial}{\partial t}(E + E_\mathrm{r}) + \nabla \cdot [(E + P_\mathrm{gas})\boldsymbol{v} + \boldsymbol{F}_\mathrm{r} - (\rho \boldsymbol{v} \Phi)] = -\Phi \nabla \cdot (\rho \boldsymbol{v}) = -\Phi \frac{\partial}{\partial t}\rho. \tag{5.8}$$

In a steady state, $\partial/\partial t \to 0$ when we take the time average $\langle \cdots \rangle_t$. Taking the radial component of the divergence we find

$$\left\langle \frac{1}{r^2}\frac{\partial}{\partial r}[r^2(E + P_\mathrm{gas})v_r + r^2 F_{\mathrm{r},\hat{r}} - r^2(\rho v_r \Phi)] \right\rangle_t = 0. \tag{5.9}$$

Thus if $r^2 \left\langle (E + P_\mathrm{gas})v_r + F_{\mathrm{r},\hat{r}} - (\rho v_r \Phi) \right\rangle_t \equiv r^2 \langle F_\mathrm{tot} \rangle$ is spatially constant, the model can be considered to have equilibrated. This expression is equivalent to the time-average of the volume-weighted average of the total luminosity L_tot, including enthalpy, gravity, kinetic energy, and radiation terms, divided by 4π. Though there is a net change in L_tot due to mass gained/lost near the IB, in the region of interest, our steady state criteria are sufficiently satisfied by both models in the region of interest, as shown in Fig. 5.9. The transparent colored lines show the volume-averaged total luminosity from days 4001−5864 in approximately 3 day intervals for the RSG1L4.5 model (red) and evolution from day 4501−5766 in approximately 5 day intervals for the RSG2L4.9 model

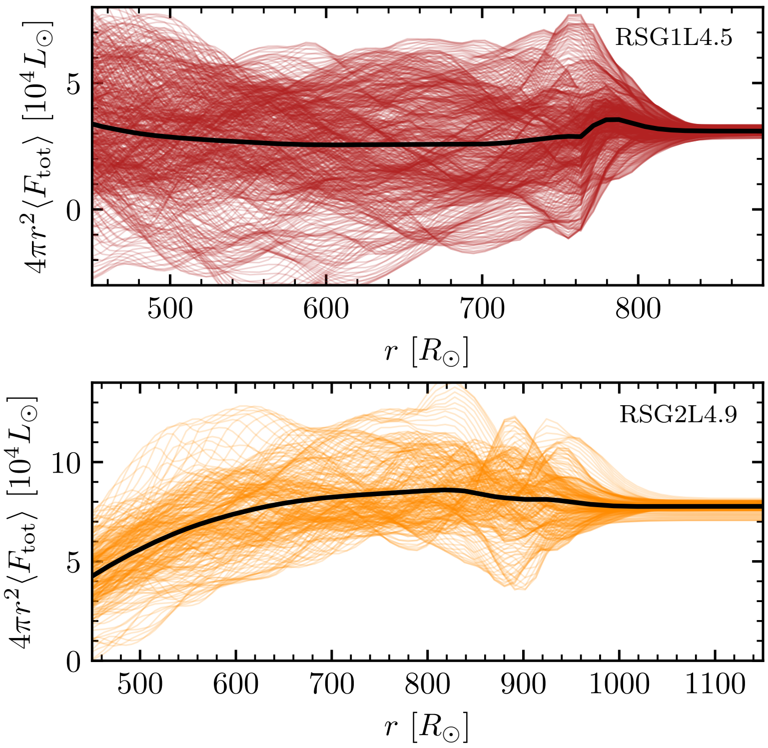

Figure 5.9: Volume-average of $4\pi r^2((E + P_{\rm gas})v_r + F_{{\rm r},\hat{r}} - (\rho v_r \Phi))$ at different times (thin colored lines) compared to the time-average (solid black line) for our RSG1L4.5 (red, upper panel) and RSG2L4.9 (orange, lower panel) models outside $r = 450 R_\odot$.

(orange). The solid black lines give the time-average of this quantity, whose variance at different radii is significantly less than the scatter at different times. The small number of distinct convective plumes implies a fundamental variance in the stellar luminosity reflected in the scatter at large radii that we discuss in more detail in §5.3.4.

5.3 3D Model Properties

Having shown how to initiatlize a 3D RSG model and evolve it to its effectively equilibrium state, we now will describe the properties of the resulting models, compare to prior work, and discuss some of the unique properties of these highly luminous models.

5.3.1 Convective Properties and Comparison to Prior 3D `CO5BOLD` RSG Work

Aspects of the observable 3D structure of RSGs have been studied in a series of pioneering papers (e.g. Chiavassa et al. (2009, 2010b, 2011b,a); Kravchenko et al. (2018)) using the RHD "star-in-a-box" COnservative COde for the COmputation of COmpressible COnvection in a BOx of L Dimensions, L=2,3 (`CO5BOLD`, Freytag et al., 2002, 2010, 2012). In those simulations, the computational grid was cubic equidistant with typical mesh spacing of $\approx 8.6R_\odot$, with LTE radiation transport by short characteristics using opacity tables as function of P, T interpolated from PHOENIX data at $T \lesssim 12,000\,\mathrm{K}$ (Hauschildt et al., 1997) and OPAL values (Iglesias et al., 1992) at higher T. The EOS included ideal gas and ionization, but radiation was only present in the energy equation, and not as a pressure source. The gravitational potential was modeled by a Plummer potential $\Phi = -GM_*/(r_0^4 + r^4/\sqrt{1+(r/r_1)^8})^{1/4}$ fixed to the static Cartesian mesh with $M_* = 12M_\odot$ and $3M_\odot$ of material contained in the simulation domain, and the luminosity was supplied via an energy source within the inner Plummer radius (r_0).

That work focused on stellar properties at low optical depth, where radiation transport dominates, and have been compared to recent tomagraphic observations of nearby RSGs to interpret their surface convective structure (e.g., Kravchenko et al., 2019, 2020, 2021). The neglect of radiation pressure deep within the star inhibited the ability to

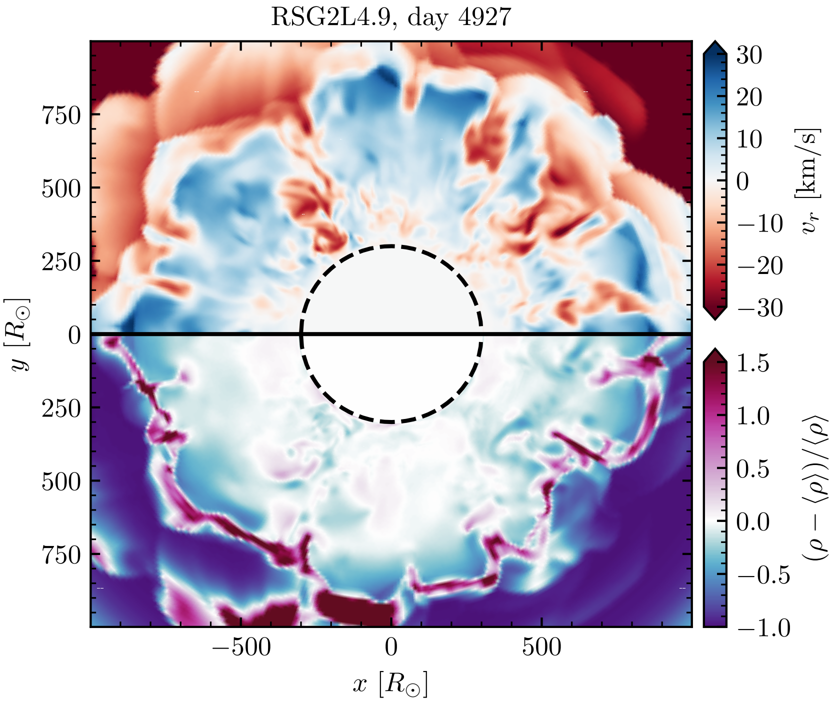

Figure 5.10: Equatorial ($\theta = \pi/2, z = 0$) slice of a characteristic snapshot of the RSG2L4.9 model, showing (upper half of the figure:) radial velocities and (lower half of the figure:) density fluctuations relative to the shellular volume-averaged density at each radius. The simulation domain is from $\phi = 0$ to π; thus the image is reflected about $y = 0$ as indicated by the axis labels.

correctly simulate the deeper nearly-constant-entropy convective zone there. Hence, the convective flux in the interior of those RSG models is significantly lower than the radiative flux, with radiation carrying over 80% of the flux everywhere. Because of this, those simulations exhibit a positive entropy gradient out to ≈75% of the stellar radius (see Fig. 3 of Chiavassa et al. 2011a). While this is no concern when restricting analysis to the turbulent surface layers where the entropy profile does decline, it is counter to the theoretical expectations for a fully turbulent RSG envelope, which should have a nearly-flat, declining entropy profile throughout the convective envelope, with enthalpy and kinetic flux accounting for a significant fraction of the total flux.

In agreement with the `CO$^5$BOLD` models, our `Athena++` RSG simulations show a handful of large-scale, coherent convective plumes across the star, with radial velocities of tens of km/s and density fluctuations of 10% increasing to factors of a few at larger radii (see Figs. 5.7 and 5.10). As emphasized by Stein & Nordlund (1998), we see a topology of large area upwellings surrounded by narrow lanes of downward flows. Additionally, the specific entropy, radiative luminosity, and ratio of kinetic to thermal energy density in representative snapshots of our two models are shown in Fig. 5.11. The red/orange shaded regions give a sense of the scatter. Like in the `CO$^5$BOLD` models, we observe a 'halo' of bound, high-entropy material above the conventional photosphere, with density fluctuations exceeding an order of magnitude in the outer-most parts of the star. The entropy profile in the interior of our `Athena++` models is nearly adiabatic, declining slightly out to $100 - 200 R_\odot$ beneath the 1D photosphere, and declining more rapidly as

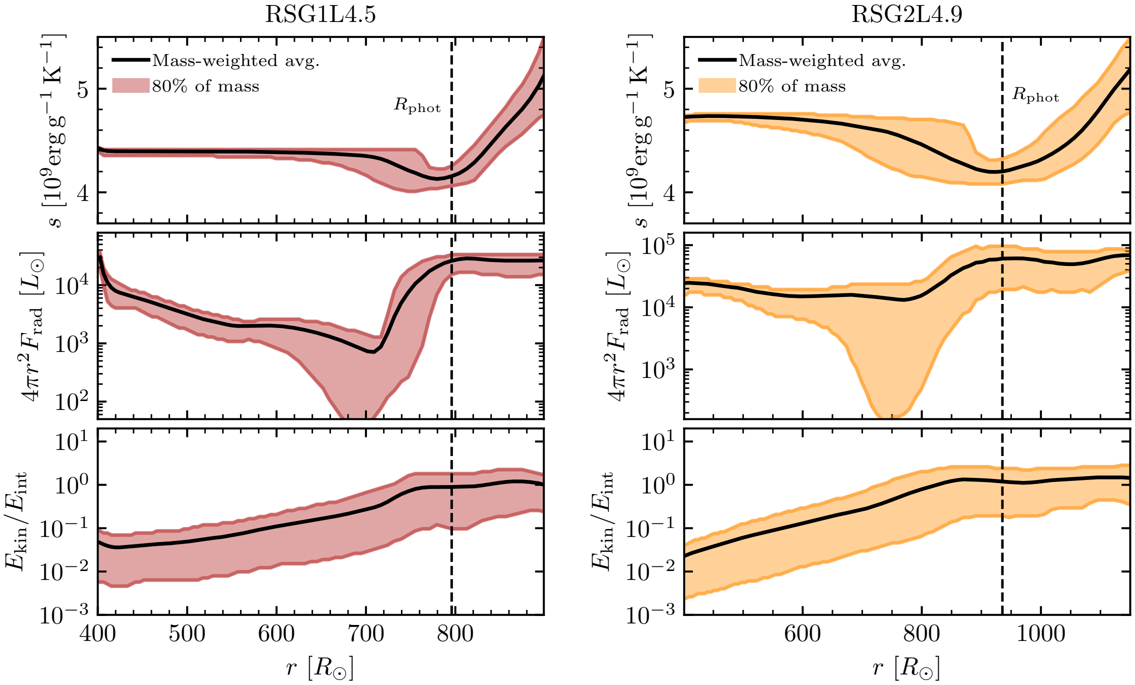

Figure 5.11: Specific entropy (top panels), radiative luminosity (middle panels), and ratio of the turbulent kinetic energy to the internal energy (bottom panels) in our RSG1L4.5 model at day 4707 (red, left) and RSG2L4.9 at day 4927 (orange, right). Mass-weighted averages are shown in black, with 80% of the mass lying within the shaded regions. The 1D photosphere, where $\langle L(r)\rangle = 4\pi r^2 \sigma_{\rm SB} \langle T_r(r)\rangle^4$, is given by the vertical dashed line.

radiation is able to carry more of the flux. These entropy profiles are similar to those seen in lower-luminosity RHD models (e.g. Stein & Nordlund, 1998; Magic et al., 2015).

Following Chiavassa et al. (2011a), we define the 1D photosphere by calculating 1D radial profiles of the luminosity $\langle L(r)\rangle$ and radiation temperature $\langle T_r(r)\rangle$; $r = R_{\rm phot}$ is then defined as the location where $\langle L(r)\rangle = 4\pi r^2 \sigma_{\rm SB} \langle T_r(r)\rangle^4$. The energy transport in the stellar interior is dominated by convection, and radiation carries ≈ 10% of the luminosity in the convective region. Moreover, the turbulent kinetic energy density from the vigorous convective motions dominates over the thermal energy in the outer envelope, in agreement with the findings of (Chiavassa et al., 2011a).

5.3.2 Stochastic Angular Momentum

The 3D properties of convection in RSG interiors are also of interest for predicting properties of the remnant in failed SNe (e.g. Coughlin et al., 2018; Quataert et al., 2019). Recently, Antoni & Quataert (2022) completed a detailed study of convective fluid motion with applications to collapsing RSGs using 3D hydrodynamical simulations of idealized RSG models spanning a factor of 20 in stellar radius. Their work considers an ideal gas with polytropic index $\gamma = 1.462$ in a Plummer potential $\Phi = -GM/(r^n + a^n)^{1/n}$ with $n = 8$ for a smoothing radius $a \ll r_o$ in their dimensionless code units where $r_o = R_{\rm phot}/6$. This converges to a point mass in their region of interest. These pure-hydro simulations enforce a photospheric radius by providing a cooling sink at large fixed radii and smoothly decreasing the temperature outside the photosphere to be equal to their temperature floor. Their study focused on quantifying the randomly distributed angular momentum of the inner layers of the convective RSG envelope, and how these shells evolve during later collapse.

In our models, we likewise observe large tangential velocity fluctuations due to the random convective fluid motion with coherence across many scale heights. Fig. 5.12 shows the radial and tangential components of the fluid velocity for equatorial ($z = 0$, $\theta = \pi/2$) slices through our `Athena++` models, as well as the density structure. The large radial velocity plumes carry material out beyond $R_{\rm phot}$ (the dotted lines). As the fluid becomes optically thin, the temperature plummets and the pressure scale height drops, and the very large convective plumes fragment into smaller bubbles of surface

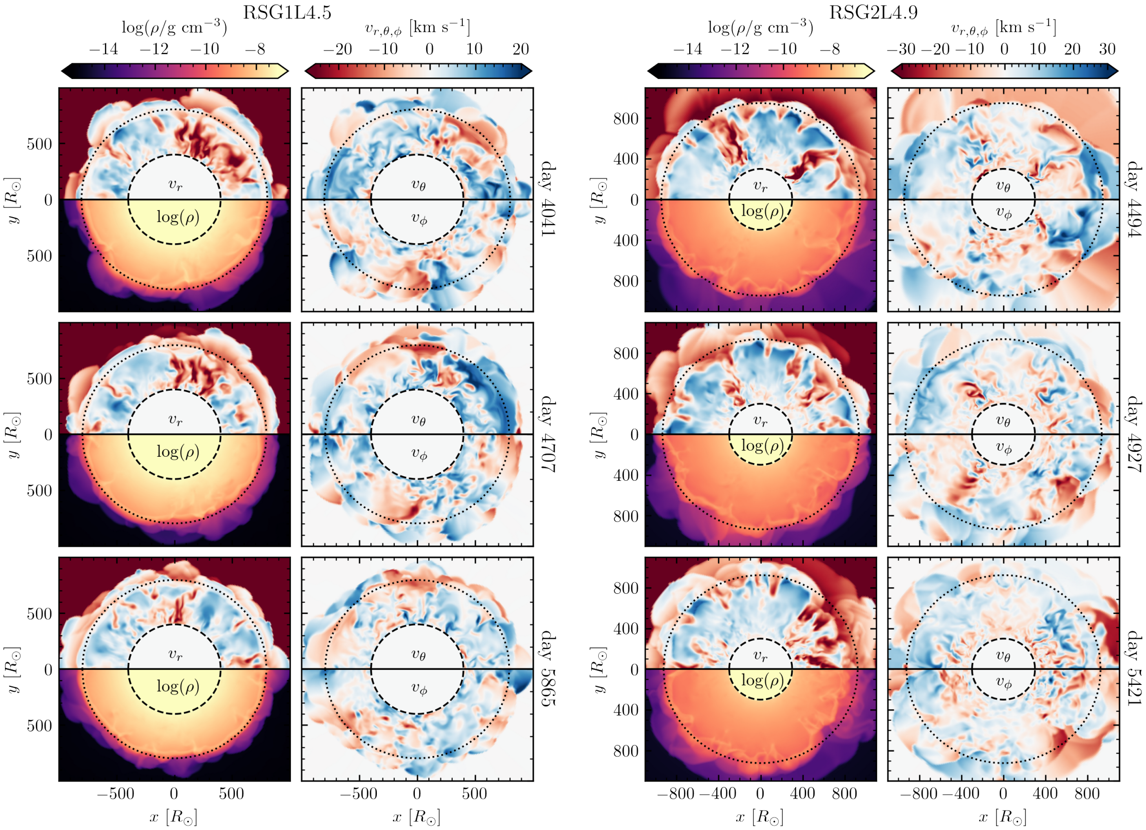

Figure 5.12: Equatorial ($\theta = \pi/2, z = 0$) slices for our RSG1L4.5 (left 6 panels) and RSG2L4.9 (right 6 panels) models at different simulation times. At each time for each model, the left panel shows radial velocity (red/blue colors) and density (orange/purple colors) is beneath. The right panel shows polar tangential velocity (v_θ) and azimuthal velocity (v_ϕ) is beneath. The simulation domain is from $\phi = 0$ to π; thus the y-axis is reflected in the lower half of each panel as indicated by axis labels. With $\theta = 0$ along the $+z$ axis and $\phi = 0$ along the $+x$ axis, $v_\theta > 0$ indicates material flowing into the page, and $v_\phi > 0$ indicates material flowing clockwise around the page (due to the inverted y-axis). The dashed line indicates the simulation inner boundary and the dotted line denotes the 1D photosphere.

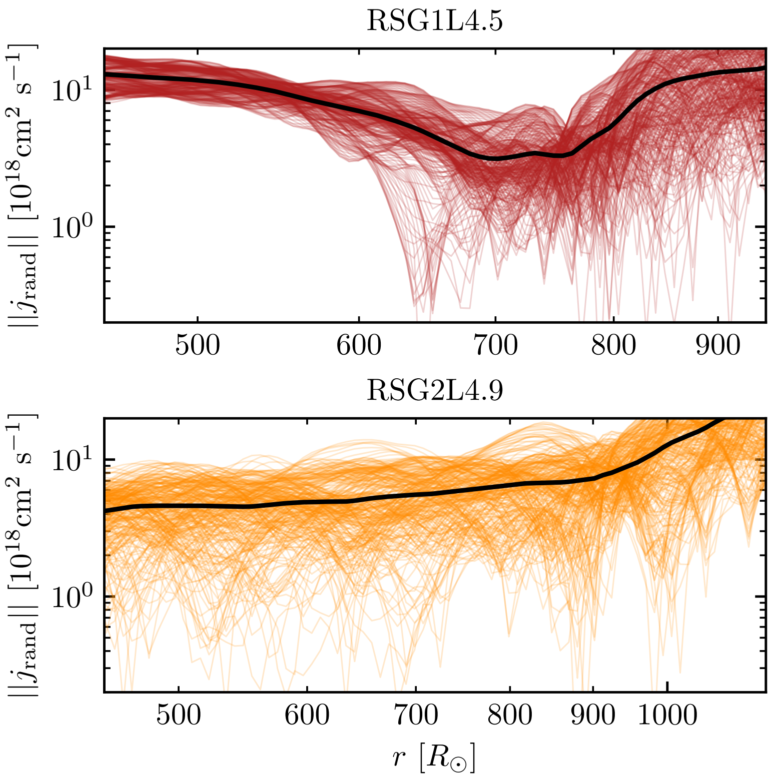

Figure 5.13: Specific angular momentum profiles at different snapshots (thin colored lines), compared to the time-average (solid black lines), for our RSG1L4.5 (red, upper panel) and RSG2L4.9 models (orange, lower panel).

convection. This is especially apparent in the more luminous RSG2L4.9 model (right 6 panels). Additionally, there is some outward-moving high-density material evident at large radii. We will discuss this material in greater detail in §5.3.4. The velocities in r, θ, and ϕ are comparable, with values of tens of km/s. The tangential flows (v_θ and v_ϕ) exhibit smaller-scale structures at smaller radii, in agreement with the results of Antoni & Quataert (2022).

Although the net angular momentum in the envelope is nearly zero, these tangential velocity fluctuations result in finite specific angular momentum $j_{\rm rand}$ at a given radius at any given time. The magnitude (denoted $||\cdots||$) of the mass-weighted average of the random specific angular momentum profiles, equivalent to $||j_{\rm rand}|| = ||\langle\rho\boldsymbol{v}\times\boldsymbol{r}\rangle/\langle\rho\rangle||$, is shown in Fig. 5.13. As in Fig. 5.9, faint colored lines correspond to individual snapshots in our models, and the solid black line indicates the time-average. In agreement with Antoni & Quataert (2022), these simulations exhibit relatively flat specific angular momentum profiles, pointing to the non-local coherent nature of the convective plumes. Due to the high ~ 10 km/s tangential velocities and the fact that our simulation domain emphasizes large radii ($r > 400R_\odot$), we find specific angular momenta of $10^{18} - 2\times10^{19}\mathrm{cm}^2/\mathrm{s}$ throughout our simulation domain. Transforming to a local rotational velocity $\omega_{\rm rot} = ||j_{\rm rand}||/r^2$, this corresponds to a range of $\omega_{\rm rot}$, declining from $\approx 10^{-3}$ rad/day to 10^{-4} rad/day before rising outside $R_{\rm phot}$ in RSG1L4.5, and a flatter, slightly declining time-averaged profile around a few $\times10^{-3}$ rad/day in RSG2L4.9 with the scatter between snapshots ranging from a few times 10^{-5} to 8×10^{-4} rad/day. These values are slightly larger than those reported by Antoni & Quataert (2022), likely owing to the larger convective velocities present in our simulations.[4] Following Quataert et al. (2019), we should reduce our estimate by the expected scaling for the larger number of eddies available in a 4π steradian simulation, which would then be a factor of $(\Omega/4\pi)^{1/2} \approx 0.6\times$ smaller. This modifies our values to a few$\times10^{17} - 10^{19}$ cm^2/s, which are closer to those found by Antoni & Quataert (2022).

---

[4] Antoni & Quataert (2022) reported values for volume-averaged specific angular momentum $||\langle\boldsymbol{v}\times\boldsymbol{r}\rangle||$, which are nearly equivalent to the mass-weighted average in their region of interest where $r < \frac{5}{6}R_{\rm phot}$. At large radii, the mass-weighted average, equal to the total angular momentum in a shell divided by the total mass of the shell, favors the denser turbulent plumes rather than the high-volume low-density background, leading to larger values of $||j_{\rm rand}||$. However this effect is not so dramatic that reporting the volume-weighted average would account for the apparent difference.

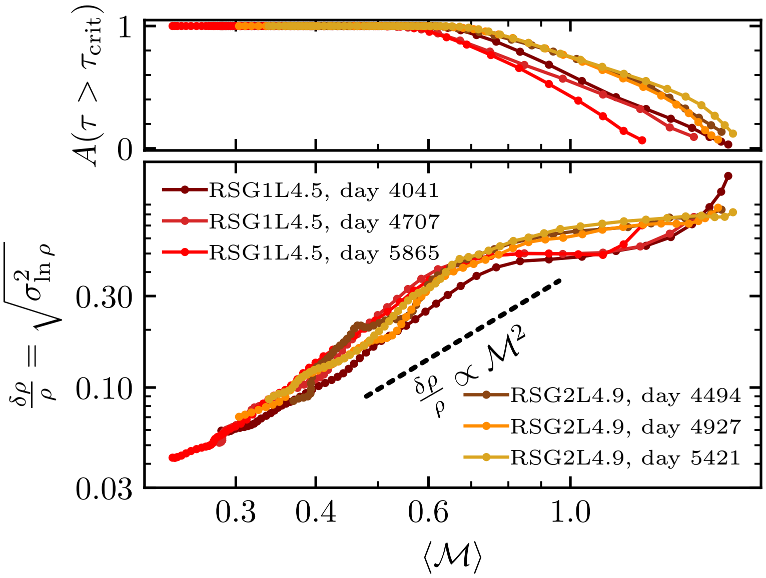

Figure 5.14: Characteristic density fluctuations versus the (volume-weighted) average turbulent mach number for the 6 model snapshots shown in Fig. 5.12. Each point corresponds to the averaged value in each radial shell. The upper panel shows the area fraction of the star at each location with $\tau < \tau_{\rm crit}$ along a radial line of sight. Where $A(\tau > \tau_{\rm crit}) = 1$ we expect the flow to follow the $\delta\rho/\rho \propto \mathcal{M}^2$ scaling, indicated by the black dashed line.

5.3.3 Nature of 3D Convective Structure

In a clumpy or turbulent medium, density fluctuations are often characterized by $\sigma^2_\rho = \frac{\langle\rho^2\rangle}{\langle\rho\rangle^2}$ (see, e.g. Owocki & Sundqvist, 2018, in the context of stellar winds). For a log-normal density distribution typical of convective flows, this is related to the characteristic density fluctuations by $(\delta\rho/\rho)^2 = \sigma^2_{\ln\rho} = \ln\left(\frac{\langle\rho^2\rangle}{\langle\rho\rangle^2}\right)$ (Schultz et al., 2020). Locally, the buoyant acceleration felt by a perturbed fluid element with density $\rho+\delta\rho$ will be related to gravity as $a \approx (\delta\rho/\rho)g$. The perturbation will approximately traverse a scale height (or mixing length) in time t with velocity $v \sim a\ t \sim (\delta\rho/\rho)(H/v)g$. Thus $v^2 \sim gH(\delta\rho/\rho)$, or $\delta\rho/\rho \propto \mathcal{M}^2$, where $\mathcal{M} = v/c_{\rm s}$ is the Mach number. Fig. 5.14 shows the characteristic density fluctuations $\delta\rho/\rho = \sqrt{\sigma^2_{\ln\rho}}$ versus the average Mach number in each spherical shell for $450R_\odot < r < R_{\rm phot}$ using the snapshots shown in Fig. 5.12. The area fraction of the star where the optical depth along a radial line of sight is greater than the angle-averaged $\tau_{\rm crit}$, $A(\tau > \tau_{\rm crit})$, is also shown. Where $A(\tau > \tau_{\rm crit})$ is large, the fluid in both models follows closely with the expected $\delta\rho/\rho \propto \mathcal{M}^2$ scaling. As $A(\tau > \tau_{\rm crit})$ decreases and convection no longer dominates the energy transport everywhere, the scaling flattens and the density fluctuations begin to saturate. Other snapshots exhibit the same behavior in both models.

Other stellar properties also exhibit large fluctuations at a given radius, particularly in the outer stellar layers, where the transition to radiation-dominated energy transport does not happen at one single radial location. Fig. 5.15 shows radial profiles of the density, gas temperature, $P_{\rm rad}/P_{\rm gas}$ ratio, and opacity for characteristic snapshots of RSG1L4.5 and RSG2L4.9 (day 4707 and 4927, respectively), with solid black lines showing the volume-averaged radial profiles and color indicating the scatter. The density, which falls like $1/r^2$ in the nearly-adiabatic interior, exhibits variations over 2-3 orders of magnitude near $R_{\rm phot}$, with an extended atmosphere which is absent in 1D models (compare to the cyan line in the upper left panel).

The ratio of radiation to gas pressure is also significant, with $\langle P_{\rm rad}/P_{\rm gas}\rangle = 0.15$ at $r = 450R_\odot$ in the RSG1L4.5 model, and $\langle P_{\rm rad}/P_{\rm gas}\rangle = 0.48$ at $r = 450R_\odot$ in RSG2L4.9 owing to the larger luminosity and lower density within the envelope. Moreover, rather than a smooth transition from the H opacity peak to electron scattering, the temperature

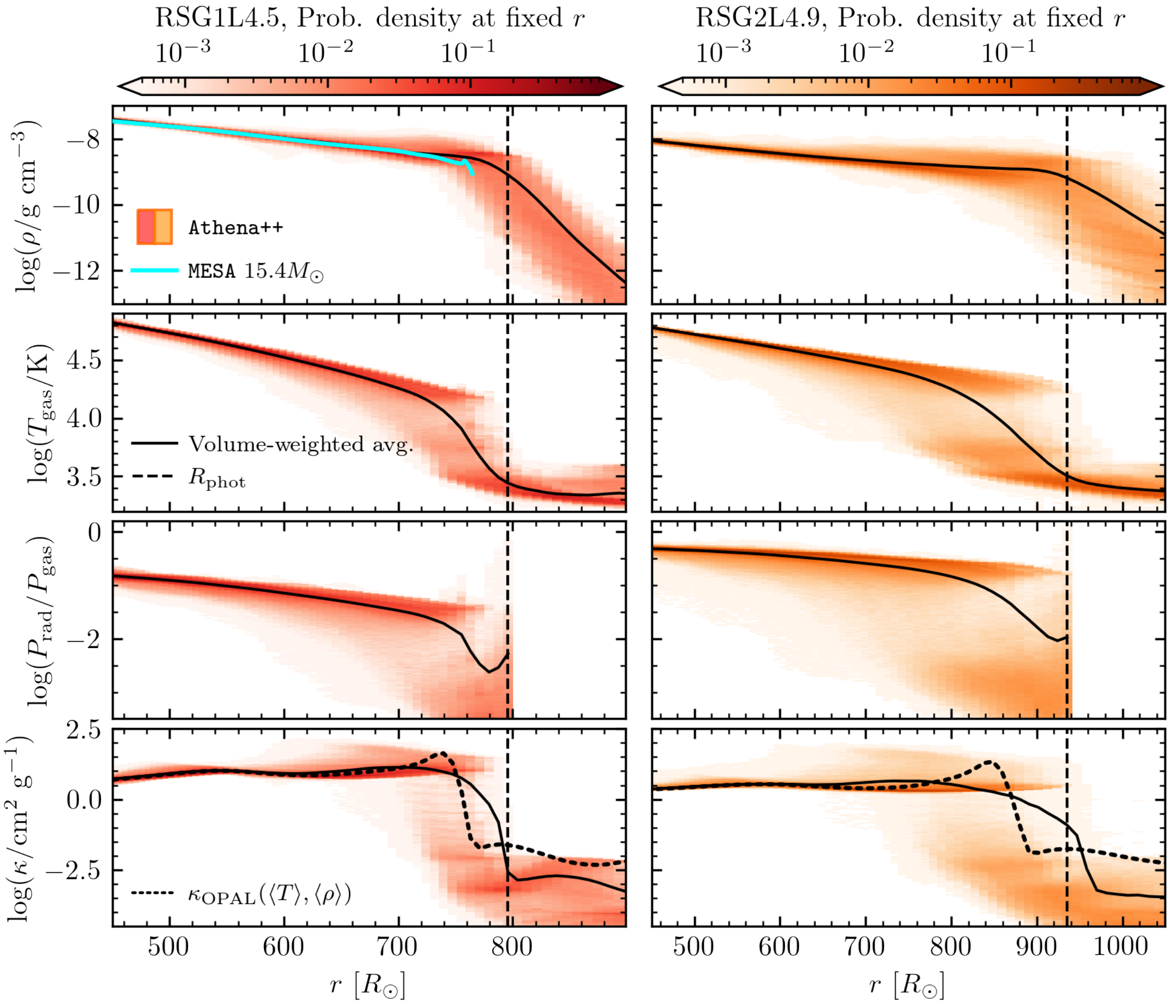

Figure 5.15: Top to bottom: Density, temperature, $P_{\rm rad}/P_{\rm gas}$ ratio, and opacity for our RSG1L4.5 model at day 4707 (red, left panels) and our RSG2L4.9 model at day 4927 (orange, right panels). Color saturation indicates the volume-weighted probability of finding a fluid element at a given $(\rho, T, H/r, P_{\rm rad}/P_{\rm gas}, \kappa)$ at each radial coordinate, and solid black lines give the volume-weighted averages of each (non-log) quantity $(\langle\rho\rangle, \langle T\rangle, \langle H/r\rangle, \langle P_{\rm rad}/P_{\rm gas}\rangle, \langle\kappa\rangle)$. The vertical black dashed line is $R_{\rm phot}$. As $P_{\rm rad}$ is not defined in the free-streaming regime, the ratio $P_{\rm rad}/P_{\rm gas}$ is only shown for $r \leq R_{\rm phot}$. The κ panels (bottom) show both the volume-averaged opacity $\log(\langle\kappa\rangle)$ reported by `Athena++` (solid lines), and the recovered OPAL opacity (dotted lines) from the volume-averaged T and ρ profiles. For reference, the cyan line in the upper left panel shows the density profile of the fiducial `MESA` model (green line in the left panels of Fig. 5.2).

and opacity display bimodal behavior in the $\approx 100 - 200 R_\odot$ region beneath $R_{\rm phot}$. This bimodality is not seen in the ρ profile. Near and even within the 1D photosphere, at some angular locations outer convective plumes exhibit large opacities, whereas other angular locations are dominated by cool material beyond the H opacity peak. Due to the dramatic 4-order-of-magnitude differences in opacity of different material at fixed radius, a linear volume-average of the opacity, given by the black line in the bottom panels, will necessarily favor the high-opacity material. Most notably, the opacity above which L locally exceeds $L_{\rm Edd}$, $\kappa_{\rm Edd} = 4\pi G c m / L_{\rm surf}$, is $\kappa_{\rm Edd} \approx 6$ cm^2/g for RSG1L4.5 and $\kappa_{\rm Edd} \approx 2$ cm^2/g for RSG2L4.9. In the bimodal transitionary region, a large fraction of the material has $\kappa > \kappa_{\rm Edd}$! Moreover, the presence of bimodal temperature and opacity distributions in this transitionary region causes a smearing out of the H-opacity peak, so the H opacity cliff, predicted by OPAL using the volume-averaged ρ and T profiles, is less steep in the 3D simulation.

This transitionary region corresponds to the place where $A(\tau > \tau_{\rm crit})$ goes from 1 to 0 and the turbulent motions deviate from classical convection. We now turn to exploring the fundamentally 3D properties of this convection in the RSG regime.

5.3.4 Transition to Radiation-Dominated Energy Transport

In classical MLT, a flow of fluid parcels, or "bubbles," approximately maintain their entropy and carry heat out as they rise with convective velocity v_c over a mixing length ℓ (See Ludwig et al. 1999 Appendix A for a review). As hot bubbles rise, there is a temperature contrast between the bubble and the surroundings, and on sufficiently long timescales, a rising convective plume loses its heat via diffusion at a rate $L_{\mathrm{bubble}} \approx f 4\pi \ell^2 c P_{\mathrm{rad}}/\tau_{\mathrm{b}}$, where τ_{b} is the optical depth of the bubble, and f depends on the geometry of the bubble. The ratio of the heat content of the bubble to the heat lost as the bubble rises over distance ℓ is given by γ, the convective efficiency factor (see, e.g. Henyey et al., 1965; Cox & Giuli, 1968; Ludwig et al., 1999; Kippenhahn et al., 2013). In a radiation-pressure-dominated plasma ($P_{\mathrm{rad}} \gg P_{\mathrm{gas}}$), $\gamma = (v_c \tau_{\mathrm{b}})/(cf)$, and in a gas-pressure-dominated regime $\gamma = [(P_{\mathrm{gas}}/P_{\mathrm{rad}})\tau_{\mathrm{b}} v_c]/(2fc)$, as a parcel needs to evacuate the radiation field $\sim P_{\mathrm{rad}}/P_{\mathrm{gas}}$ times in order to lose its thermal content. In the radiation-dominated regime then $\tau_{\mathrm{crit}} = c/v_c$, and in the gas-dominated regime $\tau_{\mathrm{crit}} = (P_{\mathrm{rad}} c)/(P_{\mathrm{gas}} v_c)$. Up to a geometric prefactor, where $\tau_{\mathrm{b}} \sim \tau$, the efficiency γ thus decreases with decreasing $\tau/\tau_{\mathrm{crit}}$. In both regimes, where $\tau < \tau_{\mathrm{crit}}$, a bubble radiates a significant portion of its heat as it rises.

In solar-like convection, and in evolved lower-mass stars, the transition through $\tau = \tau_{\mathrm{crit}}$ is at low enough optical depth, $\tau \sim$ a few, that it can be studied in detailed, plane parallel RHD conputations (e.g. Trampedach et al., 2013, 2014a,b; Magic et al., 2013a,b, 2015; Chiavassa et al., 2018a; Sonoi et al., 2019), and incorporated into 1D stellar models via a tabulated boundary condition (e.g. Trampedach et al., 2014a; Salaris & Cassisi, 2015; Magic, 2016; Mosumgaard et al., 2018; Spada et al., 2021). However, in our spherical-polar near-super-Eddington RSG models, the large density fluctuations in the global convective plumes discussed in the previous section extend out into the $\tau \leq \tau_{\mathrm{crit}}$

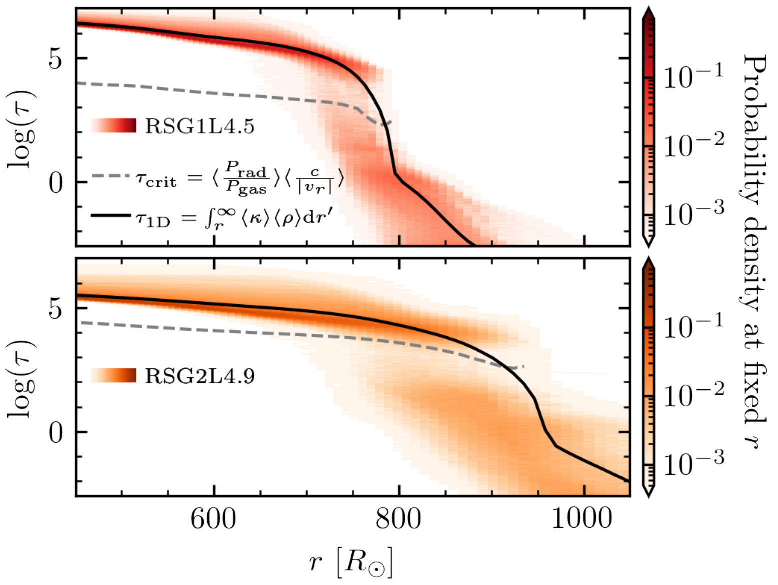

Figure 5.16: Optical depth τ in characteristic snapshots of our RSG1L4.5 (day 4707; red, upper panel) and RSG2L4.9 (day 4927; orange, lower panel) models. Color saturation indicates the volume-weighted probability of finding a fluid element at each radial coordinate with a given τ, calculated along radial lines of sight. Optical depth $\tau_{\rm 1D}$, integrating the volume-averaged opacity and volume-averaged density, is given by the black line. The grey dashed line indicates the average $\tau_{\rm crit}$ at each radius (truncated outside $r = R_{\rm phot}$); near the outer layers of the star, most material is either significantly above or below $\tau_{\rm crit}$, with little material with $\tau \approx \tau_{\rm crit}$.

region, and behave somewhat differently.

Fig. 5.16 compares the optical depth profile integrated along radial lines of sight in our 3D `Athena++` simulations to the critical optical depth $\tau_{\rm crit}$ where we use the amplitude of the radial velocity $|v_r| = \sqrt{v_r^2}$ as our proxy for v_c. Due to the bimodal opacity distribution of material above and below H-recombination, at a given radius near where $\tau_{\rm 1D} = \tau_{\rm crit}$, there is very little material with τ near $\tau_{\rm crit}$. Rather, most of the fluid has $\tau \gg \tau_{\rm crit}$ by over an order of magnitude, or $\tau \ll \tau_{\rm crit}$ by more than an order of magnitude. This is yet another signature of the large-scale plume structure; within a given plume, the convective velocities are set nonlocally, and except at interfaces between plumes there is little opportunity for radiative losses as fluid interacts primarily within the same plume. Comparing to the same snapshots in Fig. 5.11, while the entropy profiles begin to decline due to superadiabatic convection even where $\tau > \tau_{\rm crit}$ (especially in the more luminous RSG2L4.9 model), the entropy profiles decline significantly in the region where some material has $\tau < \tau_{\rm crit}$, due to the plumes losing heat via diffusion and, where $\tau \lesssim 1$, non-local radiative losses.

At optical depths with radiation-dominated energy transport where $\tau < \tau_{\rm crit}$, but still $\tau > 1$, radiation forces may significantly impact fluid motion at high $L \sim L_{\rm Edd}$. In our simulations, we observe a change in the dynamics between regions of high and low $\tau/\tau_{\rm crit}$. This change can be seen in Fig. 5.17, which shows the area fraction of material with $\tau < \tau_{\rm crit}$, compared to correlations between the radial velocity and the density, opacity, and entropy of the fluid, defined by

$$\mathrm{corr}(x,y) = \frac{\sum\left(x_i - \langle x\rangle\right)\left(y_i - \langle y\rangle\right)}{\sqrt{\sum\left(x_i - \langle x\rangle\right)^2 \sum\left(y_i - \langle y\rangle\right)^2}} \tag{5.10}$$

and the sum is taken over all zones (subscript i) in each radial shell. Where $A(\tau < \tau_{\rm crit}) = 0$, the density and opacity are anti-correlated with the radial velocity, and the entropy is positively correlated with the radial velocity (where $+v_r$ is defined as moving outwards). This is as expected for typical MLT-like convection; the material that sinks is denser, lower-entropy (colder), and more opaque material than the surrounding medium. However, for the outer radii where $\tau < \tau_{\rm crit}$, the correlation switches and cold (low-entropy), opaque, dense regions rise! The shaded area indicates radii where the fluid

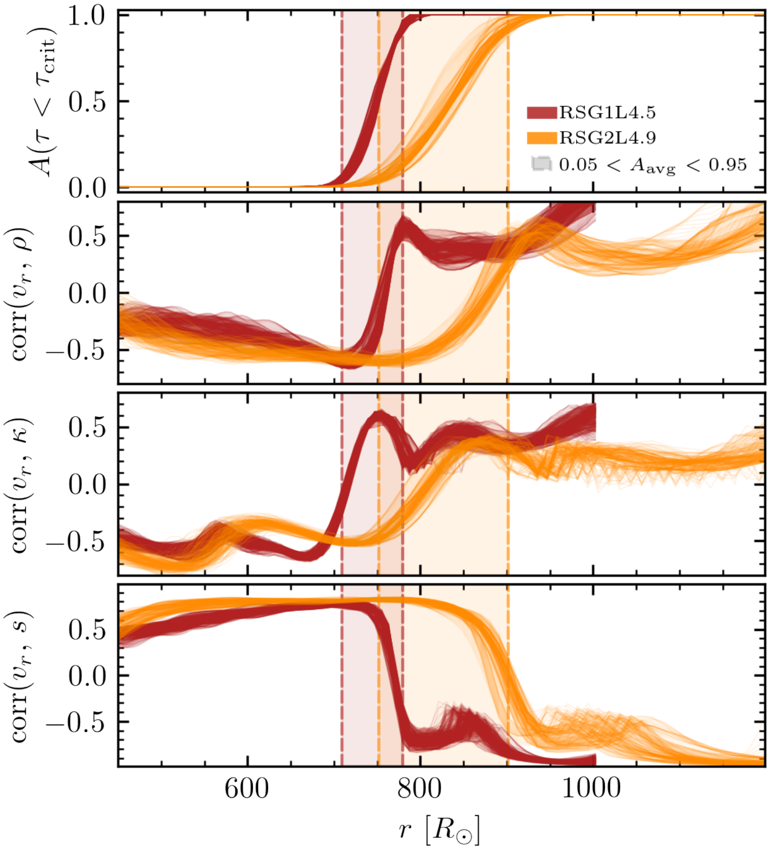

Figure 5.17: Fraction of the solid angle where $\tau < \tau_{\rm crit}$ along a radial line of sight (top panel), as well as the correlations of radial velocity with the density (second panel), opacity (third panel), and entropy (bottom panel). Colored lines show $\approx$ 350 total snapshots starting from day 4000 in RSG1L4.5 and day 4500 in RSG2L4.9, until the end of the simulations. The shaded area indicates radii where the time-average of $A(\tau < \tau_{\rm crit})$ is between 5% and 95%. The RSG1L4.5 data are truncated at $r = 1000 R_\odot$, where the density approaches the density floor.

shows a mix of $\tau > \tau_{\rm crit}$ and $\tau < \tau_{\rm crit}$ material, quantified by where the time-average of $A(\tau < \tau_{\rm crit})$ is between 5% and 95%, and it also captures the region in the star where the correlations invert. This inverted correlation is also characteristic of surface turbulence driven by the Fe opacity peak in younger massive stars (Schultz et al., in prep). In these highly luminous stars, L can exceed $L_{\rm Edd}$ at the $\tau = \tau_{\rm crit}$ location due to the presence of opacity peaks, and further analysis is required to understand what drives these near-surface dynamics. Because the nature the RHD turbulence changes where $\tau < \tau_{\rm crit}$, we thus presume for now that $\tau \approx \tau_{\rm crit}$ is an outer boundary where MLT treatments may cease to be appropriate in the RSG regime.

Moreover, the observable photosphere around $R_{\rm phot}$ is in this lossy, inverted-correlation, turbulent-pressure-dominated region! The convective motions here give rise to luminosity variations on timescales comparable to the timescales of the global convection cells. Fig. 5.18 shows the lightcurves of the last ≈2000 days of our simulations, determined at the simulation outer boundary as $L(t) = \frac{4\pi}{\Omega_{\rm sim}} \int r^2 F_r(t) {\rm d}\Omega$, where $\Omega_{\rm sim} = \int_{\theta=\frac{\pi}{4}}^{\frac{3\pi}{4}} \int_{\phi=0}^{\pi} {\rm d}(\cos\theta){\rm d}\phi$ is the solid-angle of our simulation domain. Fitting a second-order polynomial to the lightcurves[5] and subtracting $L(t) - L_{\rm poly}(t)$, we compute the time-weighted variance as $\sigma_L^2 = \sum [L(t) - L_{\rm poly}(t)]^2 {\rm d}t / \sum {\rm d}t$, and the fluctuation amplitude as $\max[L(t) - L_{\rm poly}(t)] - \min[L(t) - L_{\rm poly}(t)]$. The lightcurves beyond day 4000 exhibit ≈ 3% mean luminosity fluctuations, with $\sqrt{\sigma_L^2} = 0.89 \times 10^3 L_\odot$ in RSG1L4.5, and $\sqrt{\sigma_L^2} = 1.9 \times 10^3 L_\odot$ in RSG2L4.9. Fluctuation amplitudes are ≈10%: $3.6 \times 10^3 L_\odot$ in RSG1L4.5 and $8.6 \times 10^3 L_\odot$ in RSG2L4.9. The peak-to-peak fluctuations in the lightcurves

---

[5] in python, using `numpy.polyfit`

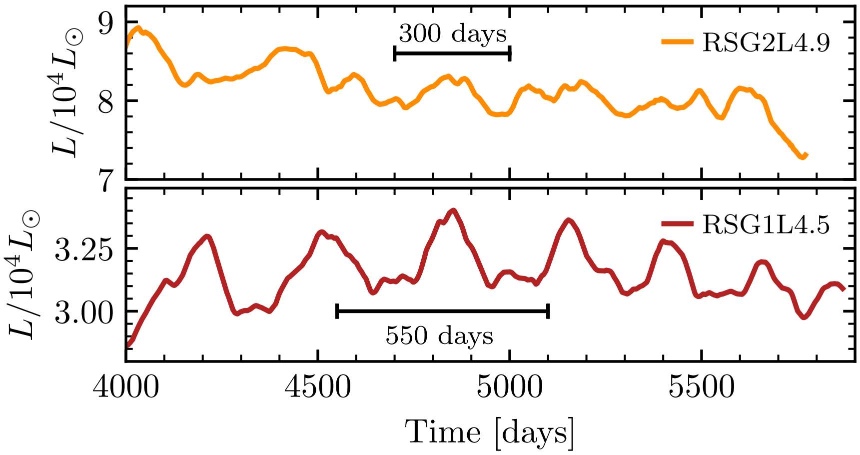

Figure 5.18: Lightcurves starting at day 4000 for both simulation runs. The RSG1L4.5 lightcurve is shown red on the lower panel and RSG2L4.9 in orange on the upper panel. Characteristic velocity decorrelation times for each model are indicated on the figure.

are irregular in time, and for RSG2L4.9 a single dominant period could not be found in the power spectrum. This is likely due to the stochastic nature of the convective fluctuations. For the de-trended RSG1L4.5 power spectrum calculated from day 4500 onward, there is some excess power centered around 310 days/cycle with a 70 day spread resembling quasi-periodic oscillations with a wide window function. This flattens out when considering the lightcurve after day 4000, and disappears when considering the lightcurve from much earlier than that. We discuss briefly in the Conclusions (§5.5) how this variability compares to observations.

5.3.5 Caveats of the 3D models

There are a few caveats which we believe do not impact any of the results presented here, but are worth stating. First, while we include radiation pressure in the stellar interior, the radiation transport module in `Athena++` is not yet compatible with arbitrary gas equations of state. As such, our assumed value of $\mu = 0.645$ entails that the gas pressure may be overestimated by up to a factor of 2 in the outer regions with $T \lesssim 10^4$K, which could help account for the relatively low $T_{\rm eff}$ of our models. However, it should be noted that this region is exactly where turbulent pressure is expected to dominate over thermal pressure, which would be even more significant if the gas pressure were lower than in our models here due to H recombination. Secondly, while these simulations employ full self-consistent coupling between radiation and hydrodynamics, the grey OPAL opacities do not account for frequency-dependent effects. As shown by Chiavassa et al. (2011a), non-grey opacities could lead to a steeper thermal gradient in the optically thin region, with weaker temperature fluctuations, which affects the stellar spectrum and thereby interferometric determinations of stellar radii. The small changes in the mass within the simulation domain are dominated by IB effects and not outflows. The incorporation of non-grey phenomena would also be required to place first-principles constraints on mass loss and other important observable stellar properties. Finally, while our simulation domain captures a very large fraction of the $\Omega = 2\pi$ hemisphere, the relatively few convective plumes suggest that a full $\Omega = 4\pi$ simulation might yield more accurate cancellation of random angular momenta than our estimate, and may have an impact on the RSG lightcurve, which shows variability consistent with these stochastic convective fluctuations.

5.4 Implications for 1D calculations

Computational RHD models of convection enable tests of MLT assumptions, possible calibrations, and incorporation into 1D models. A fundamental set of early 2D RHD simulations (Ludwig et al., 1999) calibrated MLT parameters for portions of the low-optical-depth regime in $L \ll L_{\mathrm{Edd}}$ stars, which was followed up with 3D simulations by Sonoi et al. (2019), who do not definitively conclude if any particular convection model gives the best correspondence between 1D and 3D models, but constrain $\alpha \approx 1 - 2$ across a grid of cool giant atmospheres (Red Giants with $T_{\mathrm{eff}} > 4000\mathrm{K}$), in agreement with some observational constraints (e.g. Joyce & Chaboyer, 2018). Other works (e.g. Trampedach et al. 2014b; Magic et al. 2015; Salaris & Cassisi 2015) recovered similar calibrations in similar $L \ll L_{\mathrm{Edd}}$ stars, though as convection becomes more vigorous in stars with higher luminosity and stronger opacity peaks and plumes take up larger and larger fractions of the star, the convective motions, particularly at the stellar surface, can deviate significantly from MLT (see e.g. discussion in Trampedach et al., 2013). We now discuss the implications of our 3D models for 1D calculations, focusing on the region where $\mathrm{corr}(v_r, \rho) < 0$ so convection can be fairly compared to MLT's working hypothesis. Hereafter, we will refer to the location where the $v_r - \rho$ correlation inverts ($\mathrm{corr}(v_r, \rho) = 0$) as the "correlation radius," R_{corr}.

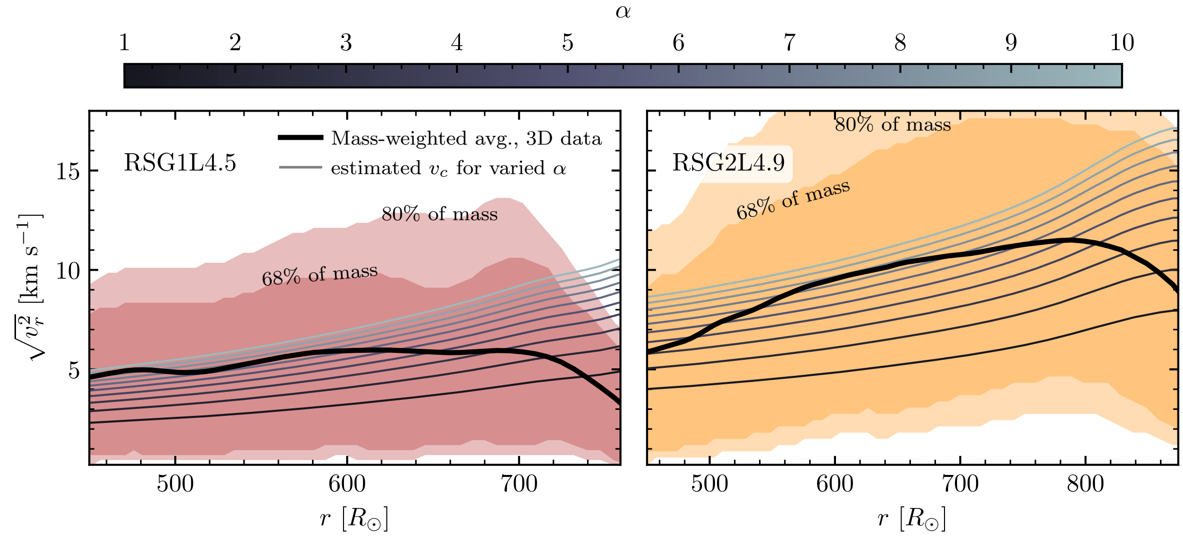

Figure 5.19: Radial fluid velocity magnitudes at characteristic snapshots of our models compared to MLT. The left panel shows RSG1L4.5 at day 4707, and the right panel shows RSG2L4.9 at day 4927. Mass-weighted average velocities are shown as thick black lines, with 68% and 80% of the mass lying within the dark and light shaded regions, respectively. The grey lines indicate the convective velocities predicted from MLT given the volume-averaged temperature and density profiles and the model luminosity, for integer values of $\alpha = 1 - 10$. The plots are truncated where $\mathrm{corr}(v_r, \rho) = 0$, outside of which the turbulent motions do not resemble MLT-like convection.

5.4.1 Comparing Convective Velocities to MLT Expectations

We first check the fluid velocities in our models against expectations from MLT for spherical stellar envelopes with luminosity L, and $\rho(r)$, and $T(r)$ profiles matching averages of our 3D models. Where convection carries most of the flux, as in the RSG interior, $F_{\rm conv} \approx L/4\pi r^2$, and from Eqs (5.2) and (5.3),

$$v_c \approx \left(\frac{\alpha}{4}\right)^{1/3} \left(\frac{L}{4\pi r^2}\frac{PQ}{\rho^2 c_p T}\right)^{1/3}. \tag{5.11}$$

Fig. 5.19 compares this expectation to the fluid motion in our two RSG envelope models as a function of the mixing length parameter α, with the diagnostic velocity taken to be $\sqrt{v_r^2}$ in the 3D models. We represent the 3D data via bands, with 80% of the mass having velocities lying within the light colored regions, and 68% having velocities within the darker colored regions. The mass-weighted averages are indicated by the thick black lines. For clarity, we show here the comparison for individual model snapshots; the time-averaged profiles display similar behavior. The azimuthal and polar velocity profiles are comparable, with $\langle\sqrt{v_\theta^2}\rangle_m \approx \langle\sqrt{v_\phi^2}\rangle_m \approx 5-8$ km/s in RSG1L4.5 and 7-9 km/s in RSG2L4.9, with large scatter ($\gtrsim \pm 5$km/s), and radial motion accounts for $\approx 1/3-1/2$ of the turbulent kinetic energy density. We see good (factor of ≈ 2) agreement between the convective velocities predicted by MLT and the 3D models, and the scatter in convective velocities is much larger than the factor of $10^{1/3}$ introduced by varying α by a factor of 10. In both models, the velocity profile is flatter across a larger radial domain than MLT would predict for a fixed α. We speculate that this can be attributed to the nonlocal, large-scale nature of the plumes, as the velocity profile is set by the motion of a mixture of plumes which do not change significantly over the simulation domain; this is also noted in, e.g., Brun & Palacios (2009) in 3D simulations of RGB stars.

5.4.2 Calibration of Mixing Length Parameters in the Absence of P_{turb}

Convective efficiency is important in determining the stellar radius as discussed in detail in §5.1; therefore it is valuable to have a first-principles calibration of mixing length parameters, especially α, within the RSG regime motivated by 3D models. Because the nature of the turbulent energy and momentum transport changes outside R_{corr}, we treat R_{corr} as an outer boundary beyond which MLT treatments cannot be calibrated, and perhaps cease to be appropriate, in the high-luminosity RSG regime.

Most 1D stellar-evolutionary models do not account for turbulent pressure, and when included, it is a challenge (see discussion in Trampedach et al. 2014b), so we first explore the case where $P = P_{\text{therm}} = P_{\text{rad}} + P_{\text{gas}}$. We generate a 1D model from the 3D simulations by finding the time-averaged, volume-averaged radial density and temperature profiles from each 3D simulation run ($\rho_{\text{1D}}(r)$ and $T_{\text{1D}}(r)$, respectively). We choose volume-averages along surfaces of constant gravity (radial coordinates) due to the loosely-bound nature of the envelope, though where $r < R_{\text{corr}}$ different averages do not significantly affect our results. We calculate κ from these profiles using the OPAL tables. The total luminosity is taken to be the time-averaged luminosity in the outermost zone $L = L_{\text{surf}}$, up to the end of the simulation starting from day 4000 in RSG1L4.5 and from day 4500

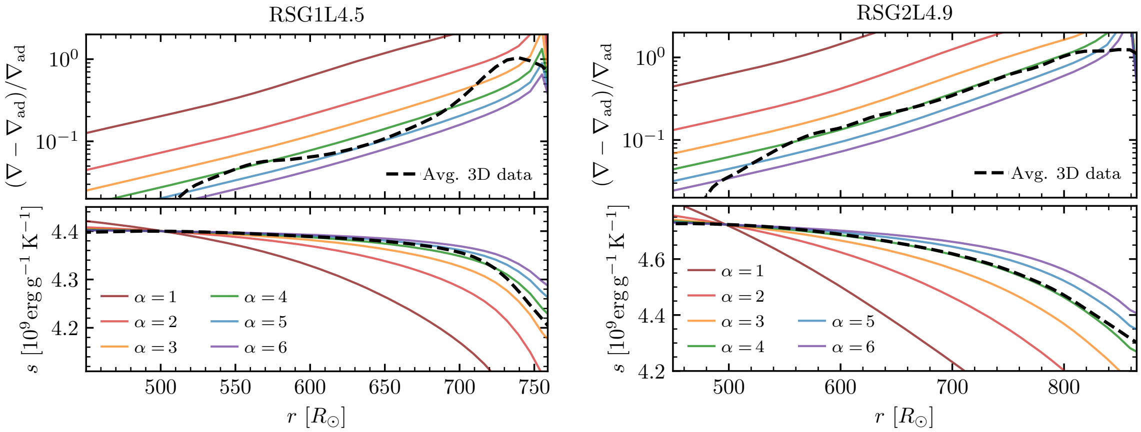

Figure 5.20: Comparison of superadiabaticity (upper panels) and specific entropy (lower panels) derived from our 3D models (black dashed lines) and from MLT (solid colored lines), for RSG1L4.5 (left) and RSG2L4.9 (right) when P_{turb} is neglected. All values shown are derived from the time-averaged, shellular (volume-weighted) averaged density and temperature profiles, as well as the time-averaged luminosity at the simulation outer boundary, beyond day 4000 in RSG1L4.5 and beyond day 4500 in RSG2L4.9.

in RSG2L4.9. We assume an EOS of ideal gas + radiation with $\mu = 0.645$, as in our 3D model, which is appropriate for $r < R_{\mathrm{corr}}$ as $T \gtrsim 10^4$K. We then solve the Henyey et al. (1965) MLT equations assuming $y = 3/4\pi^2$, and consider only material inside R_{corr} (where $\tau > \tau_{\mathrm{crit}} \gg 1$) for different values of α (see Appendix C for more specific details).

The upper panels of Fig. 5.20 show the comparison between the superadiabaticity, expressed as $(\nabla - \nabla_{\mathrm{ad}})/\nabla_{\mathrm{ad}}$, using ∇ predicted by MLT and ∇ derived directly from the averaged 3D data. The x-axis limits are $450R_\odot$ and R_{corr}, respectively. We see significant deviations between ∇ from ∇_{ad}, with nearly-adiabatic behavior in the interior and increasing superadiabaticity outward. The lower panels show entropy profiles, which are often used to calibrate MLT parameters to 3D atmosphere models in more compact, less luminous stellar environments (e.g. Trampedach et al., 2014b; Magic et al., 2015; Magic, 2016; Sonoi et al., 2019). For our averaged 3D data, we calculate s including radiation and gas entropy, $s = \frac{k_{\rm B}}{\mu m_p} \ln\left(T^{3/2}/\rho\right) + \frac{4}{3} a_r T^3/\rho$, where T is in K and ρ is in g/cm^3, and for MLT we integrate $\mathrm{d}s = c_P \, \mathrm{d}\ln T \, [1 - \nabla_{\rm ad}/\nabla]$ using ∇ given by MLT, connecting to the nearly-adiabatic $r = 500 R_\odot$ location to ensure agreement in the additive constant. Both models display nice agreement with $\alpha = 4$ in the interior. At larger radii, the RSG1L4.5 model (left panels) exhibits greater superadiabaticity than implied by $\alpha = 4$, in better agreement with $\alpha = 2 - 3$. This contributes to the entropy profile, which falls more steeply than $\alpha = 4$ and approaches the value predicted by $\alpha = 3$ in our region of consideration. The more luminous RSG2L4.9 model (right panels of Fig. 5.20) closely follows the $\alpha = 4$ predictions throughout most of the domain of interest, with generally excellent agreement for the entropy profile, becoming more shallow as r approaches $R_{\rm corr}$.

5.4.3 Estimating $P_{\rm turb}$ in a 1D model and MLT Implications

In a vigorously convective stellar envelope, turbulent pressure can become comparable to the thermal pressure and provide hydrostatic support. A fully self-consistent 1D implementation of turbulent pressure in 1D models remains an open challenge, as the inclusion of turbulent pressure leads to unrealistically steep pressure gradients near convective boundaries, especially near the stellar surface (Trampedach et al., 2014b). In MLT, turbulent pressure can be incorporated by modifying the pressure scale height and the adiabatic temperature gradient. Using the chain rule to include $P_{\rm tot} = P_{\rm turb} + P_{\rm therm}$, the modified adiabatic temperature gradient, $\nabla'_{\rm ad}$, is given by (Henyey et al., 1965),

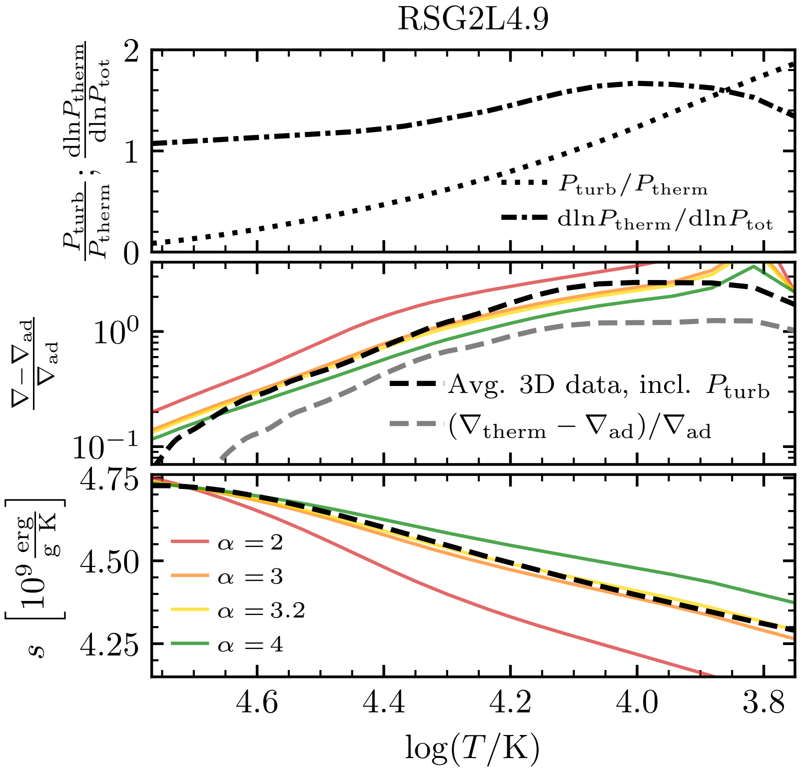

Figure 5.21: Impact of turbulent pressure on mixing length calibration. Comparison of superadiabaticity (middle panel) and entropy (lower panel) are shown, for our averaged 3D RSG2L4.9 model (black dashed lines) and MLT with different α (solid colored lines) as a function of temperature. The upper panel shows $P_{\rm turb}/P_{\rm therm}$ (dotted line) and $\mathrm{d}\ln P_{\rm therm}/\mathrm{d}\ln P_{\rm tot}$ (dash-dot line), which are included in the MLT calculation and in the averaged 3D ∇. The grey dashed line in the middle panel shows $\nabla_{\rm therm}=\mathrm{d}\ln T/\mathrm{d}\ln P_{\rm therm}$ to facilitate direct comparison to Fig. 5.20. All values shown are derived from the time-averaged (beyond day 4500), shellular (volume-weighted) averaged density, temperature, and kinetic energy profiles, as well as the time-averaged luminosity at the simulation outer boundary. The x-axis extends from $r = 450R_\odot$ to $R_{\rm corr} = 865R_\odot$.

$$\nabla'_{\mathrm{ad}} = \left(\frac{\mathrm{d}\ln T}{\mathrm{d}\ln P_{\mathrm{therm}}}\right)_{\mathrm{ad}} \times \frac{\mathrm{d}\ln P_{\mathrm{therm}}}{\mathrm{d}\ln P_{\mathrm{tot}}}. \tag{5.12}$$

The substitution $\nabla_{\mathrm{ad}} \rightarrow \nabla'_{\mathrm{ad}}$ is then made where ∇_{ad} appears in the MLT equations (Henyey et al. 1965; see also our Appendix D) and H is calculated as $P_{\mathrm{tot}}/\rho g$. The lack of a reliable method to estimate P_{turb} inhibits such an incorporation in most 1D MLT implementations. For convenience, definitions of different gradients we used are also summarized in Appendix D.

Quantifying the pressure associated with turbulent kinetic energy densities from 3D RHD models allows us to explore how the 1D gradients are modified for these stars. The nonlocal nature of the convective motions means that the characteristic fluid velocity used in calculating P_{turb} is not simply identified with the velocity parameter in MLT. Therefore, in order to estimate the impact of turbulent pressure on the thermodynamic gradients and recovered values of α, we determine $\mathrm{d}\ln P_{\mathrm{therm}}/\mathrm{d}\ln P_{\mathrm{tot}}$ directly from 1D averages of our 3D models. For this initial exploration, we calculate P_{turb} and thereby $\mathrm{d}\ln P_{\mathrm{therm}}/\mathrm{d}\ln P_{\mathrm{tot}}$ using the time-average of the angle-averaged $P_{\mathrm{turb}} = \langle \rho v_r v_r \rangle$. We then use Henyey et al. (1965)'s formula with turbulent pressure motivated by the 3D data to solve for ∇ at different values of α.

Fig. 5.21 shows the results of this exercise for the RSG2L4.9 model. The upper panel shows the adiabatic correction term ($\mathrm{d}\ln P_{\mathrm{therm}}/\mathrm{d}\ln P_{\mathrm{tot}}$; dash-dot line), as well as the ratio of turbulent pressure to thermal pressure (dotted line). The value of $\nabla = \mathrm{d}\ln T/\mathrm{d}\ln P_{\mathrm{tot}}$ from the averaged 3D data, for which we now include turbulent pressure as $P_{\mathrm{tot}} = P_{\mathrm{therm}} + P_{\mathrm{turb}}$, is shown by the black dashed line in the middle panel. For direct comparison to Fig. 5.20, we compare ∇ here to $\nabla_{\rm ad}$ rather than $\nabla'_{\rm ad}$. To further facilitate direct comparison, the grey dashed line in the middle panel shows the value of $\nabla_{\rm therm} = {\rm d}\ln T/{\rm d}\ln P_{\rm therm}$, which was taken to be equivalent to the true ∇ in §5.4.2 and is equivalent to the dashed black line in the upper right panel of Fig. 5.20. The lower panel shows the entropy, calculated using $\nabla'_{\rm ad}$ and ∇. The black dashed line in the lower panel gives the entropy profile for our 3D-motivated 1D model, which is equivalent to the black dashed line in the lower right panel in Fig. 5.20, as the turbulent pressure terms cancel in the expression for s (i.e. $\nabla'_{\rm ad}/\nabla = \nabla_{\rm ad}/\nabla_{\rm therm}$). For the MLT values, shown by the colored lines, each value of α recovers a larger value of ∇ compared to §5.4.2, but a slightly shallower s profile (as the turbulent pressure correction in $\nabla'_{\rm ad}$ accounts for a greater portion of the $\nabla - \nabla_{\rm ad}$ excess). Therefore, if a 1D stellar evolution code were to include a turbulent pressure correction to MLT using the Henyey et al. (1965) parameters, we would recommend a value of $\alpha = 3.2$ from this model.

5.5 Discussion & Conclusions

We have constructed global 3D radiation hydrodynamical simulations in the RSG regime which include an accurate gravitational potential and radiation pressure in the convective interior for the first time. These simulations span $\approx$70% of the 2π hemisphere and yield predictions for the turbulent structure and dynamics from the middle of the convective envelope out beyond the photosphere. Our incorporation of radiation pressure in optically thick regions has enabled realization of the expected nearly-constant entropy profile and convective-luminosity domination in the convective interior. In agreement with Freytag et al. (2002) and Chiavassa et al. (2009) we find that the convection is dominated by a few large-scale plumes which flow through most of the simulation domain and survive for timescales of $\approx$300 and $\approx$550 days (for RSG1L4.5 and RSG2L4.9, respectively; see Fig. 5.8). When the models reach a convective steady state, RSG1L4.5 has $\log(L/L_{\odot}) \approx 4.5$ and $R_{\rm phot} \approx 800 R_{\odot}$, and RSG2L4.9 has $\log(L/L_{\odot}) \approx 4.9$ and $R_{\rm phot} \approx 900 R_{\odot}$.

Both models display $\approx$10% variation in luminosity owing to the large-scale turbulent surface structure (see Fig. 5.18). Temporal observations (see, e.g. Kiss et al. 2006; Soraisam et al. 2018; Conroy et al. 2018; Chatys et al. 2019; Ren et al. 2019; Soraisam et al. 2020) reveal RSG variability on timescales of a few hundred to thousands of days in a variety of host environments. These signals include both periodic and stochastic behavior, with increasing ubiquity of larger-amplitude fluctuations for brighter stars. In M31, for example, all RSGs brighter than $\log(L/L_{\odot}) > 4.8$ display lightcurve fluctuations with $\Delta m_R > 0.05$ mag, up to around $\Delta m_R \approx 0.4$ (Soraisam et al., 2018). Periodic variability is interpreted as radial pulsations (Stothers, 1969; Stothers & Leung, 1971; Guo & Li, 2002), likely driven by a hydrogen ionization region inside the convective envelope (Heger et al., 1997; Yoon & Cantiello, 2010). The stochastic fluctuations (e.g. Ren & Jiang, 2020) qualitatively agree with our models, and we intend further analysis to compare these convective models directly to observations.

In the outer stellar layers, radiation carries an increasing fraction of the total luminosity as convection becomes lossy. This transition is associated with reaching an optical depth $\tau < \tau_{\rm crit} \approx 100$. Moreover, large density fluctuations and appreciable bimodality in κ and T lead to a range of radii with increasing amounts of material at $\tau < \tau_{\rm crit}$ (see Figs. 5.15,5.16). In the region where τ along some lines of sight falls below $\tau_{\rm crit}$, the correlations of radial velocity with the fluid density, entropy, and opacity fluctuations invert from what is characteristic of convective fluid motions (see Fig. 5.17); indeed the denser, lower-entropy, higher-opacity material rises! These inverse correlations at $A(\tau < \tau_{\rm crit}) < 1$ where L locally exceeds $L_{\rm Edd}$ will not be seen if radiation pressure is not inlcuded. The change in the nature of convective motions in the outermost stellar layers of these highly luminous RSGs also prohibits a comparison to MLT treatments. Hence, we define the radius where these correlations invert as $R_{\rm corr}$, taking it as an outer boundary where MLT-like treatments cease to be appropriate.

Inside $R_{\rm corr}$, where MLT is applicable, the velocity profiles are flatter than MLT-like convection due to the nonlocal, large-scale convective plumes, but display good order-of-magnitude agreement (see Fig. 5.19). By comparing entropy profiles and superadiabatic gradients inside $R < R_{\rm corr}$, we find from our 3D simulations that the mixing length α appropriate for convection in this regime is $\alpha \approx 3 - 4$ (see Fig. 5.20 for models which neglect pressure from the turbulent motions and Fig. 5.21 which includes an estimate for such a correction). This convective efficiency is more consistent with estimates of larger-than-solar mixing lengths from the HR position of RSG populations (Chun et al., 2018), supernova color evolution (Dessart et al., 2013), and even some 3D treatments of the Sun which compare conventional MLT to other prescriptions for handling the different flux terms (e.g. Porter & Woodward, 2000). Future work of immediate interest will focus on better understanding the nature and implications of the surface turbulence outside of $R_{\rm corr}$. Similar inverted-correlation behavior is also seen in other simulations of luminous stars (e.g. in OB-star envelopes; Schultz et al. (2022)), but not in simulations of solar-like convection (e.g. Stein & Nordlund 1998), and may owe to RHD effects where $\tau_{\rm crit} \gg 1$ and $L \gtrsim L_{\rm Edd}$.

In addition to exhibiting large density fluctuations which increase at large radii, the `Athena++` RSG models display shallower density profiles in their outer stellar halos compared to traditional 1D hydrostatic models, and material near $\tau = 1$ ($\approx$50$-$100$R_\odot$ beyond $R_{\rm corr}$) reaches densities $1-2$ orders of magnitude lower than barren 1D model photospheres. In the eventual explosion of a RSG as a Type IIP Supernova, shock propagation (and therefore the SN emission) may be moderated by these 3D envelopes. Early SN emission (first ≈ 30 days) is sensitive to the outermost $< 0.01 - 0.1 M_\odot$ of material; thus the inverted-correlation surface-turbulent outer halo defines the emitting region for the shock breakout and shock cooling phases of SN evolution. These phases have been studied extensively for 1D hydrostatic models with a well-defined outer radius (e.g., Nakar & Sari 2010; Morozova et al. 2016; Shussman et al. 2016a; Sapir & Waxman 2017; Faran et al. 2019; Kozyreva et al. 2020), but not for fundamentally 3D envelopes. The outer halo of material will also modify the predicted UV shock breakout signatures. The extent to which the 3D envelope properties discussed above may aid in our understanding of early-time Type IIP SN emission is thus an exciting avenue for our future exploration.

Chapter 6

Shock Breakout in 3-Dimensional Red Supergiant Envelopes

The explosion resulting from the core-collapse of a massive ($10M_\odot \lesssim M \lesssim 25M_\odot$) star generates a strong shock, unbinding the hydrogen-rich red supergiant (RSG) envelope. As the shock nears the outer layers, radiation escapes, leading to a hot ($T > 10^5$K), bright flash, known as the "shock breakout" (SBO). For 1D (spherically-symmetric) models with a well-defined outer radius, semi-analytical solutions exist for the shock propagation (e.g. Lasher & Chan, 1979; Matzner & McKee, 1999; Katz et al., 2010), with extensive predictions for the bolometric and optical-UV lightcurves (Nakar & Sari, 2010; Rabinak & Waxman, 2011; Sapir et al., 2011; Katz et al., 2012; Sapir et al., 2013; Shussman et al., 2016a; Sapir & Waxman, 2017; Kozyreva et al., 2020). One important prediction of these 1D models is that the observed SBO duration is set by the light-travel time across the stellar surface, $R/c \lesssim 1$hour, which if measured would provide a direct constraint on the stellar radius, R. This is a crucial measurement, as it would constrain the ejected mass ($M_{\rm ej}$) and explosion energy ($E_{\rm exp}$) when combined with information from the Type IIP Supernova (SN-IIP) lightcurve (Goldberg et al., 2019; Goldberg & Bildsten, 2020).

Observations of SBO from SNe-IIP are presently sparse, with only a few serendipitous detections by NASA's *GALEX* satellite, all of which show durations of > 6 hours (e.g. Schawinski et al., 2008; Gezari et al., 2008, 2010, 2015). This prolonged duration is often attributed to interaction with a dense wind beyond a traditional 1D photosphere (e.g. Gezari et al., 2008; Haynie & Piro, 2021) or by assuming an outer density orders of magnitude lower than traditional 1D models (Schawinski et al., 2008). This prolonged SBO is further corroborated by differences between SNe-IIP seen by *Kepler* (Garnavich et al., 2016) and *TESS* (Vallely et al., 2021; Tinyanont et al., 2022) compared to spherically-symmetric SBO models. In upcoming years, the data are expected to improve dramatically, as future satellites such as *ULTRASAT* (Sagiv et al., 2014; Asif et al., 2021) are poised to capture hundreds of SBO's at high cadence, a number which will grow when combined with data from wide-field X-ray satellites (Bayless et al., 2022).

SBO in realistic 3D RSG envelopes, which exhibit large-scale coherent plumes spanning large fractions of the stellar surface (e.g. Chiavassa et al., 2011b; Goldberg et al., 2022), has not been explored. We show that large-scale, fully convective, intrinsically 3D envelopes yield significant differences in the predicted SBO signal, which has implications for the detectability of these transients, as well as the ability to extract information about the progenitors and explosions from the lightcurves. This work is organized as follows: in §6.1, we discuss our simulation setup and verification. In §6.2, we discuss the shock evolution in a fiducial explosion of one of our models, and in §6.3, we discuss the temperature structure of the 3D SBO and properties of the bolometric lightcurves and present our initial energy scalings of the SBO brightness and duration when the 3D surface is taken into account.

6.1 Setup and Model Properties

We use the 3D radiation hydrodynamic (RHD) simulations of RSG envelope models performed by Goldberg et al. (2022) using `Athena++` (Stone et al., 2020; Jiang, 2021) with $X = 0.6,\ Z = 0.02$ (mean molecular weight $\mu = 0.645$) and opacities from OPAL (Iglesias & Rogers, 1996), described in Chapter 5. Table 6.1 summarizes the properties of these models; we treat RSG1L4.5 as our fiducial model. The stellar photospheric radius R_{phot} is taken where shell-averaged radial profiles of the luminosity $\langle L(r)\rangle$ and radiation temperature $\langle T_r(r)\rangle$ agree, $\langle L(r)\rangle = 4\pi r^2 \sigma_{\mathrm{SB}} \langle T_r(r)\rangle^4$ where σ_{SB} is the Stefan-Boltzmann constant, following Chiavassa et al. (2011b). We use the RHD scheme presented by Jiang (2021) with the same simulation domain as in Goldberg et al. (2022) for each model. This is a spherical polar grid with 120 angles per grid cell for the specific intensities, 128 bins from $\theta = \pi/4 - 3\pi/4$ and 256 bins from $\phi = 0 - \pi$ with periodic θ/ϕ boundary conditions, covering 70.6% of the face-on hemisphere, $\Omega = 1.41\pi$). For RSG1L4.5 (RSG2L4.9) we use 384 (256) bins in radius, for $r = 400 - 22,400 R_\odot (r = 300 - 6,700 R_\odot)$, with $\delta r/r = 0.01$,

Progenitor Model	$R_{\rm IB}/R_\odot$	$R_{\rm out}/R_\odot$	resolution ($r \times \theta \times \phi$)	$m_{\rm IB}/M_\odot$	$R_{\rm phot}/R_\odot$	$\Delta R/R_\odot$
RSG1L4.5*	400	22400	$384 \times 128 \times 256$	12.8	796	80
RSG2L4.9	300	6700	$256 \times 128 \times 256$	10.79	902	200

Table 6.1: Properties of the 3D progenitor models from Goldberg et al. (2022), including inner boundary ($R_{\rm IB}$), outer boundary ($R_{\rm out}$), resolution, mass interior to the simulation domain ($m_{\rm IB}$),
photospheric radius $R_{\rm phot}$, and span of the fluctuations in the expected radius of SBO ΔR (see discussion in §6.2). The simulation domain extends from $\theta = \pi/4 - 3\pi/4$ and $\phi = 0 - \pi$, with $\delta r/r \approx 0.01$. The naming scheme indicates $\log(L/L_\odot)$. The * denotes the model used in our fiducial explosion.

and an outflow outer boundary. No initial perturbations are necessary, as fluctuations in the fluid properties are achieved by the full 3D RHD treatment in the convectively unstable envelope in its convective quasi-steady-state. For more details about the 3D RSG envelope models, see Goldberg et al. (2022).

To simulate the ejection of the 3D RSG envelope, we drive a strong, initially spherical shock through the `Athena++` models, introduced at $R_{\rm IB}$. The required time-dependent inner boundary condition is derived from a 1D hydrodynamic simulation of the shock and ejecta evolution for an appropriately scaled thermal-bomb explosion of a 1D RSG envelope. The 1D explosion is carried out in `MESA` r-15140(Paxton et al., 2011, 2013, 2015, 2018, 2019), with a modified version of the `example_ccsn_IIp` test suite case, adapted to excise the entire He core and deposit energy only in the H-rich envelope. It is run to 10 days past SBO, yielding T, ρ, m, radiative flux $F_{\rm rad}$, and velocity v_r at $R_{\rm IB}$.

When the 1D shock front has just passed $R_{\rm IB}$ (at radius $r_{\rm sh} \approx R_{\rm IB} + 30R_\odot$), we map the post-shock ρ, T, and v to our `Athena++` simulation domain from $R_{\rm IB}$ to $r_{\rm sh}$, leaving the pre-shock 3D envelope above that location unchanged. We then demand that the time-dependent boundary condition for T, ρ, v, m, and $F_{\rm rad}$ at $r = R_{\rm IB}$ in `Athena++` match that of the exploded `MESA` model at the $R_{\rm IB}$ coordinate at each time step thereafter. We discuss this setup and verification in greater detail below, in §6.1.1. For our fiducial RSG1L4.5 explosion, 8×10^{50} erg is deposited into the H-rich envelope, comparable to an $\approx 10^{51}$ erg explosion of the whole star.

6.1.1 Shock Initialization and Verification

We now discuss our `MESA`-motivated `Athena++` inner boundary explosion scheme, and compare spherical explosions on our 3D grid. The spherically symmetric SN shock problem is well-understood in the strong-shock, radiation-dominated limit. Matzner & McKee (1999) provide an analytic expression for the shock velocity at radius r,

$$v_{\rm sh}(r) = A \left(\frac{E_{\rm exp}}{\Delta m}\right)^{1/2} \left[\frac{\Delta m}{\rho_0 r^3}\right]^{0.19}, \tag{6.1}$$

where $E_{\rm exp}$ is the explosion energy, $\rho_0(r)$ is the local pre-shock density, Δm is the mass entrained by the shock, and $A = 0.736$ (Tan et al., 2001). In the radiation-dominated post-shock plasma ($\gamma = 4/3$) the velocity of the fluid just behind the strong shock front is $v_{\rm fast} = 6v_{\rm sh}/7$. The density contrast between the pre- and post-shock material is $\rho_1/\rho_0 = (\gamma+1)/(\gamma-1) = 7$ for $\gamma = 4/3$, where a 1 subscript denotes the post-shock properties and 0 denotes pre-shock properties (Zel'dovich & Raizer, 1967). This expression is valid when radiation is unable to leak out of the shock front ($\tau \gg c/v_{\rm sh}$). Paxton et al. (2018) showed excellent agreement between explosions in `MESA` and these semi-analytic expectations.

In an exploding star, reverse shocks from core boundaries alter the final structure and composition of the inner SN ejecta via the Rayleigh-Taylor Instability (RTI). This is captured in `MESA` via the Duffell (2016) RTI prescription. However, we show below that when studying the propagation of the forward shock through the hydrogen-rich envelope and the properties of the outer ejecta shortly after shock breakout, these effects can safely be ignored. To provide a 1D model which we can import into `Athena++` as a new bottom boundary condition, we excise the entire He core in the `MESA` model, and put a thermal bomb in the innermost $0.2 M_\odot$ of the H-rich envelope to reach a specified total final energy.

As a first verification, we explode the 99em16 progenitor model from Paxton et al. (2018) in `MESA` with the full core-envelope structure included, and then again with a lower explosion energy and the entire He core excised. In both cases, we excise the core with an entropy cut (at 4 kb/baryon for the Fe core and 20 kb/baryon for the He core) before causing the infall to stall (at 400 km for the Fe core and $1 R_\odot$ for the He core) and depositing the explosion energy in the innermost $0.2 M_\odot$ of the ejecta. We then allow the resulting shock to propagate out through the envelope following the `MESA`-r15140 test_suite case `ccsn_IIp` (see Paxton et al. 2018 for discussion).

A comparison of the shock properties from the two `MESA` simulations is shown in Figure 6.1. Snapshots are selected such that the shock fronts are at approximately the same radius. The grey lines show profiles of the 10^{51} erg full-star explosion, while the thin colored lines show the equivalent 8.0×10^{50} erg shock in the H-envelope. We see good

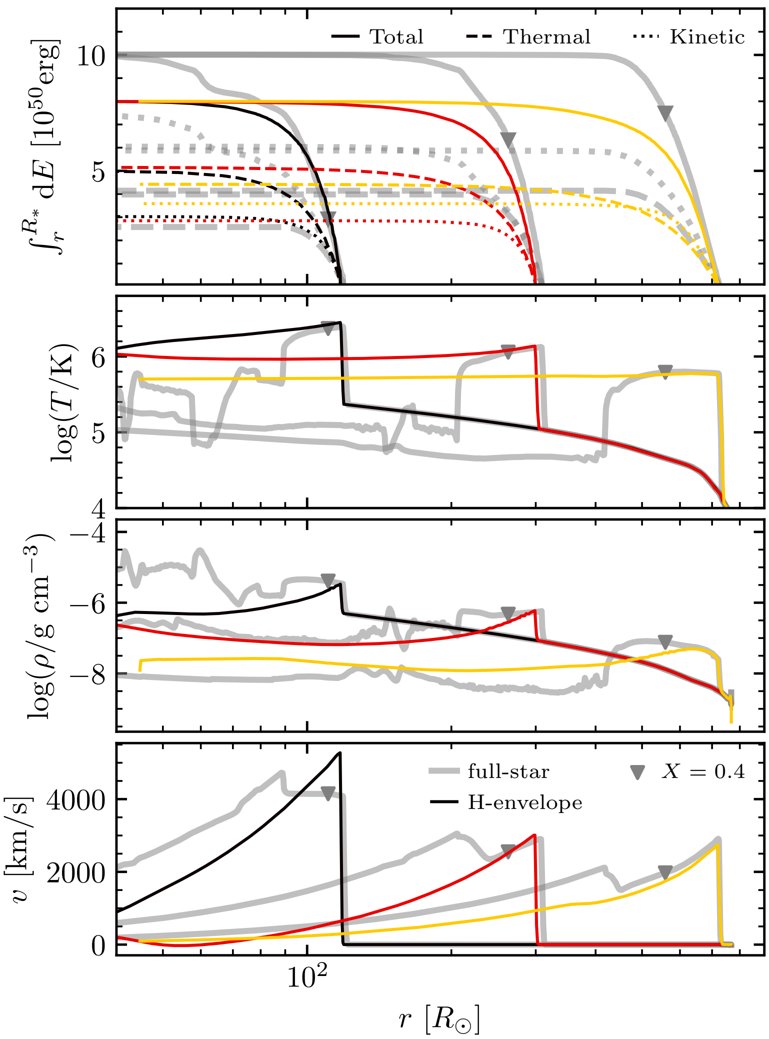

Figure 6.1: Upper panel: Cumulative energy integrated from the surface for three snapshots from `MESA` at different times, in a 10^{51}erg full-star explosion (thick grey lines) and a 8×10^{50}erg explosion of the hydrogen-rich envelope (thin colored lines). Integrated thermal energy (dashed lines), kinetic energy (dotted lines), and total energy (solid lines) are shown. Temperature (second panel), density (third panel), and velocity (fourth panel) are shown for the same three snapshots. Grey triangles approximate the He core boundary where $X = 0.4$ in the full-star explosions.

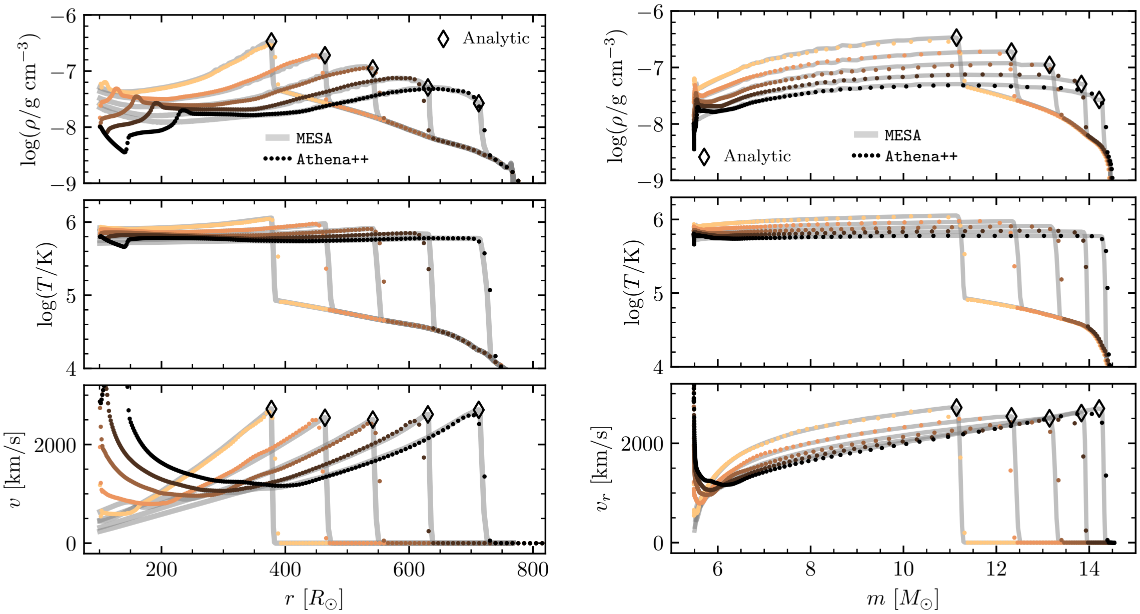

Figure 6.2: Density (upper panels), Temperature (middle panels), and velocity (lower panels) profiles as a function of radius (left column) and mass coordinate (right column) for the same spherical shock in `MESA` (thick grey lines) and `Athena++` (colored points). Point spacing indicates the radial grid resolution in `Athena++`. Black diamonds show analytic expectations for post-shock density $\rho_1 = 7\rho_0$ and and fluid velocity $v_{\rm fast} = 6v_{\rm sh}(r)/7$ using values from `MESA`.

agreement in the post-shock temperatures and velocities, and satisfactory agreement in the outer post-shock density, especially at late times as the shock wave has had sufficient time to propagate. The post-shock material is nearly isothermal, and the shock velocity behaves as predicted by Equation (6.1). In the full-star explosion, roughly 80% of the energy is deposited within the H-rich envelope, which motivates the choice of an 8.0×10^{50}erg energy deposition to compare to a 10^{51}erg full-star explosion and for our fiducial 3D explosion. Although the reverse shock in the full-star explosion accounts for $< 20\%$ of the explosion energy, it is not relevant to the surface material nor the propagation of the forward-shock.

To ensure that this spherically symmetric explosion is also captured in `Athena++`, we import the H-only explosion from `MESA` to `Athena++` at a time when the shock front is at $r \approx 300 R_\odot$, 0.435 days after the onset of the explosion in `MESA`. We use a similar spherical polar grid as in our 3D RSG model, with periodic boundary conditions in θ and ϕ ($\theta = \pi/4 - 3\pi/4$, $\phi = 0 - \pi$), a reflective-velocity inner boundary (at $100 R_\odot$), and an outflow outer boundary beyond $r = 2200 R_\odot$. Figure 6.2 compares the resulting shock profiles in `MESA` (thick grey lines) and `Athena++` (colored dotted lines). Snapshots are again selected such that the shock fronts are at approximately the same radius at times $t =$0.19, 0.41, 0.67, 0.85, and 1.07 days since handoff in `MESA` and $t =$0.19, 0.39, 0.64, 0.83, and 1.08 days since handoff in `Athena++`. The radial mesh resolution in `Athena++` is given by the dotted points. The `Athena++` data shown are angle-averages, though individual radial rays show the same results for spherical explosions. The two

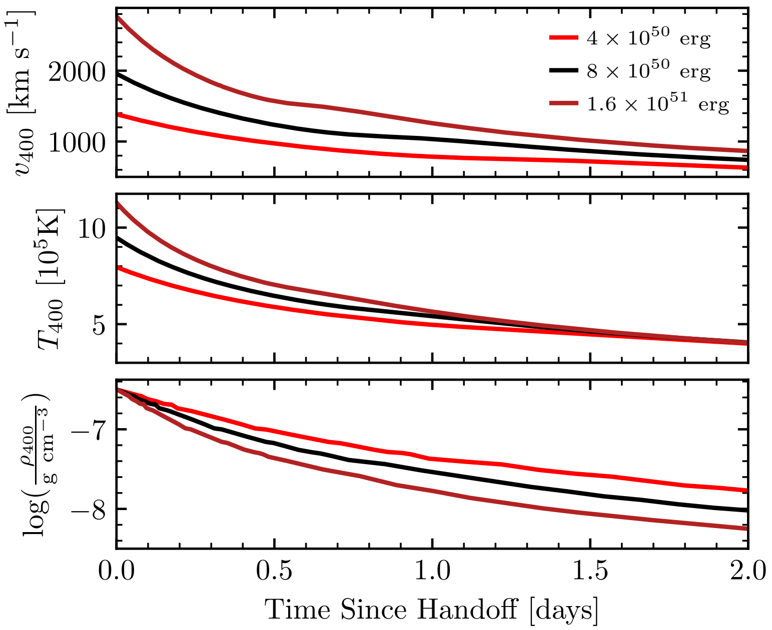

Figure 6.3: Velocity, temperature, and density at $r = r_{\rm IB} = 400R_\odot$ in `MESA` starting at the time of handoff to `Athena++` for the 3 explosion energies discussed in §6.3.

software instruments agree well with each other and with the analytic expectations, with differences arising only due to the `Athena++` resolution near the shock front and reflection of some low-density material off of the inner boundary. These differences do not impact the shock propagation or the early post-shock-breakout evolution of the outer envelope. This agreement gives us confidence in our use of `Athena++` for the next stage of our exploration.

The inner boundaries of our 3D RSG envelope simulations are at $r = 300 - 400R_\odot$ rather than $r = 100R_\odot$, which means the scheme discussed above must be modified to explode the 3D envelopes. As seen in Figure 6.1, a significant portion of the mass and explosion energy passes through $r = 400R_\odot$ as the explosion approaches SBO. We thus developed a second explosion scheme on the exact same grid as our fiducial 3D envelope model, but instead of a fixed inner boundary with specified initial conditions, we specify the time-dependent fluid velocity v, density ρ, temperature T, and co-moving radiative flux $F_{\rm rad}$ in the ghost zones at the $r = 400R_\odot$ inner boundary to match a `MESA` model at the $r = 400R_\odot$ coordinate at each timestep. This allows energy and mass to be fed into the model through the inner boundary in order to power the shock.

For this, we must choose a `MESA` model which matches the average properties of the RSG1L4.5 envelope model at the $r = 400R_\odot$ coordinate. We thus select a `MESA` model selected from the Goldberg & Bildsten (2020) grid of progenitors with pre-shock $\rho(r = 400R_\odot)$, $T(r = 400R_\odot)$, and $m(r = 400M_\odot)$ approximately matching the shell-averaged values at the $r = 400R_\odot$ in the fiducial RSG1L4.5 envelope. The chosen model has a progenitor mass of $19M_\odot$, mixing length in the H-rich envelope $\alpha_H = 3.0$, modest wind $\eta_{\rm wind} = 0.2$, no rotation ($\omega/\omega_{\rm crit} = 0$), no overshooting ($f = f_0 = 0$), and metallicity $Z = 0.02$. The mass and radius of this `MESA` RSG progenitor model at the time of core-collapse are $18.5M_\odot$ and $659R_\odot$.

As a first test of this scheme, we populate the `Athena++` grid with data from the profile of the H-envelope only explosion in `MESA` from $r = 400R_\odot$ outward at the time when the shock radius in `MESA` is at $r_{\rm shock} = 426R_\odot$, near but outside the inner boundary in `Athena++`. At the time of handoff to `Athena++`, the enclosed mass below $r = 400R_\odot$ is $12.7M_\odot$. Figure 6.3 then shows our time-dependent inner boundary condition on v, T, and ρ taken from the $r = 400R_\odot$ coordinate in `MESA`, with the time of handoff identified when $r_{\rm sh} = 426R_\odot$. The radiative luminosity, which is also passed to `Athena++`, is

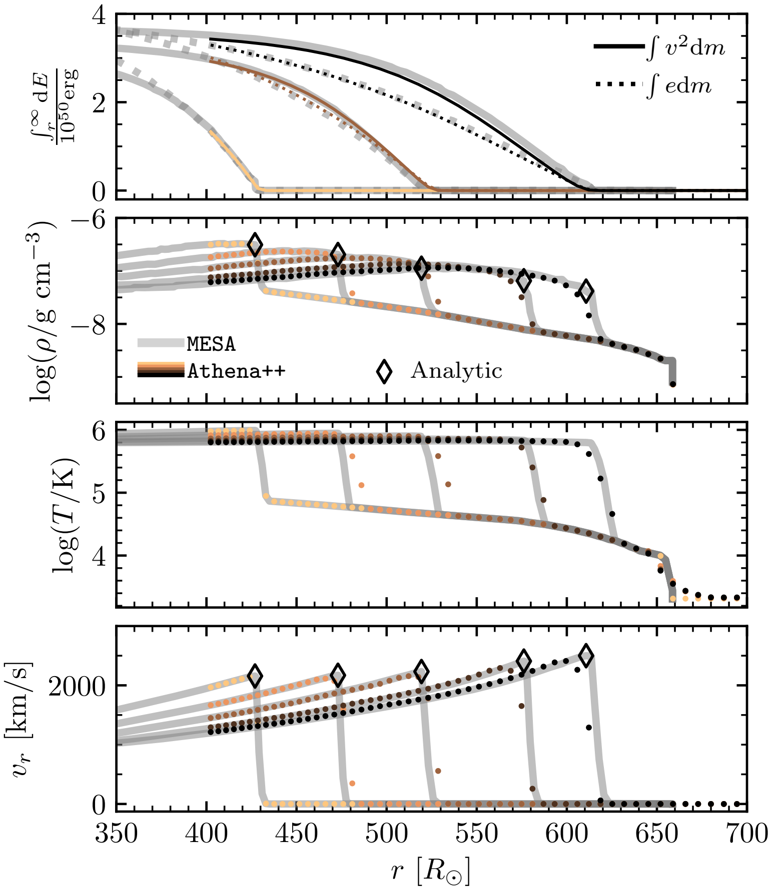

Figure 6.4: Upper panel: Cumulative kinetic (solid lines) and thermal (dashed lines) energy integrated from the surface to radius r for different shock locations in `MESA` (thick grey lines) and `Athena++` (colored lines/points) using the time-dependent boundary condition at $r = 400R_\odot$. Density (second panel), temperature (third panel), and velocity (fourth panel) profiles are also shown. Point spacing in the lower three panels indicates the radial grid resolution in `Athena++`. Black diamonds show analytic expectations for post-shock density $\rho_1 = 7\rho_0$ and and fluid velocity $v_{\mathrm{fast}} = 6v_{\mathrm{sh}}(r)/7$ using values from `MESA`.

small compared to the advective luminosity and the sign is negative, as the temperature gradient is positive in the post-shock material. The comoving radiative luminosity can also be estimated from $F_{\rm r} = \frac{1}{3}(c/\kappa\rho)aT^4/400R_\odot$, where ρ, T, and κ are taken at the $400R_\odot$ coordinate, which gives $\log(F_{r,400}/{\rm erg\,s^{-1}\,cm^{-2}})$ $\approx$13.3, 13.0, and 13.6 for the fiducial (black), low-energy (light red) and high-energy (dark red) explosions.

Figure 6.4 compares the shock propagation and energetics in `MESA` and `Athena++` for the 8×10^{50} erg energy deposition, at times t =0.0, 0.15, 0.29, 0.46, and 0.56 days after handoff (which occurs 0.96 days after explosion) in `MESA` and t =0.0, 0.15, 0.30, 0.44, and 0.54 days since handoff in `Athena++`. The upper panel only shows every other profile for clarity, and the `Athena++` grid is given by the rounded points in the lower 3 panels. We see excellent agreement between shock properties in `MESA` and `Athena++`, with discrepancies arising primarily due to the slight time differences between the `MESA` and `Athena++` profile output. At the time of shock breakout, nearly 80% of the total shock energy is contained within the `Athena++` simulation domain, nearly equipartitioned between kinetic and thermal energy, with thermal energy accumulated deeper in the ejecta. This continued agreement further bolsters our confidence in the use of `Athena++` to explore the 3D problem.

6.1.2 The 3D shock

To drive this explosion in the 3D envelope, we start with the 3D RHD `Athena++` envelopes at the end of the simulation run described in Goldberg et al. (2022). We then populate the innermost portion of the `Athena++` simulation domain with the post-shock ρ, T, and v values from the exploded `MESA` model between $R_{\rm IB}$ to $r_{\rm sh}$ when $r_{\rm sh} \approx R_{\rm IB} + 30R_\odot$, leaving the pre-shock 3D envelope above that location unchanged. We then demand that the time-dependent T, ρ, v, m, and $F_{\rm rad}$ at $r = R_{\rm IB}$ in `Athena++` match that of the exploded `MESA` model thereafter. The mass in our simulation domain in the fiducial explosion is $4.5M_\odot$ at the time of the peak bolometric luminosity ($L_{\rm bol}$) in the SBO, which extrapolates to $M_{\rm ej} = 12.7M_\odot$ accounting for the limited solid angle, which is a combination of the initial mass within the simulation domain and the mass fed in by this time-dependent boundary condition.

The shock propagation is shown in Fig. 6.5 for our fiducial explosion with $M_{\rm ej} \approx 12.7M_\odot$ and $E_{\rm exp} = 0.8 \times 10^{51}$erg. We show 128 radial rays equally distributed across the stellar surface, and highlight four rays corresponding to different topographical features of the 3D stellar surface: a "valley" (A), a "hillside" (B), a "plateau" (C), and a "mountain" (D) on the stellar surface, with shock breakout expected to occur approximately in alphabetical order. We discuss this expectation in greater detail in §6.2. Times are labelled as time to the maximum observed $L_{\rm bol}$ integrated over the simulation angular domain. The Matzner & McKee (1999) prediction for the fluid velocity is shown where valid, using values of $r_{\rm sh}$ and ρ_0 along point C, displaying good agreement. We verified agreement along all radial rays, and the variety in v_r at the shock front at any given time is consistent with the variation in ρ_0 and $r_{\rm sh}$. Additionally, we confirm that the post-shock $\rho_1 = 7\rho_0$ as expected analytically.

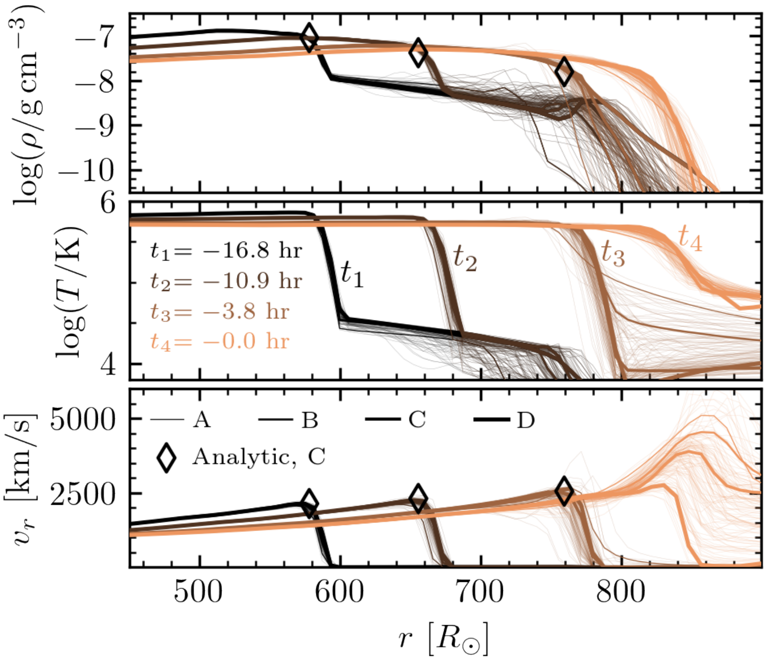

Figure 6.5: Density (top), temperature (middle), and v_r (bottom) radial profiles for our fiducial 3D explosion along 128 rays (thin, faint lines) uniform in (θ, ϕ), with four lines of sight with different expected SBO times emphasized (thicker solid lines), at different times. Where applicable, the analytic expressions are shown for the density, $7\rho_0$, and fluid velocity near the shock front, $v_{\rm fast} = 6v_{\rm sh}/7$ where $v_{\rm sh}$ is given by Eq. 6.1 using values for point C.

Prior to the explosion, the convective velocity (v_c) fluctuations are a few to 20km/s. As $v_{\rm sh} > 2000{\rm km\,s^{-1}} \gg v_c$, the resulting change in the shock frame is only at the 1% level. As the shock passes, the post-shock energy is split in near-equipartition between the radiation energy density and kinetic energy density of the fluid, and the kinetic energy density of the fluid is dominated by the radial velocity v_r. Although the radial motion of the shock front dominates the kinetics, the impact of the shock on convective-like fluctuations can be quantified by the tangential velocity dispersion, $\sigma^2_{v_\perp} = \sum_i (v_{\perp,i}{\rm d}m_i - \langle v_{\perp,i}{\rm d}m_i\rangle)^2/\sum_i({\rm d}m_i)$, where $v_\perp^2 = v_\theta^2 + v_\psi^2$, ${\rm d}m_i$ is the mass in zone i and the sum is over all zones in a given radial shell. This is shown in Fig. 6.6, which compares the characteristic tangential velocity dispersion (colored lines) to the forward-shock velocity (grey lines), $v_{\rm rms} = \sqrt{v_r^2 + v_\theta^2 + v_\phi^2 +} \approx |v_r|$, where $v_{\rm rms}$ is calculated as the kinetic energy in each radial shell divided by the shell mass. The underlying stellar convective dispersion around 4km/s can be seen in the pre-shock material. Due to the envelope inhomogeneities, the velocity dispersion grows as transverse pressure gradients accelerate the fluid; however there is insufficient variety in the shock arrival time for these fluctuations to grow appreciably, and the tangential velocity dispersion remains an order of magnitude below the shock velocity.

As the explosion progresses, the shock front begins to corrugate from differing density profiles seen along each radial ray. Fig. 6.7 shows these growing inhomogeneities in shock temperature, velocity, and radius in progressive snapshots before SBO for a zoom-in patch of the stellar surface, compared to the angle-averages (denoted $\langle \cdots \rangle$). Quantities

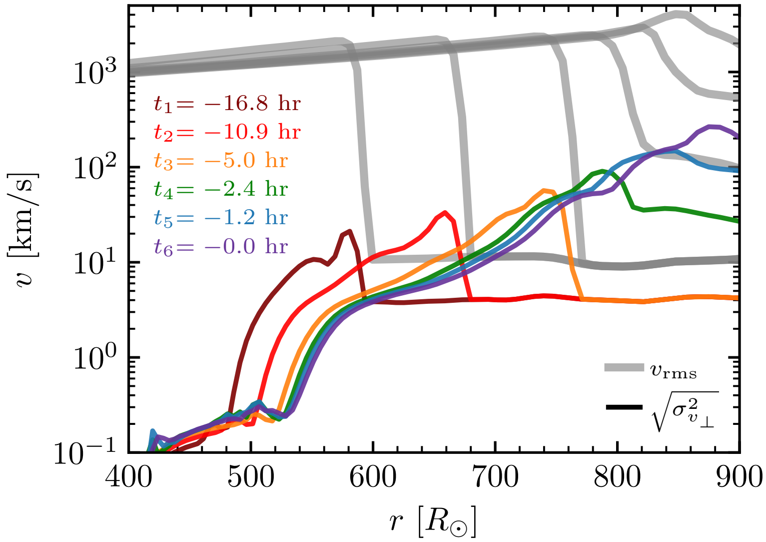

Figure 6.6: Tangential velocity dispersion (rainbow lines) compared to the mass-weighted rms velocity (thick grey lines) for 6 snapshots of our fiducial explosion.

are shown at the radial coordinate of the fastest-moving material at each angular location (denoted $r_{\rm fast}$), and the radial velocity and radiation temperature $T_r = (E_r/a)^{1/4}$ at that coordinate are denoted $v_{r,\rm fast}$ and $T_{\rm fast}$ respectively. Locations A, B, C, and D, are labeled. As the shock propagates further through the envelope, the shock radius begins to vary, but before breakout remains at the level of $\approx \pm 3\%$. Temperature fluctuations reach the 10% level, and velocity fluctuations grow to the 15% level.

SBOs in aspherical axisymmetric explosions have been considered in prior works, primarily in the case of oblique shock breakout in more compact (e.g. blue supergiant) stellar sources (e.g. Couch et al., 2011; Suzuki et al., 2016; Afsariardchi & Matzner, 2018), as well as semi-analytically (Suzuki & Shigeyama, 2010; Linial & Sari, 2019; Irwin et al., 2021). Some 3D simulations of the core-collapse explosion itself have examined shock propagation all the way up to SBO with neutrino-powered core-collapse explosions

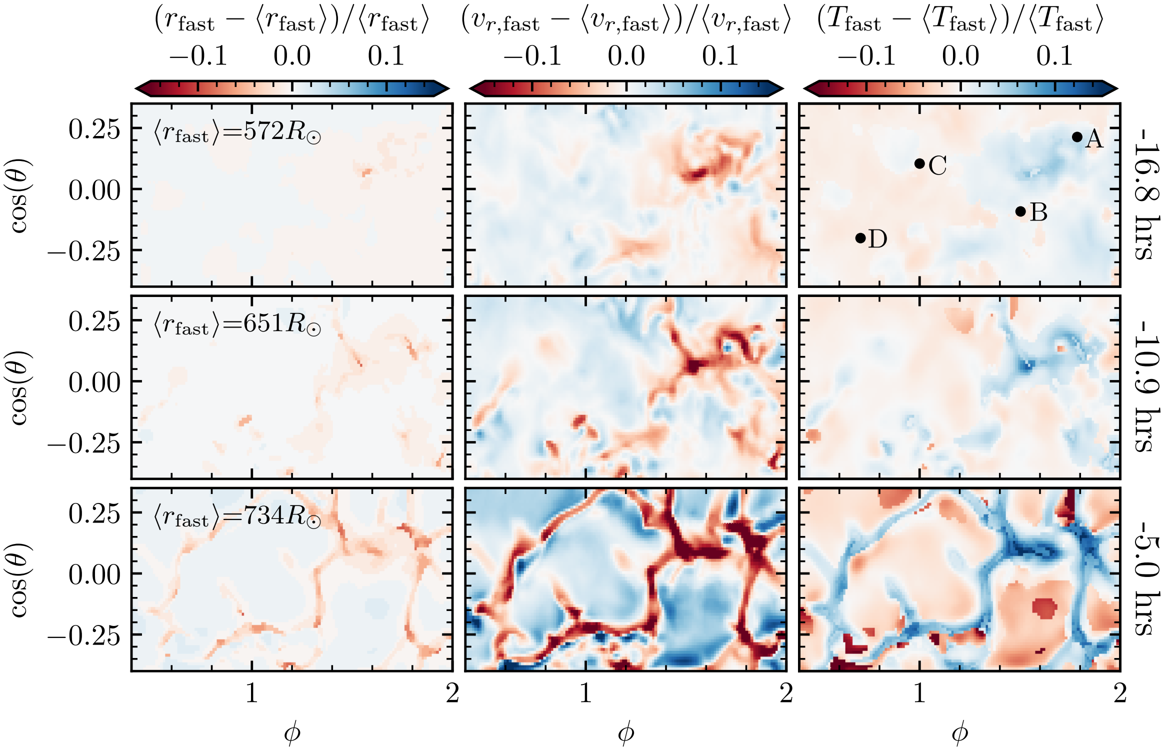

Figure 6.7: Corrugation of the shock front as it travels through the convective H-rich envelope prior to SBO. Color indicates fluctuations in radial coordinate (left column), v_r (middle), and T (right) of the fastest-moving material at each angular location. The approximate radius of the shock front is labeled in the left column and the time before peak $L_{\rm bol}$ is labeled on the right.

(e.g. Wongwathanarat et al. 2015; Stockinger et al. 2020; Sandoval et al. 2021; Kozyreva et al. 2022) in RSG envelopes coming from 1D stellar models; in those works, asymmetric shocks, which sphericalize as they propagate, are introduced by the explosion mechanism. In contrast, all effects discussed here are introduced by the 3D convective envelope itself.

6.1.3 Measuring the Bolometric Luminosity

We calculate $L_{\rm bol}$ as the integrated F_r passing through our simulation domain at fixed radius scaled to the full $\Omega = 4\pi$. We choose $2700 R_\odot$ for a representative location, and we confirmed that the lightcurve properties are independent of this choice. Because an observer sees light coming from the whole star at once, not just light that travels along radial rays, this representative location, which has a horizon encompassing 95% of the solid angle of the $r \approx 820 R_\odot$ SBO surface, is convenient for estimating the variation in $L_{\rm bol}$, by taking the bolometric flux at different angular locations. When showing fluid properties, time 0 is when the star is emitting radiation that corresponds to the peak in $L_{\rm bol}$. This is another motivation to use $2700 R_\odot$ rather than, e.g., $r = 2500 R_\odot$ or $3000 R_\odot$, as the light travel time from the star to the representative location is commensurate with the time sampling of the 3D simulation output.

6.2 The 3D breakout

Radiation escapes ahead of the shock when the shock reaches an optical depth $\tau_{\rm sbo} = c/v_{\rm sh}$ (Lasher & Chan, 1979). The escaping radiation ionizes the pre-shock material and the opacity thereafter can be well-approximated by electron-scattering, $\kappa_{\rm es} = 0.32\,{\rm cm}^2/{\rm g}$. The radial scattering optical depth ($\tau_{\rm s}$) is then related to the column depth $y = \int_r^\infty \rho {\rm d}r'$ as $\tau_{\rm s} \equiv \kappa_{\rm es} y$, and the breakout occurs where $\tau_{\rm s} \lesssim \tau_{\rm sbo}$. In the outer layers, 3D simulations reveal scale heights which are significantly larger than traditional 1D hydrostatic models, likely owing to turbulent pressure (Chiavassa et al., 2011b). A low-density 'halo' of material out to a few hundred $R_\odot$ past the photosphere is also present above a bulbous surface with large-scale plumes and order-of-magnitude density fluctuations spanning tens to hundreds of $R_\odot$. Fig.6.8 shows density (ρ) and $\tau_{\rm s}$ profiles immediately prior to explosion for RSG1L4.5. At $R_{\rm phot} = 796 R_\odot$, the shell-averaged density is $\langle\rho\rangle = 6.9 \times 10^{-10}\,{\rm g\,cm^{-3}}$ and column depth is $\langle y \rangle = 780\ {\rm g\,cm^{-2}}$, with 80% of the material between $\rho = 4.0 \times 10^{-11} - 1.9 \times 10^{-9}\,{\rm g\,cm^{-3}}$ and $y = 50 - 2100\,{\rm g\,cm^{-2}}$. Before the explosion, the opacity in this outer material is $\kappa \sim 10^{-3}\,{\rm cm^2\,g^{-1}}$. For RSG2L4.9, not shown, $R_{\rm phot} = 902 R_\odot$, and $\langle\rho\rangle = 7.1 \times 10^{-10}\,{\rm g\,cm^{-3}}$, with 80% between $\rho = 3.4 \times 10^{-11} - 1.8 \times 10^{-9}\,{\rm g\,cm^{-3}}$.

Our fiducial explosion of RSG1L4.5 generates a shock with $v_{\rm sh} \approx 3000$km/s approaching breakout, corresponding to $\tau_{\rm sbo} \approx 100$. The $\tau_{\rm s} = 100 \approx \tau_{\rm sbo}$ surface, spanning $\Delta R \approx 80 R_\odot$, is shown in Fig.6.9, which would correspond to a horizontal slice through the bottom panel of Fig. 6.8. The dashed box shows the characteristic patch which we zoom into, with four points at different topography labeled: a "valley" (A), a "hillside" (B), a "plateau" (C), and a "mountain" (D). The radial profiles corresponding to each of these locations are shown as black lines in Fig. 6.8. The location of SBO often lies outside the traditionally-defined $R_{\rm phot}$, at characteristically lower densities. In contrast,

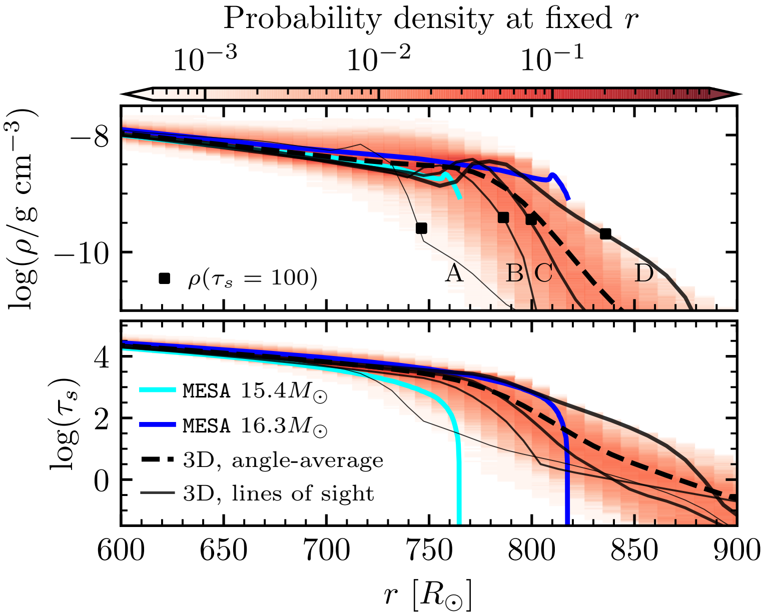

Figure 6.8: Profiles of density (upper) and τ_s (lower) for our pre-explosion snapshot of the fiducial 3D RSG1L4.5 model, compared to 1D profiles `MESA` models with ZAMS masses of $16M_\odot$ (cyan) and $17M_\odot$ (blue) and final stellar masses of $15.4M_\odot$ and $16.3M_\odot$ respectively. Red colors indicate volume-weighted probability of finding a fluid element at a given radial coordinate with a given (ρ, τ_s). Dashed black lines give the angle-averages $\langle\rho\rangle$, $\langle\tau_s\rangle$, and solid black lines show radial profiles along locations A, B, C, and D, with thicker lines indicating larger $r(\tau_s = 100)$. Squares in the upper left panel indicate ρ where $\tau_s = 100$.

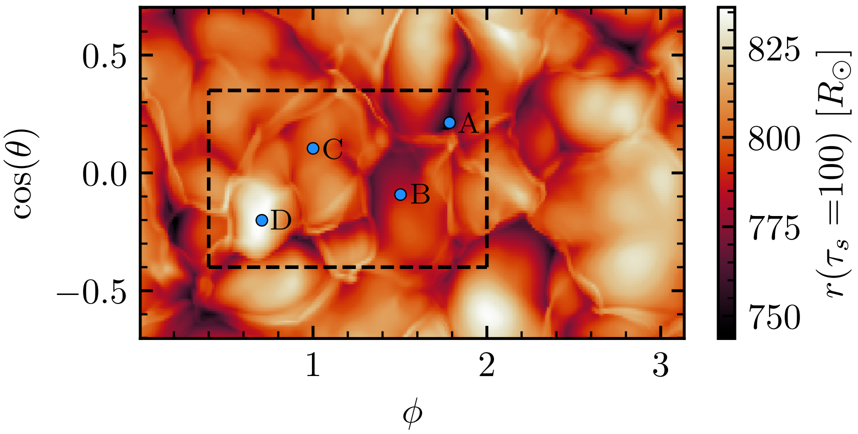

Figure 6.9: Topographical map of the radius where $\tau_s = 100$ along each radial direction. Four characteristic lines of sight (A,B,C,D) are labeled, and the dashed box indicates the zoom-in region for Figs. 6.7 and 6.11.

1D RSG models with a barren photosphere (i.e. no circumstellar material; blue lines in Fig.6.8), show $\tau_{\rm s}$ plummeting from 1000 to 1 over $\approx 7R_\odot$ ($\approx$1% of the stellar radius) and $\rho \approx 10^{-9}\,\mathrm{g\ cm^{-3}}$ for the lowest-density material, about 5× higher than we find at $\tau_{\rm sbo}$ in 3D models.

Two timescales are relevant to the observed SBO duration from a 3D turbulent star. The first is the local radiation diffusion time along a radial ray at the moment of SBO (Katz et al., 2012)

$$t_{\rm diff} \approx \frac{H_\rho}{c}\tau \approx \frac{c}{\kappa \rho_0 v_{\rm sh}^2}, \tag{6.2}$$

where H_ρ is the local (radial) density scale height and the second expression eliminates H_ρ by equating the first expression and the time for the shock to cross H_ρ ($H_\rho/v_{\rm sh}$; i.e. the breakout condition) and expressing τ as $\kappa\rho H_\rho$ near the surface. For our fiducial model where $\tau_{\rm s} = 100$, ρ_0 ranges from $1.25 - 3 \times 10^{-10}\mathrm{g\,cm^{-3}}$, yielding $t_{\rm diff} \approx 1 - 2.2$ hours, $3-10\times$ longer than $t_{\rm diff}$ in 1D models with barren photospheres (Shussman et al., 2016a). The second timescale, intrinsic to 3D stars, is the time it takes the shock to reach all of the fluid elements spanned by the $\Delta R \approx 80R_\odot$ corrugation at the surface,

$$t_{\rm cross} \approx \Delta R / v_{\rm sh}. \tag{6.3}$$

For $\Delta R = 80R_\odot$ and $v_{\rm sh} = 3000-5000\,\mathrm{km\,s^{-1}}$ as is typical in the broken-out rays for the fiducial explosion seen in Fig. 6.5, this is 5 hours to 3 hours. For the 3D stellar progenitor, this timescale dominates $t_{\rm diff}$, and most importantly, the light-travel time across the star, R/c, which is ≈ 0.5 hours for $R \approx 800R_\odot$.

This timing spread can be seen as the shock reaches the inhomogeneous outer layers

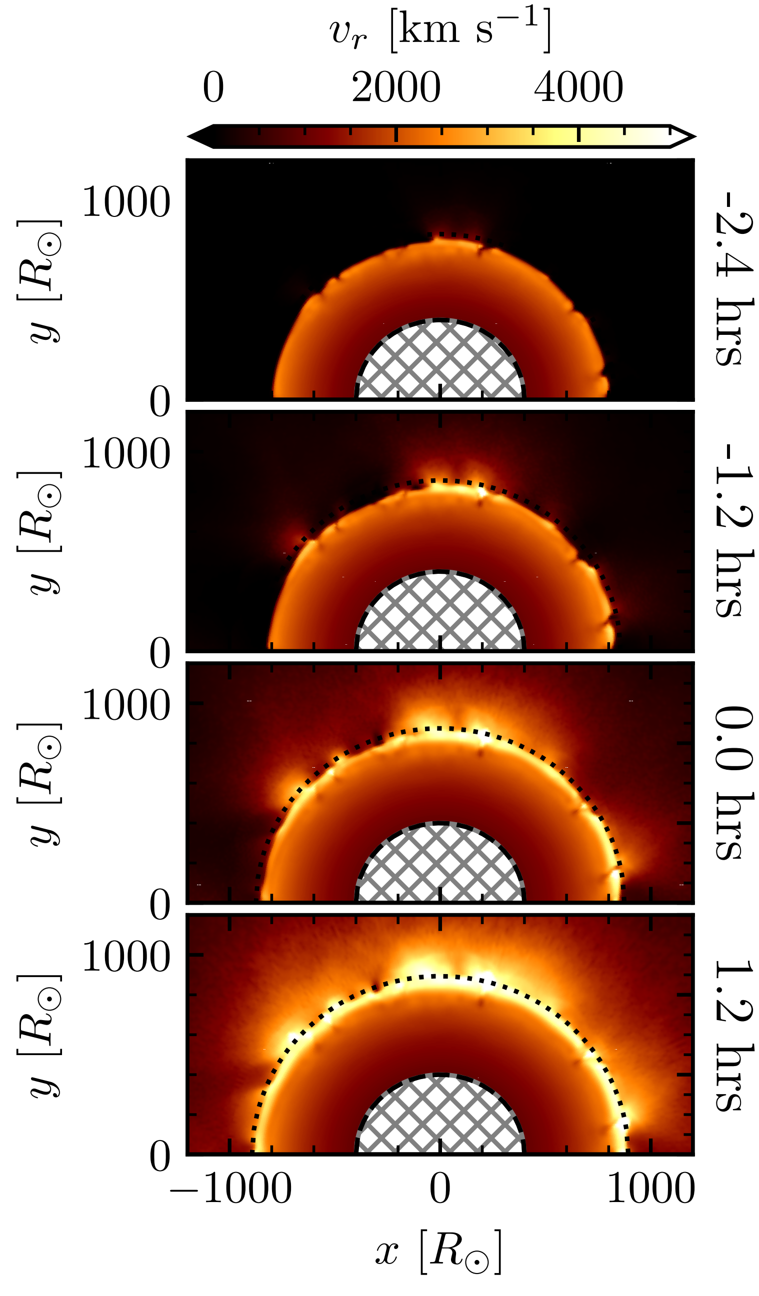

Figure 6.10: Time lapse of radial velocities (orange colors) for equatorial slices of our fiducial explosion, with time snapshots indicated relative the lightcurve peak. The dotted line denotes R_{phot}, which moves outwards as the surface expands, and the simulation inner boundary is shown by grey thatches.

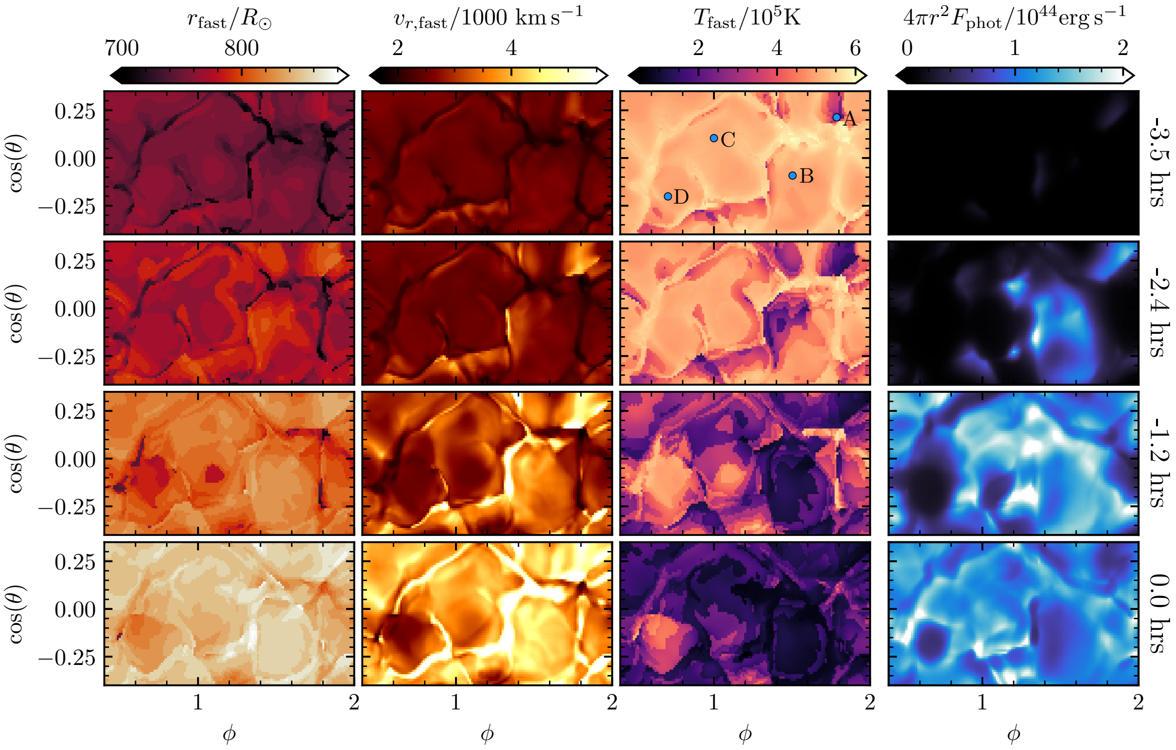

Figure 6.11: Left to right: Radial coordinate (first column), radial velocity (second column), and temperature (third column) taken at the fastest-moving ejecta along each radial line of sight, as well as $4\pi r^2 F_r$ at the photospheric surface (fourth column). The solid-angle spans the dash-enclosed region of Fig.6.9, for our fiducial explosion at different times approaching the peak in the bolometric luminosity (labeled to the right of each row). Reference locations A, B, C, and D are shown in the ($T_{\rm fast}$, -3.5 hours) panel.

and accelerates down the steeper outer density gradient. Valleys on the stellar surface (like point A) are shocked first, and mountains (like point D) are shocked later. Fig.6.10 shows the radial velocity, v_r, for equatorial slices of our fiducial explosion at four snapshots, with $t = 0$ at the bolometric luminosity ($L_{\rm bol}$) peak. Most of the motion of the shock remains radial. When the shock velocity is $v_r \approx 3000\,{\rm km/s}$ (see Fig. 6.6), the transverse velocities are $v_\perp \approx 300{\rm km/s}$; even in broken-out layers where fluctuations begin to span an order of magnitude in ρ and the shock accelerates to $4000 - 10000{\rm km/s}$, $v_\perp$ stays below 1000 km/s.

Fig.6.11 shows the radial coordinate of the fastest-moving material at each angular location (denoted $r_{\rm fast}$), the radial velocity and radiation temperature $T_r = (E_r/a)^{1/4}$ at that coordinate (denoted $v_{r,{\rm fast}}, T_{\rm fast}$ respectively), and the local flux at the first location where $F_r/E_r = 1/3$ inwards along each radial ray. We focus on a zoom-in (dashed box in Fig.6.9) of our fiducial 0.8×10^{51} erg explosion of the RSG1L4.5 model. Times are relative to peak $L_{\rm bol}$. We do not find sufficient obliquity that material accelerated in transverse directions is able to wrap around and reach the outer layers before the forward shock arrives (which is to be expected, see Matzner et al. 2013 and also discussions in Irwin et al. 2021). Rather, the “valleys” (A:$\phi = 1.78, \cos(\theta) = 0.21$) have already undergone breakout and cooled over $t_{\rm diff}$, before the “mountains” are hit (D:$\phi = 0.7, \cos(\theta) = -0.2$). This manifests in lower $T_{\rm fast}$, higher v_r, and higher $F_{\rm phot}$ for point A at -3.5 hours, whereas for point D, the shock front retains its heat and $v_{r,{\rm fast}}$ remains lower, not yet undergoing breakout even at the time of peak $L_{\rm bol}$. Another intriguing outcome is that as the material in the valleys is shocked first and accelerated at an earlier time it gets to larger radii first, inverting the topography of the surface of maximum velocity, evident in the lower left panel of Fig. 6.11.

6.3 Observed properties of the 3D SBO

6.3.1 Temperature Structure

In the 1D picture, the observed temperature is set by the energy density at the breakout location $T \approx (\rho v_{\rm sh}^2/a)^{1/4}$ up to a factor of order unity accounting for thermalization of the radiation and gas (Nakar & Sari, 2010; Sapir et al., 2013). For $v_{\rm sh} = 3000-5000$km/s and $\rho = 1.25 - 3 \times 10^{-10}{\rm g\,cm^{-3}}$, this would predict $\log(T/{\rm K}) = 5.3 - 5.5$. As the post-shock temperature profile is nearly constant throughout the deep envelope, a similar estimate is $4\pi r_{\rm sh}^3 a T_{\rm sh}^4/3 = E_{\rm exp}/2$, with $r_{\rm sh}$ taken at the average radius where $\tau_{\rm s} = c/v_{\rm sh}$, or

$$T_{\rm sh} = \left(\frac{3E_{\rm exp}}{8\pi r_{\rm sh}^3 a}\right)^{1/4}. \tag{6.4}$$

Fig. 6.12 shows radiation temperature as a function of (radial) optical depth $\tau = \int_r^\infty \kappa\rho {\rm d}r$, for snapshots corresponding to the peak in $L_{\rm bol}$ for 3 explosions of RSG1L4.5 at different $E_{\rm exp}$. Shaded regions indicate the spread in $T-\tau$ relations for 80% of Ω, and the arrows show the prediction for the asymptotic shock temperature from Eq. 6.4 using the average shock front location across the breakout surface, $r_{\rm sh} = 820R_\odot$. The thin black lines show $T-\tau$ relations along an intermediate ray (point C) which has recently been hit by the forward shock. The radiation and gas temperatures are approxi-

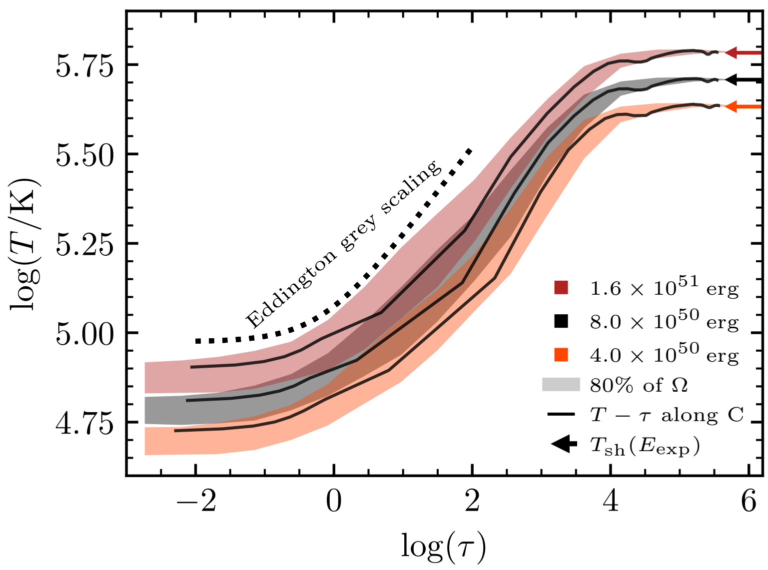

Figure 6.12: $T - \tau$ relations for 3 explosions varying $E_{\rm exp}$, taken at peak $L_{\rm bol}$. Shaded regions show relations for 80% of the solid-angle, and arrows indicate the asymptotic shock temperature predicted by Eq. 6.4. Thin black lines show $T - \tau$ relations at location C. The scaling for an Eddington grey atmosphere assuming constant flux is shown for reference.

mately thermalized in the material which has already broken out, and the profile follows the Eddington grey atmosphere assuming constant flux, $T^4 = \frac{3}{4}T_{\rm eff}^4\left(\tau + \frac{2}{3}\right)$ (Rybicki & Lightman 1986, dotted line). When $t_{\rm diff} \ll t_{\rm cross}$, we expect a diversity of $T_{\rm eff}$ across the stellar solid-angle, which is not the case in the limit of $t_{\rm diff} \gg t_{\rm cross}$.

6.3.2 Bolometric properties

The resulting SBO lightcurves of our 3D explosions are fainter, and longer-duration, than explosions of 1D stellar models. Fig.6.13 shows $L_{\rm bol}$ for different explosions, and the explosion properties are summarized in Table 6.2. The upper panel compares log($L_{\rm bol}$) of our fiducial explosion (black curves) to a $8{\times}10^{50}$erg explosion of the RSG2L4.9 model, as well as characteristic 1D explosion models from Goldberg & Bildsten (2020) using `MESA` and `STELLA` (Blinnikov & Sorokina, 2004; Baklanov et al., 2005; Blinnikov et al., 2006) selected for their comparable $E_{\rm exp}$, $M_{\rm ej}$, and radii (blue and cyan). The 1D lightcurves are corrected for light-travel time as $L_{\rm bol}(t) = \frac{1}{R/c}\int_{t-R/c}^{t} L\left(t'\right) {\rm d}t'$ (Shussman et al., 2016a), which dominates the SBO duration $t_{\rm SBO} \approx R/c$ in 1D explosion models. These 1D explosion lightcurves agree well with the Shussman et al. (2016a) semi-analytical models (see also the detailed discussions in Kozyreva et al. 2020). The RSG2L4.9 explosion (orange line in the upper panel) has a smaller $M_{\rm ej} = 3.5M_{\odot}$ in the simulation domain and therefore larger $v_{\rm sh}$, with similar ρ_0 but with greater variety and some material below $10^{-10}\,{\rm g\,cm^{-3}}$. The greater variety of shock arrival times across the larger $\Delta R = 200R_{\odot}$ also leads to a greater diversity in velocities and lightcurves along different lines of sight. In both models, the intrinsic ΔR dominates over the possible diversity of radii at which SBO would occur at $20 < \tau_{\rm s} < 200$ corresponding to an order of magnitude in $c/v_{\rm sh}$. The lower panel compares three different explosions of the RSG1L4.5 model, with $E_{\rm exp} = 4\times10^{50}\,{\rm erg}$, $8\times10^{50}\,{\rm erg}$, and $1.6\times10^{51}\,{\rm erg}$; lower-energy explosions have a longer duration with lower peak luminosity compared to higher-energy explosions. In the 3D explosions, the spread of possible SBO signals is estimated by $4\pi r^2 F_r$ at 64 viewing angles across the surface, shown as faint lines. A full-star simulation would allow for a more complete sampling of SBO radii which might increase the duration of the lightcurve. This can be quantified with explosions at different time snapshots in the star's evolution.

In the 1D model explosions, the intrinsic rise time of the SBO pulse is equal to $t_{\rm diff}$

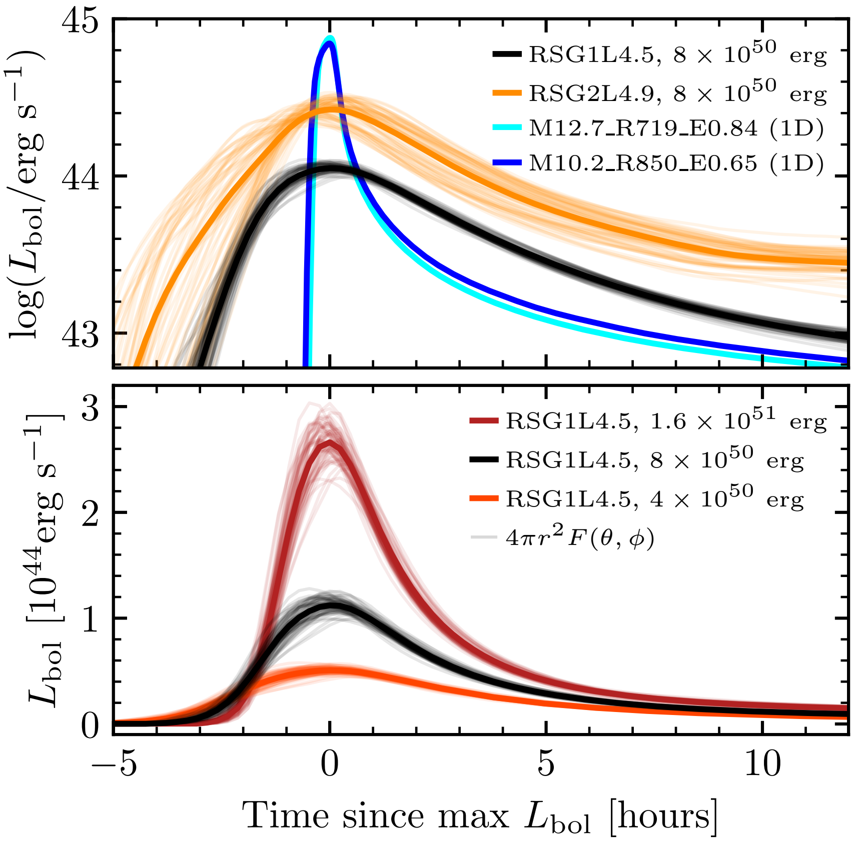

Figure 6.13: Bolometric lightcurves calculated for varied progenitor model (top) and explosion energy (bottom). Black curves correspond to the fiducial 8×10^{50}erg explosion of the RSG1L4.5 model with $\Delta R = 80R_{\odot}$. Faint lines are calculated from the flux an observer would see at $r = 2700R_{\odot}$ looking back at the star for a particular θ, ϕ location. For comparison, SBO lightcurves from spherically symmetric `MESA+STELLA` explosion models (Goldberg & Bildsten, 2020) are shown in the upper panel (blues), labeled M[$M_{\rm ej}/M_{\odot}$]_R[$R_{\rm phot}/R_{\odot}$]_E[$E_{\rm exp}/10^{51}$erg]. The x-axis for all 3D curves is the time since the maximum shell-averaged $L_{\rm bol}$ (i.e. the peak of the thick curves).

(Nakar & Sari, 2010; Sapir et al., 2011), but the observed duration of the SBO pulse is smeared out over the light-travel time R/c (Calzavara & Matzner, 2004; Katz et al., 2012; Shussman et al., 2016a), as $t_{\rm diff}$ is typically less than or comparable to R/c for 1D stellar models with no circumstellar material. For more extended envelopes ($R \gtrsim 700R_{\odot}$) and lower surface densities, the diffusion time can dominate over the light-travel time, but is still expected to be under $\approx$ 1hr or so (see discussion in Calzavara & Matzner 2004) In the 3D models, due to the lower densities and larger scale height of material where SBO occurs, both $t_{\rm diff}$ and $t_{\rm cross}$ are significantly longer than R/c. Additionally, the diffusion time and the shock traversal time across the inhomogeneous outer layers scale differently with the explosion energy. The shock traversal time, $t_{\rm cross} \propto v_{\rm sh}^{-1} \underset{\sim}{\propto} E_{\rm exp}^{-1/2}$, whereas $t_{\rm diff} \propto (\rho_0 v_{\rm sh}^2)^{-1} \underset{\sim}{\propto} E_{\rm exp}^{-1}$ (this scaling varies for assumptions about the outer density profile, but is steeper than $E_{\rm exp}^{-0.8}$; see Rabinak & Waxman 2011, Shussman et al. 2016a, and others).

We define a characteristic SBO duration, $\Delta t_{1/2}$, as the width of the SBO pulse from half of the peak luminosity on the rise ($t_{\rm rise}$) to half the peak luminosity on the fall ($t_{\rm fall}$), $\Delta t_{1/2} = t_{\rm rise} + t_{\rm fall}$. Characterizing the breakout by $\Delta t_{1/2}$, rather than $t_{\rm rise}$, is motivated by the fact that when the SBO duration is mediated by the 3D inhomogeneities, the morphology of the $\tau_{\rm s} = c/v_{\rm sh}$ surface will determine the shape of the breakout pulse. This is also evident when comparing the RSG1L4.5 and RSG2L4.9 lightcurves, which have similar $t_{\rm cross}$ but different morphology where $\tau_{\rm s} = c/v_{\rm sh}$. For the 1D explosions shown, $\Delta t_{1/2} = 0.55$ hrs for the $850R_{\odot}$ model and 0.45 hrs for the $719R_{\odot}$ model, consistent

Progenitor Model	$E_{\mathrm{exp}}/10^{51}\mathrm{erg}$	$M_{\mathrm{ej}}/M_{\odot}$	$r(\tau_s = 100)/R_{\odot}$	$L_{\mathrm{peak}}/10^{44}\mathrm{erg\,s^{-1}}$	$t_{\mathrm{rise}}/\mathrm{hr}$	$\Delta t_{1/2}/\mathrm{hr}$
RSG1L4.5	0.4	12.7	≈ 820	0.51	2.33	6.09
	0.8*	12.7	≈ 820	1.12	1.64	4.36
	1.6	12.7	≈ 820	2.66	1.20	3.02
RSG2L4.9	0.8	3.5	≈ 960	2.65	1.56	4.03

Table 6.2: Summary of the properties of the 3D explosion models, including E_{exp} and M_{ej} in the simulation domain at the time of peak L_{bol}, the approximate average location of SBO, the peak luminosity, rise time, and duration. The * denotes the fiducial explosion.

with R/c. In the 3D SBOs, $\Delta t_{1/2} \gg R/c$, and the relative durations exhibited by the 3D models are consistent with the semi-analytic expectation that$\Delta t_{1/2} \sim t_{\mathrm{cross}} \underset{\sim}{\propto} \Delta R\ v_{\mathrm{sh}}^{-1}$, which scales like $\underset{\sim}{\propto}\ E_{\mathrm{exp}}^{-1/2}$ for fixed M_{ej} and R. This agreement, rather than steeper dependence on E_{exp} expected for $t_{\mathrm{diff}} > t_{\mathrm{cross}}$ or no dependence on E_{exp} if the duration were set by R/c, further supports the notion that t_{cross} is setting the SBO duration for these explosions. In fact, the numerical values of $\Delta t_{1/2}$ for the explosions summarized in Table 6.2 agree well with $\Delta t_{1/2} \approx t_{\mathrm{cross}}$ from Eq. 6.3.

In the 3D star, due to the different SBO times at different patches on the stellar surface, individual SBO signals coming from each angular location peak at different times within the span of $t_{\mathrm{cross}} \approx$a few hours, and the duration of each of those individual local breakout signals would be approximately set by $t_{\mathrm{diff}} \approx$an hour or two as expected for the nearly planar case discussed by, e.g., Nakar & Sari (2010) and Irwin et al. (2021). However, an observer far away from the star does not only see emission coming from a shock breakout along the radial ray directly pointed directly at them. Rather, because emission streaming out of the photosphere at each location on the stellar surface is somewhat isotropic (mediated in part by the stellar surface topography), and because the difference in light travel time from different patches of the stellar surface ($\approx R/c$) is shorter than $t_{\rm cross}$, observers at different viewing locations far away from the star will see a SBO signal that is integrated from the broken-out patches across the portion of the star that they see. This is why the timing of the peak luminosity shown in Fig. 6.13 is more similar for different observer locations, and the duration of the breakout for all observers matches more closely with $t_{\rm cross}$.

Since $t_{\rm diff} \propto v_{\rm sh}^{-2}$ but $t_{\rm cross} \propto v_{\rm sh}^{-1}$ for a given star, the diffusion time may dominate the shock traversal time at lower $v_{\rm sh}$ (i.e. low $E_{\rm exp}$). This occurs when $v_{\rm sh} < c/(\kappa\rho_0\Delta R)$, or $v_{\rm sh}$ ≈1,300 $\rm km\,s^{-1}$ for $\Delta R = 80R_\odot$ and $\rho_0 = 1.25\times10^{-10}\,\rm g\,cm^{-3}$. In those cases, the emission would appear more spherical and we would also expect less diversity in the observed temperature.

Furthermore, a characteristic luminosity can be predicted as the internal energy contained outside $\tau < \tau_{\rm sbo}$, E_0, divided by the relevant timescale, t_0, or $L_{\rm char} = E_0/t_0$. Following Nakar & Sari (2010), $E_0 \approx 4\pi r_{\rm sh}^2\rho_0 v_{\rm sh}^2(c/\kappa\rho_0 v_{\rm sh}) = 4\pi r_{\rm sh}^2 c v_{\rm sh}/\kappa$, with $r_{\rm sh}\approx 820R_\odot$ for RSG1L4.5 as the average radius of the $\tau_{\rm s}\approx 100$ surface. When $t_{\rm cross} > t_{\rm diff}$, $L_{\rm char}\approx E_0/t_{\rm cross}$ rather than identifying $t_0 = t_{\rm diff}$, so

$$L_{\rm char} \approx 4\pi r_{\rm sh}^2 \frac{c}{\kappa}\frac{v_{\rm sh}^2}{\Delta R} \underset{\sim}{\propto} E_{\rm exp} \tag{6.5}$$

where the energy scaling is for fixed stellar properties. Because $t_{\rm cross}$ (a few hours) in the 3D models is larger than $t_{\rm diff}$ for a 1D stellar model with a barren photosphere (tens of minutes) or R/c (≈half an hour), this entails a SBO signal a factor of ≈3-10 times fainter than 1D models predict, as seen in Fig. 6.13. Moreover, the energy scaling is in rough agreement with the peak bolometric luminosity $L_{\rm peak}$ seen in the 3D explosion models with varied explosion energy, and the magnitude of $L_{\rm peak}$ matches Eq. 6.5 for $L_{\rm char}$ within the variance in $v_{\rm sh} \approx 3000 - 5000 {\rm km\,s^{-1}} \left(E_{\rm exp}/0.8 \times 10^{51}{\rm erg}\right)^{1/2}$ for a given explosion along different lines of sight, which is less than a factor of 2.

Finally, when $t > t_{\rm cross}$ such that most parcels have undergone SBO, but while the fluid elements have not yet doubled their radius, the emission follows the expected $L_{\rm bol} \underset{\sim}{\propto} t^{-4/3}$ decline predicted for this planar shock cooling phase (see, e.g., Nakar & Sari, 2010).

The NUV/*ULTRASAT* band pass (2200-2800Å) is near the peak of the blackbody for the expected $T = 10^5 - 10^{5.5}$K near the maximum $L_{\rm bol}$, so the rise time and duration of the bolometric luminosity signal are nearly that which would be observed by *ULTRASAT*. The emission cools into NUV bands beyond the UV/bolometric peak, which does extend the decline in those bands; a full frequency-dependent calculation of SBO emission will yield further predictions about the radiation temperature which would better map to the observables expected from future and current high-energy satellite missions.

6.4 Discussion

By driving a SN shock through global 3D RHD simulations of RSG envelopes in `Athena++`, in this Chapter we have explored the effects of the 3D surface on the resulting SBO emission. Two important physical differences serve to prolong the SBO duration compared to the spherically symmetric case (see, e.g. Nakar & Sari, 2010; Sapir et al., 2011; Katz et al., 2012; Sapir et al., 2013; Sapir & Waxman, 2017). First, the intrinsic radiation diffusion time increases due to lower-density material outside the traditional photosphere present in 3D models which contributes non-negligibly to the optical depth near SBO. Most importantly, the bulbous 3D surface with a handful of large-scale plumes spanning $\Delta R \approx 100 R_\odot$ yields a variety of shock arrival times at the stellar surface, on a timescale $t_{\rm cross} \approx \Delta R / v_{\rm sh}$. This is an intrinsically 3D phenomenon, setting the observed SBO duration for typical explosion energies.

Both timescales dominate over the light-travel time across the stellar surface, R/c, which is approximately equal to the observed rise time in explosions of 1D stellar progenitors in the absence of circumstellar material (see, e.g. Sapir et al., 2013; Shussman et al., 2016a; Kozyreva et al., 2020). This new 3D understanding provides better agreement with the hours-long SBO signal observed in the few existing detections of SN SBO in the UV (e.g. Gezari et al., 2008; Schawinski et al., 2008; Gezari et al., 2010, 2015). The implied longer durations additionally lead to fainter peak luminosities for a given explosion energy, by a factor of $\approx 3-10$. Thus, while useful for constraining the amount of surface asymmetry and the shock velocity as it reaches the stellar surface, SBO observations cannot independently constrain the stellar radius.

Additionally, at any point in time near the peak in $L_{\rm bol}$, fluid elements across the surface coexist at different stages pre-, mid-, and post-shock-breakout, leading to a diversity in the temperature as a function of optical depth along different lines of sight. Specifics of the radiation spectrum await a multi-group 3D calculation, and the 3D nature of the envelope may have further implications for early-time spectropolarimetric measurements (e.g. Leonard et al., 2001; Wang & Wheeler, 2008; Kumar et al., 2016), as well as flash spectroscopy (e.g. Khazov et al., 2016; Kochanek, 2019; Soumagnac et al., 2020).

Chapter 7

Implications and Future Directions

As the most common class of massive star explosions, Type II-Plateau Supernovae from Red Supergiant progenitors have the potential to probe the final stages of the massive star life cycle, encoding information about their stellar properties, explosion dynamics, radioactive ^{56}Ni production, and more. This dissertation utilizes 1D stellar evolution models combined with radiation-hydrodynamical calculations of the SN emission, as well as 3D RHD simulations, to explore the extent to which we can and cannot extract these explosion properties from lightcurves and velocity observations. First: what can't we recover? We show in Chapter 2 that the standardizable candle relationship between the plateau luminosity and plateau velocity (see, e.g. Hamuy & Pinto, 2002; Hamuy, 2003; Kasen & Woosley, 2009) forbids the unique identification of a single explosion model from lightcurves and velocity information alone, and we show in Chapter 4 that a wide swath of $M_{\rm ej} - R$ parameter space can be filled by stellar evolution models when allowing for reasonable variations in input physics. This is also found to be true both in non-evolutionary models for the progenitor structure (e.g. Martinez & Bersten, 2019) and in other evolutionary calculations (e.g. Dessart & Hillier, 2019). We also show in Chapter 6 that the shock breakout timing variations due to large-scale 3D fluctuations in the RSG outer layers entail that future observations of SBO will likely not be able to directly constrain the progenitor radius via light-travel-time effects.

So what can we infer? Foremost, independent constraints on either the progenitor radius, ejecta mass, or explosion energy can allow for the unique identification of these explosion properties. Moreover, despite the inherent degeneracy, the scaling relations derived in Chapter 2 provide good fits across a variety of Nickel-rich events (see both Chapter 4, and also Hiramatsu et al. (2021b) for applications towards interpreting observations of a proposed Electron Capture Supernova candidate), and even in principle for changes in radius due to stellar pulsations (discussed in Chapter 3). Thus, when combined with a large sample of lightcurves and reasonable priors on, e.g., the population of RSG radii, this work can allow us to characterize observed populations of SNe-IIP in an ensemble fashion. For example, Murphy et al. (2019) used the scaling relations described in Chapter 2 with the observed distribution of RSG radii as a prior to highlight an apparent gap in between the distribution of explosion energies recovered from the Pejcha & Prieto (2015a) lightcurve sample and the explosion energies recovered by 3D neutrino-hydrodynamic simulations of the CCSN explosion mechanism. Such an approach could be reproduced and extended for larger observed SN samples, such as the recently published Carnegie Supernova Project sample (Martinez et al., 2022a,b,c), for which the present analysis involves fitting to a grid of hydrodynamic explosions of polytropic stellar models which likely span an insufficient region of the $M_{\rm ej} - R - E_{\rm exp}$ parameter space to capture all valid solutions within the possible family of explosions.

There are a variety of additional future prospects for building upon and extending this work. While plateau-phase luminosities and expansion velocities as probed by the Fe II 5169Å line measured near the SN photosphere during the plateau follow a standard candle relationship, the full ejecta velocity profile does scale independently with only the ejected mass and explosion energy (see Figs. 2.17 and 2.18). Two observable spectroscopic features stand out as likely candidates for probing that velocity profile, which might then yield additional constraints on $M_{\rm ej}$ and $E_{\rm exp}$. Foremost, differences in the depths of P-Cygni absorption features have been associated with differences in total envelope mass (see e.g. Hillier & Dessart, 2019), with some evidence that higher envelope masses correspond to deeper absorption features relative to emission. Secondly, lines formed at different locations outside the photosphere may exhibit different Doppler shifts, particularly between lines formed systematically closer to the photosphere (e.g. Fe II 5169Å) and lines formed farther outside the photosphere (e.g. Hα/β), as the velocity profile changes with $\sqrt{E_{\rm exp}/M_{\rm ej}}$. A diversity of velocity ratios is indeed seen in samples of SNe-IIp (e.g. Takáts & Vinkó 2012; Gutiérrez et al. 2017a,b). Future spectroscopic modeling efforts could yield quantitative relationships between these (and other) spectroscopic observables and the explosion properties of models producing identical lightcurves, which will in turn allow $E_{\rm exp}$ (and $M_{\rm ej}$ and R) to be constrained.

Furthermore, advancements in 3D modeling have led the development of 1D prescriptions to mimic the neutrino-powered CCSN explosion mechanism, such as the STIR (Couch et al., 2020) and PUSH (Perego et al., 2015; Ebinger et al., 2019; Curtis et al., 2019; Ebinger et al., 2020; Ghosh et al., 2022) methods. Existing studies using these implementations to create model lightcurve have used grids of stellar models which fix stellar input physics such as core-boundary mixing, MLT α, and stellar wind efficiency and primarily explore sensitivity to the initial stellar mass (e.g. Curtis et al., 2021; Barker et al., 2022). However, the prospect of having only one allowable explosion energy for a given stellar model, predicted from first principles, is exciting, and extensions of this line of work to a broader grid of RSG models spanning the uncertainties in the stellar modeling prescriptions might nonetheless place additional theoretical constraints on allowable parameter space, e.g. in the $M_{\rm ej} - E_{\rm exp}$ plane.

Down the line, once we gain a good understanding of the explosion energy function from observations, we can then directly constrain the relationship between the explosion energy and the productive of radioactive ^{56}Ni (e.g. Müller et al., 2017). Moreover, the Type II SN explosion energy scale, approximately equal to the asymptotic kinetic energy of the ejecta, is important to supernova feedback in models of star formation and the interstellar medium. At present, even the most state-of-the-art cosmological simulations such as FIRE-2 (Hopkins et al., 2018a) and Illustrius-TNG (Pillepich et al., 2018a; Naiman et al., 2018; Nelson et al., 2018; Springel et al., 2018; Marinacci et al., 2018) use a standard explosion energy of 10^{51} erg for *every* Supernova energy injection (see, e.g., discussions in Hopkins et al. 2018b and Pillepich et al. 2018b). We hope that with more precise constraints on the typical SN explosion energy and dependence on stellar properties, future simulations will be able to more accurately capture these dynamics.

There is also progress to be made in the 3D simulations of RHD-convective envelopes and their explosions. One caveat of the 3D `Athena++` simulations are the lack of the enthalpy of recombination and the fixed value of μ in the equation of state (EOS). While pressure from the trans-sonic turbulent motions dominates in the outer stellar regions where H recombination may occur, these EOS artifacts might affect the outer envelope structure (and/or also lead to additional sensitivity to RHD perturbations). One avenue forward is to explore the sensitivity to a more realistic EOS for the gas. An additional caveat is the grey treatment of the opacity in the Jiang (2021) RHD module. Chiavassa et al. (2011a) show some differences in the temperature structure at the RSG surface between grey-opacity and multi-group calculations with the `CO`^{5}`BOLD` and `OPTIM3D` codes. A multi-group radiation-transport module has been developed (Y-F Jiang, in prep.) which can be used to study such effects in the `Athena++` simulations. Applied to the 3D SBO problem, multi-group radiation transport calculations would also validate and quantify our prediction of a range of photon temperatures around the time of the peak luminosity, due to the mix of emission from different patches of the stellar surface at varied stages of shock breakout and radiative cooling. This would also enable synthetic lightcurve calculations for specific UV bandpasses in *ULTRASAT* and other instruments.

These calculations will also be useful towards interpreting the first ~ 10 days of shock-cooling emission when coming from the intrinsically 3D outer envelope, which have yet to be fully explored in the 3D simulations.

Another avenue for exploration in 3D is moving beyond barren *3D* stellar photospheres, as mass loss during the RSG phase prior to explosion affects early-time SN emission. There are two mechanisms which might cause significant mass loss during that time: Wave-driven heating generated by vigorous convection in burning regions (Quataert & Shiode, 2012; Fuller, 2017; Wu & Fuller, 2021), and pulsationally-driven superwinds (Yoon & Cantiello, 2010). Spherically symmetric models of the wave-driven mass loss mechanism show promise in resolving some of the discrepancies in early emission between models and observations (Morozova et al., 2019; Tinyanont et al., 2022), but both of these mechanisms may interact differently in 3D envelope structures compared to 1D. To explore the effects of a wave-heating-driven mass-loss mechanism in a realistic 3D environment, we could resume our 3D RSG envelope models with a sudden, abrupt increase in the luminosity at the inner boundary, with energy deposition and rates matching analytic expectations, and study the dynamical effects of such energy injections on the surface material (to complement very recent work by Tsang et al., 2022, using the `FLASH` code). Linking the 3D models to the work on pulsating RSGs described in Chapter 3, it would be interesting to investigate the structure of pulsationally driven winds (Yoon & Cantiello, 2010) within our the 3D `Athena++` envelope simulations. Perhaps resuming the envelope simulations with a background velocity field resembling large-amplitude fundamental-mode pulsations, we could self-consistently quantify the mass loss due to these pulsations or characterize any extended material within the stellar atmosphere.

Current ongoing efforts are also being made to extend our understanding of the convective properties of supergiant envelopes more broadly across the HR diagram, with a Yellow Supergiant envelope simulation currently running on NASA computing resources.

Appendix A

Quantifying Fallback in Core-Collapse SNe

Here we discuss modifications relative to MESA IV, of `MESA` modeling of the ejecta evolution after core collapse in massive stars (roughly M $> 8M_\odot$). These are focused on cases where the total final explosion energy is positive, but insufficient to unbind the entirety of the material which does not initially collapse into the compact object. In these weak explosions, there is some amount of fallback material which does not become unbound. Our emphasis here is to quantify and remove fallback in model explosions of RSG progenitor stars. Although we describe models of Type IIP SN explosions, this scheme can be similarly applied to core collapse events in massive stars which have lost the majority of their outer Hydrogen envelope, which produce Type IIb and Ib SNe.

In MESA IV, three options existed to treat fallback:

1. Set the velocity of all inward-moving material with negative total energy to be zero, which creates a hydrostatic shell that can be excised from the ejecta before handing off to the radiation hydrodynamics code `STELLA` to calculate SN observables.

2. During the shock propagation phase, remove material at the inner boundary (IB) if it has negative velocity (i.e. if it is infalling).

3. Remove material at the IB if it is moving with negative velocity and also has net negative energy (i.e. it is bound and infalling).

However, triggering fallback based only on conditions in the innermost zone can lead to problems. For example, in many models at lower explosion energies, while the innermost zone may have negative cell-centered velocity, it can be in thermal contact with neighboring zones. Therefore to remove cells solely based upon their having negative velocity creates a vacuum at the IB which can remove energy and mass which could otherwise remain in the ejecta. Moreover, energy deposited at the IB by any inward-propagating shock can cause the innermost zones to have positive total energy, while being surrounded by a larger amount of material with net negative energy. Because of this, in some models, checking only if the innermost zone is bound before triggering fallback can lead to bound material piling up on top of a small number of cells with positive total energy. If not removed this can lead to a globally bound hydrostatic shell building up in the center, which might interact with the ejecta and affect concentrations of important species such as H and ^{56}Ni, thus affecting SN properties. Such a region can also lead to numerical problems if not properly excised before handing off to radiative transfer codes such as `STELLA`.

Paxton et al. (2019) (MESA 5) introduces two new user controls to better account for material which could fall onto the central object during the hydrodynamical evolution of low explosion energy core-collapse SNe. First, a new criterion is implemented to select which material is excised from the model.[1] At each timestep, `MESA` calculates the integrated total energy from the innermost cell to cell j above it:

$$E_j = \sum_{i=\text{inner}}^{j} \left[e_i - \frac{Gm_i}{r_i} + \frac{1}{2}u_i^2 \right] \mathrm{d}m_i, \tag{A.1}$$

where for cell i at mass m_i and radius r_i, e_i is the internal energy in erg g^{-1} and u_i is the velocity in cm s^{-1}. If $E_j < 0$, then there is a bound inner region, and `MESA` continues this calculation outward until it reaches a cell k with local positive total energy ($e_k - Gm_k/r_k + u_k^2/2 > 0$), causing the integral to be at a local minimum. `MESA` deletes material inside this zone, and moves the IB, fixing the inner radius of zone k to be the new radius of the inner boundary `r_center`, and setting the velocity at the inner boundary `v_center`=0. A schematic diagram of this calculation, in a case where fallback is triggered but the innermost zones are unbound, is shown in Figure A.1.

Figure A.2 shows the evolution of the inner boundary for explosions of varying total energy just after the explosion (E_{tot}, defined in Section 2.1), using the new fallback criterion for the M12.9_R766 progenitor model, which has a total energy of -4.4×10^{50} ergs just before the explosion. Nearly all of the mass lost to fallback occurs while the forward-moving shock is in the Helium layer, beginning around the time that the reverse

---

[1] This criterion is triggered when `fallback_check_total_energy` is set to `.true.` in `star_job`.

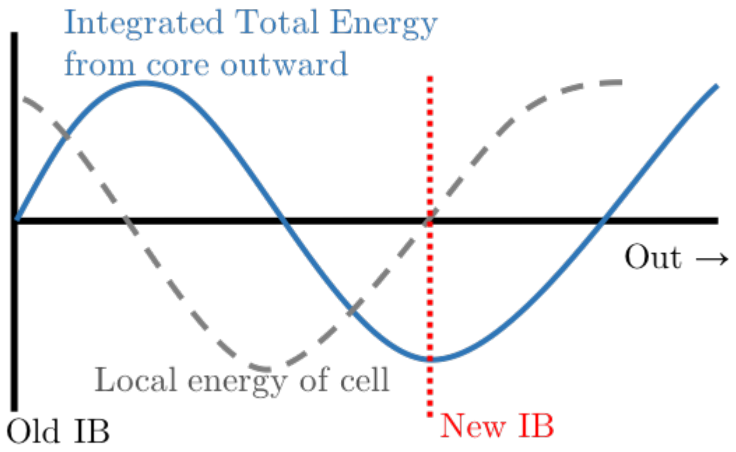

Figure A.1: Diagram for new fallback criterion at a timestep where there is net positive energy near the inner boundary, but a larger, gravitationally bound region above it which will eventually fall back.

shock generated at the interface between the CO/He layers reaches the inner boundary. Because the new fallback prescription sets `v_center`=0 and fixes `r_center` except in the case of fallback being triggered, all changes in the radius of the inner boundary are due to cells being removed from the inner boundary. For sufficiently large explosion energies, little to no fallback is seen, although some cells of negligible mass are removed from the inner boundary, causing the radius of the inner boundary to move outward.

Second, in order to remove any slow-moving, nearly hydrostatic material left near the inner boundary as a result of the fixed `r_center`, which may cause problems after handing off to radiation hydrodynamic codes (see Figure A.4), `MESA` allows the user to specify a minimum innermost velocity for material which gets included in the final ejecta profile that is handed off to `STELLA`.[2] `MESA` will then exclude all material beneath the

---

[2] This is controlled by the`star_job` inlist parameter `stella_skip_inner_v_limit`, which is the minimum velocity of the inner ejecta to include in the profile handed off to `STELLA` in units of cm s^{-1}.

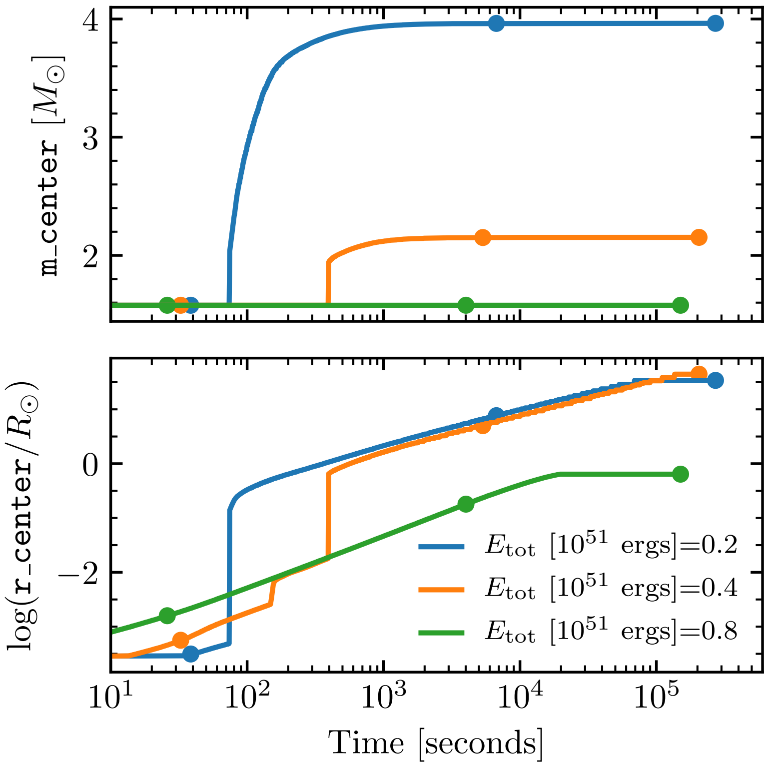

Figure A.2: Evolution of the mass (upper panel) and radial (lower panel) coordinate of the inner boundary for the new fallback prescription for the M12.9_R766 progenitor model from MESA IV for explosions of increasing energy. Colored dots correspond to times that the forward shock crosses a sharp compositional gradient: entering the He layer, entering the H layer, and shock breakout. Because the fallback prescription holds `r_center` fixed and `v_center`$= 0$, all changes in `r_center` result from inner cells being removed from the model.

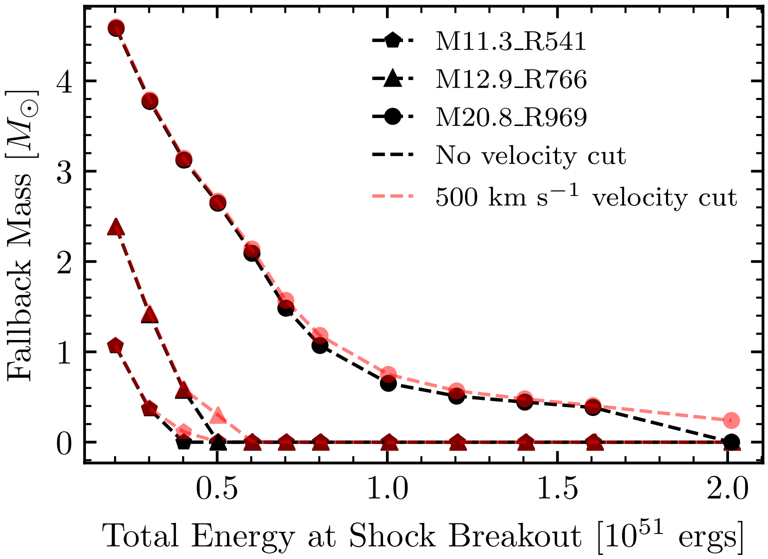

Figure A.3: Mass of fallback material at shock breakout as a function of the total energy of the exploded model at the time of shock breakout for three different progenitor models exploded with 12 different explosion energies. Results are shown for the new integrated energy fallback criterion with no additional velocity cut (black points), and the same criterion with a 500 km s^{-1} velocity cut at shock breakout (red points).

innermost zone that has velocity greater than this velocity cut. This can lead to a small amount of additional mass which is excluded from the final ejecta profile at handoff.

The result of both modifications is shown in Figure A.3, for three different models exploded at 12 different explosion energies. This can be loosely compared with Figure 6 of Perna et al. (2014). Included are the M12.9_R766 and M11.3_R541 models from our standard suite, as well as an additional model, named M20.8_R969, which has binding energy -8.4×10^{50} ergs just before the explosion, included in order to demonstrate an explosion in a more massive star where there would be more fallback material due to more strongly bound core material. Generally, models with and without a velocity cut end with roughly the same amount of fallback. In cases where the explosion energy is just

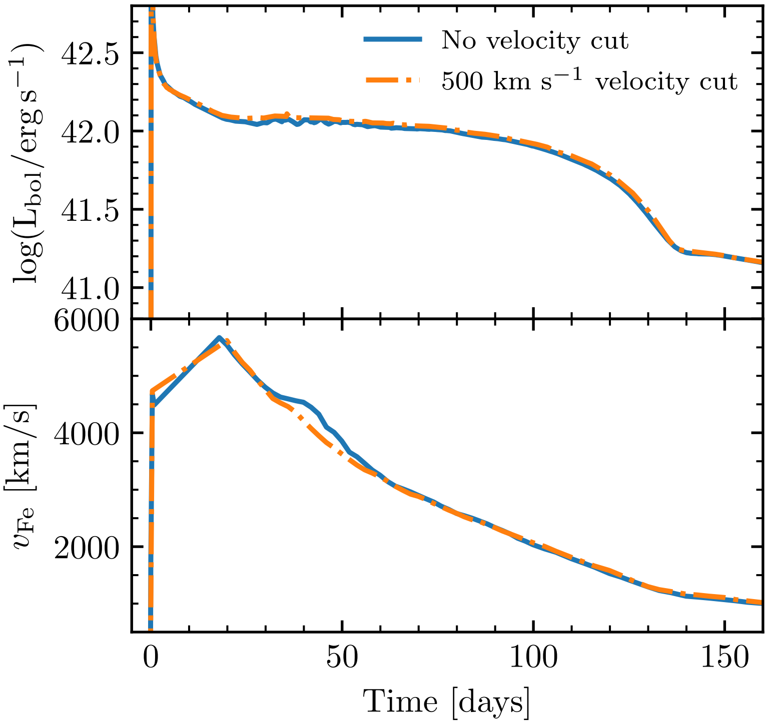

Figure A.4: Effects of a velocity cut on `STELLA` light curves and Fe II 5169Å line velocities for our M12.9_R766 progenitor model exploded with $E_{\mathrm{tot}} = 5.0 \times 10^{51}$ ergs and a nickel mass $M_{\mathrm{Ni}} = 0.042 M_{\odot}$, where we see a noticeable difference between the mass of fallback material with and without a velocity cut ($\approx 0.3 M_{\odot}$).

barely enough to unbind all of the mass, the velocity cut can remove a small additional amount of material. However, as seen in Figure A.4, even in this case, a suitable velocity cut between 100 - 500 km s^{-1} has very little effect on light curve properties and the photospheric evolution of the SN, and can greatly reduce numerical artifacts which may arise from an inward-propagating shock hitting the inner boundary in `STELLA`. Such a cut also can lead to a factor of 10 or more speedup in number of timesteps required to produce a light curve.

Appendix B

Extension of the Plateau due to Ni-56 Decay

We start with the thermodynamic equation, where a fluid is heated by nuclear decay (in our case, of ^{56}Ni) with complete trapping

$$TdS = dE + PdV = L_{\rm nuc} dt \tag{B.1}$$

In a 1-zone, radiation-dominated regime, we can express $P = E/3V$ and $V = 4\pi(vt)^3/3$. Assuming homology, $dV/V = 3dt/t$, and this becomes

$$\frac{1}{t} d(Et) = L_{\rm nuc} dt. \tag{B.2}$$

To find the total energy at time t, integrate from from $t_{\rm SB}$ to obtain:

$$E(t) = E_0 \frac{t_{\rm SB}}{t} + \frac{1}{t} \int_{t_{\rm SB}}^{t} t' L_{\rm nuc} \, dt', \tag{B.3}$$

where $L_{\rm nuc}$ is due to the ^{56}Ni → ^{56}Co → ^{56}Fe decay chain, following Nadyozhin (1994):

$$L_{\rm nuc} = \frac{N_{\rm Ni} Q_{\rm Ni}}{\tau_{\rm Ni}} \exp\left(\frac{-t}{\tau_{\rm Ni}}\right) + \frac{N_{\rm Ni} Q_{\rm Co}}{\tau_{\rm Co} - \tau_{\rm Ni}} \left[\exp\left(\frac{-t}{\tau_{\rm Co}}\right) - \exp\left(\frac{-t}{\tau_{\rm Ni}}\right)\right], \tag{B.4}$$

where $N_{\rm Ni} = M_{\rm Ni}/(56\,{\rm amu})$, $\tau_{\rm X}$ is the lifetime of radioactive species X, and $Q_{\rm X}$ is the energy per decay of species X.

Assuming only ^{56}Ni is produced in the explosion and all ^{56}Co comes from ^{56}Ni decay, the contribution to the internal energy due to the ^{56}Ni decay chain over the lifetime of the SN is

$$E_{\rm tot,Ni} = \frac{1}{t_{\rm p}} \int_{t_{\rm SB}}^{t_{\rm p}} t L_{\rm nuc}\, dt. \tag{B.5}$$

We now make a few approximations: First, by the end of the plateau, ^{56}Ni has undergone many decay times. Thus we take $t_{\rm SB} \to 0$ and $t_{\rm p}/\tau_{\rm Ni} \to \infty$ when in the bounds of our integrals. However, the decay time of ^{56}Co is 111.3 days, which is comparable to $t_{\rm p}$. Thus we approximate $t_{\rm p}/\tau_{\rm Co} \approx 1$ when in the bounds of our integrals. Outside the integrals, we assume that the time to shock breakout is roughly the expansion time, $t_{\rm SB} \approx t_{\rm e}$, where, as in Section 2.2,

$$t_{\rm e} = R_0/v_{\rm e},$$
$$v_{\rm e} = \sqrt{\frac{2E_{\rm exp}}{M_{\rm ej}}} \approx 3.16 \times 10^8 M_{10} E_{51} \text{ cm s}^{-1}.$$

Any numerical quantities are, in reality, dependent on the specifics of the relevant timescales. Here we aim primarily to capture the relevant scaling relationships, fitting against our models to find appropriate numerical prefactors.

Computing these integrals and simplifying, we find that

$$E_{\rm int}(t_{\rm p}) = \frac{E_0\, t_e}{t_{\rm p}} + \frac{N_{\rm Ni}}{t_{\rm p}}\left[Q_{\rm Ni}\tau_{\rm Ni} + Q_{\rm Co}\left(\frac{0.26\tau_{\rm Co}^2 - \tau_{\rm Ni}^2}{\tau_{\rm Co} - \tau_{\rm Ni}}\right)\right] \tag{B.6}$$

$$= \frac{E_0\, t_e}{t_{\rm p}} \times f_{\rm rad}, \text{ where} \tag{B.7}$$

$$f_{\rm rad} \equiv 1 + \frac{N_{\rm Ni}}{t_e E_0}\left(Q_{\rm Ni}\tau_{\rm Ni} + Q_{\rm Co}\tau'_{\rm Co}\right) \text{ and} \tag{B.8}$$

$$\tau'_{\rm Co} \equiv \left(\frac{0.26\tau_{\rm Co}^2 - \tau_{\rm Ni}^2}{\tau_{\rm Co} - \tau_{\rm Ni}}\right), \tag{B.9}$$

noting that E_0, the internal energy at $t_{\rm SB}$, is roughly half the total energy of the explosion (mentioned as a comment in K&W), we set $E_0 = E_{\rm exp}/2$.

We can re-express $f_{\rm rad}$ as

$$f_{\rm rad} = 1 + \frac{M_{\rm Ni}}{E_0}\frac{\tau_{\rm Ni}}{t_e}\left(q_{\rm Ni} + q_{\rm Co}\frac{\tau'_{\rm Co}}{\tau_{\rm Ni}}\right) \tag{B.10}$$

where $q_{\rm X}$ is the specific (per gram) energy released by the decay of species X; in this case $q_{\rm X} = Q_{\rm X}/56\,{\rm amu}$.

Following Nadyozhin (1994), we use $Q_{\rm Ni} = 1.75$ MeV/nucleon, $Q_{\rm Co} = 3.73$ MeV/nucleon, $\tau_{\rm Ni} = 8.8$ days, and $\tau_{\rm Co} = 111.3$ days. We thus find that

$$f_{\rm rad} \approx 1 + 7.0\left(M_{{\rm Ni},\odot}\, E_{51}^{-1/2}\, R_{500}^{-1}\, M_{10}^{-1/2}\right). \tag{B.11}$$

This argument ignores the effects of the distribution of ^{56}Ni, as we necessarily have assumed in this simple 1-zone model that the nickel is distributed evenly throughout the ejecta. If the heat from the ^{56}Ni decay is trapped inside the core of the star until that material becomes optically thin, then this would further extend the duration of the plateau. Thus, we should treat the factor of 7.0 as a rough lower bound, rather than an expectation.

We can also recast Equation (B.11) in terms of ET and $\eta_{\rm Ni}$. Although our derivation assumes all internal energy is trapped to be radiated away, and the Shussman et al. (2016a) derivation of ET assumes that all energy is radiated away, this is just a difference in terms and not a difference in physics. Thus at $t = t_{\rm p}$, plugging in $ET = E_0 t_{\rm SB} \approx E_0 t_e$ and $\eta_{\rm Ni} = \left(\int_{t_{\rm SB}}^{t_{\rm p}} t L_{\rm nuc}\, dt \right) / ET$ to Equation (B.3), we recover

$$E_{\rm int}(t_{\rm p}) = E_0 \frac{t_e}{t_{\rm p}} + \frac{ET\, \eta_{\rm Ni}}{t_{\rm p}} \approx \frac{E_0\, t_e}{t_{\rm p}} (1 + \eta_{\rm Ni}), \tag{B.12}$$

so $f_{\rm rad} \approx 1 + \eta_{\rm Ni}$.

Appendix C

MLT Calibration Details and Sensitivities

In MLT, as deployed by Henyey et al. (1965), the optical thickness of a bubble is $\omega = \kappa\rho\ell$, akin to $\tau_{\rm b}$ discussed in §5.3.4, which is typically comparable to the optical depth to the surface (τ) when the opacity is not changing drastically. The convective efficiency parameter is then given by

$$\gamma = \frac{\nabla - \nabla_{\rm e}}{\nabla_{\rm e} - \nabla_{\rm ad}} = \gamma_0 v_c \tag{C.1}$$

where $\gamma_0 = c_p\rho/\left(8\sigma_{\rm SB}T^3\theta\right)$, $\theta = \omega/(1+y\omega^2)$, and y depends on the geometry of the bubble. We solve for γ via the cubic equation

$$\gamma + \gamma^2 + \phi\gamma^3 = \frac{gHQ\left(\alpha\gamma_0^2\right)}{\nu}\left(f\nabla_{\rm rad} - \nabla_{\rm ad}\right), \tag{C.2}$$

where $F = L_{\rm surf}/4\pi r^2 = 16\sigma T^4\nabla_{\rm rad}/3\kappa\rho H$ defines $\nabla_{\rm rad}$ as the gradient required to carry all flux by radiative diffusion, $\phi = \frac{3}{4}f\omega\theta$, $\nu = 8$, and $f = 1$ as $\tau > \tau_{\rm crit} \gg 1$ inside

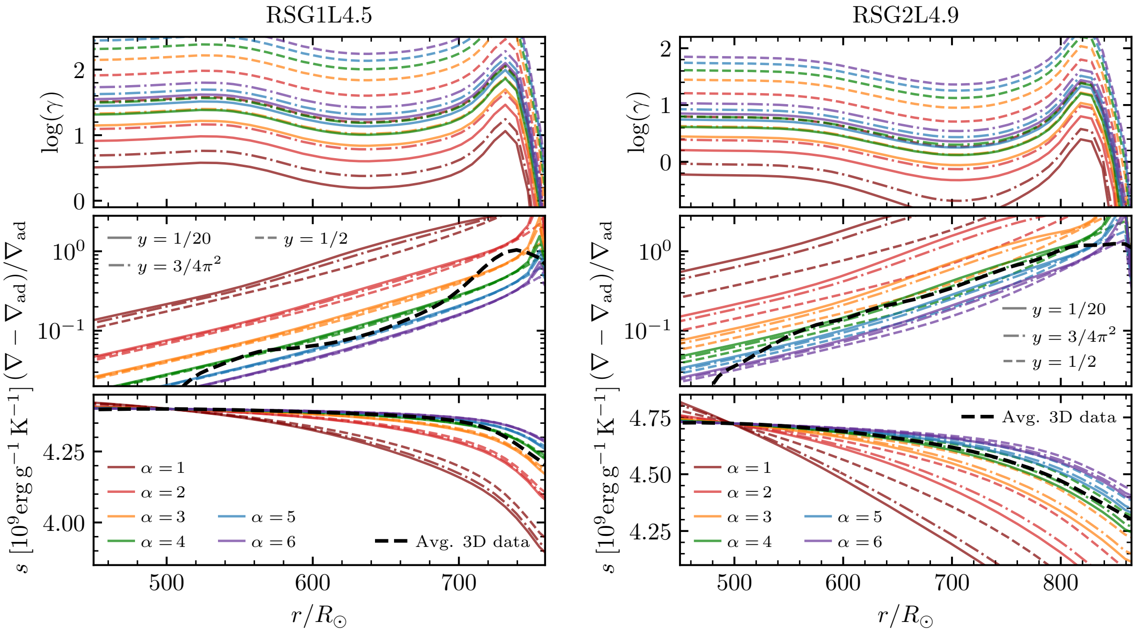

Figure C.1: Comparison of efficiency factor γ (upper panels), superadiabaticity (middle panels) and entropy (lower panels) derived from our 3D models (black dashed lines) and from MLT (pastel colored lines) against profiles derived from RSG1L4.5 (left) and RSG2L4.9 (right) when $P_{\rm turb}$ is neglected. Each color corresponds to a different value of α, and each linestyle (solid, dash-dot, dashed) corresponds to a different value of y.

$R_{\rm corr}$. For an ideal gas + radiation, EOS properties vary with $\alpha_P \equiv P_{\rm rad}/P_{\rm gas}$ (Mihalas & Mihalas 1984; P subscript added to distinguish from $\alpha = \ell/H$), with

$$c_P = \frac{5}{2}\frac{k_B}{\mu m_p}\left(1 + 8\alpha_P + \frac{32}{5}\alpha_P^2\right), \tag{C.3}$$

and

$$\nabla_{\rm ad} = \frac{1 + 5\alpha_P + 4{\alpha_P}^2}{\frac{5}{2} + 20\alpha_P + 16{\alpha_P}^2}. \tag{C.4}$$

From this, MLT yields a prediction for ∇, which we compare to the gradients derived from $\rho_{\rm 1D}$ and $T_{\rm 1D}$:

$$\nabla = \frac{(1+\gamma)f\nabla_{\rm rad} + \phi\gamma^2\nabla_{\rm ad}}{1 + \gamma + \phi\gamma^2}. \tag{C.5}$$

Following Henyey et al. (1965), we use $y = 3/4\pi^2$ for our analysis in §5.4. We repeated this analysis varying y for values ranging from 1/20, which is the prediction for a parabolic temperature distribution inside a bubble, to 1/2 (as used by Böhm-Vitense (1958)) which corresponds to a linear temperature distribution (see discussion in Henyey et al., 1965). This is shown in Fig. C.1. The region inside $r < R_{\rm corr}$ is in the limit of higher ω ($\tau \gg 1$), so $\gamma_0 \underset{\sim}{\propto} y$, leading to a strong y-dependence in γ for both models. However, variations in γ lead to large differences in ∇ and s only when $\gamma \lesssim 1$. For the RSG1L4.5-derived model, ω is sufficiently large due to the slightly larger envelope mass and smaller radius, so fractional changes in γ do not lead to significant differences in ∇ or the recovered entropy profile except for the $\alpha = 1$ line (which disagrees with the model profiles). In the case of RSG2L4.9, ω is smaller due to the lower envelope density, so changes in y do affect the recovered superadiabatic gradient and entropy profiles even for $\alpha \lesssim 3$, with higher values of y leading to smaller $\nabla - \nabla_{\rm ad}$ and flatter s profiles. However, this effect is still not substantial for $\alpha = 4$, which also agrees best with the model. In all cases, variation in ∇ and s introduced by varying y is dominated by differences for different α.

Comparing the luminosity carried by radiation recovered by MLT to the time-averaged shell-averaged F_r of the 3D models, there is good agreement between the MLT values in both models within ≈5% for $r \lesssim 700 R_\odot$. Outside of those locations, however, MLT predicts dramatically lower radiative fluxes and higher convective fluxes due to the presence of the H opacity peak. This is not surprising for two reasons. First, we consider κ from a 1D OPAL call, where the H opacity spike is sharper (see the bottom panels of Fig. 5.15) compared to the 3D data which displays a bimodal distribution of κ in a given radial shell. Secondly, different values of τ along different lines of sight where there is appreciable bimodality (see Figs. 5.15,5.16) allow radiation to carry more of the flux than one would expect from radiative diffusion through a 1D shell with no density fluctuations.

Appendix D

Thermodynamic Gradient Definitions Including Turbulent Pressure

For convenience, we reproduce here how the MLT equations in 5.4.2 include the Henyey et al. (1965) turbulent-pressure correction. For clarity, the definitions of the relevant gradients are given in Table D.1.

Including a turbulent pressure in the expression for the total pressure, $P_{\rm tot} = P_{\rm therm} + P_{\rm turb}$, the modified Eq. C.1 becomes

$$\gamma = \frac{\nabla - \nabla_{\rm e}}{\nabla_{\rm e} - \nabla'_{\rm ad}} = \gamma_0 v_c, \tag{D.1}$$

Eq. C.2 becomes

$$\gamma + \gamma^2 + \phi\gamma^3 = \frac{gHQ\left(\alpha\gamma_0^2\right)}{\nu}\left(f\nabla_{\rm rad} - \nabla'_{\rm ad}\right), \tag{D.2}$$

gradient	Definition
∇	actual $\frac{\mathrm{d}\ln T}{\mathrm{d}\ln P}$ in the star
∇_{therm}	$\frac{\mathrm{d}\ln T}{\mathrm{d}\ln P_{\mathrm{therm}}}$ in the star
∇_{e}	∇ inside an eddy as it moves
∇_{ad}	$\left(\frac{\mathrm{d}\ln T}{\mathrm{d}\ln P_{\mathrm{therm}}}\right)_{\mathrm{ad}}$ from the fluid properties
∇'_{ad}	$\nabla_{\mathrm{ad}} \times \frac{d\ln P_{\mathrm{th}}}{d\ln P_{\mathrm{tot}}}$
∇_{rad}	∇ required to carry L_{surf} solely by radiative diffusion$= (3L_{\mathrm{surf}}\kappa\rho H)/(64\pi r^2\sigma_{\mathrm{SB}}T^4)$

Table D.1: Definitions of various gradients discussed in this work.

and Eq. C.5 becomes

$$\nabla = \frac{(1+\gamma)f\nabla_{\mathrm{rad}} + \phi\gamma^2\nabla'_{\mathrm{ad}}}{1+\gamma+\phi\gamma^2}. \tag{D.3}$$

Bibliography

Afsariardchi, N., & Matzner, C. D. 2018, ApJ, 856, 146

Anderson, J. P., González-Gaitán, S., Hamuy, M., et al. 2014, ApJ, 786, 67

Andrews, J. E., Sand, D. J., Valenti, S., et al. 2019, ApJ, 885, 43

Antoni, A., & Quataert, E. 2022, MNRAS, 511, 176

Arnett, W. D. 1980, ApJ, 237, 541

Arroyo-Torres, B., Wittkowski, M., Chiavassa, A., et al. 2015, A&A, 575, A50

Asif, A., Barschke, M., Bastian-Querner, B., et al. 2021, in Society of Photo-Optical Instrumentation Engineers (SPIE) Conference Series, Vol. 11821, Society of Photo-Optical Instrumentation Engineers (SPIE) Conference Series, 118210U

Baklanov, P. V., Blinnikov, S. I., & Pavlyuk, N. N. 2005, Astronomy Letters, 31, 429

Barker, B. L., Harris, C. E., Warren, M. L., O'Connor, E. P., & Couch, S. M. 2022, ApJ, 934, 67

Bayless, A. J., Fryer, C., Brown, P. J., et al. 2022, ApJ, 931, 15

Bellm, E. C., Kulkarni, S. R., Graham, M. J., et al. 2019, PASP, 131, 018002

Bersten, M. C., Benvenuto, O., & Hamuy, M. 2011, ApJ, 729, 61

Bersten, M. C., & Hamuy, M. 2009, ApJ, 701, 200

Blinnikov, S., Lundqvist, P., Bartunov, O., Nomoto, K., & Iwamoto, K. 2000, ApJ, 532, 1132

Blinnikov, S., & Sorokina, E. 2004, Ap&SS, 290, 13

Blinnikov, S. I., Eastman, R., Bartunov, O. S., Popolitov, V. A., & Woosley, S. E. 1998, ApJ, 496, 454

Blinnikov, S. I., Röpke, F. K., Sorokina, E. I., et al. 2006, A&A, 453, 229

Böhm-Vitense, E. 1958, ZA, 46, 108

Brayton, R. K., Gustavson, F. G., & Hachtel, G. D. 1972, Proceedings of the IEEE, 60, 98

Brown, T. M., Baliber, N., Bianco, F. B., et al. 2013a, PASP, 125, 1031

—. 2013b, PASP, 125, 1031

Brun, A. S., & Palacios, A. 2009, ApJ, 702, 1078

Burrows, A., Radice, D., & Vartanyan, D. 2019, MNRAS, 538

Calzavara, A. J., & Matzner, C. D. 2004, MNRAS, 351, 694

Castor, J. I. 1970, MNRAS, 149, 111

Chatys, F. W., Bedding, T. R., Murphy, S. J., et al. 2019, MNRAS, 487, 4832

Chevalier, R. A., & Klein, R. I. 1978, ApJ, 219, 994

Chiavassa, A., Casagrande, L., Collet, R., et al. 2018a, A&A, 611, A11

Chiavassa, A., Collet, R., Casagrande, L., & Asplund, M. 2010a, A&A, 524, A93

Chiavassa, A., Freytag, B., Masseron, T., & Plez, B. 2011a, A&A, 535, A22

Chiavassa, A., Freytag, B., & Schultheis, M. 2018b, A&A, 617, L1

Chiavassa, A., Haubois, X., Young, J. S., et al. 2010b, A&A, 515, A12

Chiavassa, A., Plez, B., Josselin, E., & Freytag, B. 2009, A&A, 506, 1351

Chiavassa, A., Pasquato, E., Jorissen, A., et al. 2011b, A&A, 528, A120

Chiavassa, A., Norris, R., Montargès, M., et al. 2017, A&A, 600, L2

Chiavassa, A., Kravchenko, K., Millour, F., et al. 2020, A&A, 640, A23

Chugai, N. N. 1991, Soviet Astronomy Letters, 17, 210

Chun, S.-H., Yoon, S.-C., Jung, M.-K., Kim, D. U., & Kim, J. 2018, ApJ, 853, 79

Colgate, S. A. 1968, Canadian Journal of Physics Supplement, 46, 476

Conroy, C., Strader, J., van Dokkum, P., et al. 2018, ApJ, 864, 111

Couch, S. M., Pooley, D., Wheeler, J. C., & Milosavljević, M. 2011, ApJ, 727, 104

Couch, S. M., Warren, M. L., & O'Connor, E. P. 2020, ApJ, 890, 127

Coughlin, E. R., Quataert, E., Fernández, R., & Kasen, D. 2018, MNRAS, 477, 1225

Cox, J. P., & Giuli, R. T. 1968, Principles of stellar structure

Crockett, R. M., Smartt, S. J., Pastorello, A., et al. 2011, MNRAS, 410, 2767

Curtis, S., Ebinger, K., Fröhlich, C., et al. 2019, ApJ, 870, 2

Curtis, S., Wolfe, N., Fröhlich, C., et al. 2021, ApJ, 921, 143

Davies, B., & Beasor, E. R. 2018, MNRAS, 474, 2116

—. 2020a, MNRAS, 496, L142

—. 2020b, MNRAS, 493, 468

Davis, A., Jones, S., & Herwig, F. 2019, MNRAS, 484, 3921

Dessart, L., Hillier, D., & Audit, E. 2017, A&A, 605, A83

Dessart, L., & Hillier, D. J. 2010, MNRAS, 405, 2141

—. 2019, A&A, 625, A9

Dessart, L., Hillier, D. J., Waldman, R., & Livne, E. 2013, MNRAS, 433, 1745

Dorch, S. B. F. 2004, A&A, 423, 1101

Dorn-Wallenstein, T. Z., Levesque, E. M., Neugent, K. F., et al. 2020, ApJ, 902, 24

Drout, M. R., Massey, P., & Meynet, G. 2012, ApJ, 750, 97

Duffell, P. C. 2016, ApJ, 821, 76

Ebinger, K., Curtis, S., Fröhlich, C., et al. 2019, ApJ, 870, 1

Ebinger, K., Curtis, S., Ghosh, S., et al. 2020, ApJ, 888, 91

Ekström, S., Georgy, C., Eggenberger, P., et al. 2012, A&A, 537, A146

Eldridge, J. J., Guo, N. Y., Rodrigues, N., Stanway, E. R., & Xiao, L. 2019, PASA, 36, e041

Ertl, T., Janka, H. T., Woosley, S. E., Sukhbold, T., & Ugliano, M. 2016, ApJ, 818, 124

Faran, T., Goldfriend, T., Nakar, E., & Sari, R. 2019, ApJ, 879, 20

Farmer, R., Fields, C. E., Petermann, I., et al. 2016, ApJS, 227, 22

Farrell, E. J., Groh, J. H., Meynet, G., & Eldridge, J. J. 2020, MNRAS, 494, L53

Feast, M. W., Catchpole, R. M., Carter, B. S., & Roberts, G. 1980, MNRAS, 193, 377

Flaugher, B., Diehl, H. T., Honscheid, K., et al. 2015, AJ, 150, 150

Förster, F., Moriya, T. J., Maureira, J. C., et al. 2018, Nature Astronomy, 2, 808

Freytag, B., & Höfner, S. 2008, A&A, 483, 571

Freytag, B., Liljegren, S., & Höfner, S. 2017, A&A, 600, A137

Freytag, B., Steffen, M., & Dorch, B. 2002, Astronomische Nachrichten, 323, 213

Freytag, B., Steffen, M., Ludwig, H. G., et al. 2012, Journal of Computational Physics, 231, 919

Freytag, B., Steffen, M., Wedemeyer-Böhm, S., et al. 2010, CO5BOLD: COnservative COde for the COmputation of COmpressible COnvection in a BOx of L Dimensions with l=2,3

Fuller, J. 2017, MNRAS, 470, 1642

Garnavich, P. M., Tucker, B. E., Rest, A., et al. 2016, ApJ, 820, 23

Gear, C. W. 1971, Numerical initial value problems in ordinary differential equations, Prentice-Hall Series in Automatic Computation (Prentice-Hall, Engelwood Cliffs)

Georgy, C., Ekström, S., Eggenberger, P., et al. 2013, A&A, 558, A103

Gezari, S., Dessart, L., Basa, S., et al. 2008, ApJL, 683, L131

Gezari, S., Rest, A., Huber, M. E., et al. 2010, ApJL, 720, L77

Gezari, S., Jones, D. O., Sanders, N. E., et al. 2015, ApJ, 804, 28

Ghosh, S., Wolfe, N., & Fröhlich, C. 2022, ApJ, 929, 43

Glebbeek, E., Gaburov, E., de Mink, S. E., Pols, O. R., & Portegies Zwart, S. F. 2009, A&A, 497, 255

Goldberg, J. A., & Bildsten, L. 2020, ApJL, 895, L45

Goldberg, J. A., Bildsten, L., & Paxton, B. 2019, ApJ, 879, 3

—. 2020, ApJ, 891, 15

Goldberg, J. A., Jiang, Y.-F., & Bildsten, L. 2022, ApJ, 929, 156

Goldberg, J. A., Jiang, Y.-F., & Bildsten, L. 2022, ApJ, 933, 164

Guo, J. H., & Li, Y. 2002, ApJ, 565, 559

Gutiérrez, C. P., Anderson, J. P., Hamuy, M., et al. 2017a, ApJ, 850, 89

—. 2017b, ApJ, 850, 90

Hamuy, M. 2003, ApJ, 582, 905

Hamuy, M., & Pinto, P. A. 2002, ApJL, 566, L63

Harris, C. R., Millman, K. J., van der Walt, S. J., et al. 2020, Nature, 585, 357–362

Hauschildt, P. H., Baron, E., & Allard, F. 1997, ApJ, 483, 390

Haynie, A., & Piro, A. L. 2021, ApJ, 910, 128

Heger, A., Jeannin, L., Langer, N., & Baraffe, I. 1997, A&A, 327, 224

Hendry, M. A., Smartt, S. J., Crockett, R. M., et al. 2006, MNRAS, 369, 1303

Henyey, L., Vardya, M. S., & Bodenheimer, P. 1965, ApJ, 142, 841

Hillier, D. J., & Dessart, L. 2019, A&A, 631, A8

Hiramatsu, D., Howell, D. A., Moriya, T. J., et al. 2021a, ApJ, 913, 55

Hiramatsu, D., Howell, D. A., Van Dyk, S. D., et al. 2021b, Nature Astronomy, 5, 903

Hopkins, P. F., Kereš, D., Oñorbe, J., et al. 2014, MNRAS, 445, 581

Hopkins, P. F., Wetzel, A., Kereš, D., et al. 2018a, MNRAS, 480, 800

Hopkins, P. F., Wetzel, A., Kereš, D., et al. 2018b, Monthly Notices of the Royal Astronomical Society, 477, 1578

Hosseinzadeh, G., Valenti, S., McCully, C., et al. 2018, ApJ, 861, 63

Hunter, J. D. 2007, Computing in Science Engineering, 9, 90

Iglesias, C. A., & Rogers, F. J. 1996, ApJ, 464, 943

Iglesias, C. A., Rogers, F. J., & Wilson, B. G. 1992, ApJ, 397, 717

Irwin, C. M., Linial, I., Nakar, E., Piran, T., & Sari, R. 2021, MNRAS, 508, 5766

Ita, Y., Tanabé, T., Matsunaga, N., et al. 2004, MNRAS, 347, 720

Ivezić, Ž., Kahn, S. M., Tyson, J. A., et al. 2019, ApJ, 873, 111

Janka, H.-T. 2012, Annual Review of Nuclear and Particle Science, 62, 407

Jerkstrand, A., Fransson, C., Maguire, K., et al. 2012, A&A, 546, A28

Jermyn, A. S., Bauer, E. B., Schwab, J., et al. 2022, arXiv e-prints, arXiv:2208.03651

Jiang, Y.-F. 2021, ApJS, 253, 49

Jiang, Y.-F., Cantiello, M., Bildsten, L., Quataert, E., & Blaes, O. 2015, ApJ, 813, 74

Jiang, Y.-F., Cantiello, M., Bildsten, L., et al. 2018, Nature, 561, 498

Jiang, Y.-F., Stone, J. M., & Davis, S. W. 2014, ApJS, 213, 7

Johnson, S. A., Kochanek, C. S., & Adams, S. M. 2018, MNRAS, 480, 1696

Joyce, M., & Chaboyer, B. 2018, ApJ, 856, 10

Joyce, M., Leung, S.-C., Molnár, L., et al. 2020, ApJ, 902, 63

Jurcevic, J. S., Pierce, M. J., & Jacoby, G. H. 2000, MNRAS, 313, 868

Kasen, D., Thomas, R. C., & Nugent, P. 2006, ApJ, 651, 366

Kasen, D., & Woosley, S. E. 2009, ApJ, 703, 2205

Katz, B., Budnik, R., & Waxman, E. 2010, ApJ, 716, 781

Katz, B., Sapir, N., & Waxman, E. 2012, ApJ, 747, 147

Khazov, D., Yaron, O., Gal-Yam, A., et al. 2016, ApJ, 818, 3

Kilpatrick, C. D., & Foley, R. J. 2018, MNRAS, 481, 2536

Kippenhahn, R., Weigert, A., & Weiss, A. 2013, Stellar Structure and Evolution; 2nd ed., Astronomy and astrophysics library (Berlin: Springer)

Kiss, L. L., Szabó, G. M., & Bedding, T. R. 2006, MNRAS, 372, 1721

Kochanek, C. S. 2019, MNRAS, 483, 3762

—. 2020, MNRAS, 493, 4945

Kochanek, C. S., Beacom, J. F., Kistler, M. D., et al. 2008, ApJ, 684, 1336

Kochanek, C. S., Fraser, M., Adams, S. M., et al. 2017a, MNRAS, 467, 3347

Kochanek, C. S., Shappee, B. J., Stanek, K. Z., et al. 2017b, Publications of the Astronomical Society of the Pacific, 129, 104502

Kozyreva, A., Janka, H.-T., Kresse, D., Taubenberger, S., & Baklanov, P. 2022, MNRAS, 514, 4173

Kozyreva, A., Nakar, E., & Waldman, R. 2018, MNRAS, 483, 1211

Kozyreva, A., Nakar, E., Waldman, R., Blinnikov, S., & Baklanov, P. 2020, MNRAS, 494, 3927

Kravchenko, K., Chiavassa, A., Van Eck, S., et al. 2019, A&A, 632, A28

Kravchenko, K., Van Eck, S., Chiavassa, A., et al. 2018, A&A, 610, A29

Kravchenko, K., Wittkowski, M., Jorissen, A., et al. 2020, A&A, 642, A235

Kravchenko, K., Jorissen, A., Van Eck, S., et al. 2021, A&A, 650, L17

Kumar, B., Pandey, S. B., Eswaraiah, C., & Kawabata, K. S. 2016, MNRAS, 456, 3157

Landau, L. D., & Lifshitz, E. M. 1987, Fluid Mechanics, Second Edition: Volume 6 (Course of Theoretical Physics), 2nd edn., Course of theoretical physics / by L. D. Landau and E. M. Lifshitz, Vol. 6 (Butterworth-Heinemann)

Lasher, G. J., & Chan, K. L. 1979, ApJ, 230, 742

Leonard, D. C., & Filippenko, A. V. 2001, PASP, 113, 920

Leonard, D. C., Filippenko, A. V., Ardila, D. R., & Brotherton, M. S. 2001, ApJ, 553, 861

Leonard, D. C., Filippenko, A. V., Ganeshalingam, M., et al. 2006, Nature, 440, 505

Levesque, E. M., Massey, P., Olsen, K. A. G., et al. 2006, ApJ, 645, 1102

Li, W., Van Dyk, S. D., Filippenko, A. V., & Cuillandre, J.-C. 2005, PASP, 117, 121

Liljegren, S., Höfner, S., Freytag, B., & Bladh, S. 2018, A&A, 619, A47

Linial, I., & Sari, R. 2019, Physics of Fluids, 31, 097102

Lisakov, S. M., Dessart, L., Hillier, D. J., Waldman, R., & Livne, E. 2017, MNRAS, 466, 34

Litvinova, I. Y., & Nadyozhin, D. K. 1983, Astrophysics and Space Science, 89, 89

LSST Science Collaboration, Abell, P. A., Allison, J., et al. 2009, arXiv e-prints, arXiv:0912.0201 [astro-ph.IM]

Ludwig, H.-G., Freytag, B., & Steffen, M. 1999, A&A, 346, 111

Magic, Z. 2016, A&A, 586, A88

Magic, Z., Collet, R., Asplund, M., et al. 2013a, A&A, 557, A26

Magic, Z., Collet, R., Hayek, W., & Asplund, M. 2013b, A&A, 560, A8

Magic, Z., Weiss, A., & Asplund, M. 2015, A&A, 573, A89

Marinacci, F., Vogelsberger, M., Pakmor, R., et al. 2018, MNRAS, 480, 5113

Martinez, L., & Bersten, M. C. 2019, A&A, 629, A124

Martinez, L., Bersten, M. C., Anderson, J. P., et al. 2022a, A&A, 660, A40

—. 2022b, A&A, 660, A41

Martinez, L., Anderson, J. P., Bersten, M. C., et al. 2022c, A&A, 660, A42

Masci, F. J., Laher, R. R., Rusholme, B., et al. 2019, PASP, 131, 018003

Massey, P., Neugent, K. F., Levesque, E. M., Drout, M. R., & Courteau, S. 2021, AJ, 161, 79

Massey, P., & Olsen, K. A. G. 2003, AJ, 126, 2867

Matzner, C. D., Levin, Y., & Ro, S. 2013, ApJ, 779, 60

Matzner, C. D., & McKee, C. F. 1999, ApJ, 510, 379

Meynet, G., & Maeder, A. 1997, A&A, 321, 465

Meynet, G., Chomienne, V., Ekström, S., et al. 2015, A&A, 575, A60

Mihalas, D. 1978, Stellar atmospheres, 2nd edition

Mihalas, D., & Mihalas, B. W. 1984, Foundations of radiation hydrodynamics

Montargès, M., Cannon, E., Lagadec, E., et al. 2021, Nature, 594, 365

Moriya, T., Tominaga, N., Blinnikov, S. I., Baklanov, P. V., & Sorokina, E. I. 2011, MNRAS, 415, 199

Moriya, T. J., Förster, F., Yoon, S.-C., Gräfener, G., & Blinnikov, S. I. 2018, MNRAS, 476, 2840

Moriya, T. J., Yoon, S.-C., Gräfener, G., & Blinnikov, S. I. 2017, MNRAS, 469, L108

Morozova, V., Piro, A. L., Fuller, J., & Van Dyk, S. D. 2019, arXiv e-prints, arXiv:1912.10050

Morozova, V., Piro, A. L., Renzo, M., & Ott, C. D. 2016, ApJ, 829, 109

Morozova, V., Piro, A. L., & Valenti, S. 2017, ApJ, 838, 28

Morozova, V., Radice, D., Burrows, A., & Vartanyan, D. 2018, ApJ, 861, 10

Mosumgaard, J. R., Ball, W. H., Silva Aguirre, V., Weiss, A., & Christensen-Dalsgaard, J. 2018, MNRAS, 478, 5650

Mosumgaard, J. R., Jørgensen, A. C. S., Weiss, A., Silva Aguirre, V., & Christensen-Dalsgaard, J. 2020, MNRAS, 491, 1160

Müller, T., Prieto, J. L., Pejcha, O., & Clocchiatti, A. 2017, ApJ, 841, 127

Murphy, J. W., Mabanta, Q., & Dolence, J. C. 2019, MNRAS, 489, 641

Nadezhin, D. K. 1980, Ap&SS, 69, 115

Nadyozhin, D. K. 1994, ApJS, 92, 527

Nagao, T., Cikota, A., Patat, F., et al. 2019, MNRAS, 489, L69

Nagy, A. P., Ordasi, A., Vinkó, J., & Wheeler, J. C. 2014, A&A, 571, A77

Nagy, A. P., & Vinkó, J. 2016, A&A, 589, A53

Naiman, J. P., Pillepich, A., Springel, V., et al. 2018, MNRAS, 477, 1206

Nakar, E., Poznanski, D., & Katz, B. 2016, ApJ, 823, 127

Nakar, E., & Sari, R. 2010, ApJ, 725, 904

Nelson, D., Pillepich, A., Springel, V., et al. 2018, MNRAS, 475, 624

Norris, R. P., Baron, F. R., Monnier, J. D., et al. 2021, ApJ, 919, 124

Nugis, T., & Lamers, H. J. G. L. M. 2000, A&A, 360, 227

Owocki, S. P., & Sundqvist, J. O. 2018, MNRAS, 475, 814

Patton, R. A., & Sukhbold, T. 2020, MNRAS, 499, 2803

Paxton, B., Bildsten, L., Dotter, A., et al. 2011, ApJS, 192, 3

Paxton, B., Cantiello, M., Arras, P., et al. 2013, ApJS, 208, 4

Paxton, B., Marchant, P., Schwab, J., et al. 2015, ApJS, 220, 15

Paxton, B., Schwab, J., Bauer, E. B., et al. 2018, ApJS, 234, 34

Paxton, B., Smolec, R., Schwab, J., et al. 2019, ApJS, 243, 10

Pejcha, O., & Prieto, J. L. 2015a, ApJ, 799, 215

—. 2015b, ApJ, 806, 225

Percy, J. R., & Khatu, V. C. 2014, Journal of the American Association of Variable Star Observers (JAAVSO), 42, 1

Perego, A., Hempel, M., Fröhlich, C., et al. 2015, ApJ, 806, 275

Perna, R., Duffell, P., Cantiello, M., & MacFadyen, A. I. 2014, ApJ, 781, 119

Pillepich, A., Nelson, D., Hernquist, L., et al. 2018a, MNRAS, 475, 648

Pillepich, A., Springel, V., Nelson, D., et al. 2018b, MNRAS, 473, 4077

Plez, B., & Chiavassa, A. 2013, Memorie della Societa Astronomica Italiana Supplementi, 24, 105

Popov, D. V. 1993, ApJ, 414, 712

Porter, D. H., & Woodward, P. R. 2000, ApJS, 127, 159

Quataert, E., Lecoanet, D., & Coughlin, E. R. 2019, MNRAS, 485, L83

Quataert, E., & Shiode, J. 2012, MNRAS, 423, L92

Rabinak, I., & Waxman, E. 2011, ApJ, 728, 63

Ren, Y., & Jiang, B.-W. 2020, ApJ, 898, 24

Ren, Y., Jiang, B.-W., Yang, M., & Gao, J. 2019, ApJS, 241, 35

Renzo, M., Ott, C. D., Shore, S. N., & de Mink, S. E. 2017, A&A, 603, A118

Ricks, W., & Dwarkadas, V. V. 2019, ApJ, 880, 59

Rui, L., Wang, X., Mo, J., et al. 2019, MNRAS, 485, 1990

Rybicki, G. B., & Lightman, A. P. 1986, Radiative Processes in Astrophysics

Sagiv, I., Gal-Yam, A., Ofek, E. O., et al. 2014, AJ, 147, 79

Sahu, D. K., Anupama, G. C., Srividya, S., & Muneer, S. 2006, MNRAS, 372, 1315

Salaris, M., & Cassisi, S. 2015, A&A, 577, A60

Sandoval, M. A., Hix, W. R., Messer, O. E. B., Lentz, E. J., & Harris, J. A. 2021, ApJ, 921, 113

Sapir, N., Katz, B., & Waxman, E. 2011, ApJ, 742, 36

—. 2013, ApJ, 774, 79

Sapir, N., & Waxman, E. 2017, ApJ, 838, 130

Schawinski, K., Justham, S., Wolf, C., et al. 2008, Science, 321, 223

Schultz, W. C., Bildsten, L., & Jiang, Y.-F. 2020, ApJ, 902, 67

—. 2022, ApJL, 924, L11

Schwarzschild, M. 1975, ApJ, 195, 137

Shappee, B. J., Prieto, J. L., Grupe, D., et al. 2014, ApJ, 788, 48

Shussman, T., Nakar, E., Waldman, R., & Katz, B. 2016a, arXiv e-prints, arXiv:1602.02774 [astro-ph.HE]

Shussman, T., Waldman, R., & Nakar, E. 2016b, arXiv e-prints, arXiv:1610.05323 [astro-ph.HE]

Smartt, S. J. 2009, ARA&A, 47, 63

—. 2015, Publications of the Astronomical Society of Australia, 32, e016

Sobolev, V. V. 1960, Moving envelopes of stars

Sonoi, T., Ludwig, H. G., Dupret, M. A., et al. 2019, A&A, 621, A84

Soraisam, M. D., Bildsten, L., Drout, M. R., et al. 2020, ApJ, 893, 11

Soraisam, M. D., Bildsten, L., Drout, M. R., et al. 2018, ApJ, 859, 73

Soumagnac, M. T., Ganot, N., Irani, I., et al. 2020, ApJ, 902, 6

Spada, F., Demarque, P., & Kupka, F. 2021, MNRAS, 504, 3128

Spetsieri, Z. T., Bonanos, A. Z., Yang, M., Kourniotis, M., & Hatzidimitriou, D. 2019, A&A, 629, A3

Springel, V., Pakmor, R., Pillepich, A., et al. 2018, MNRAS, 475, 676

Stein, R. F., & Nordlund, A. 1989, ApJL, 342, L95

Stein, R. F., & Nordlund, Å. 1998, ApJ, 499, 914

Stockinger, G., Janka, H. T., Kresse, D., et al. 2020, MNRAS, 496, 2039

Stone, J. M., Tomida, K., White, C. J., & Felker, K. G. 2020, ApJS, 249, 4

Stothers, R. 1969, ApJ, 156, 541

Stothers, R., & Leung, K. C. 1971, A&A, 10, 290

Stothers, R. B., & Chin, C.-W. 1995, ApJ, 440, 297

Sukhbold, T., Ertl, T., Woosley, S. E., Brown, J. M., & Janka, H.-T. 2016, ApJ, 821, 38

Sukhbold, T., Woosley, S. E., & Heger, A. 2018, ApJ, 860, 93

Suzuki, A., Maeda, K., & Shigeyama, T. 2016, ApJ, 825, 92

Suzuki, A., & Shigeyama, T. 2010, ApJL, 717, L154

Szalai, T., Vinkó, J., Könyves-Tóth, R., et al. 2019, ApJ, 876, 19

Szczygieł, D. M., Gerke, J. R., Kochanek, C. S., & Stanek, K. Z. 2012, ApJ, 747, 23

Szczygieł, D. M., Stanek, K. Z., Bonanos, A. Z., et al. 2010, AJ, 140, 14

Takáts, K., & Vinkó, J. 2012, MNRAS, 419, 2783

Takáts, K., Pignata, G., Pumo, M. L., et al. 2015, MNRAS, 450, 3137

Tan, J. C., Matzner, C. D., & McKee, C. F. 2001, ApJ, 551, 946

Thyng, K. M., Greene, C. A., Hetland, R. D., Zimmerle, H. M., & DiMarco, S. F. 2016, Oceanography

Tikhonov, N. A. 2014, Astronomy Letters, 40, 537

Tinyanont, S., Ridden-Harper, R., Foley, R. J., et al. 2022, MNRAS, 512, 2777

Townsend, R. H. D., Goldstein, J., & Zweibel, E. G. 2018, MNRAS, 475, 879

Townsend, R. H. D., & Teitler, S. A. 2013, MNRAS, 435, 3406

Trampedach, R., Asplund, M., Collet, R., Nordlund, Å., & Stein, R. F. 2013, ApJ, 769, 18

Trampedach, R., Stein, R. F., Christensen-Dalsgaard, J., Nordlund, Å., & Asplund, M. 2014a, MNRAS, 442, 805

—. 2014b, MNRAS, 445, 4366

Tsang, B. T. H., Goldberg, J. A., Bildsten, L., & Kasen, D. 2020, ApJ, 898, 29

Tsang, B. T. H., Kasen, D., & Bildsten, L. 2022, arXiv e-prints, arXiv:2207.13090

Tsvetkov, D. Y., Shugarov, S. Y., Volkov, I. M., et al. 2018, Astronomy Letters, 44, 315

Utrobin, V. P. 2007, A&A, 461, 233

Utrobin, V. P., Wongwathanarat, A., Janka, H.-T., & Müller, E. 2017, ApJ, 846, 37

Valenti, S., Howell, D. A., Stritzinger, M. D., et al. 2016, MNRAS, 459, 3939

Vallely, P. J., Kochanek, C. S., Stanek, K. Z., Fausnaugh, M., & Shappee, B. J. 2021, MNRAS, 500, 5639

van der Velden, E. 2020, The Journal of Open Source Software, 5, 2004

Van Dyk, S. D. 2017, Philosophical Transactions of the Royal Society of London Series A, 375, 20160277

Van Dyk, S. D., Zheng, W., Maund, J. R., et al. 2019, ApJ, 875, 136

Vink, J. S., de Koter, A., & Lamers, H. J. G. L. M. 2001, A&A, 369, 574

Virtanen, P., Gommers, R., Oliphant, T. E., et al. 2020, Nature Methods, 17, 261

Wang, L., Howell, D. A., Höflich, P., & Wheeler, J. C. 2001, ApJ, 550, 1030

Wang, L., & Wheeler, J. C. 2008, ARA&A, 46, 433

Waxman, E., & Katz, B. 2017, in Handbook of Supernovae, ed. A. W. Alsabti & P. Murdin, 967

Weaver, T. A., & Woosley, S. E. 1980, in American Institute of Physics Conference Series, Vol. 63, Supernovae Spectra, ed. R. Meyerott & H. G. Gillespie, 15

Wolf, W. M., & Schwab, J. 2017, wmwolf/py_mesa_reader: Interact with MESA Output

Wongwathanarat, A., Müller, E., & Janka, H.-T. 2015, A&A, 577, A48

Woosley, S. E., & Weaver, T. A. 1988, PhR, 163, 79

Wu, S., & Fuller, J. 2021, ApJ, 906, 3

Yang, M., & Jiang, B. W. 2011, ApJ, 727, 53

Yang, M., & Jiang, B. W. 2012, ApJ, 754, 35

Yang, M., Bonanos, A. Z., Jiang, B.-W., et al. 2018, A&A, 616, A175

Yoon, S.-C., & Cantiello, M. 2010, ApJ, 717, L62

Zapartas, E., de Mink, S. E., Justham, S., et al. 2021, A&A, 645, A6

Zel'dovich, Y. B., & Raizer, Y. P. 1967, Physics of shock waves and high-temperature hydrodynamic phenomena